Numerical study of biomass combustion of a grate-firing furnace with emphasis on gas-phase combustion modeling

By

Mohammadreza Farokhi

A Thesis submitted to the Faculty of Graduate Studies of

The University of Manitoba

in partial fulfillment of the requirements of the degree of

Doctor of Philosophy

Department of Mechanical Engineering

University of Manitoba

Winnipeg

Abstract

As a renewable energy resource, biomass is slowly becoming a substitute for traditional fossil fuels due to global warming concerns and limited availability of fossil fuel resources. Direct combustion of biomass in grate-firing furnaces is the most widespread established technology to produce power and heat from biomass fuel. This is driven by low investment cost of grate-firing furnaces and their capability of burning biomass over a wide range of particles size, ash and moisture contents. Nevertheless, relatively small scale grate-firing biomass furnaces suffer from generating high level of emissions (e.g., CO and NO_x) due mainly to their smaller volume, and consequently poor mixing between fuel and injected air, and also shorter residence time of combustion. Hence, further improvements need to be developed and implemented in their design in order to maximize thermal efficiency and further reduce pollutant emissions. Such improvements require comprehensive understanding of biomass conversion as well as gas-phase combustion of volatiles in the free room above the bed, known as a freeboard.

The present research aims to develop a reliable gas-phase combustion scheme suitable for modeling biomass combustion in grate-firing furnaces by means of computational fluid dynamics (CFD). The study investigates the influence of chemical mechanisms and turbulence models on temperature field and species concentrations predicted by CFD platform. Alongside the aforementioned parameters, a substantial effort is devoted to understand the role of the combustion model in modeling gas-phase biomass combustion, which resulted in the development of a novel combustion approach.

The performance of the proposed combustion model is examined under different flow-field conditions relevant to practical biomass furnaces. The results of this research clearly reveal

superior performance of the proposed combustion model compared to currently available models used for the simulation of biomass combustion. Particularly, the performance of the new model is more highlighted in the predicting minor species such as CO and NO.

Acknowledgements

First, I have to thank my research supervisor Dr. Madjid Birouk who offered his continuous advice and encouragement throughout the course of this thesis. Without his assistance and dedicated involvement in every step throughout the process, this thesis would have never been accomplished. I really would like to appreciate him for his support and understanding over these past four years.

I also would like to thank my committee members, Dr. Eric Croiset, Dr. Scott Ormiston, and Dr. Aniruddha Gole for their efforts put into reviewing the thesis, and their invaluable comments and suggestions. I would also like to thank Mr. Etienne Lafleur, project engineer at Biovalco Inc., who helped me understand the engineering application of this project.

I would like to acknowledge the financial support received from the Natural Sciences and Engineering Research Council of Canada (NSERC) and the industrial partner, Biovalco Inc., as well as the Faculty of Graduate studies at the University of Manitoba.

Carrying out my thesis demanded more than academic aids, and I have many friends to express my appreciation for their friendship. I would also like to thank the following members of the Energy and Combustion Laboratory at the University of Manitoba for their help and fruitful discussions; Dr. Meghdad Saediamiri, Dr. Mohsen Broumand, Zahra Taban, Mahmoud Moussa Abdelazim, Sviatoslaw Karnaoukh and Trevor Mazak, as well as all the other students in the lab and the staff of Mechanical Engineering Department.

Finally, and most importantly, none of this was possible without the encouragement and supports that I received from my family who have sacrificed their lives for me and provided unconditional

love and care. I would like to dedicate this thesis to my beloved parents and sister. They have always given me the determination to overcome many trying moments to pursue my dreams.

Table of Contents

List of figures:

List of tables:

List of Abbreviations

Nomenclature

A_p	particle's surface area, m^2
C_{D1}	EDC model constant
C_{D2}	EDC model constant
C_γ	EDC Model fine scale length fraction constant
C_τ	EDC Model constant
D_c	intermittency parameter
$D_{w,m}$	diffusion coefficient of vapor in bulk gas, $m^2\ s^{-1}$
E_Δ	energy per unit mass at characteristic scale, $J\ kg^{-1}$
E_η	energy per unit mass at Kolmogorov scale, $J\ kg^{-1}$
h	convective heat transfer coefficient, $W\ m^{-2}\ K^{-1}$
h_{fg}	latent heat of water, $J\ kg^{-1}$
k	turbulent Kinetic Energy, $m^2\ s^{-2}$; thermal conductivity, $W\ m^{-1}\ K^{-1}$
K_c	mass transfer coefficient, $m\ s^{-1}$
l^*	fine structure length scale, m
l'	integral length scale, m
m_p	particle's mass, kg
N_η	number of locally generated dissipative scales
Pr	Prandtl number
R_i	reaction rate of species i, $kg\ m^{-3}\ s^{-1}$
Re^*	Reynolds number in fine structure

Re_t	turbulent Reynolds number
Re_{tmin}	EDC minimum turbulent Reynolds number
Sc	Schmidt number
T_p	particle's temperature, K
T_t	turbulent time scale, s
u^*	velocity scale corresponding to the fine structure, m s^{-1}
u'	velocity scale corresponding energy containing range of the spectrum, m s^{-1}
u_η	Kolmogorov velocity scale, m s^{-1}
Y_i	mean mass fraction of species i
Y_i^*	fine structure mass fraction of species i
$Y_{w,s}$	mass fractions of vapor at the surface of the particle
Y_w	mass fractions of vapor at bulk gas

Greek symbol

θ	radiation temperature, K
ε	turbulent dissipation rate, m^2 s^{-3}- emissivity
σ	Stefan-Boltzmann constant, W m^{-2} K^{-4}
ϑ	kinematic viscosity, m^2 s^{-1}
ϑ_Δ	kinematic viscosity of surrounding fluid, m^2 s^{-1}
ρ	density, kg m^{-3}
τ_{EDC}	EDC time scale, s

τ_η	Kolmogorov time scale, s
τ_{mix}	characteristic mixing time scale, s
τ^*	EDC time scale, s
γ	length fraction of fine scale
γ^*	volume fraction of a fine structure
$\gamma°$	volume fraction of a surrounding fluid
γ_λ^2/τ^*	Mass exchange rate between fine structure and surrounding fluid, s^{-1}
η	Kolmogorov length scale, m

Acronym

CFD	Computational fluid dynamics
Da	Damköhler Number
DPM	Discrete phase model
EBU	Eddy Break-up
EDC	Eddy dissipation concept
EDM	Eddy dissipation model
FBM	Fuel-bound nitrogen
FGR	Flue gas recirculation
FKR	Finite kinetic rate
FM	Fractal modeling
GRI	Gas research institute
ISAT	In-Situ adaptive tabulation
LHV	Low heating value

MILD	Moderate to intense low-oxygen dilution
PFR	Plug flow reactor
PSR	Perfectly stirred reactor
RANS	Reynolds Averaged Navier-Stokes
RKE	Realizable $k-\varepsilon$
RNG	Renormalization group
RSM	Reynolds stress model
SFM	Steady flamelet model
UFM	Unsteady flamelet model
WSGG	Weighted-sum-of-gray-gas

Declaration of the academic achievement

The outline of this thesis follows "sandwich format" whose guidelines are appointed by the Faculty of Graduate Studies, University of Manitoba. It merges five individual papers prepared for publication in peer-reviewed journals. Chapter 1 contains an introduction about the problem statement and the thesis contributions; Chapters 2 to 6 are manuscripts containing an abstract, introduction, methods, results and discussion; Chapter 7 provides the conclusions of the work and recommendations for future research directions. UDF codes developed and used in this study are provided in Appendices.

Chapters 2 to 5 are papers which have already been published, and Chapter 6 has just been submitted for publication in a peer-reviewed journal. The contribution of M. Farokhi consisted mainly of developing the mathematical model and UDF C++ codes, performing comparison and validation between numerical predictions and experimental measurements, data analysis, and preparing the first drafts of manuscripts. My supervisor (Dr. Birouk) supervised the research, including constant feedback during the development of the model, analysis of data and manuscripts preparations. My Co-author (Dr. Tabet) contribution in chapter 4 consisted of providing invaluable discussion of the results presented in the manuscript.

Copyright notice

1. With permission from American Chemical Society:

   M. Farokhi and M. Birouk, "Application of Eddy Dissipation Concept for modeling biomass combustion, Part 1: Assessment of the model coefficients" *Energy and Fuels*, 2016 (30) pp-10789-10799.

2. With permission from American Chemical Society:

   M. Farokhi and M. Birouk, "Application of Eddy Dissipation Concept for modeling biomass combustion, Part 2: Gas-phase combustion modeling of a small-scale fixed bed furnace" *Energy and Fuels*, 2016 (30) pp-10800-10808.

3. With permission from Elsevier:

   M. Farokhi, M. Birouk and F. Tabet, "A computational study of a small-scale biomass burner: The influence of chemistry, turbulence and combustion sub-models", *Energy Conversion and Management*, 2017 (143), pp 203-217.

4. With permission from Elsevier:

   M. Farokhi and M. Birouk, "A new EDC approach for modeling turbulence/chemistry interaction in the gas-phase of biomass combustion", *Fuel*, 2018 (220), pp 420-436.

5. With permission from Elsevier

   M. Farokhi and M. Birouk, "Modeling of the gas-phase combustion of a grate-firing biomass furnace using an extended approach of Eddy Dissipation Concept", *Fuel*, 2018 (227), pp 412-423.

Chapter 1: Introduction

1.1 Background and scope

Traditional fossil fuel-based energy sources cover most of the global energy demand including land, sea and air transportation, as well as industrial and residential combustion plants. However, global warming can be regarded as one of the most serious consequences of pollutants such as carbon monoxide (CO), carbon dioxide (CO_2), nitrous oxide (NO_x), etc., which are generated as result of combusting fossil fuels [1]. This environmental impact along with the limited availability of these type of energy sources have attracted growing interest in renewable energy sources such as biomass [2].

Biomass refers to organic material of plant origin, which stores solar energy through photosynthesis. Biomass is CO_2-neutral, meaning the amount of carbon dioxide absorbed by plants during photosynthesis is equal to the emitted amount in the environment when these plants are later used to produce energy [3]. Direct combustion of biomass in furnaces is the most widespread established technology to produce power and heat from biomass fuel [1, 2, 4]. As a renewable energy source, it is expected that biomass combustion devices (e.g., fluidised and grate-firing biomass furnaces) produce far less emissions into the environment compared to those of fossil fuels. However, like other combustion technologies, biomass combustion can also produce harmful pollutants due primarily to incomplete combustion. This happens even more in small scale biomass furnaces due to the fact that they have a small volume. Consequently, this smaller furnace volume results in poor air/fuel mixing as well as shorter available time for complete combustion

[4]. Therefore, more research is needed to further develop this technology in order to meet national and international emissions regulations.

Biomass furnaces are commonly classified in three types of furnaces for direct combustion of biomass fuel, known as fluidised bed, pulverised bed and fixed bed systems [5]. In fluidised bed systems, solid biomass particles are mixed with an inert material (mostly sand), and suspended in a partial volume of the furnace through high velocity of the injected air. The inert material acts as a thermal storage medium that significantly improves heat transfer and mixing between fuel and air. This results in a uniform temperature throughout the furnace and also a significant benefits to the emissions [6]. Fluidised bed furnaces, on the other hand, suffers from high costs of operation control and maintenance compared to other types of biomass furnaces [5].

Pulverised beds are primarily designed for coal combustion systems. For this technology, fuel particles are injected into the furnace and suspended throughout the volume of the furnace via the injection of high velocity airflow. For this to occur, the size of particles must be small enough, preferably below 100 μm [5]. In comparison to coal, it is difficult to prepare biomass particles to be as small as coal particles. Moreover, because the energy density in biomass is much lower than that of coal, the biomass furnace must have greater volume and must use more biomass fuel to produce similar amount of energy that a coal furnace is capable of producing. Low moisture and high volatile content biomass particles are preferable in this type of furnaces [5, 6].

Fixed bed systems are the oldest technologies to employ biomass for heat generation. Fixed bed furnaces have the fuel bed resting on either a moving or a fixed grate. This technology is commonly known as a grate-firing biomass furnace. Grate-firing furnaces are widely used due to their flexibility in burning fuels with various chemical and physical properties [7]. In addition, the cost of manufacturing this type of furnaces is the lowest among all biomass combustion technologies

[8]. Grate-firing furnaces consist of two main regions known as the grate (or bed) and out of the bed (also known as freeboard). In the first zone (i.e., bed), biomass produces combustible and non-combustible gases (known as volatiles) as well as char particles through some conversion processes. A part of the combustion takes place through a set of heterogeneous reaction mechanisms within the bed, where a fresh under-bed airflow (i.e., primary air supply) interacts with char particles. Combustion occurs mainly in the freeboard where combustible gases released from the bed are mixed with freshly injected oxidizer (usually air) into the freeboard. Table 1-1 presents a brief comparison between all types of biomass furnaces.

Table 1-1. Comparison of bed technologies for biomass furnaces [9, 7]

	Fixed-bed	**Fluidised bed**	**Pulverised bed**
Fuel averaged size [mm]	Less than 20	Less than 10	Less than 1.0
Plant power [MW_{th}]	Less than 20	Higher than 30	Higher than 30
Furnace temperature [K]	1350-1650	1050-1200	1500-1800
Air inlet velocity [m/sec]	0.1-1.2	3.6-10	Higher than 10
Moisture content [%wt]	Less than 65	Less than 65	Less than 20
Operation cost	Low	High	High
Most common issues	High level of emissions, non-homogenous combustion and temperature	Sensitive to air/fuel distribution within furnace, particles emissions	Sensitive to fuel, small size fuel particles, particles emissions

1.2 Research aims

1.2.1 Problem definition and motivations

When biomass furnaces enable conditions of complete combustion, they are known as a friendly low-emissions technology. However, biomass furnaces suffer from generating both solid particles as well as gas pollutant emissions into the environment. Gas pollutant emissions is a common issue of grate-firing devices. This technology (i.e., grate-firing bed) is often labelled as a “high unburned

carbon" furnace, due to incomplete mixing of the fuel and oxidizer (air). This leads to a significant part of the solid fuel remaining as unburned char [8, 10], which consequently reduces thermal efficiency. Also, incomplete combustion raises the levels of emissions of CO and other unburned hydrocarbons.

The other major gas pollutant produced in grate-firing furnaces is related to NO_x. NO_x emissions in a combustion device are commonly generated through three main pathways; thermal NO_x, prompt NO_x and fuel NO_x [11]. The main source of this pollutant in a grate-firing biomass furnace is the nitrogen content in fuel particles released from bed during the conversion process [12, 13].

Biomass combustion technologies clearly has a negative impact on the environment via gas emissions. This is particular the case when using small scale grate-firing furnaces due to the fact that they have a small volume of freeboard, resulting in a shorter available time for complete combustion, as well as smaller portion of the freeboard to achieve acceptable level of mixing between combustible volatile gases and fresh air [4, 14]. Therefore, further improvements should be carried out on grate-firing combustion devices, which requires a comprehensive understanding of biomass conversion in the bed as well as volatile combustion in the freeboard [14, 15, 16]. Hence, this research focuses on these issues of biomass combustion related to small-scale grate-firing furnaces.

1.2.2 An over-view of research methodologies on grate-firing biomass combustion

Studies on grate-firing biomass combustion have been performed using both physical experiments and computational fluid dynamics (CFD). The physical experiments not only provide valuable insights into the phenomena, but they also provide invaluable data which can be used as inputs for modeling and simulation studies [8]. However, the high costs along with technical challenges have restricted physical testing mostly to pilot lab-scale devices. Recently published experimental

investigations in the literature have mostly focused on the influence of operating conditions (e.g., over fire air staging ratio, over fire and under fire FGR ratio, etc.) on the level of gas emissions produced from biomass furnaces (e.g., Refs. [13, 17, 18]).

CFD methods, on the other hand, can help achieving a reasonable understanding of biomass combustion by introducing a virtual view of the process in a computational domain. In contrast to experimental studies, CFD tools are noticeably cheaper [19]. CFD modeling of a grate-firing furnace is divided into modeling biomass conversion within the bed (i.e., bed model), and modeling the gas-phase mixing, combustion and pollutant formation in the freeboard (i.e., gas-phase reacting flow simulation) [8].

In CFD simulation of the grate-firing biomass combustion, the decomposition of solid biomass fuel as well as char reactions on the grate can be described using a bed model, which introduces the fuel inlet boundary for simulating the gas-phase combustion in the freeboard [16]. The bed model requires the fuel properties (e.g., elemental mass fraction of carbon, hydrogen, oxygen, etc., contained in a solid biomass particle) as inputs data. These required fuel properties can be obtained from experimental tests on biomass samples, known as proximate analysis and ultimate analysis [20]. Table 1-2 illustrates the properties of biomass particles obtained from experimental tests of different types of biomass. Simple bed models provide species mass fractions and temperature profiles at the fuel inlet boundary of the freeboard. These profiles can be obtained using the experimental measurements of temperature and species concentration above the bed, or calculated on the basis of mass and energy conservation between inlet (i.e., primary air and raw biomass particles) and outlet (i.e., released volatile gases) of the bed [19, 21, 14]. Complex bed models use separate sub-models that compute each conversion process to provide local temperature and mass

fractions of released species [22, 23]. These conversion processes can be introduced as drying process, devolatilization process, and char combustion, which will be briefly described as below.

At first, the water content within a particle is vaporized and the particle becomes dry. This process is called drying. When a dried particle absorbs enough heat, it produces non-combustible and combustible gases such as carbon dioxide, hydrogen and light hydrocarbons, as well as heavy hydrocarbons. The gases produced in this process are called volatiles, and this process is known as devolatilization. After the devolatilization process, the char remains in the particle. Through local mixing between oxygen and char in the bed, a set of heterogeneous reactions occurs on the surface of the remainder of the particle.

Table 1-2. Biomass composition based on proximate and ultimate analysis [20]

Type	**Proximate analysis**				**Ultimate analysis**				**LHV[1]**
	Moisture	Ash	Volatile	Char	C	H	O	N	[MJ/kg]
Straw	9.6-12.4	<4.7	<79.3	16.3	47.2	7.8	44	1.0	23.3
Pinewood	7.5	0.1	79.7	12.7	47.9	6.2	38.3	7.6	18.0
Willow	7.2	>1	74.7	16.2	45.9	6.6	>39.3	<8.0	18.3
Wood pellet	8.1	0.3	78.2	13.4	47.8	5.8	45.7	>0.1	16.6

Freeboard consists of the volume of a grate-firing furnace situated above the bed section. The bed provides fuel inlet conditions into the freeboard. Secondary air, and in some cases tertiary air, provide additional inlet airflows into the freeboard. The mixing process occurs between the combustible (volatiles) gases coming out of the bed and fresh air from the injected secondary and tertiary airflows in the freeboard. CFD simulation of the freeboard consists of modeling the flow-field and gas-phase combustion process in the freeboard.

[1] LHV: Lower heating value

1.2.3 Motivation of the research

Numerical modeling of grate-firing biomass furnaces requires a reliable CFD platform capable of simulating this type of combustion devices. The reliability of CFD predictions strongly depends on the sub-models used for modeling the conversion processes within the bed section as well as the freeboard combustion (e.g., turbulent sub-model, chemical kinetic reaction mechanism and flow/chemistry interaction sub-model known as combustion models) [15].

The first problem in the numerical modeling of a furnace's freeboard concerns adequate predictions of the flow-field. In most regions of the furnace, flow regime is sufficiently turbulent. However, there exist several regions within the furnaces where the flow regime is weakly turbulent especially in the vicinity of the bed [14, 24]. Therefore, an appropriate turbulence modeling which represents both highly and weakly turbulent flow regimes is vitally important. An overview of the most used turbulence sub-models for grate-firing combustion is reported in [15]. The second issue is related to the influence of chemistry scheme on the numerical predictions. The sensitivity analysis of chemical mechanisms has been performed only in a few published studies on grate-firing biomass combustion (e.g., [15, 25]). Due to the relatively high computational cost of simulating industrial biomass furnace geometries, reduced chemical mechanisms are preferred. Only a few studies examined the effect of detailed chemistry in the modeling of grate-firing biomass combustion (e.g., [16]). The third issue is related to the modeling of the interaction between chemistry and flow-field (also known as combustion modeling). Most of simplified combustion models have been developed for limited conditions such as highly turbulent flow and fast chemistry combustion. However, the reacting flow-field in the freeboard of a furnace can be laminar, weakly or highly turbulent [15, 14, 16]. Also, the formation/reduction of species, such as CO, are known to be slow-forming and cannot be accurately followed by fast chemistry models

[24, 26]. In the case of biomass combustion, classical species transport combustion models are extensively used (e.g., finite kinetic/eddy dissipation model (FKR/EDM) [27], eddy dissipation concept (EDC) [28]). Recently, the mixture fraction based approaches (e.g., Steady/Unsteady flamelet models (SFM/UFM) [29, 30]) have been employed for simulating the gas-phase combustion of a grate-firing biomass furnaces in a few studies (e.g., [15, 16]). However, the application of these models to biomass combustion is limited to small-scale biomass combustors.

Despite numerous studies performed on the combustion scheme (i.e., modeling chemistry and turbulence flow-field, and the interaction between chemistry/flow-field) of grate-firing biomass furnaces, the development of a reliable and computationally affordable combustion scheme is still lacking, especially for the predictions of gas-pollutants, e.g., CO and NO_x. The weakness of the currently available combustion schemes is in the simulation of weakly turbulent reacting flows, as well as reacting flows where chemical and mixing time scales are comparable [31, 15, 32]. In grate-firing combustors, such conditions may occur in the vicinity of the bed, where high temperature volatile gases leave the bed with low velocity and relatively low level of turbulence [33]. Consequently, further research is necessary to develop reliable gas-phase biomass combustion schemes.

1.2.4 Research objectives

The main aim of this thesis is to develop a reliable combustion scheme for simulating gas-phase combustion of grate-firing biomass furnaces. To do so, the role of sub-models, such as turbulence models, chemical kinetic mechanisms and combustion models, on the simulation of the gas-phase of biomass combustion is examined. Specifically, the overall objectives of the present thesis are summarized as follows:

- Examine the benefits, limitations and weaknesses of published combustion models for modeling the gas-phase of biomass combustion.
- Examine the effects of turbulence model and chemical mechanism on the predictions of species concentrations and temperature field of a practical grate-firing biomass furnace.
- Develop a reliable combustion model suitable for a wide range of turbulent flow regimes pertaining to those encountered in practical biomass furnaces.
- Propose and evaluate a reliable and computationally affordable combustion scheme (which encompasses chemical mechanisms, and turbulence and combustion models) for simulating the gas-phase biomass combustion of a grate-firing combustor.

1.3 Outline of the thesis

The objective of the thesis is to develop a numerical CFD code capable of modeling the gas-phase combustion of a grate firing furnace. To do so, different chemical mechanisms, turbulence and combustion sub-models are tested. Since the CFD simulation of the freeboard depends on the adopted bed model, two simplified bed models are tested to account for the conversion of the solid biomass particles within the bed section.

Chapter 2 presents a literature review of the classical species transport combustion models and their applications. Based on this literature review, the EDC model is adopted to account for the interaction of chemistry and the turbulent flow-field, owing to its ability to incorporate detailed chemical kinetic rates. The limitations of the EDC in modeling gas-phase biomass combustion are studied and addressed. In this chapter, a sensitivity analysis is performed on the EDC model's two main coefficients (i.e., fine-scale length fraction coefficient (C_γ), and EDC time scale (C_τ)), with the aim of improving the predictions of the model in different reacting turbulent flow conditions (i.e., weakly and highly turbulent flow conditions).

Based on the conclusion achieved in chapter 2, the values of the EDC model's coefficient are modified for the simulation of a 8kW lab-scale grate-firing biomass combustor, which is adopted from the literature (e.g., [4]). That is, based on the characteristics of turbulent flow-field (e.g., turbulent Reynolds number and turbulent time scale), a method for modifying the values of C_γ and C_τ is introduced and examined. The predictions of both the standard EDC and the EDC with modified coefficients are compared with their experimental counterparts of temperature, major species concentrations (e.g., CO_2 and O_2), and CO gas emissions.

In chapter 4, a group of parametric studies is performed in order to examine the effect of turbulence model, chemical mechanism and combustion model on the gas-phase combustion simulation of the combustor reported in chapter 3. Numerous CFD simulations are performed to assess the effect of the aforementioned parameters. The effect of turbulence model is examined in the predictions of species concentration, velocity and temperature fields using standard, RNG and realizable $k-\varepsilon$ turbulence models. The effect of chemical kinetics is examined on the temperature and species concentrations using three different detailed chemical mechanisms and two reduced chemical mechanisms. The effect of combustion model is examined on the predictions of temperature and species concentrations using two different mixture fraction based combustion models with detailed mechanisms (i.e., SFM, UFM), and the standard EDC and EDC with modified coefficients using reduced chemical mechanisms. This study examines the interplay between the adopted chemical mechanisms, turbulence and combustion sub-models on the gas-phase predictions (i.e., temperature field and species concentrations).

Based on the conclusions of Chapters 4 and 2, an extended EDC model is proposed in Chapter 5. The capability of the proposed model is assessed at different turbulent flow conditions pertaining

to those encountered in practical biomass furnaces. The mathematical evaluation of the extended EDC's parameters has been presented in Appendix E.

Chapter 6 presents a reliable combustion scheme package, which includes the combination of a simplified particle-based bed model, a turbulence model, a reduced chemical mechanism and the extended EDC combustion model. The main focus of this chapter is on the application of the extended EDC, presented in Chapter 5, for modeling the gas-phase biomass combustion of the combustion system described in chapters 3 and 4. The pathways of the formation and reduction of NO pollutant are also investigated. Moreover, to highlight the performance of the proposed model, all the predictions are compared against those of standard EDC and published experimental measurements.

Finally, Chapter 7 summarizes the key findings, implications and limitations of the proposed combustion scheme in this thesis, followed by some recommendations for future work.

1.4 References

[1] M. Momenikouchaksaraei, "Fundamental Study of Single Biomass Particle Combustion," Department of Energy Technology, Aalborg University, Denmark, 2013.

[2] S. Sukumaran and S. Kong, "Modeling fuel NOx formation from combustion of biomass-derived producer gas in a large burner," Combustion and flame, vol. 160, pp. 2159-2168, 2013.

[3] H. Lu, P. Foster, M. Vickers and L. Baxter, "Effects of particle shape and size on devolatilization of biomass particle," Fuel, vol. 89, pp. 1156-1168, 2010.

[4] T. Klason and X. Bai, "Computational study of the combustion process and NO formation in a small-scale wood pelletfurnace," Fuel, vol. 86, pp. 1465-1474, 2007.

[5] T. Klason, Writer, Modelling of Biomass Combustion in Furnaces, PhD thesis. [Performance]. Lund Institute of Technology, Sweden, 2006.

[6] N. Duffy, Writer, Investigation of Biomass Combustion in Grate Furnaces using CFD, PhD thesis. [Performance]. B.E. National university of Ireland, Galway., 2007.

[7] S. Van Loo and J. Koppejan, The Handbook of Biomass Combustion and Co-firing, Earthscan, 2008.

[8] C. Yin, L. Rosendahl and S. Kær, "Grate-firing of biomass for heat and power production," Progress in Energy and Combustion Science, vol. 34, pp. 725-754, 2008.

[9] B. Miller and D. Tillman, "Combustion Engineering Issues for Solid Fuel Systems," Academic Press, Elsevier, 2008.

[10] L. Ruth, "Energy from municipal solid waste: a comparison with coal," Progress in Energy and Combust Science, vol. 24, pp. 545-564, 1998.

[11] J. Warnatz, U. Mass and R. Dibble, Combustion Physical and Chemical Fundamentals, Modeling and Simulation, Experiments, Pollutant Formation, Berlin: Springer, 1995.

[12] P. Glarborg, A. Jensen and J. Johnsson, "Fuel-N conversion in solid fuel fired," Progress in Energy and Combust Science, vol. 29, pp. 89-113, 2003.

[13] E. Houshfar, R. Khalil, T. Lovas and O. Skreiberg, "Enhanced NOx reduction by combined staged air and flue gas recirculation in Biomass grate combustion," Energy and fuels, vol. 26, pp. 3003-3011, 2012.

[14] M. Farokhi and M. Birouk, "Application of eddy dissipation concept for modeling biomass combustion, part 2: gas-phase combustion modeling of a small-scale fixed bed furnace," Energy and fuels, vol. 30, pp. 10800-10808, 2016.

[15] M. Farokhi, M. Birouk and F. Tabet, "A computational study of a small-scale biomass burner: The influence of chemistry, turbulence and combustion sub-models," Energy Conversion and Management, vol. 143, pp. 203-217, 2017.

[16] M. Buchmayr, J. Gruber, M. Hargassner and C. Hochenauer, "A computationally inexpensive CFD approach for small-scale biomass burners equipped with enhanced air staging," Energy Conversion and Management, vol. 115, pp. 32-42, 2016.

[17] E. Houshfar, O. Skreiberg, D. Todorovic, A. Skreiberg, T. Lovas, A. Jovovic and L. Sorum, "NOx emission reduction by staged combustion in grate combustion of biomass fuels and fuel mixtures," Fuel, vol. 98, pp. 29-40, 2012.

[18] F. Qian, C. Chyang, J. Chiou and J. Tso, "Effect of flue gas recirculation (FGR) on NOx emission in a pilot-scale vortexing fluidized-bed combustor," Energy and fuels, vol. 25, pp. 2539-5646, 2011.

[19] J. Chaney, H. Liu and J. Li, "An overview of CFD modelling of small-scale fixed-bed biomass pellet boilers with preliminary results from a somplified approach," Energy Conversion and Management, vol. 63, pp. 149-156, 2012.

[20] H. Khodaei, Y. Al-Abdeli, F. Guzzomi and G. Yeoh, "An overview of processes and considerations in the modeling of fixed-bed biomass combustion," Energy, pp. 946-972, 2015.

[21] C. Yin, L. Rosendahl, S. Kaer, C. Sonnik, S. Hvid and T. Hille, "Mathematical modeling and experimental study of biomass combustion in a 108 MW Grate-Fired Boiler," Energy and Fuels, vol. 22, pp. 1380-1290, 2008.

[22] J. Porterio, J. Collazo, D. Patino, E. Granda, J. Gonzalez and L. Miguez, "Numerical modeling of a biomass pellet boiler," Energy and Fuel, vol. 23, pp. 1067-1075, 2009.

[23] X. Zhang, Q. Chen, R. Bradford, V. Sharifi and J. Swithenbank, "Experimental investigation and mathematical modeling of wood combustion in a moving grate boiler," Fuel Processing Technology, vol. 91, pp. 1491-1499, 2010.

[24] A. Shiehnejadhesar, R. Scharler, R. Mehrabian and I. Obernberger, "Developement and validation of CFD models for gas phase reactions in biomass grate furnaces considering gas streak formation above the packed bed," Fuel processesing Technology., vol. 139, pp. 142-158, 2015.

[25] C. Yin, S. Kaer, L. Rosendahl and S. Hvid, "Co-firing straw with coal in a swirl-stabilized dual-feed burner: modelling and experimental validation," Bioresource Technology., vol. 101, pp. 4169-4178, 2010.

[26] M. Farokhi and M. Birouk, "Application of eddy dissipation concept for modeling biomass combustion, part 1: assessment of the model coefficients," Energy and fuels, vol. 30, pp. 10789-10799, 2016.

[27] B. Magnussen and B. Hjertager, "On the mathematical modeling of turbulent combustion with special emphasis on soot formation and combustion," Proceedings of the Combustion Institute, vol. 16, pp. 719-729, 1977.

[28] B. Magnussen, "On the structure of turbulence and a generalized eddy dissipation concept for chemical reaction in turbulent flow," in 19th AIAA aerospace science meeting, St. Louis, Missouri..

[29] N. Peters, "Laminar diffusion flamelet models in non-premixed turbulent combustion," Progress in Energy and combust. Science., vol. 10, pp. 319-339, 1984.

[30] H. Pitsch, M. Chen and N. Peters, "Unsteady flamelet modeling of turbulent hydrogen-air diffusion flames," ," Proceedings of the Combustion Institute, vol. 27, pp. 1057-1064, 1998.

[31] M. Farokhi and M. Birouk, "Application of Eddy Dissipation Concept for modeling biomass combustion, Part 1: Assessment of model coefficients," Energy and Fuels, vol. 12, pp. 10789-10799, 2016.

[32] A. Parante, M. Malik, F. Contino, A. Cuoci and B. Dally, "Extension of the eddy dissipation concept for turbulent/chemistry interaction to MILD combusiton," Fuel, vol. 163, pp. 98-111, 2016.

[33] A. Shiehnejadhesar, K. Schulze, R. Scharler and I. Obernberger, "A new innovative CFD-based optimization method for biomass combustion plants," Biomass bioenergy, vol. 53, pp. 48-53, 2013.

Chapter 2: Application of Eddy Dissipation Concept for Modeling Biomass Combustion, Part 1: Assessment of the Model Coefficients

2.1 Abstract

Eddy dissipation concept (EDC) model has the ability to incorporate detailed chemistry in turbulent combustion, which makes it attractive for simulating a wide range of industrial combustion systems. However, its application for modeling weakly turbulent reacting flows and slow chemistry poses a real challenge. The present study examines the influence of the EDC model's coefficients with respect to turbulent flow field characteristics. In order to assess the sensitivity of EDC model's constants, simulations of two distinct jet flames covering weakly and highly turbulent flow conditions are performed. The predictions are compared with published experimental measurements. The findings of this study revealed that EDC predictions of the characteristics of weakly turbulent reacting flow can be improved by changing the model's constants. The study also showed that, in comparison with the standard EDC, modifying the model's coefficients produced more accurate predictions of the characteristics of highly turbulent reacting flow regions. The conclusions of the analysis carried out in this study are used to simulate the gas-phase combustion of a small-scale biomass furnace using EDC model, which is presented in the second part of this study.

Nomenclature

C_γ	EDC Model constant	Y_i	Mass fraction of species i
C_τ	EDC Model constant	ε	Turbulent dissipation rate
k	Turbulent Kinetic Energy	ϑ	Kinematic viscosity
R_i	Reaction rate of species i	γ	Length fraction of fine scales
Re^*	Reynolds number in fine structure	ρ	Density
Re_t	Turbulent Reynolds number	τ_{EDC}	EDC time scale
Re_{tmin}	EDC minimum turbulent Reynolds number	τ_η	Kolmogorov time scale
T_t	Turbulent time scale	τ_{mix}	Characteristic mixing time scale

2.2 Introduction

Driven by interest in developing renewable energy power and heat engineering systems, the prevalence of industrial biomass combustion plants has increased in recent decades. Although this technology has already been established in the market, further improvements need to be developed and implemented in order to maximize thermal efficiency and further reduce pollutant emissions [1]. To do so, comprehensive understanding of biomass conversion as well as the combustion of gas-phase volatile is required. Computational fluid dynamics (CFD) can help achieve a reasonable understanding of biomass combustion process at noticeably lower cost compared to physical experiments [2]. However, the reliability of CFD simulation highly depends on the degree of the problem's simplification and the capability of sub-models. In this regard, the sensitivity analysis of sub-models on CFD predictions is still an open area for further research.

The gas-phase combustion sub-model, which is used to model combustion of biomass volatile gases, plays a key role in the predictions of temperature and gaseous emissions [3]. Gas-phase combustion can be modeled using turbulence-chemistry interaction sub-models, commonly performed using species transport methods (i.e., FRK/EDM and EDC) [1]. The modified version of eddy break-up (EBU) models [4], which is known as finite-rate kinetic/eddy dissipation model (FRK/EDM) [5], has been widely employed for modeling a variety of combustion systems due to its high stability and low computational cost [6, 7, 8, 9, 10]. FRK/EDM calculates both kinetics and mixing rates of reaction where the lowest of the two reaction rates determines whether the combustion reaction is kinetically or mixing limited. For this model, detailed reactions chemistry is not considered for mixing limited conditions. Consequently, while the average temperature and mass fraction of major species can be predicted reasonably well, the predictions of pollutants such as CO, NO_x and intermediate species still pose a challenge.

Eddy Dissipation Concept (EDC) model, which is proposed by Magnussen [11] as an extended version of EBU models [3], has been widely used in biomass combustion simulations [12, 13, 14, 15] owing to its capability for incorporating detailed chemical reactions mechanisms (e.g., GRI 3.0 and GRI 1.2 [16]) required for predicting pollutant emissions. However, this model is developed mainly for highly turbulent flowfield conditions to account for the interaction between turbulence and detailed reaction kinetics. Employing EDC model at low Reynolds turbulent flow conditions has shown to lead to significant errors in the predictions of temperature and flue gas species [3]. Therefore, this model needs improvement in order to use it for simulating low/weakly turbulent flow regions (e.g., in the vicinity of the bed of grate firing biomass furnaces). The applicability and adaptability of EDC have been recently investigated for different types of applications [17, 18, 19, 20, 21, 3]. For instance, Rehm et al. [17] performed studies on the

gasification process and reported that the predictions of the standard EDC are partially in agreement with their counterparts' experimental data. De et al. [18] simulated Delft-Jet-in-Hot-Coflow (DJHC) burner for the case of Moderate and Intense Low-oxygen Dilution (MILD) combustion, and reported that the ignition predicted by EDC model was too early in comparison with experiments. However, the model was able to show the decreasing trend of flame lift-off height with respect to fuel jet Reynolds number. Parante et al. [19] proposed a modified EDC model depending on local parameters such as turbulent Reynolds and Damköhler numbers for MILD combustion regime. They examined the model by simulating Adelaide Jet in Hot Co-flow (JHC) burner at different co-flow compositions and fuel jet Reynolds numbers. The predictions of the modified EDC model, when compared with experimental measurements, showed remarkably better results of temperature and intermediate species (e.g., CO) in flow regions of weakly turbulent flow field. However, the model showed flame extinction and poor predictions of species especially for diluted conditions. Recently, Shiehnejadhesar et al. [3] proposed a hybrid reaction rate model involving both FKR and EDC to account for, respectively, weakly and highly turbulent flow regions. They assessed this model by examining three different jet flames covering weak/low, moderate and high turbulent flow conditions. They reported improved predictions of low turbulent flow conditions when compared with the standard EDC model and experimental measurements. In the case of moderate to high turbulent flow conditions, Evans et al. [22] performed parametric study on EDC model constants for lifted jet flames in a heated co-flow, and they reported that, compared to standard EDC model, the modified EDC with optimized constants produced better predictions of peak temperature and species concentrations.

The briefly reviewed literature above, concerning MILD and biomass combustion system, showed that the standard EDC is incapable of predicting accurately the profiles of temperature and species

at low Damköhler number as well as weakly turbulent flow conditions. Despite the widespread use of EDC model, only a few published studies examined its limitations for applications to biomass combustion in fixed bed furnaces (e.g. Ref [1]). Therefore, the present study aims at examining the sensitivity of the predictions of the characteristics of reacting flow (flame) to the EDC model's parameters under weak and high turbulent conditions. To achieve this objective, two distinct turbulent flow conditions: flame A of Barlow and Frank [23] and Sandia flame B [24, 25] are selected for the numerical simulation study. These flames (i.e., Flames A and B) encompass both weak/low and high turbulent flow regions/conditions. Therefore, the effect of modifying EDC model's constants at different flow conditions are studied and examined by comparing the numerical predictions with their counterparts' experimental measurements.

2.3 Methodology

Reynolds Averaged Navier-Stokes (RANS) of continuity, momentum, energy and species transport equations are solved. The effect of enthalpy transport is included in the energy equation to account for species diffusion. Radiation is modeled using P_1- approximation model [26] along with the domain based weighted-sum-of-gray-gas (WSGG) [27]. Turbulence is modelled using the renormalization group (RNG) $k-\varepsilon$ which has been shown to produce accurate predictions of low Reynolds and rapidly strained flows in comparison with standard $k-\varepsilon$ model [28, 29]. DRM-22 [30], which is the reduced version of GRI 1.2, is employed as the chemical mechanism for combustion. It requires substantially less computational time while still capable of reproducing experimental results with reasonable accuracy [3]. EDC model is used to examine the effect of turbulence/chemistry interaction. EDC has been developed based on turbulent energy cascade. Reactions take place at the so-called fine structures, as the combustible fluid is mixed at micro-scale level where turbulent kinetic energy dissipation occurs [18, 19]. This model assumes that

fine structures are isobaric, adiabatic and perfectly stirred reactors (PSR) [31]. In each computational cell, the fluid cell is divided into volume fraction of a fine structure, $\gamma^* = \gamma^3$, and a volume fraction of its surroundings, $(1-\gamma^3)$. The length fraction of fine scales, γ, and the time scale of mass transfer between a fine structure and its surrounding fluid, τ_{EDC}, can be expressed based on the flow turbulence characteristics as follows [15]:

$$\gamma = \left(\frac{3C_{D2}}{4C_{D1}^2}\right)^{0.25}\left(\frac{\vartheta\varepsilon}{k^2}\right)^{0.25} = C_\gamma (Re_t)^{-0.25} \tag{2-1}$$

$$\tau_{EDC} = \left(\frac{C_{D2}}{3}\right)^{0.5}\left(\frac{\vartheta}{\varepsilon}\right)^{0.5} = C_\tau\left(\frac{\vartheta}{\varepsilon}\right)^{0.5} = C_\tau\tau_\eta = C_\tau (Re_t)^{-0.5}\frac{k}{\varepsilon} \tag{2-2}$$

$$Re^* = \frac{2}{3}\frac{C_{D2}}{C_{D1}} \tag{2-3}$$

where $\tau_\eta = (\vartheta/\varepsilon)^{0.5}$ is Kolmogorov time scale, $Re_t = (k^2/\vartheta\varepsilon)$ is turbulent Reynolds number, Re^* is the fine structure scale Reynolds number, C_{D1} and C_{D2} are the model constants set as 0.135 and 0.5, respectively, which consequently set up the default values of the fine structure volume and its residence time constants as $C_\gamma = 2.1377$ and $C_\tau = 0.4082$, respectively [32, 31]. In the original energy cascade concept that EDC has been developed for, the value of C_{D2} is approximated from the best fit of different flow (different Reynolds numbers) conditions, and the value of C_{D1} is chosen based on the assumption of no dissipation at the eddies with the largest turbulent kinetic energy at high Re_t [19]. This implies that EDC is appropriate for simulating highly turbulent flow conditions with a clear separation between large and small flow scales. Based on this assumption, the fine structure scale becomes of the same order of magnitude as Kolmogorov scale, i.e., $Re^* = 2.5$.

Chemical reactions proceed based on Arrhenius expression over EDC time scale where mass exchanges between fine structures and their surroundings. The mean chemical reaction rate can be defined as [32]:

$$R_{i,EDC} = \frac{\bar{\rho}\chi\gamma^2}{\tau_{EDC}}(Y_i^* - Y_i^0) \tag{2-4}$$

Where $\bar{\rho}$ denotes the average density of the mixture, Y_i^* and Y_i^0 are, respectively, the fine structure and surrounding mass fraction of species i, and χ is a factor which represents the fraction of fine structures within which the reactions occur. It is recommended to choose a value of unity for χ when using EDC model with detailed chemistry [33]. The mean mass fraction of species i can be obtained using a linear relation between the properties of fine structure and its surroundings fluid [3, 18] as follows (using $\chi = 1$):

$$\bar{Y}_i = \gamma^3 Y_i^* + (1 - \gamma^3)Y_i^0 \tag{2-5}$$

where $\bar{Y}_i$ is the mean mass fraction of species i. The final expression for the mean reaction rate can be obtained using the mean species mass fraction (Eq.(2-5)) as follows:

$$R_{i,EDC} = \frac{\bar{\rho}\gamma^2}{\tau_{EDC}(1 - \gamma^3)}(Y_i^* - \bar{Y}_i) \tag{2-6}$$

In the original EDC formulation, the value of Y_i^* in each computational cell is achieved at the end of the reactions assuming PSR conditions. The reaction rates are computed via numerical integration of a set of non-linear algebraic equations over τ_{EDC}, which requires a considerable numerical effort [3, 33]. Therefore, instead of using PSR conditions, the assumption of plug flow

reactors (PFR) is adopted to simplify the computational process. This is a practical way which is also used by CFD code ANSYS FLUENT.

As mentioned earlier, EDC time scale is the mean residence time of the mass exchange between fine structures and the surroundings fluid. Re-writing the term (γ^2/τ_{EDC}) in Eq.(2-4) with respect to turbulent flow characteristics shows that this term is proportional to the inverse of turbulent time scale, (ε/k). This indicates the reason for poor predictions of EDC in regions of very small/weak turbulent kinetic energy such as near walls or boundary layer flow regions. EDC model assumes that the chemical reaction rate is a linear function of the mass transfer between a fine structure and its surroundings fluid [3]. Therefore, from Eq.(*2-6*) we can introduce a characteristic mixing time scale of the linear function as follows [18]:

$$\frac{1}{\tau_{mix}} = \frac{\gamma^2}{(1-\gamma^3)}\frac{1}{\tau_{EDC}} = \frac{1}{(1-\gamma^3)}\frac{{C_\gamma}^2}{C_\tau T_t} \tag{2-7}$$

where T_t is a turbulent time scale defined as $T_t = (k/\varepsilon)$. As the value of γ is calculated based on turbulence characteristics, it is not directly related to the cell geometry. This may result in unphysical size of the reaction zone that is greater than the size of the computational cell for flow conditions where the level of turbulence is very low [34]. To avoid this problem, γ and the ratio of EDC time scale to mixing time scale should be lower than unity. This leads to define the upper limit for γ and also C_γ in terms of turbulent Reynolds number using Eq.(2-1) as follows:

$$\frac{\tau_{EDC}}{\tau_{mix}} = \frac{\gamma^2}{(1-\gamma^3)} < 1 \Rightarrow \gamma < 0.75 \tag{2-8}$$

$$C_\gamma < 0.75 Re_t^{0.25} \tag{2-9}$$

Figure 2-1 exhibits the effect of turbulent Reynolds number on γ and C_γ according to Eqs.(2-1) and (2-9). This figure presents the profiles of the fine structure length fraction (γ) and also C_γ as a function of turbulent Reynolds number. As shown in Figure 2-1, the profile of the fine structure length fraction (γ) with the default value of C_γ (= 2.1377) indicates that, for Re_t < 64, γ is greater than 0.75 while its maximum acceptable value is 0.75 according to Eq.(2-8). This figure shows that using a smaller C_γ (i.e., 15% less than the default value; i.e., 1.817) results in $\gamma = 0.75$ at $Re_t = 34.45$. In contrast, using a higher value of C_γ (i.e., 15% greater than the default value; 2.458) results in $\gamma = 0.75$ at $Re_t = 115.37$. As mentioned previously, EDC has been developed for flow fields with high turbulent Reynolds number with a clear separation between turbulent scales (i.e., Re_t > 64 based on default value of $C_\gamma = 2.1377$). Thus, this model is not valid for conditions of weakly turbulent flows (i.e., for Re_t < 64) as the size of turbulent large and small scales are almost comparable and combustion can occur over a wide range of scales [19]. In fact some computational codes, such as Fluent [29] use $\gamma = 0.75$ for low turbulent flow regions where Re_t < 64.

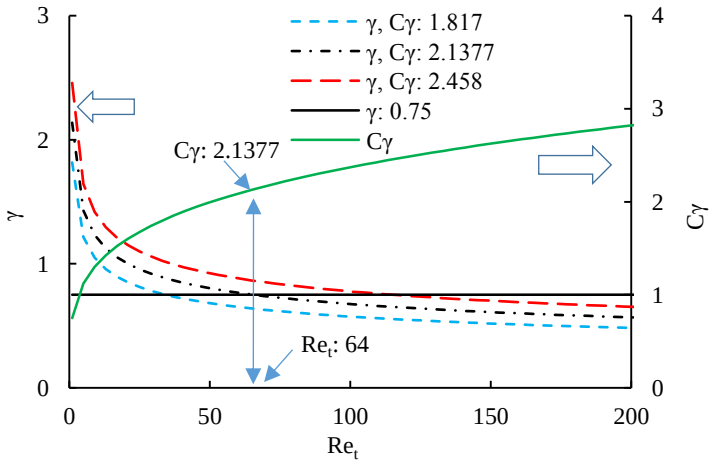

Figure 2-1. Effect of turbulent Reynolds number on γ and C_γ

It can be concluded from Figure 2-1 that, from mathematical point of view, using lower value of C_γ makes it possible to apply EDC for low turbulent flow regions. In fact, reasonable predictions were reported particularly for MILD combustion when lowering C_γ [18, 22]. It was stated that using lower C_γ led to a decrease in the size of fine structures and also prevented unphysical predictions of the reaction rate in regions where Re_t < 64 [18, 22]. However, some studies (e.g., Ref [35]) showed that decreasing C_γ resulted in an early ignition while the model predictions improved by using larger C_γ. Using larger C_γ is in a way similar to accounting for a part of the surroundings fluid in the reactions zone (i.e., extending the volume of fine structure to the surroundings fluid). This implies that a larger volume fraction of the computational cell is involved in the chemical reactions. The assumption of extending the reactions zone to the surroundings fluid has been suggested by Kjaldman et al. [36] for slow chemistry reactions.

The influence of C_τ on the reaction rate can typically be accounted for by considering its effect on Y_i^*, which is implicitly related to detailed chemistry. To account for the effect of C_τ on the reaction rate, Eq.(2-7) can be re-written as a function of Re_t and T_t, using Eqs.(2-1) and (2-2) as:

$$\frac{T_t}{\tau_{mix}} = \frac{1}{(1-\gamma^3)}\frac{{C_\gamma}^2}{C_\tau} = \frac{1}{\left(1-{C_\gamma}^3 (Re_t)^{-0.75}\right)}\frac{{C_\gamma}^2}{C_\tau} \qquad (2\text{-}10)$$

As can be seen from Eq.(2-10), the value of C_τ is related to the characteristic mixing time scale, C_γ, as well as the characteristics of turbulent flow field. Previous studies on the sensitivity of the reaction rate to C_τ showed different trends based on the case being investigated (i.e., geometry, detailed chemistry and its interaction with flow/turbulence). For instance, Kjaldman et al. [36] studied the effect of three different time scales of EDC model in a natural-gas sudden expansion reactor geometry. In their simulations, by applying Taylor time scale,$(4\,k/\varepsilon)$, and a time scale

related to a geometrical mean turbulent and Kolmogorov time scale $\sqrt{T_t \tau_\eta}$ [36], they showed better agreement with experimental measurements of temperature when compared with the default EDC time scale. De et al. [18] modified C_τ from its default value to 3.0 for simulating DJHC flame and reported a lower peak temperature. This improvement (i.e., a low temperature peak) may be attributed to an increase in the residence time of (mild combustion) reactions [22]. Rehm et al. [17] used EDC at high-pressure gasification conditions and showed that the mean reaction rate is almost independent on C_τ, which they attributed to a large flow time scale (e.g., τ_η) observed in each computational cell. Therefore, the predictions became less sensitive to the value of C_τ for large flow time scales. It is expected that, for high turbulent flow regions where the flow time scale is so small, the impact of C_τ on the reaction rate becomes more visible. Thus, in a such flow regime with high Damköhler number, using T_t as a mixing time scale can produce improved predictions since the mixing process is predominantly controlled by turbulence [17].

Considering the volume of a fine structure and its residence time, EDC model is faced with two main challenges: under-prediction of the reaction rate for species that are related to slow chemistry reaction or low Damköhler number, and over-prediction of the reaction rate in low turbulent flow regions. Therefore, a modification of this model's constants needs to be performed by considering both the chemistry and flow altogether. For instance, while a lower value of C_γ may result in an improved prediction at low turbulent flow conditions, it may lead to underestimating the reaction rate related to slow chemistry mechanisms.

2.4 Physical and numerical setups

The main purpose of the simulation is to investigate the influence of EDC model's constants on its predictions. In doing so, the simulation study is carried out using two different burner geometries. The first burner is the flame A of Barlow and Frank [23] experiment (referred to

hereafter as case A) and the second burner is Sandia jet flame B [24] (referred to hereafter as case B). It has widely been demonstrated experimentally [37, 38, 39] that combustible gases released from biomass particles are independent on the biomass source, and are predominately CO, H_2 and other hydrocarbons [40]. In both burners (cases A and B) adopted for this simulation, the fuel composition is similar to that of the flue gas coming out of the bed in grate biomass furnace. Moreover, the flow of flame A is at low turbulence and thus its flow conditions are similar to those above the bed of a biomass combustion grate furnace. Therefore, this case can be used to evaluate the EDC model's constants in flow regions with low turbulence. The flow of Sandia flame B is characterized by a mixing time scale that is so small. Thus, this flame can be used to evaluate EDC model's constants for the formation of species related to slow chemistry in highly turbulent flow conditions.

The simulation study is first performed on a laboratory non-premixed jet flame burner (case A), where a jet fuel with a composition of 25% CH_4 and 75% air by volume is supplied with $2.44\,m/sec$ through a nozzle of a diameter of d_j = 7.2 mm at $292\,K$ ($Re_{jet} \approx 1100$). The co-airflow is supplied at $0.9\,m/sec$ and a temperature of $290\,K$. Also, the burner consists of a concentric pilot jet pipe with a diameter of D_j = 18.2 mm, which is not considered for this flame. Further detail of the geometry and experiments can be found in Ref [23].

The second flame configuration adopted for the simulation is a laboratory non-premixed Sandia jet flame B (case B). A fuel with a composition of 40% CO, 30% H_2 and 30% N_2 by volume is supplied at $45\,m/sec$ and $292\,K$ ($Re_{jet} \approx 17500$) through a nozzle with inner and outer diameters of d_j = 7.72 and D_j = 9.46 mm, respectively. The co-airflow is supplied at $0.75\,m/sec$ and a temperature of $290\,K$. Further detail of the geometry and experiments of Sandia jet flame B can

be found in Refs. [24, 40]. A summary of the physical and numerical setup used in this study is given in Table 2-1.

Table 2-1. Summary of the physical and numerical setup [23, 24]

Parameter	**Setup used for case A:**	**Setup used for case B:**
Fuel jet inner diameter (d_j) [mm]	7.2	7.72
Pilot jet inner diameter (D_j) [mm]	18.2	9.46
Axial distance used in simulation [mm]	756	810.6
Radial distance used in simulation [mm]	360	386
Jet Reynolds Num.	1100	17500

The CFD simulations are carried out using the commercial code ANSYS Fluent R15. Second order upwind spatial discretization scheme is adopted for all conservation equations. SIMPLEC method is applied for the velocity-pressure coupling algorithm. Due to the symmetry of both burner geometries, two-dimensional (2D) axisymmetric domain along with structured grids are adopted for the simulation. The computational domain, for each flame geometry, is extended from $5d_j$ upstream of the fuel nozzle exit plane up to $100d_j$ downstream in the axial direction and $50d_j$ in the radial direction. The grid consists of about 38,000 elements with a local increase in grid resolution close to the nozzle exit. For both cases, further grid refinement did not show significant change in the simulation predictions. To reduce the computational time required for EDC model, the In-Situ Adaptive Tabulation (ISAT) [41] algorithm is used to increase the CPU-intensive treatment of detailed chemistry with an ISAT error tolerance of 10^{-5}. A converged solution is achieved when all the residuals of the computed species are less than 10^{-4}, and 10^{-5} for the rest of computed parameters.

Velocity inlet conditions are specified for fuel jet and co-flow air inlet as mentioned earlier. Pressure outlet condition is used for outflow boundary. Table 2-2 reports the adopted boundary conditions for both cases A and B. It should be mentioned that these conditions are based on the

suggested values and experimental measurements reported in Refs. [24, 23]. Turbulence characteristics of the co-flow at the inlet are set by specifying an inlet turbulent intensity of 5% (Table 2-2) and a turbulent viscosity ratio of 10%.

Table 2-2. Details of the boundary conditions for cases A and B. [23, 24]

Case A:	**Mole fraction**			**Vel**	**Temp**	**Turbulence**	
	CH_4	N_2	O_2	(m/s)	(K)	I(%)	L(m)
Fuel jet	0.25	0.5925	0.1575	2.44	292	7	7.2e-3
Co-flow	-	0.79	0.21	0.9	290	5	-

Case B:	**Mole fraction**				**Vel**	**Temp**	**Turbulence**	
	CO	H_2	N_2	O_2	(m/s)	(K)	I(%)	L(m)
Fuel jet	0.4	0.3	0.3	-	45	292	7	7.72e-3
Co-flow	-	-	0.79	0.21	0.7	290	5	-

2.5 Results and discussions

The simulation results of the two flow cases (cases A and B) are presented below. As mentioned previously, cases A and B cover the application of EDC for weak/low and high turbulent flow conditions, respectively, where the effect of EDC model's constants are examined. The ultimate aim of the simulation is to adjust EDC model's constants in order to reasonably predict temperature and species profiles at different flow conditions pertaining to biomass combustion in commercial furnaces. This can be achieved by performing sensitivity analysis on the model's constants and comparing the predictions with their experimental measurements counterparts. Thereafter, the conclusions achieved through this analysis will be used to simulate the gas-phase combustion in a fixed bed biomass furnace which will be presented in the second part (Part II [42]) of this study.

2.5.1 Case A

Results of case A are presented in order to evaluate EDC model at near-laminar and weakly turbulent flow conditions. To perform the sensitivity analysis on the model's constants, the simulation of this case is carried out using eight numerical tests (Cases A1-A8) with different values of C_τ and C_γ. Table 2-3 presents the values which are used for C_τ and C_γ. The three values of C_γ were selected as to have a 50% higher and lower (i.e., 2.46 and 1.80, respectively) than the standard value (i.e., 2.1377). As for C_τ, in addition to the standard value (i.e., 0.4085), a value which reproduces an EDC time scale identical to Kolmogorov time scale, and another one that is 50% higher than Kolmogorov time scale (i.e., C_τ=1 and 1.5, respectively) were selected. Based on these values and Eqs.(2-8) and (2-9), the values of C_γ^2/C_τ and the minimum turbulent Reynolds number for EDC model (Re_{tmin}) according to Eq.(2-8) are computed and presented in Table 2-3 for each numerical test case. It should be mentioned that this flame could not be stabilized using the default value of C_τ regardless of the value of C_γ.

Table 2-3. Details of flame A cases

	Case A1	**Case A2**	**Case A3**	**Case A4**	**Case A5**	**Case A6**	**Case A7**	**Case A8**
C_τ	1.0	1.5	1.0	1.5	1.0	1.5	1.0	1.5
C_γ	1.8	1.8	2.1377	2.1377	2.46	2.46	1.12	1.12
${C_\gamma}^2/C_\tau$	3.24	2.16	4.57	3.04	6.05	4.03	1.2544	0.8362
Re_{tmin}	33.17	33.17	64	64	115.7	115.7	4.97	4.97

It is well known that while turbulent diffusion overwhelms molecular diffusion in turbulent flows, the effect of molecular diffusion on the mixing process becomes comparable to that of turbulent mixing under weak turbulent flow conditions [3]. Particularly, the influence of molecular diffusion becomes more important for a fuel jet stream with a Reynolds number lower than 10,000 [43]. It was observed that for all studied cases, A1-A8, the flame could not be simulated without

considering the effect of molecular diffusion. That is, in fact, expected for this flame as the Reynolds number of the jet fuel stream is only 1,100. Shiehnejadhesar et al. [3] showed that, in the case of a diffusion jet flame with weak to moderate turbulent flow conditions, considering molecular diffusion along with turbulent diffusion can significantly improve numerical predictions. Thus, the effect of molecular diffusion is considered for both cases A and B.

It should be mentioned that the experimental data for this flame is available only at one axial position ($x/d_j = 10$) [3, 23]. Figure 2-2 shows a comparison between the present numerical predictions and experimental data of the radial profiles of temperature and species mass fractions as a function of the mixture mean fraction. According to this figure, for cases A1-A6 ($33.17 \leq Re_{Tmin} \leq 115.7$), it can be seen that all the predictions are independent of the value of C_γ, whereas C_τ shows significant effect. This figure indicates that, higher C_τ results in a lower peak of temperature (Figure 2-2a), CO (Figure 2-2b) and CO_2 (Figure 2-2c) species mass fraction profiles, and higher minima of O_2 mass fraction profile (Figure 2-2d). In addition, regardless of the values of the model's constants, the trends of all predicted profiles are in agreement of their experimental counterparts. To examine the effect of the size of reaction zone of EDC, case A is simulated with very low value of C_γ (cases A7 and A8 in Table 2-3). According to Figure 2-2, the prediction of the peak temperature is significantly improved with case A8. In addition, case A8 predicts higher temperature compared to case A7 which has a lower value of C_τ. This is in contrast with the observations of cases A1-A6 as well as the literature [22, 18]. This figure clearly demonstrates that case A8 exhibits better predictions of CO_2 and O_2 mass fractions. However, case A8 exhibits improved predictions of CO at only low mixture fraction region, but no significant change at high mixture fraction and peak value when compared with cases A1-A6.

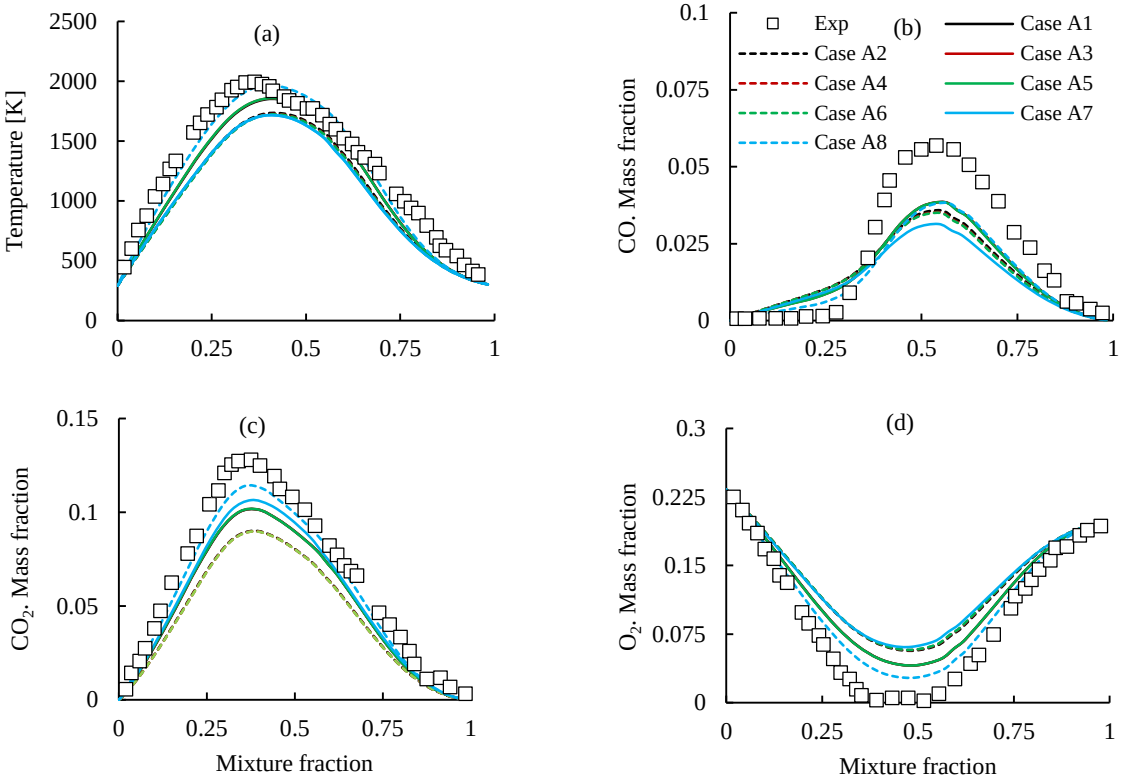

Figure 2-2. Radial profiles of temperature and species mass fraction for case A, at x/d_j=10. C_γ= 1.8 (cases A1 and A2), = 2.1377 (cases A3 and A4), = 2.46 (cases A5 and A6), = 1.12 (cases A7 and A8). C_τ =1 (cases A1, A3, A5, A7), = 1.5 (cases A2, A4, A6, A8).

The effect of C_γ and C_τ on the reaction rate is investigated in more detail in Figure 2-2a-d and 2-3. Figure 2-3 presents the radial profiles of γ and turbulent Reynolds number at $x/d_j = 10$. This figure shows that the value of γ remains fixed at its maxima (0.75) throughout all flow regions where turbulent Reynolds number is lower than Re_{Tmin} (see Figure *2-3*). Consequently, the reaction rate becomes independent on C_γ for cases A1-A6, and hence only C_τ influences the predictions of temperature and species (Figure 2-2a-d). Therefore, higher value of C_τ, when using γ as a constant in Eq.(2-6), results in a decrease in the reaction rate, and consequently a reduction in the peak temperature, CO_2 and CO mass fractions (Figure 2-2a-d), which are in agreement with the literature. [18, 22]. On the other hand, the value of C_γ for cases A7 and A8 results in a Re_{Tmin}

lower than the turbulent Reynolds number along the radial direction (Figure 2-3). This implies that γ is no longer a constant quantity and depends upon local turbulent flow characteristics. In addition, Figure 2-3 shows that using smaller value for C_γ leads to $\gamma < 0.75$ for case A7; in this case, both C_γ and C_τ exert an influence on the reaction rate. This is exhibited in Figure 2-2a-d through the temperature and species predictions when comparing cases A7 and A8 with the other cases. It was reported that increasing C_τ results in a decrease in the reaction rate and consequently the temperature peak [18, 22]. This could be caused by a decay in the local turbulent Reynolds number to below its critical value (i.e., Re_{Tmin}). However, a comparison between the temperature profiles of cases A7 and A8, in Figure *2-2*.a, indicates that, if the value of C_γ results in $\gamma < 0.75$, higher C_τ could result in an increased reaction rate and consequently higher peak of temperature.

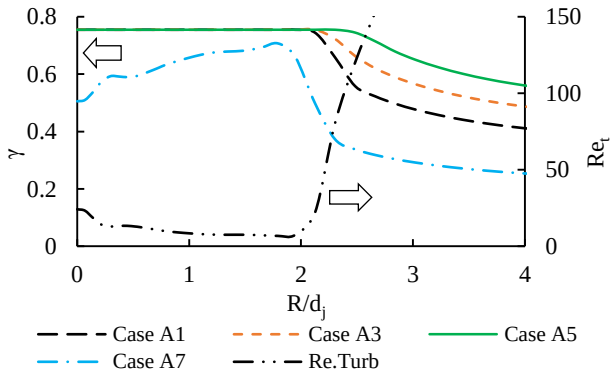

Figure 2-3. Radial profiles of γ and Re_t at x/d_j=10

2.5.2 Case B

Case B is used to evaluate the predictions of EDC model for a turbulent flow. Case B consists of 8 numerical tests (Cases B1-B8) while using different values of C_τ and C_γ as indicated in case A. Table 2-4 presents the values of C_τ, C_γ, C_γ^2/C_τ and Re_{tmin} used for each numerical simulation test. It should be mentioned that another case has been examined using the default value of EDC time scale constant with C_γ=1.8, but the mixture could not be ignited and the flame was unstable.

Table 2-4. Details of Sandia flame B cases

	Case B1	**Case B2**	**Case B3**	**Case B4**	**Case B5**	**Case B6**	**Case B7**	**Case B8**
C_τ	1.0	1.5	0.4082	1.0	1.5	0.4082	1.0	1.5
C_γ	1.8	1.8	2.1377	2.1377	2.1377	2.46	2.46	2.46
${C_\gamma}^2/C_\tau$	3.24	2.16	11.2	4.57	3.04	14.82	6.05	4.03
Re_{tmin}	33.17	33.17	64	64	64	115.7	115.7	115.7

Figure 2-4 shows the predictions of the normalized axial velocity profiles along the centerline (Figure 2-4a-d), and the normalized axial velocity profiles along the radial direction at $x/d_j = 20$ (Figure 2-4e-h) and 50 (Figure 2-4i-l). Overall, the model predictions are in acceptable agreement with their counterparts' measurements for all cases. As it can be seen in this figure, changing C_τ at constant C_γ does not show significant difference in the velocity profiles; whereas the influence of C_γ on the velocity profiles along both axial and radial directions is clearly noticeable. Figure 2-4 also illustrates the effect of temperature on the predictions of the velocity field. It is evident that at $x/d_j = 20$, where according to Figure 2-5 this region has lower temperature, the predictions of the radial axial velocity profile matches the experimental data for all cases; whereas the predictions are slightly higher at $x/d_j = 50$ which are located in a higher temperature zone. It can be concluded that the characteristics of the velocity field are very weakly influenced by the EDC model's constants in accordance with published literature (e.g., Ref [18]).

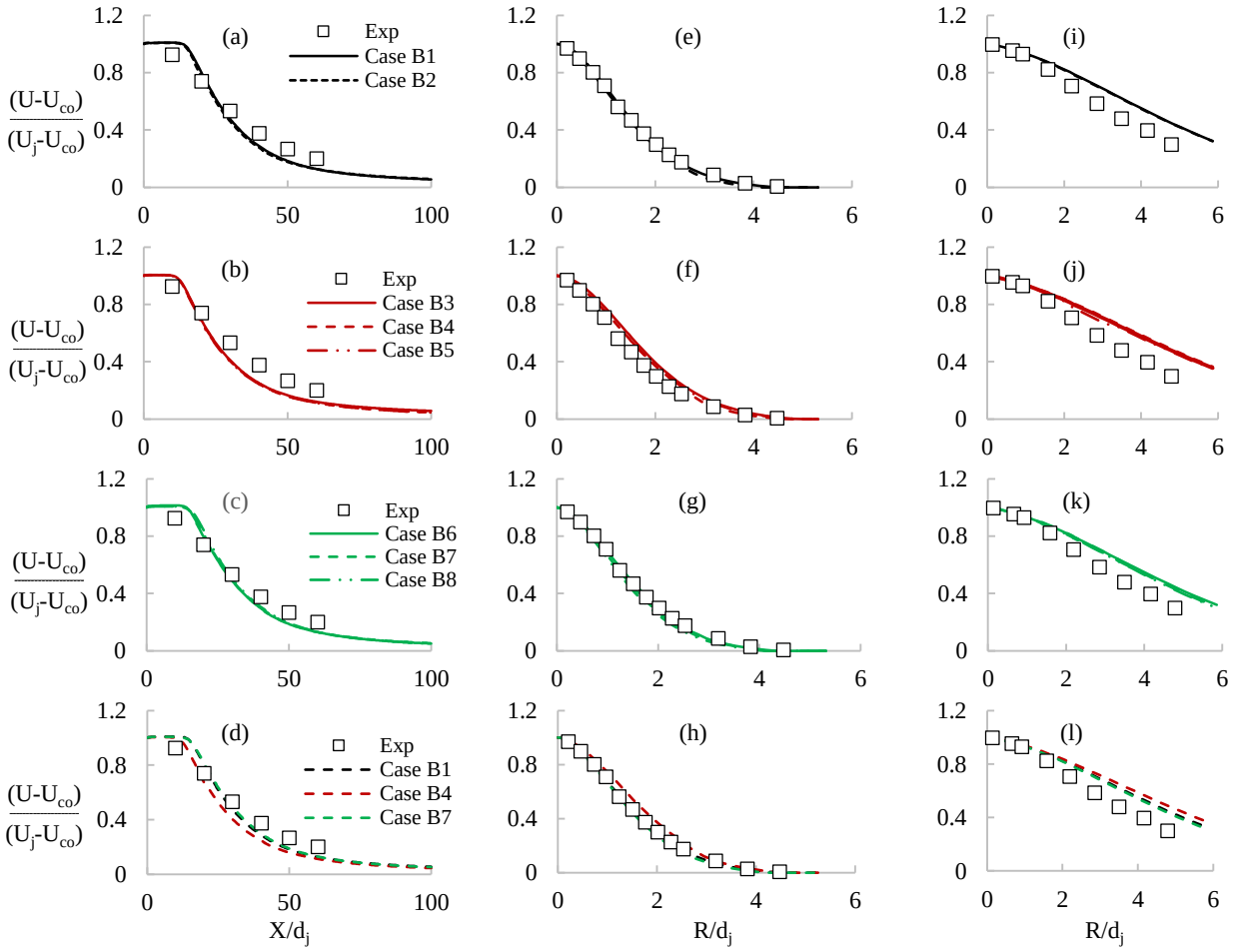

Figure 2-4. Normalized axial velocity along the (a-d) axial and (e-h) radial direction at x/d_j=20, and (i-l) in the radial direction at x/d_j=50. $C_\gamma = 1.8$ (cases B1 and B2), = 2.1377 (cases B3-5), = 2.46 (cases B6-8); $C_\tau = 0.4082$ (cases B3 and B6), =1 (cases B1, B4 and B7), =1.5 (cases B2, B5 and B8).

The influence of the EDC model's constants on the predictions of the temperature field is examined and presented in Figure 2-5. Figure 2-5 presents the axial temperature profiles along the centerline (Figure 2-5a-c) and radially at x/d_j = 20 (Figure 2-5d-f) and x/d_j = 50 (Figure 2-5g-i). Figure 2-5a-c suggest that, along the centerline where the flow is sufficiently turbulent, cases B6-B8 (see Table 2-4) show the best predictions compared with their experimental measurements' counterparts. Also, it is evident that C_τ has almost no impact on the predictions except for case B2. This figure shows also that the peak temperature is captured reasonably well though it is slightly under-predicted in cases B1 and B2 and shifted upstream of the flow. This could be caused by the

predictions of an early ignition by EDC model [18]. Figure 2-5d-f (at x/d_j=20) show that the temperature profile including its peak is captured reasonably well for cases B6-B8 and practically matches the measurements for case B2. However, the predictions at x/d_j=50 indicate substantial discrepancy with measurements. These differences are independent of the EDC model constants as the trends of temperature profiles are the same for all tested cases. It can be concluded from the predictions presented in Figure *2-5* that, in the flow regions where the local turbulent Reynolds number is sufficiently high (e.g., along the centerline), the influence of C_γ on the predictions of the temperature field is more evident than that of C_τ. Accordingly, cases with higher value of C_γ show better predictions (Figure 2-5c). However, in the radial direction, the influence of C_τ becomes more visible only for the case with lowest value of C_τ (Figure 2-5d).

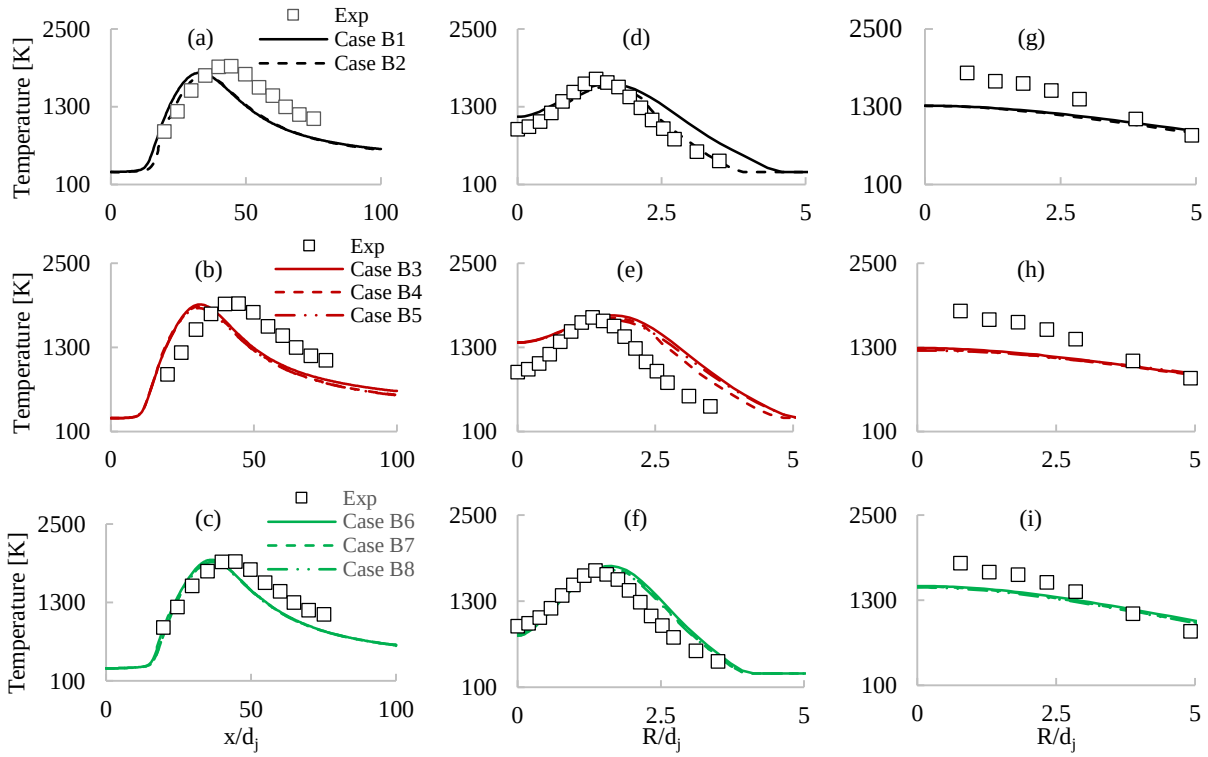

Figure 2-5. Temperature profiles in the (a-c) axial and (d-f) radial direction at x/d_j=20, and (g-i) radial direction at x/d_j=50. C_γ = 1.8 (Cases B1 and B2), = 2.1377 (cases B3-5), = 2.46 (cases B6-8); C_τ = 0.4082 (cases B3 and B6), = 1 (cases B1, B4 and B7), = 1.5 (cases B2, B5 and B8)

Figure 2-6 presents a comparison of the mean mass fractions of CO, CO_2 and O_2 profiles along the centerline (Figure 2-6a, 2-6e and 2-6f) and also in the radial direction at x/d_j=20 (Figure 2-6b-d) between the model predictions and experimental data for all cases. Figure 2-6a, which presents CO mass fraction profiles along the centreline, shows a slight underestimation of the predictions compared with measurements. It can be seen in this figure that the closest prediction to the measurements is achieved with case B8 ($C_\gamma = 2.46, C_\tau = 1.5$). Figure 2-6b, which presents the radial profiles of CO mass fractions, reveals that, with the exception of cases B1 and B2, it is evident that the influence of C_τ on the model predictions is negligible whereas C_γ has a noticeable impact. The effect of C_τ and C_γ is more evident on the radial profiles of CO_2 mass fraction, as shown in Figure 2-6c. This figure reveals that, for each fixed value of C_γ, C_τ affects the peak value of CO_2 mass fraction. That is, higher C_τ results in a decrease in the peak value (cases B2, B5 and B8); while the most improved peak value is captured with case B5. Furthermore, the best and the worst profile of CO_2 mass fraction are predicted in the vicinity of the centerline and also farther away using case B2 and B3, respectively. Figure 2-6d, which presents the radial profiles of O_2 mass fraction, shows that, close to the centerline, the predictions of all cases are in satisfactory agreement with experiments, whereas the difference between the numerical results and measurements become more evident farther away from the centerline. Moreover, this figure reveals that while C_γ shows strong impact on the model predictions, C_τ only weakly affects the predictions. For instance, according to Figure 2-6d, the predictions of cases B3-B5 (C_γ is fixed) show no significant difference; while comparing the predictions of case B2 with those of B5 shows noticeable differences farther away from the centerline. Figures 6e and 6f present the mass fraction profiles of CO_2 and O_2along the centerline. These figures reveal noticeable influence of C_γ but negligible impact of C_τ (for each fixed value of C_γ) on the predictions. Cases B6-B8 with the

highest value of C_γ predict the closest peak value of CO_2 mass fraction to the measurements. Figure *2-6*f shows also that, compared to the other cases, the O_2 mass fraction predicted in cases B6-B8 is the closest to its experimental counterpart.

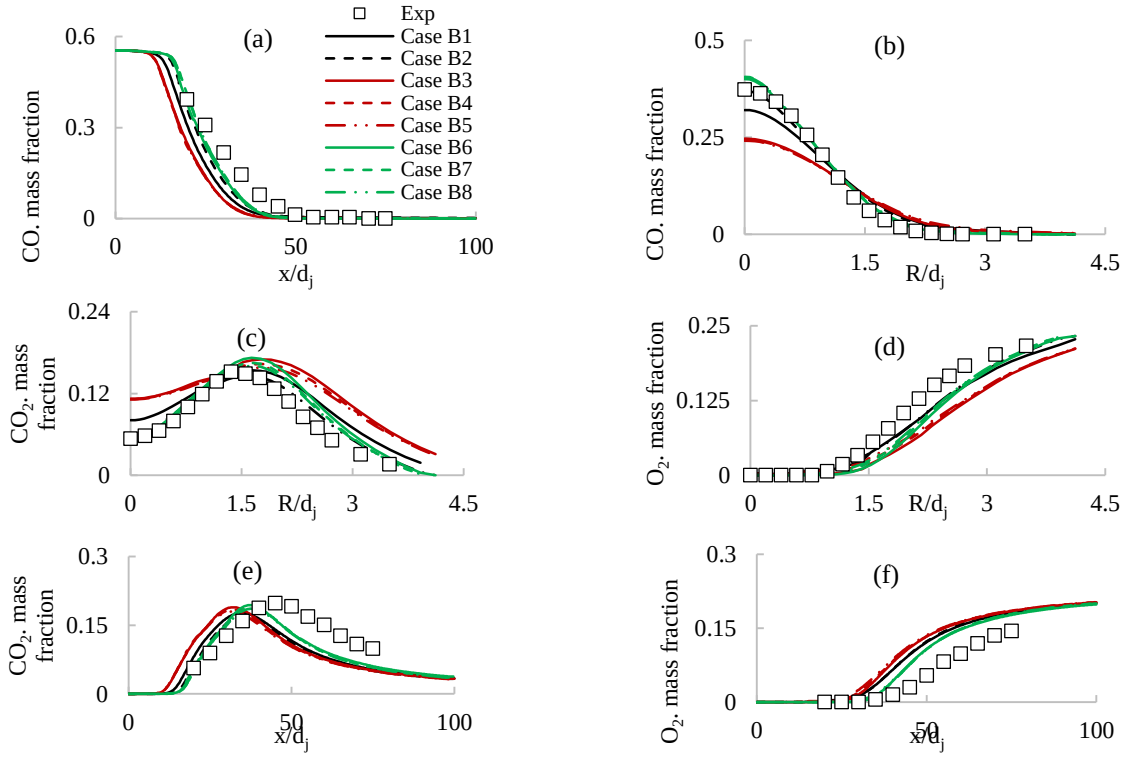

Figure 2-6. Mean mass fraction of CO (in the a) centreline and b) radial direction), CO_2 (in the c) radial direction), and O_2 (in the d) radial direction) at x/d_j=20, CO_2 (in the e) centerline and O_2 (in the f) centerline). C_γ= 1.8 (Cases B1 and B2), = 2.1377 (cases B3-5), = 2.46 (cases B6-8); C_τ ≔ 0.4082 (cases B3 and B6), = 1 (cases B1, B4 and B7), =1.5 (cases B2, B5 and B8)

The effect of EDC model constants on the characteristics of turbulent flowfield (i.e., turbulent kinetic energy, turbulent Reynolds number and the ratio of turbulent time scale over characteristics mixing time scale) are examined and presented in Figure 2-7. Figure 2-7a-c presents a comparison of the axial profiles of turbulent kinetic energy compared between the predictions and experimental measurements along the centerline. As can be seen in this figure, there is a good agreement with experiments. The same figures show also that all cases produce almost identical predictions. This is expected as it is strongly believed that the reaction model has a very weak impact on the turbulent

flowfield [18, 40]. Figure 2-7d-f show that the radial profiles of turbulent Reynolds number at x/d_j=20 are nearly similar between different cases. These figures clearly suggest that the predictions are independent on the values of the model's constants. Figure 2-7d-f reveal also that turbulent Reynolds number reaches its minima at the position where the shear layer is fully developed as a result of the interaction of the co-flow with the jet flow. Figure 2-7g-i present the radial profiles of the ratio of turbulent time scale over the characteristics mixing time scale at x/d_j=20. It shows that the time scale ratio remains almost constant in the flow regions where turbulent Reynolds number is higher than Re_{tmin} (see Table 2-4). This reveals that, according to Eq.(2-10), while the time scale is a function of γ and C_γ^2/C_τ, it is independent on the size of fine structures for highly turbulent flow regions. In addition, this figure in conjunction with Figure 2-7d-f indicate that the time scale ratio has its maxima at flow locations where turbulent Reynolds number is lower than Re_{tmin}. This is expected as, according to Eq.(2-10), for turbulent Reynolds number less than Re_{tmin}, $\gamma = 0.75$ and consequently the value of $1/(1-\gamma^3)$ in Eq.(2-10) reaches its maxima.

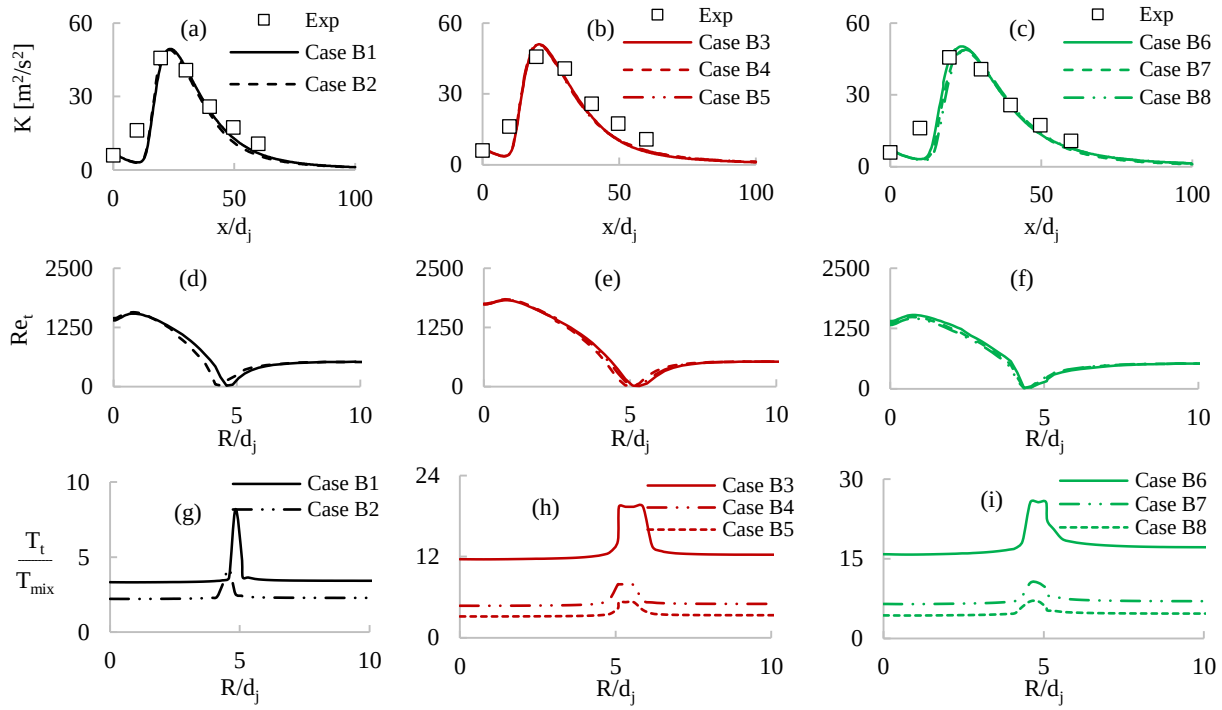

Figure 2-7. Profiles of (a-c) turbulent kinetic energy in the axial direction; (d-f) turbulent Reynolds number and (g-i) time scale ratio in the radial direction at x/d_j=20. C_γ= 1.8 (Cases B1 and B2), = 2.1377 (cases B3-5), = 2.46 (cases B6-8); C_τ := 0.4082 (cases B3 and B6), = 1 (cases B1, B4 and B7), = 1.5 (cases B2, B5 and B8)

2.6 Conclusions

The present numerical study examined the effect of the coefficients of EDC model on the predictions of temperature and species for different flow conditions. Sensitivity analysis is performed on the model's constants for two non-premixed jet flames under weak and high turbulent flow conditions.

The application of EDC for predicting the characteristics of a weakly turbulent flame is studied using a laboratory jet-flame burner ($Re_{jet} \approx 1100$). The influence of molecular diffusion is found to be very important as the flame could not be simulated without considering this term. Also, the flame could not be stabilized using the default value of C_τ. It is found that at low/weakly turbulent flowfield conditions, when turbulent Reynolds number is lower than Re_{tmin}, using higher value of C_τ resulted in under predicting the peak of temperature, CO and CO_2 mass fraction profiles. In

contrast, a lower value of C_τ improved the predictions, when compared with experimental measurements. Under these conditions, the size of the fine structure is fixed to its maxima and therefore the reaction rates depended only on C_τ, and consequently, using a lower value of C_τ results in predicting high reaction rate. Also, the results showed that, when Re_{tmin} is smaller than the flow turbulent Reynolds number, the influence of both EDC model constants (C_τ and C_γ) on the reaction rate becomes important, where C_γ leads to smaller reaction zones. In addition, under this condition (i.e., Re_{tmin} is smaller than the flow turbulent Reynolds number), the results showed that higher value of C_τ results in predicting higher peak of temperature and CO_2 mass fraction. This indicates that when the reaction rate depends on both model constants, the trend explained above for C_τ is no longer valid. Furthermore, under this condition, where the flow turbulent Reynolds number is smaller than Re_{tmin}, the predictions approaches their experimental data counterpart. The species and temperature profiles showed the same trends regardless of the values selected for the model's constants for all studied flame cases A.

The application of EDC to highly turbulent flames is studied using Sandia laboratory jet-flame B ($Re_{jet} \approx 17500$). The simulation results showed that changing the model's constants has a very weak impact on the velocity and turbulent fields. In addition, it can be concluded from these results that the influence of C_γ on the predictions of temperature and species is more pronounced than that of C_τ. In particular, for the temperature profiles, the studied cases predicted nearly similar peak of temperature regardless of the value of C_τ when keeping constant the value of C_γ constant. However, higher values of C_τ (cases B2, B5, B8) resulted in lower temperature profiles before and after its peak. In high temperature region (i.e., close to peak temperature), kinetics of reactions are fast due to high temperature, while as the temperature drops, kinetics of reactions become slower [2]. Hence, close to peak temperature, this is mixing time scale that controls the reaction rate;

whereas away from peak temperature, the competition between chemistry and mixing time scales becomes more important and therefore, C_γ can have more influence on the predictions [17]. As for species, the analysis showed that, when using smaller Re_{tmin}, both model's constants exert an influence on the predictions especially for slow chemistry species (e.g., CO); whereas at higher Re_{tmin}, the predictions showed dependence on only C_γ. The ratio of the turbulent time scale over the characteristic mixing time scale is found to remain almost unchanged under high turbulent flow conditions. Therefore, while this ratio is mathematically a function of the size of fine structures and the model's constants, it is independent on the size of fine structures when the local turbulent Reynolds number is high (i.e., > Re_{tmin}).

It can be concluded from the present study that the application of EDC for studying low turbulent reacting flow regions can be possible via modifying the model's constants. At low turbulent flow conditions, the choice of the model's constants should be performed based on the local turbulent Reynolds number. At high turbulent reacting flow conditions, changing the model's constants can still improve the accuracy of the predictions. The study revealed that, when Re_{tmin} is smaller than the flow turbulent Reynolds number, both constant of EDC model along with the characteristics of the turbulent field (e.g., turbulent kinetic energy and turbulent dissipation rate) have a complex dependency on the reaction rate. However, when Re_{tmin} is higher than the flow turbulent Reynolds number, only C_τ can affect the predictions as the size of reaction zone become fixed.

The sensitivity analysis performed in this study showed clearly that the accuracy of the predictions of species and temperature fields under weak and high turbulent conditions can significantly be improved via changing the EDC model's constants. This suggests that it is possible to apply EDC for modeling the flowfield in an industrial biomass furnaces which encompass a variety of flow regimes including weakly turbulent (e.g., in vicinity of the bed and walls) and highly turbulent

(e.g., close to overfire air-jets in the freeboard) conditions. However, the remaining challenge is how to select the appropriate model's coefficients for such a practical combustion case. This is examined in Part II of this study (i.e., Ref. [42]).

2.7 References

[1] M. Buchmayr, J. Gruber, M. Hargassner and C. Hochenauer, "A computationally inexpensive CFD approach for small-scale biomass burners equipped with enhanced air staging," Energy Conversion and Management, vol. 115, pp. 32-42, 2016.

[2] J. Chaney, H. Liu and J. Li, "An overview of CFD modelling of small-scale fixed-bed biomass pellet boilers with preliminary results from a somplified approach," Energy Conversion and Management, vol. 63, pp. 149-156, 2012.

[3] A. Shiehnejadhesar, R. Mehrabian, R. Scharler, G. M. Goldin and I. Obernberger, "Development of a gas phase combustion model suitable for low and high turbulent conditions," Fuel, vol. 126, pp. 177-187, 2014.

[4] D. Spalding, "Mixing and chemical reaction in steady confined turbulent flame," Proceedings of the Combustion Institute, vol. 13, pp. 649-657, 1971.

[5] B. Magnussen and B. Hjertager, "On mathematical modeling of turbulent combustion with special emphasis on soot formation and combustion," in 16th symposium (international) on combustion, The combustion institute, Pittsburgh, 1977.

[6] C. Yin, L. Rosendahl, S. Kaer, C. Sonnik, S. Hvid and T. Hille, "Mathematical modeling and experimental study of biomass combustion in a 108 MW Grate-Fired Boiler," Energy and Fuels, vol. 22, pp. 1380-1290, 2008.

[7] A. Bhuiyan and J. Naser, "CFD modeling of co-firing of biomass with coal under oxy-fuel combustion in a large scale power plant," Fuel, vol. 159, pp. 150-168, 2015.

[8] A. Bhuiyan and J. Naser, "Numerical modeling of biomass combustion with pulverized coal in small scale furnace," Procedia Engineering, vol. 105, pp. 504-511, 2015.

[9] J. Collazo, J. Porteiro, J. Miguez, E. Granada and M. Gomez, "Numerical simulation of a small scale of biomass boiler," Energy conversion and management, vol. 64, pp. 87-96, 2012.

[10] D. Djurovic, S. Nemoda, B. Repic, D. Dakic and M. Adzic, "Influence of biomass furnace volume change on flue gases burn out process," Renewable Energy, vol. 76, pp. 1-6, 2015.

[11] B. Magnussen, "On the structure of turbulence and a generalized eddy dissipation concept for chemical reaction in turbulent flow," in 19th AIAA aerospace science meeting, St. Louis, Missouri, 1981.

[12] T. Klason and X. Bai, "Computational study of the combustion process and NO formation in a small-scale wood pelletfurnace," Fuel, vol. 86, pp. 1465-1474, 2007.

[13] S. Sukumaran and S. Kong, "Modeling fuel NOx formation from combustion of biomass-derived producer gas in a large-scale burner," Combustion and flame, vol. 160, pp. 2159-2168, 2013.

[14] M. Bugge, Y. Skreiberg, N. Haugen, P. Carlsson, E. Houshfar and T. Lvs, "Numerical simulation of staged biomass grate fired combustion with an emphasis on NOx emissions," Energy Procedia, vol. 75, pp. 156-161, 2015.

[15] A. Shiehnejadhesar, K. Schulze, R. Scharler and I. Obernberger, "A new innovative CFD-based optimisation method for biomass combustion plants," Biomass Bioenergy, vol. 53, pp. 48-53, 2013.

[16] M. Frenklach, H. Wang, C. Yu, M. Goldenberg, C. Bowman and R. Hanson. [Online]. Available: http://www.me.berkley.edu/gri_mech/.

[17] M. Rehm, P. Seifert and B. Meyer, "Theoretical and numerical investigation on the EDC-model for turbulent-chemistry interaction at gasification conditions," Computers and Chemical Engineering, vol. 33, pp. 402-407, 2009.

[18] A. De, E. Oldenhof, P. Sathiah and D. Roekaerts, "Numerical Simulation of Delft-Jet-in-Hot-Coflow (DJHC) Flame Using Eddy dissipation Concept Model for Turbulent-Chemistry Interaction," Flow Turbulence Combustion, vol. 87, pp. 537-567, 2011.

[19] A. Parente, M. Malik, F. Contino, A. Cuoci and B. Dally, "Extension of the Eddy Dissipation Concept for turbulent/chemistry interaction to MILD combustion," Fuel, vol. 163, pp. 98-111, 2016.

[20] A. Shiehnejadhesar, R. Mehrabian, R. Scharler and I. Obernberger, "Developement of a streak formation model for an improved prediction of gas phase combustion in biomass grate furnaces," in 10th Europian Conference on Industrial Furnaces and Boilers, Porto, Portugal, 2015.

[21] A. Shiehnejadhesar, R. Scharler, R. Mehrabian and I. Obernberger, "Developement and validation of CFD models for gas phase reactions in biomass grate furnaces considering gas streak formation above the packed bed," Fuel Processing Technology, vol. 139, pp. 142-158, 2015.

[22] M. Evans, P. Medwell and Z. Tian, "Modeling Lifted Jet Flames in a Heated Coflow Using an Optimized Eddy Dissipation Concept Model," Combustion Science and Technology, vol. 187, pp. 1093-1109, 2015.

[23] R. Barlow and J. Frank, "Effect of turbulence on species mass fractions in methane/air jet flames," in 27th Symposium (International) on Combustion, The combustion institude, 1998.

[24] R. Barlow, G. Fiechtner, C. Carter and M. Flury, "Sandia/ETH-Zurich CO/H2/N2 flame data - Release 1.1," Sandia, 2002. [Online]. Available: http://www.ca.sandia.gov/TNF.

[25] R. Barlow, G. Fiechtner, C. C.D. and J. Chen, "Experiments on the scalar structure of turbulent CO/H2/N2 jet flames," Combustion and Flame, vol. 120, pp. 549-569, 2000.

[26] M. Modest, Radiative Heat Transfer, Academic Press, 2003.

[27] N. Kayakol and N. Selcuk, "Evaluation of descrete ordinates method for radiative transfer in rectangular furnaces," International Journal of Heat and Mass Transfer, vol. 40, pp. 213-222, 1997.

[28] V. Yakhot and S. A. Orszag, "Renormalization group and local order in strong turbulence," Nuclear Physics B - Proceedings Supplements, vol. 2, pp. 417-440, 1987.

[29] ANSYS, ANSYS Fluent Theory Guide, Release 15.0, Ansys, 2013.

[30] A. Kazakov and M. Frenklach, "DRM-22 chemical mechanism," [Online]. Available: http://www.me.berkeley.edu/drm/.

[31] B. Magnussen and I. Ertesvag, "The eddy dissipation turbulence energy cascade model," Combustion Science and Technology, pp. 213-235, 2000.

[32] B. Magnussen and I. Gran, "numerical study of a bluff-body stabilized diffusion flame. Part 2. Influence of combustion modeling and finite-rate chemistry," Combustion Science and Technology, vol. 119, pp. 191-217, 1996.

[33] H. Magel, U. Schnell and K. Hein, "Simulation of detailed chemistry in a turbulent combustor flow," Symposium (International) on Combustion, vol. 26, pp. 67-74, 1996.

[34] M. Karalus, "An investigation of lean blowout of gaseous fuel alternatives to natural gas, PHD thesis," University of Washington, 2013.

[35] M. Graca, A. Duarte, P. Coelho and M. Costa, "Numerical simulation of a reversed flow small-scale combustor," Fuel Processing Technology, vol. 107, pp. 126-137, 2013.

[36] L. Kjaldman, A. Brink and M. Hupa, "Micro mixing time in eddy dissipation concept," Combustion Science and Technology, vol. 154, pp. 207-227, 2000.

[37] G. Stubenberger, R. Scharler, S. Zahirovi´c and I. Obernberger, "Experimental investigation of nitrogen species release of different solid biomass fuels as a basis for release models," Fuel, vol. 87, pp. 793-806, 2008.

[38] C. Dupont, J. Commandre, P. Gauthier, G. Boissonnet, S. Salvador and D. Schweich, "Biomass pyrolysis experiments in an analytical entrained flow reactor between 1073 K and 1273 K," Fuel, vol. 87, pp. 1155-1164, 2008.

[39] M. Ronnback, J. Samuelsson, C. Tullin, H. Thunman and B. Leckner, "Gas composition in a fixed bed of biofuel – measurements in and above a downward propagating front," in Proc. 6th Int. Conference Science in Thermal and Chemical Biomass Conversion, Victoria, Canada, 2004.

[40] S. Zahirovic, R. Scharler, P. Kilpinen and I. Obernberger, "Validation of flow simulation and gas combustion sub-models for CFD-based prediction of NOx formation in biomass grate furnaces," Combustion Theory and Modeling, vol. 15, pp. 61-87, 2010.

[41] S. Pope, "Computationally efficient implementation of combustion chemistry using in situ adaptive tabuilation," Combustion theory and modeling, vol. 1, pp. 41-63, 1997.

[42] M. Farokhi and M. Birouk, "Application of Eddy Dissipation Concept for modeling biomass combustion, Part 2" Gas-phase combustion modeling of a small-scale fixed bed furnace," Energy and fuel, vol. 30, pp. 10800-10808, 2016.

[43] R. Barlow, J. Frank, A. Karpetis and J. Chen, "Piloted methane/air jet flames: transport effects and aspects of scalar structure," Combustion and Flame, vol. 143, pp. 433-449, 2005.

Chapter 3:Application of Eddy Dissipation Concept for Modeling Biomass Combustion, Part 2: Gas-phase Combustion Modeling of a Small Scale Fixed Bed Furnace.

3.1 Abstract

Small-scale grate-firing biomass furnaces suffer from high levels of pollutant emissions caused mainly by low level of air/fuel mixing and short residence time for combustion as a result of their small volume. Reliable gas-phase combustion modeling is key for improving the design of these systems. The present work describes a computational fluid dynamics study of biomass combustion using the modified eddy dissipation concept (EDC) model. Part 1 of this study focused on examining the main challenges of EDC model regarding its application for modeling weakly turbulent and slow chemistry reacting flows. In addition, a sensitivity analysis was carried out on the constants of the model for modeling non-premixed combustion at weakly and highly turbulent reacting flow conditions. Using the conclusions of the analysis of Part 1, gas-phase combustion of a small lab-scale grate-firing biomass furnace is simulated in the present paper (Part 2). The results revealed that the modified EDC model's parameters produced reasonable predictions of temperature and gas emissions.

Nomenclature

C_γ	EDC Model constant	ε	Turbulent Dissipation Rate
C_τ	EDC Model constant	ϑ	Kinematic viscosity
k	Turbulent Kinetic Energy	γ	Length fraction of fine scales
Re_t	Turbulent Reynolds number	τ_{EDC}	EDC time scale
Re_{tmin}	EDC minimum turbulent Reynolds number	τ_η	Kolmogorov time scale
T_t	Turbulent time scale	τ_{mix}	Characteristic mixing time scale

3.2 Introduction

The growing demand of renewable energy sources fuelled a growing interest in research on energy derived from carbon-neutral fuels such as biomass [1]. Biomass can be converted into power or heat through different processes, such as direct combustion of biomass in furnaces [1, 2]. The prevalence of industrial grate firing biomass furnaces has increased in recent decades due to their low investment cost and capability of burning biomass independently on particles size, ash and moisture contents [2, 3]. However, this technology still needs additional improvements in order to maximize thermal efficiency and further reduce pollutant emissions [4]. For instance, small scale grate firing biomass furnaces generate high level of emissions due mainly to their smaller volume and consequently shorter residence time [2]. Therefore, in order to meet the standard emissions level, further improvements of their design require comprehensive understanding of biomass conversion as well as gas-phase combustion of volatiles in free room above the bed, known as a freeboard.

Computational fluid dynamics (CFD) is becoming increasingly an important tool for the development and optimisation of biomass furnaces due mainly to their lower investment cost compared with experiments [5, 6]. However, the reliability of CFD predictions relies on the accuracy of sub-models. For instance, the conversion process within the bed consists of sub-models such as moisture evaporation sub-model, while gas-phase combustion in the freeboard uses turbulence-chemistry interaction sub-models. Thus, the degree of the problem simplification along with the capability of sub-models plays a key role for the reliability of CFD simulation.

Biomass conversion in grate firing furnaces, which is the process of solid fuel decomposition in the grate, is modeled using bed models, which are used as fuel inlet boundary for simulating the gas-phase in the freeboard [4]. There exists a variety of bed models. Simple bed models are intended to provide species mass fractions and temperature profiles at the inlet to the freeboard. These profiles can be obtained experimentally or calculated based on the principle of heat and mass balance of the fuel's components and primary air [5, 7, 8]. Complex bed models use separate sub-models for each conversion process. An interface is usually used between the bed and freeboard to share and couple the data between the bed and freeboard [9, 10]. Biomass combustion process in the freeboard is commonly modeled using species transport models (i.e., FRK/EDM and EDC) [4]. Finite-rate kinetic/eddy dissipation model (FRK/EDM) [11] is employed to model a variety of combustion applications [8, 12, 13, 14, 15]. For FRK/EDM, both mixing and kinetic reaction rate are computed at each computational cell and the lower value determines if the combustion is either kinetically or mixing limited. FRK/EDM is known by its high stability and low cost of calculation, but also by its main handicap in accounting for detailed chemistry of reactions for mixing limited regions, which implies that intermediate species and pollutants such as CO and NO_x cannot be accurately predicted.

Eddy Dissipation Concept (EDC) model [16], as an extended version of EBU models, has been widely used for biomass combustion simulations [1, 2, 6, 17, 18]. Klason and Bai [2] employed EDC with fast gas-phase combustion assumption to model a small lab-scale fixed bed biomass furnace. They indicated that turbulence intensity of air inlets has a significant impact on the model predictions of temperature and species. On the other hand, Evans et al. [19] optimized the EDC model's constants for modeling a lifted jet flame and their predictions showed less sensitivity to boundary conditions; such as jet inlet turbulence intensity and temperature. Sukumaran and Kong [1] used EDC along with a reduced chemical mechanism for modeling fuel NO_x formation of biomass-derived gas in an industrial burner and reported that, when compared with experimental measurements, their predictions captured the level and trend of NO_x resulting from different ammonia contents in the gas. Shiehnejadhesar et al. [20] proposed a hybrid FRK/EDC model for simulating combustion at weakly and highly turbulent flow conditions. They examined and compared the predictions of their hybrid model with the standard EDC for simulating a biomass grate furnace using wood pellets and straw pellets as fuel [6]. They stated that the standard EDC predicted higher level of CO concentration compared with the hybrid model. Buchmayr et al. [4] compared the predictions of the standard EDC with flamelet PDF model for simulating a fixed bed biomass furnace. They reported that while both models predicted almost similarly the temperature field, the flamelet model showed reasonable predictions of the level of CO mole fraction, whereas the standard EDC showed substantial overestimation when compared with experiments.

EDC model is capable of incorporating detailed chemical reactions mechanisms in turbulent flow and, therefore, intermediate species and pollutants emissions can be predicted. Despite the widespread use of EDC model, only a few studies have examined its limitations for simulating biomass combustion (e.g., Refs. [4, 6]). In Part I of this study, [21] the sensitivity of the EDC

model's parameters on the predictions of the characteristics of turbulent reacting flow field was performed at different conditions (e.g., weakly and highly turbulent flow field conditions). Thus, the current study (Part II) aims to examine the capability of the modified EDC model for simulating biomass combustion. Simulations are performed using a 8-11 kW lab-scale grate firing biomass furnace and the predictions are compared with published experimental measurements.

3.3 Methodology

Only the combustion of the gas-phase is simulated in this paper, which is assumed incompressible and obeys the ideal gas law. Reynolds Averaged Navier-Stokes (RANS) conservation equations of continuity, momentum, energy and species transport equations are solved. The effect of enthalpy transport is included in the energy equation to account for the effect of species diffusion. P_1- approximation model [22] is adopted along with the domain based weighted-sum-of-gray-gas (WSGG) [23] to model the effect of radiation. Turbulence is modelled using the renormalization group (RNG) $k-\varepsilon$ model [24, 25]. EDC model is employed to model the effect of turbulence-chemistry interaction. For the EDC model, the volume fraction of fine structure where chemical reactions take place, $\gamma^* = \gamma^3$, and the residence time of reactions within the fine structure, τ_{EDC}, can be expressed based on the flow turbulence characteristics as follows [18]:

$$\gamma = \left(\frac{3C_{D2}}{4C_{D1}^2}\right)^{0.25}\left(\frac{\vartheta\varepsilon}{k^2}\right)^{0.25} = C_\gamma (Re_t)^{-0.25} \tag{3-1}$$

$$\tau_{EDC} = \left(\frac{C_{D2}}{3}\right)^{0.5}\left(\frac{\vartheta}{\varepsilon}\right)^{0.5} = C_\tau\left(\frac{\vartheta}{\varepsilon}\right)^{0.5} = C_\tau\tau_\eta = C_\tau (Re_t)^{-0.5}\frac{k}{\varepsilon} \tag{3-2}$$

where γ is the length fraction of fine scales, $\tau_\eta = (\vartheta/\varepsilon)^{0.5}$ is the Kolmogorov time scale and $Re_t = (k^2/\vartheta\varepsilon)$ is the turbulent Reynolds number. C_γ and C_τ are the EDC model's constants associated to the fine structure volume and its residence time where the default values are 2.1377

and 0.4082, respectively [26, 27]. Detailed description of the EDC model is reported in Part I of this study [21].

A global two-step reaction mechanism of the combustion of hydrocarbon with CO as the intermediate species is used as the combustion scheme. The combustible volatiles and other gases produced from the bed are assumed to be C_6H_6 [14, 28] as heavy hydrocarbon, CH_4 as light hydrocarbon, CO_2, O_2, H_2O, CO, and N_2 [2]. The empirical bed model, which is developed in Ref [2], is adopted in the present study. The concentration of the gases coming out of the bed is assumed to be uniform throughout the bed. Also, the temperature of gases and the mass fractions of CO_2, O_2 and CO are known from the experiment measured at 0.02 m above the bed [2, 29]. The results of the ultimate fuel particle analysis on dry ash-free basis and mass flow rates of the primary air and fuel are presented in Table 3-1. The mass fractions of all the other species are obtained by applying the mass and energy balance principle to the fuel and primary air, as detailed in Ref. [2] (see Table *3-5*). It should be noted that based on the fuel/air mass flow and the total inlet mass flow of the primary air, the amount of ash in the fuel particles is considered negligible.

Table 3-1. Experimental data [2].

Ultimate analysis of fuel particle on dry ash-free basis (wt%)			
C	**O**	**H**	**N**
51.1	42.5	6.3	<0.1

Fuel mass flow rate (kg/s)	**Primary air mass flow rate (kg/s)**	**Total primary mass flow rate (kg/s)**
4.61e-4	5.81e-4	1.04e-3

Table *3-2* and Table 3-3 show the results of elements mass- and energy- balance, respectively, of the volatile gases coming out of the bed. It should be mentioned that the low heating value (LHV) of all compositions are selected from Ref [30].

Table 3-2. Elements mass balance between inlet and outlet of the bed.

Element mass fraction	C(%)	O(%)	H(%)	N(%)
Ultimate analysis (fuel + air)	22.7	31.9	2.79	42.9
Calculation	22.1	31.7	2.96	43.2
Relative error (%)	2.36	0.53	5.9	0.81

Table 3-3. Energy balance between inlet and outlet of the bed

	Mass flux	Temperature	Enthalpy flux	LHV flux	Total energy flux
	(kg/sec)	(K)	(kJ/sec)	(kJ/sec)	(kJ/sec)
Fuel (inlet)	4.61e-4	300	0.2351	8.87	9.105
Primary air (inlet)	5.81e-4	300	0.1743	N/A.	0.1743
Volatile gases (outlet)	-1.04e-3	1373 [44]	-2.5	-7.14	-9.64
Relative error (%)					3.89

3.4 Physical and numerical setups

The simulation study is carried out by adopting a 8-11 kW small lab-scale biomass furnace geometry [2], which consists of a cylindrical combustor having a diameter of 0.2 m and a height of 1.7 m (see Figure *3-1*). The Primary air is injected via a grate with a mass flow rate of 0.581 gr/sec, and the secondary and tertiary air inlet jets supply excess air above the bed with mass flow rates of 1.18 and 1.89 gr/s, respectively. All airflow inlets are supplied at standard ambient conditions (i.e., 298 K and 100 kPa). The fuel mass flow rate injected into the bed is 0.461 gr/s. The effluent gas coming out of the bed and the wall temperatures were measured to be 1373.15 K and 873.15 K, respectively [2]. Table *3-4* provides a summary of the physical and numerical setups used in this study. A schematic diagram of the adopted burner setup is presented in Figure 3-1. Further details can be found in Refs. [2, 29].

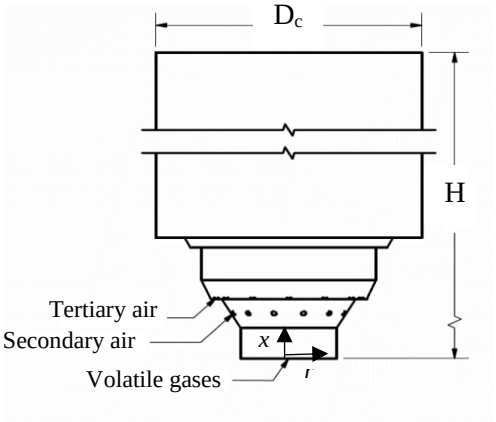

Figure 3-1. Schematic diagram of a 8-11 kW biomass furnace tested in Ref [2].

Table 3-4. Summary of the physical and numerical setup (Refs. [2, 29])

Parameter	**Value**
Total mass flow rate exiting from the bed [kg/sec]	1.04e-3
Total mass flow rate injected through the secondary air jets [kg/sec]	1.18e-3
Total mass flow rate injected through the tertiary air jets [kg/sec]	1.89e-3
Temperature of the volatile gases above the bed [K]	1373
Temperature of the injected secondary air jets [K]	298
Temperature of the tertiary air jets [K]	298
Temperature of the furnace's wall [K]	873
Diameter of the cylindrical furnace [mm]	200
Diameter of the secondary jets injector [mm]	4
Diameter of the tertiary jets injector [mm]	4
Number of secondary air jets [-]	12
Number of tertiary air jets [-]	12

The CFD simulations are carried out using the commercial code ANSYS Fluent R15. Second order upwind spatial discretization scheme is adopted for all conservation equations. SIMPLEC method is applied for the velocity-pressure coupling algorithm. A three-dimensional (3D) non-uniform grid is used to model the geometry with a height of 820 mm above the bed. The optimized grid consists of about 690,000 cells with a local increase of grid resolution in the vicinity of the bed and at the exit of the secondary and tertiary jets. Further grid refinement did not show significant change in the simulation predictions. The In-Situ Adaptive Tabulation (ISAT) [31] algorithm is used to increase the CPU-intensive treatment of the detailed kinetics of the chemistry with an ISAT error tolerance of 10^{-5}. Non-slip conditions along with zero normal gradients of species mass

fractions and constant temperature of 873.15 K are adopted for the furnace's walls. The effect of wall shear stress is performed using scalable wall function approach. Also, the emissivity of the bed and walls is set as 0.9 [2, 32]. The pressure outlet condition is used for the outflow boundary conditions. Table *3-5* presents the adapted boundary conditions for the present simulation. It should be mentioned that these data are provided based on the suggested values and experimental measurements reported in Ref [2]. A converged solution is achieved when the residuals of the computed species reaches 10^{-4}, and 10^{-5} for all the other parameters.

Table 3-5. Details of the boundary conditions (Ref [2]).

	Mass Fraction							$\dot{m}$	**Temp**	**Turbulence**	
	C_6H_6	CH_4	CO_2	O_2	H_2O	CO	N_2	(kg/s)	(K)	I(%)	L(m)
Primary	0.1305	0.0297	0.264	0.0194	0.109	0.015	0.432	1.04e-3	1373	5	7e-2
Secondary	-	-	-	0.233	-	-	0.767	1.18e-3	298	23	4e-2
Tertiary	-	-	-	0.233	-	-	0.767	1.89e-3	298	58	4e-2

3.5 Results and discussions

The simulations' results of temperature, species and velocity fields are presented below. As mentioned previously, the effect of EDC model's constants was examined in Part I [21] of this study for different flow conditions (e.g., weak and high turbulent flow conditions). In this part of study (Part II), the gas-phase combustion in a fixed bed biomass furnace is modeled based on the conclusions of the analysis of Part I. That is, the EDC model's constants are selected based on the examination carried out using cases A and B of Part I [21]. Three different numerical tests are carried out. The values of C_γ and C_τ which are used for EDC model for each case are given in Table 3-6.

Table 3-6. Details of the examined cases

parameter	**Case 1**	**Case 2**	**Case 3**
C_γ	2.1377	1.75	2.37
C_τ	0.4082	5.62	5.62

3.5.1 Validation of the model

The numerical predictions are compared with published experimental measurements using the standard EDC approach (case 1). Figure 3-2 presents the profiles of temperature and mole fraction of CO, CO_2 and O_2 along the centerline of the furnace. This figure shows that all the numerical results reasonably predict the trends of the measured temperature and gas species. The predictions are in closer to their experimental counterparts downstream of the furnace. However, Figure 3-2a shows over predictions of the temperature and CO mole fraction in the vicinity of the bed, while Figure 3-2b shows under estimations of CO_2 and O_2 mole fractions profiles at the same locations. Moreover, the predictions under estimate the profile of CO_2 mole fraction almost everywhere within the furnace. The numerical results presented in Figure 3-2 indicates that although the trend of the temperature and species can be predicted by the standard EDC, its quantitative performance (predictions) is less satisfactory when compared with experimental measurements, especially in vicinity of the bed.

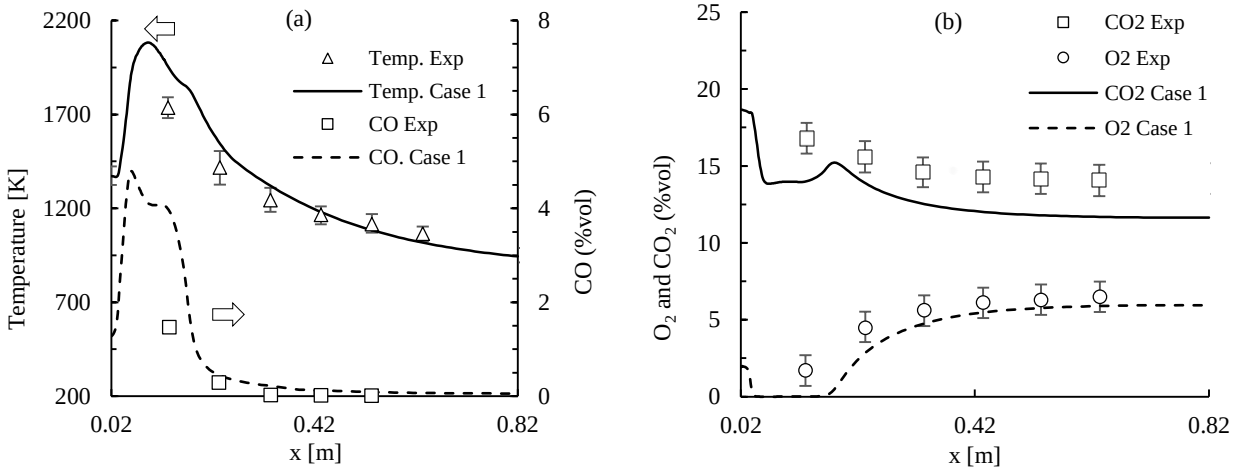

Figure 3-2. Validation of the numerical predictions of the standard EDC (case 1)

3.5.2 Choosing the constants of the model

The radial profiles of turbulent Reynolds number for case 1 are presented in Figure 3-3a at X/D_c= 0.25, 0.5 and 0.75, where $\mathrm{D}_C = 200\,mm$ is the diameter of the cylindrical furnace and X is the axial direction along the cylinder centreline. This figure shows that, except near the walls, the turbulent Reynolds number is high enough (i.e., $Re_t > 64$). The value of γ, which is associated with the size of the reaction zone, is presented in Figure 3-3b. This figure shows that, except near the walls, γ is lower than its maximum limit ($\gamma = 0.75$) elsewhere. Figure *3-2*a-b, consequently, suggest that the standard EDC is capable of producing satisfactory predictions. On the other hand, the sensitivity analysis performed on a highly turbulent combusting flow case (see case B of Part I[21]) revealed that, even within high turbulent flow regions, the modified EDC model's constants can still produce better predictions than the standard. Therefore, the present simulations are also performed using two different groups of constants (cases 2 and 3).

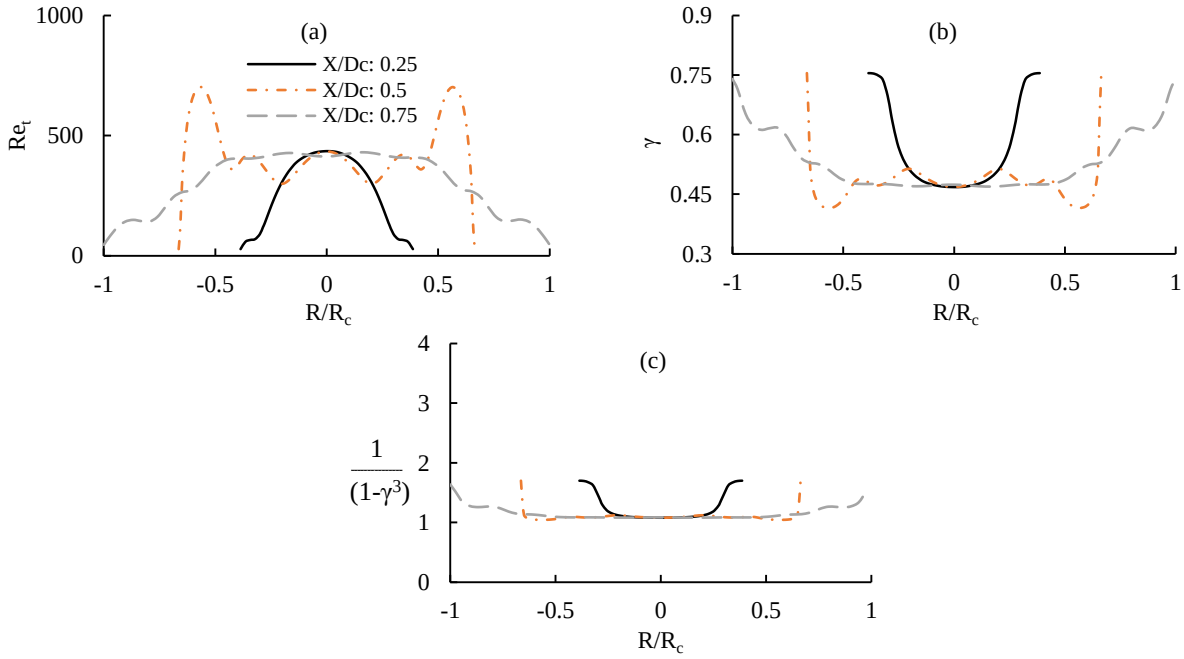

Figure 3-3. Radial profiles of (a) Re_t, (b) γ and (c) $1/(1-\gamma^3)$ (case 1)

It was previously observed that the ratio of turbulent time scale over the characteristic mixing time scale remains almost constant in the flow regions where turbulent Reynolds number is higher than Re_{tmin} (see Part I [21]). That is, this ratio is independent on the size of fine structures for high turbulent flow regions. Accordingly, based on the radial profile of turbulent Reynolds numbers at X/D_c= 0.25 (Figure *3-2*a), $Re_{tmin} = 100$ is selected to calculate C_γ as follows (see Part I [21] for more details):

$$C_\gamma < 0.75 Re_{tmin}^{0.25} \xrightarrow{Re_{tmin}=100} C_\gamma = 2.37 \tag{3-3}$$

Figure 3-3c shows the radial profiles of $(1-\gamma^3)^{-1}$ at X/D_c= 0.25, 0.5 and 0.75. This figure shows that this term is close to unity for the standard EDC model (case 1). The selected value of C_τ is based on the assumption that T_t/τ_{mix} is unity as the reaction rates is predominately controlled by turbulent mixing [2]. Hence, based on Eq.(3-4) and using $C_\gamma = 2.37$, a value of $C_\tau = 5.62$ is selected (case 3) as follows:

$$\frac{T_t}{\tau_{mix}} = \frac{1}{(1-\gamma^3)} \frac{{C_\gamma}^2}{C_\tau} \Rightarrow \frac{1}{(1-\gamma^3)} = \frac{T_t/\tau_{mix}}{{C_\gamma}^2/C_\tau} \tag{3-4}$$

$$\left.\begin{array}{l} T_t/\tau_{mix} = 1 \\ \dfrac{1}{(1-\gamma^3)} = 1 \end{array}\right\} \xrightarrow{C_\gamma=2.37} C_\tau = 5.62 \tag{3-5}$$

Based on the examination of the EDC model's constants performed in Part I [21], increasing both C_τ and C_γ for highly turbulent flow conditions improves the predictions of the slow chemistry species, such as CO. On the other hand, using a higher value of C_τ and a lower value of C_γ (than the standard values) improves the predictions of CO_2 species in addition to CO. Moreover, for flow regions such as in the vicinity of the secondary airflow injection ($X/\mathrm{D}_c \approx 0.5$) and close to the

walls, where γ sharply increases due to low level of turbulence (Figure 3-2a and b), using smaller value of C_γ (according to the sensitivity analysis performed in Part I [21] for weakly/low turbulent flow conditions) improves the predictions of the reaction rate via decreasing the size of fine structures. That is why another case (case 2) is simulated using $C_\gamma = 1.75$ with the same C_τ as in case 3. This C_γ value is calculated using Eq.(3-1) and based on a minimum turbulent Reynolds number of $Re_{tmin} = 30$ (which corresponds to low turbulent flow regions close to the furnace walls at $X/\mathrm{D_c}$= 0.25 and 0.5).

3.5.3 CO, velocity and temperature fields

Figure 3-4 shows a 2D contour of the axial velocity (Figure 3-4a) and also velocity vectors (Figure 3-4b) of region A of the furnace for case 1. As it can be seen in this figure, the interaction of the airflow injected from the secondary jets produces a recirculation zone above the bed (Zone A). The effect of the EDC model's constants on the velocity field is investigated, where the velocity vectors of region A of the furnace for cases 1-3 is presented in Figure 3-5. This figure shows that changing the EDC model's constants shifts downstream the onset of the first recirculation zone (Zone A). According to this figure, the onset (start) of Zone A shifts towards the bed in cases 2 and 3 compared with case 1; whereas the recirculation zone ends almost at the same position for all cases. This suggests that the modified constants of the EDC model have a slight impact on the velocity field.

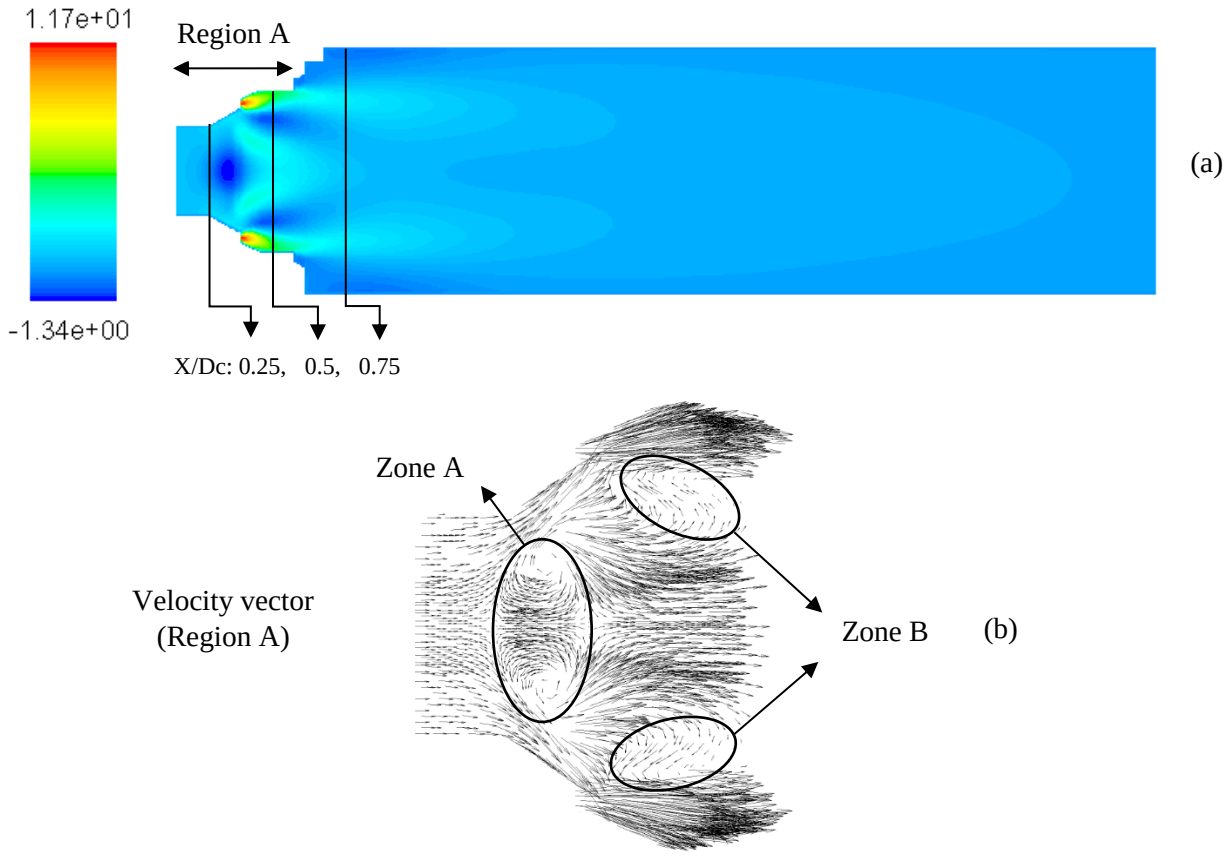

Figure 3-4. (a) Axial velocity contours [m/sec], and (b) velocity vectors for case 1

Farther downstream of zone A, further two recirculating flow zones are produced as a result of the interaction of the secondary and tertiary airflow jets with the furnace wall as well as the flow in the wake of the first recirculation zone (Zone B). Each one of these two recirculation zones has an "S" shape and named as Zone B in Figure 3-4b. The high velocity fresh air injected via tertiary jets generates a shear layer which enhances the mixing process of fresh O_2 with the combustible volatile gases in Zone B [2], and consequently the combustion of the remainder of volatile gases carried into this zone (Zone B).

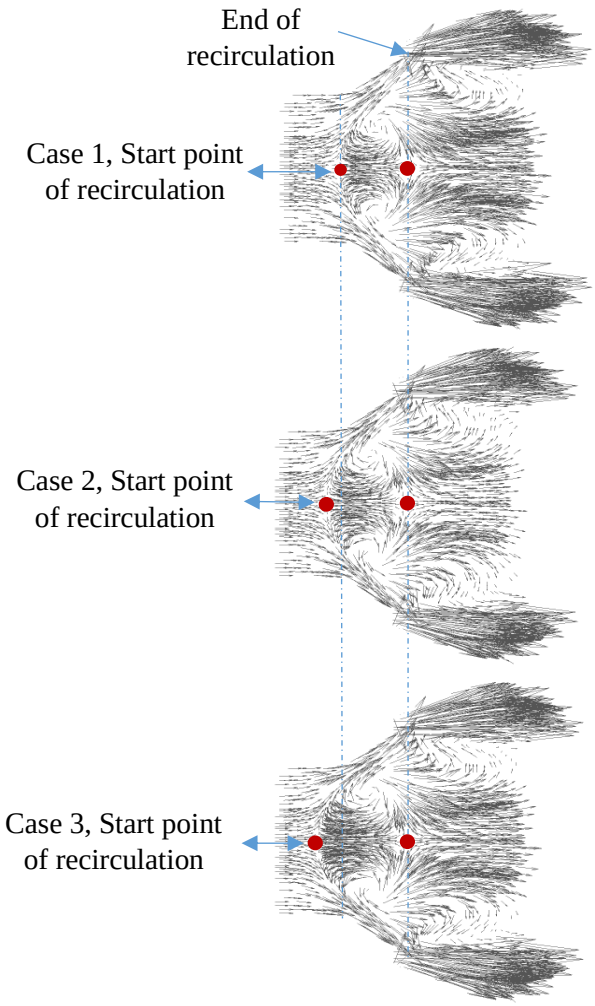

Figure 3-5. Velocity vectors for cases 1-3

The effect of recirculation in Zone A on the temperature and CO formation contours is investigated and presented in Figure *3-6* and Figure *3-7*. It is evident from Figure 3-6 that a high gradient of temperature develops near the bed, which starts at the root (onset) of the recirculation zone. The interaction of the primary flow coming out of the bed with the recirculating flow in Zone A produces a low velocity region downstream of the bed, which acts as an aerodynamic holder of the flame [33]. Moreover, the recirculation of heat and chemically active species back into this zone increases the stabilization of the flame and enhances the chemical reactions [33, 34]. It is evident from Figure 3-7 that, within zone A, CO formation is promoted and chemical reactions are

enhanced as fresh oxidizer is supplied via the secondary airflow which mixes with the recirculating chemically active species. This trend has also been observed for cases 2 and 3 which confirm their independency on the values of C_τ and C_γ. According to Figure *3-6* and Figure *3-7*, case 2, which uses the lowest value of C_γ, predicts the lowest temperature peak compared to cases 1 and 3. This observation is in line with the predictions of the axial temperature profiles at highly turbulent flow conditions presented in Part I of this study (see Figure 5 in Ref [21]). Moreover, while the location of the peak of CO mass fraction is almost similar in both cases 2 and 3, case 3 predicts less CO formation along the centerline in the vicinity of the bed.

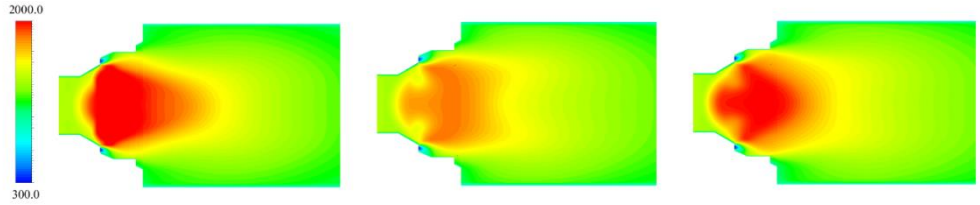

Figure 3-6. Temperature contours [in Kelvin] for cases (from left to right) 1, 2 and 3.

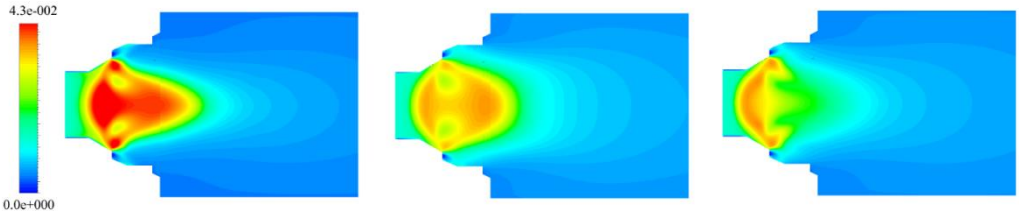

Figure 3-7. Mean CO mass fraction contours of (from left to right) cases 1, 2 and 3.

3.5.4 Comparison of the predictions with measurements

Figure 3-8 presents the temperature and mole fraction profiles of CO, CO_2 and O_2 along the centerline of the furnace for cases 1-3. In comparison with the experimental data, the profiles of temperature and CO mole fraction are captured satisfactorily downstream of the bed in all cases, whereas some differences exist in the vicinity of the bed. Figure 3-8 also shows that the trends of the profiles for all cases are nearly similar with different peak values, with the exception of case 2 which shows different trend for the temperature and CO close to the bed, which will be discussed

later. Figure 3-8a shows that the best predictions of the temperature is achieved with case 2, while case 3 shows the best results of CO. Figure 3-8b indicates that the best predictions of CO_2 are achieved with case 2, which corroborates the findings reported in (case B2) Part I [21]. This figure also shows a comparison of the numerical results of O_2 mole fraction with experimental measurements. A notable point which can be seen from the predictions of species is that all cases show no more formation of CO_2 and CO or no more consumption of O_2 after passing the injection point of the tertiary air (region A in Figure 3-4). This suggests that most of the combustion takes place in the high turbulence regions as the concentration of species remains constant farther downstream of the furnace.

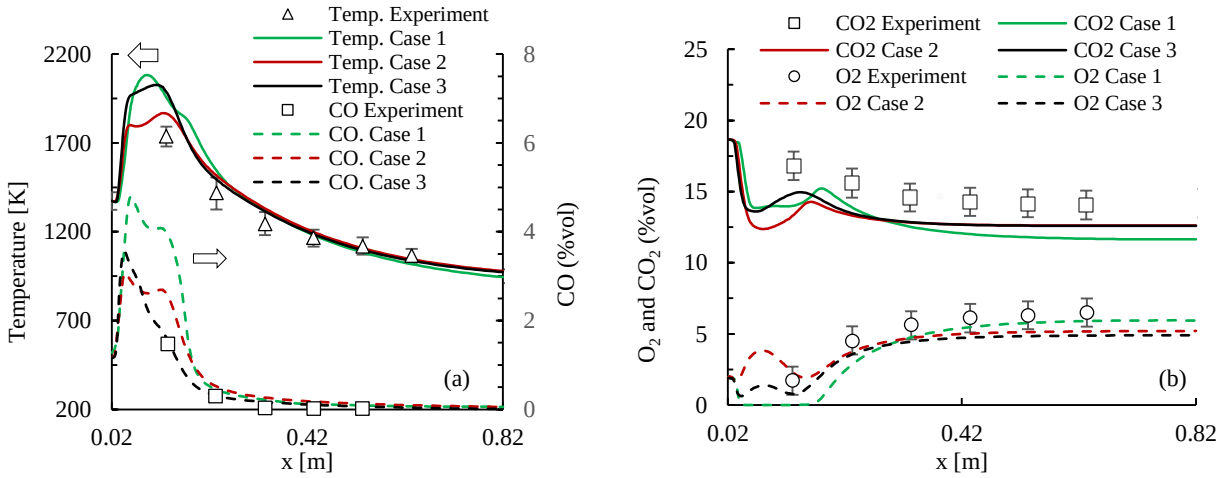

Figure 3-8. Axial profiles of the temperature and species mole fraction along the centerline of the furnace.

Figure *3-9* presents the radial profiles of temperature (Figure *3-9*a-c) and mole fractions of CO_2 (Figure *3-9*d-e) and CO (Figure *3-9*g-i) at X/D_c= 0.25, 0.5 and 0.75. According to Figure *3-9*a-c, all the three cases show slight difference in the temperature profiles close to the wall. These figures show that case 2, which has the lowest value of C_γ, predicts the lowest temperature close to the wall, and case 3, which has the highest value of C_γ, predicts the highest temperature in the same region. This can be attributed to the difference size of the reaction zone (i.e., γ^3) near the furnace

wall for cases 2 and 3. That is, the maximum size of the reaction zone corresponds to flow regions where Re_t< 30 (based on C_γ=1.75) for case 2, and Re_t< 100 for case 3 (based on C_γ=2.35). Figure *3-9*a-c also reveal that, close to the centerline, the effect of the model's constants is more apparent. This is attributed not only to the direct influence of the model's coefficients, but also to the effect of the velocity field (which is in turn affected by the model's coefficients). According to Figure 3-5, changing the model's constants leads to a change in the onset location of the recirculation zone (zone A) which consequently affects the position of the peak temperature. The peak temperature in the furnace occurs in zone A where non-premixed combustion takes place between the volatile gases and fresh oxygen injected from secondary air-jets. Figure 3-5 shows that case 3 predicts that the onset of zone A is the closest to the bed compared with the other cases. Therefore, the maximum peak temperature predicted with case 3 (see Figure *3-9*a) occurs closer to the bed (via shifting zone A to upstream of the furnace). Figure *3-9*a-c show that case 2 overall predicts the lowest temperature closer to the centerline which can be attributed to the fact that this case has the smallest size of the reaction zone compared with the other cases.

Figure *3-9*d-f show the predictions of CO_2 mole fraction in the radial direction. The lowest distribution of CO_2 in the centerline is predicted by case 2, which is in agreement with the results presented in part I (Ref. [21]) for highly turbulent flow conditions. Away from the centerline, cases 2 and 3 predict nearly the same results, which is more evident at X/D_c= 0.25 and 0.75 (Figure *3-9*d and f). Similar predictions were observed for highly turbulent flow jet (case B in Ref [21]) in the radial direction away from the jet core where the level of turbulence starts to decay. Figure *3-9*g-i present the predictions of CO mole fraction in the radial direction. The figure shows that closer to the centerline, the lowest level of CO is predicted with case 3. Slow-forming intermediate species such as CO can be more accurately predicted due to having sufficient time for the formation and

also destruction to produce CO_2 in case 3 as C_γ has the largest value amongst the other cases. This process (i.e., formation/destruction of CO) is further enhanced with longer residence time when using larger values of C_τ. It can also be seen in Figure *3*-9g-i that, close to the wall, all cases produced almost the same predictions with the exception of case 1 at X/D_c= 0.25. Comparing the radial temperature and species profiles corresponding to the highly turbulent flow conditions explored in Part I (Ref [21]) with those in Figure *3-9* suggests that the flow field of the current furnace is dominantly high turbulent conditions. This is because, with the exception near the furnace wall, the predictions of the temperature and species profiles follow similar trends as those of highly turbulent flow conditions of case B of Part I (Ref [21]).

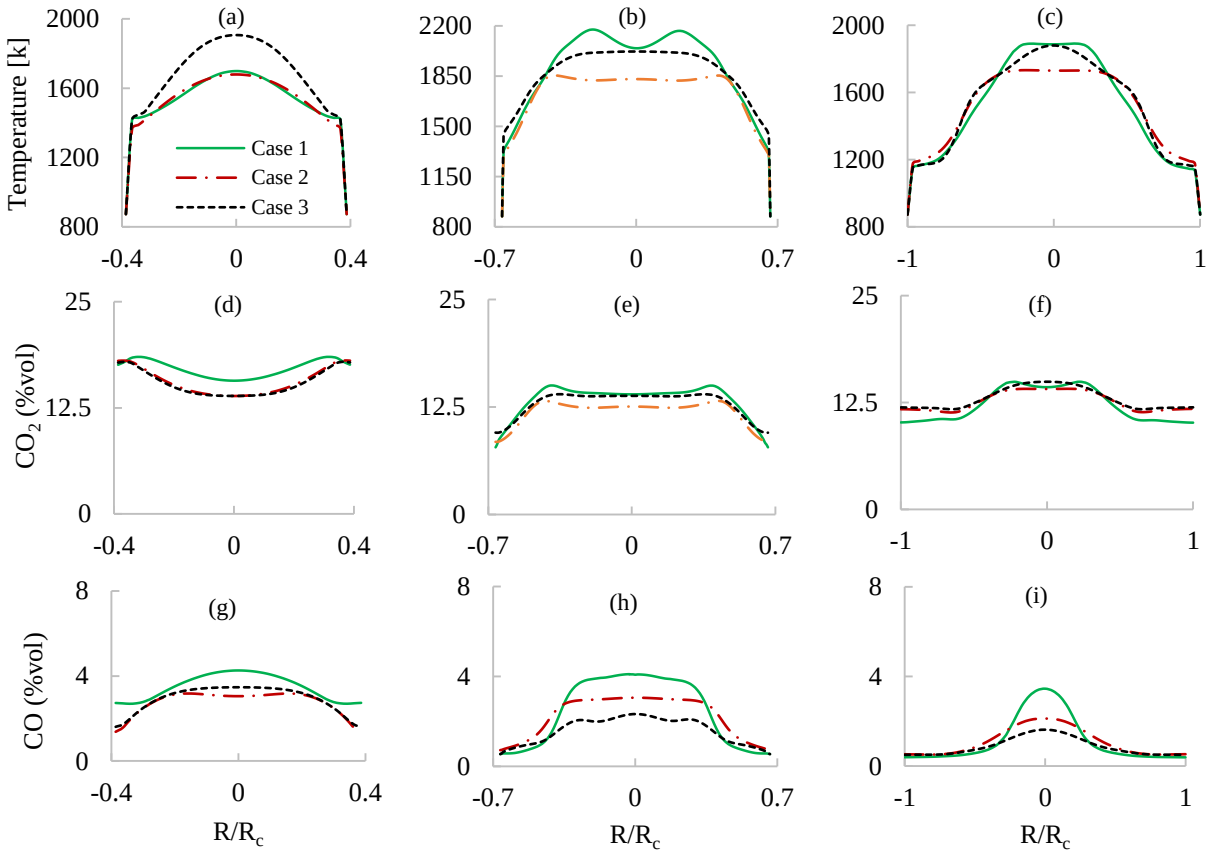

Figure 3-9. Radial profiles of the temperature, CO_2 and CO at X/Dc= 0.25 (a,d,g); = 0.5 (b,e,h), and = 0.75 (c, f, i)

3.6 Conclusions

The present numerical study examined the influence of the EDC model's coefficients on the predictions of temperature, species, turbulence and velocity fields of the gas-phase combustion of a small scale fixed bed biomass furnace. The results of turbulent flow field indicated that, in most regions inside the furnace, the flow is highly turbulent except near the furnace's wall. Consequently, the model predictions of all studied cases confirmed the conclusions achieved in Part I of this study. That is, the influence of C_τ on the predictions of temperature and species is weaker than that of C_γ. Velocity, species and temperature fields were investigated in cases 1-3. The results showed that the modified EDC model's constants can slightly affect the velocity field. Comparing the temperature and species profiles for the examined cases, it was shown that the effect of the model's constants is mostly visible in the vicinity of the bed whereas the predictions are almost independent on the model's coefficients downstream of the furnace.

The present study demonstrated that the capability of EDC model for predicting the characteristics of biomass combustion at both weakly and highly turbulent flow conditions can be improved via modifying the model's constants. That is, the modified EDC model can lead to a more accurate predictions of the temperature and gas emissions of the gas-phase combustion in industrial biomass furnaces (especially the slow-forming pollutant emissions, such as CO) where the flow is characterised by a wide range of turbulent conditions. It must be mentioned that the modification of the EDC coefficients requires a prior knowledge of the flowfield turbulence characteristics (i.e., turbulent Reynolds number and Kolmogorov time scale). This is why the standard EDC must be used for the initial simulation in order to determine the required flow characteristics. This step of the simulation can increase the computational time.

Based on the present findings, it is recommended to implement and examine the reactor model which accounts for the combustion not only in fine structures but also in the surroundings fluid. This could improve the predictions especially for slow forming species as it was suggested in Refs. [35, 36]. This will be carried out in a subsequent study.

3.7 References

[1] S. Sukumaran and S. C. Kong, Modeling fuel NOx formation from combustion of biomass-derived producer gas in a large-scale burner. Combustion and Flame 2013, 160, 2159-2168.

[2] T. Klason and X. S. Bai, Computational study of the combustion process and NO formation in a small-scale wood pelletfurnace. Fuel 2007, 86, 1465-1474.

[3] S. Van Loo and J. Koppejan, Handbook of biomass combustion and co-firing; Twente University Press, 2002.

[4] M. Buchmayr, J. Gruber, M. Hargassner, and C. Hochenauer, A computationally inexpensive CFD approach for small-scale biomass burners equipped with enhanced air staging. Energy Conversion and Management 2016, 115, 32-42.

[5] Chaney, J.; Liu, H.; Li, J. An overview of CFD modelling of small-scale fixed-bed biomass pellet boilers with preliminary results from a somplified approach. Energy Conversion and Management 2012, 63, 149-156.

[6] Shiehnejadhesar, A.; Scharler, R.; Mehrabian, R.; Obernberger, I. Developement and validation of CFD models for gas phase reactions in biomass grate furnaces considering gas streak formation above the packed bed. Fuel Processing Technology 2015, 139, 142-158.

[7] Eskilsson, D.; Ronnback, M.; Samuelsson, J.; Tullin, C. Optimisation of efficiency and emissions in pellet burners. Biomass Bioenergy 2004, 27, 541-546.

[8] Yin, C.; Rosendahl, L.; Kaer, S.; Sonnik, C.; Hvid, S.; Hille, T. Mathematical modeling and experimental study of biomass combustion in a 108 MW Grate-Fired Boiler. Energy and Fuels 2008, 22, 1380-1290.

[9] Porterio, J.; Collazo, J.; Patino, D.; Granda, E.; Gonzalez, J. C. M.; Miguez, L. Numerical modeling of a biomass pellet boiler. Energy and Fuels 2009, 23, 1067-1075.

[10] Zhang, X.; Chen, Q.; Bradford, R.; Sharifi, V.; Swithenbank, J. Experimental investigation and mathematical modeling of wood combustion in a moving grate boiler. Fuel Processing Technology 2010, 91, 1491-1499.

[11] Magnussen, B. F.; Hjertager, B. H. On mathematical modeling of turbulent combustion with special emphasis on soot formation and combustion. 16th symposium (international) on combustion, The combustion institute, Pittsburgh, 1977.

[12] Bhuiyan, A. A.; Naser, J. CFD modeling of co-firing of biomass with coal under oxy-fuel combustion in a large scale power plant. Fuel 2015, 159, 150-168.

[13] Bhuiyan, A. A.; Naser, J. Numerical modeling of biomass combustion with pulverized coal in small scale furnace. Procedia Engineering 2015, 105, 504-511.

[14] Collazo, J.; Porteiro, J.; Miguez, J. L.; Granada, E.; Gomez, M. A. Numerical simulation of a small scale of biomass boiler. Energy conversion and management 2012, 64, 87-96.

[15] Djurovic, D.; Nemoda, S.; Repic, B.; Dakic, D.; Adzic, M. Influence of biomass furnace volume change on flue gases burn out process. Renewable Energy 2015, 76, 1-6.

[16] Magnussen, B. F. On the structure of turbulence and a generalized eddy dissipation concept for chemical reaction in turbulent flow. 19th AIAA aerospace science meeting, St. Louis, Missouri, 1981.

[17] Bugge, M.; Skreiberg, Y.; Haugen, N. E. L.; Carlsson, P.; Houshfar, E.; Lvs, T. Numerical simulation of staged biomass grate fired combustion with an emphasis on NOx emissions. Energy Procedia 2015, 75, 156-161.

[18] Shiehnejadhesar, A.; Schulze, K.; Scharler, R.; Obernberger, I. A new innovative CFD-based optimisation method for biomass combustion plants. Biomass Bioenergy 2013, 53, 48-53.

[19] Evans, M. J.; Medwell, P. R.; Tian, Z. F. Modeling Lifted Jet Flames in a Heated Coflow Using an Optimized Eddy Dissipation Concept Model. Combustion Science and Technology 2015, 187, 1093-1109.

[20] Shiehnejadhesar, A.; Mehrabian, R.; Scharler, R.; Goldin, G. M.; Obernberger, I. Development of a gas phase combustion model suitable for low and high turbulent conditions. Fuel 2014, 126, 177-187.

[21] M. Farokhi and M. Birouk, Application of Eddy Dissipation Concept for modeling biomass combustion, Part 1: Assessment of model coefficients. Energy and Fuels, 2016, 30, 10789-10799.

[22] M. F. Modest, Radiative Heat Transfer; Academic Press, 2003.

[23] N. Kayakol and N. Selcuk, Evaluation of descrete ordinates method for radiative transfer in rectangular furnaces. International Journal of Heat and Mass Transfer 1997, 40, 213-222.

[24] V. Yakhot and S. A. Orszag, Renormalization group and local order in strong turbulence. Nuclear Physics B - Proceedings Supplements 1987, 2, 417-440.

[25] Ansys. ANSYS Fluent Theory Guide, Release 15.0.

[26] B. F. Magnussen and I. R. Gran, numerical study of a bluff-body stabilized diffusion flame. Part 2. Influence of combustion modeling and finite-rate chemistry. Combustion Science and Technology 1996, 119, 191-217.

[27] B. F. Magnussen and I. S. Ertesvag, The eddy dissipation turbulence energy cascade model. Combustion Science and Technology 2000, 213-235.

[28] Khodaei, H.; Al-Abdeli, Y. M.; Guzzomi, F.; Yeoh, G. H. An overview of processes and considerations in the modelling of fixed-bed biomass combustion. Energy 2015, 88, 946-972.

[29] H. Wiinikka, writer, P.hd. thesis [Performance], High temperature aerosol formation and emission minimisation during combustion of wood pellet; Lulea University of Technology, Lulea, Sweden., 2005.

[30] C. Borgnakke and R. E. Sonntag, Fundamentals of Thermodynamics, John Wiley & Sons, Inc., 2009.

[31] S. B. Pope, Computationally efficient implementation of combustion chemistry using in situ adaptive tabuilation. Combustion theory and modeling 1997, 1, 41-63.

[32] Klason, T.; Bai, X. S.; Bahador, M.; Nilsson, T. K.; Sunden, B. Investigation of radiative heat transfer in fixed bed biomass furnaces. Fuel 2008, 87, 2141-2153.

[33] M. Saediamiri, M. Birouk and J. A. Kozinski, On the stability of a turbulent non-premixed biogas flame: Effect of low swirl strength. Combustion and Flame 2014, 161, 1326-1336.

[34] M. Birouk, M. Saediamiri and J. A. Kozinski, Non-premixed turbulent biogas flame: effect of the co-airflow swirl strength on the stability limits. Combustion Science and Technology. 2014, 186, 1460-1477.

[35] M. Rehm, P. Seifert and B. Meyer, Theoretical and numerical investigation on the EDC-model for turbulent-chemistry interaction at gasification conditions. Computers and Chemical Engineering 2009, 33, 402-407.

[36] L. Kjaldman, A. Brink and M. Hupa, Micro mixing time in eddy dissipation concept. Combustion Science and Technology 2000, 154, 207-227.

Chapter 4: A computational study of a small-scale biomass burner: The influence of chemistry, turbulence and combustion sub-models

4.1 Abstract

This paper presents a computational study to evaluate the influence of turbulence and combustion models as well as chemistry schemes on the combustion of a 8-11 kW small lab-scale biomass furnace. The analysis is conducted in the zone above the bed (freeboard) where the volatiles are burned. The turbulence models tested are standard $k-\varepsilon$, RNG $k-\varepsilon$ and Realizable $k-\varepsilon$; and the combustion models are SFM (Steady Flamelet Model), UFM (Unsteady Flamelet Model) and EDC (Eddy Dissipation Concept). In addition, several chemical mechanisms with different complexity (reduced and detailed chemical kinetics) are considered. The predictions of the velocity, species, and temperature fields are compared with their counterparts' experimental measurements. The present findings reveal that all tested combustion models (SFM, UFM and EDC) are capable of predicting temperature and major species profiles; whereas only EDC is able to reliably predict slow-chemistry species.

Nomenclature

C_γ	EDC Model constant	ϑ	Kinematic viscosity
C_τ	EDC Model constant	γ	Length fraction of fine scales
k	Turbulent Kinetic Energy	τ_{EDC}	EDC time scale
Re_t	Turbulent Reynolds number	τ_η	Kolmogorov time scale
$R_{i,EDC}$	EDC mean reaction rate	τ_{mix}	Mixing time scale
T_t	Turbulent time scale	ε	Turbulent Dissipation Rate

4.2 Introduction

Global warming concern and limited fossil fuel resources prompted serious interest in developing renewable energy sources such as carbon-neutral fuel (e.g., biomass pellets and woodchips) [1, 2]. Grate firing biomass furnace is one of the widespread used technology available in the market owing to its low investment cost and flexibility in terms of feedstock (i.e., wide range of biomass particles size, moisture and ash contents) [3, 4]. However, small scale biomass furnaces still suffer from generating high levels of gas emissions. This is caused mainly by the smaller furnace volume and consequently shorter residence combustion time [4]. Therefore, in order to meet future target levels of emissions and increased thermal efficiency, further studies are required to improve this technology [5].

Computational fluid dynamics (CFD) is becoming an increasingly important tool in the development, and optimization of biomass combustion devices due primarily to its noticeably lower cost compared with physical experiments and also to its ability to provide far more details than physical tests [6, 7]. CFD simulations of biomass combustion consist of two separate sub-

domains; namely the decomposition process of solid fuel in the grate and the gas-phase combustion of the volatile gases in the free room above the bed (known as freeboard) [5]. However, the reliability of the CFD predictions strongly depends on the sub-models used in the simulation of each domain.

To model turbulent biomass gas-phase combustion process, sub-models accounting for turbulence-chemistry interaction are employed. These sub-models employ the characteristics of turbulent field, combustible and oxidizer species, and the chemistry scheme in order to model biomass combustion process. Consequently, the reliability of the predictions (e.g., temperature field and emissions) relies strongly on the degree of simplification and capability of turbulence and combustion models as well as kinetic reaction mechanisms.

Standard (STD) and realizable $k-\varepsilon$ (RKE) turbulence models have been widely used to model turbulence in industrial biomass furnaces. Tabet et al. [8] performed a comprehensive CFD modeling of a domestic biomass stove using STD $k-\varepsilon$ turbulence model along with transport equations of mixture fraction for the gas-phase combustion in the freeboard. Also, in a review study, Chaney et al. [6] examined STD $k-\varepsilon$ model on the role of CFD modelling of small-scale grate firing biomass furnaces for optimizing the combustion performance and NO_x emissions. These studies showed that STD $k-\varepsilon$ turbulence model was able to reasonably predict velocity, species and temperature fields at different inlet airflow conditions. Collazo et al. [9] used RKE turbulence model for simulating a domestic pellet boiler and focusing on the influence of boiler parameters (e.g., air inlet distributions) on the emissions level. Their model satisfactorily predicted temperature and species profiles when compared with experimental measurements. Buchmaye et al. [5] performed a three-dimensional (3D) CFD simulation of a small-scale biomass furnace where RKE turbulence model was used for the gas-phase combustion. They reported acceptable

predictions of temperature and gas emissions in comparison with experimental measurements. Fletcher et al. [10, 11] tested both STD $k-\varepsilon$ and Reynolds stress model (RSM) for predicting flow entrainment in a biomass gasifier under isothermal (cold) and flame conditions. They reported that, compared with the predictions of the cold flow case, the predictions (i.e., temperature, gas concentrations and velocity field) of the reacting flow field are less sensitive to the adopted turbulence model [11]. They attributed these differences to changes in the density and hence velocity within the gasifier due to combustion, which dominates the flowfield and makes it less sensitive to the turbulence modeling. In another study, Knaus et al. [12] performed gas-phase simulation in the freeboard of a small-scale 15 kW wood heater in order to examine the application of different turbulence models, where low-Reynolds and STD $k-\varepsilon$ models as well as RSM turbulence model under cold flow and combustion conditions were tested. They reported different flowfield predictions of the cold flow using different turbulence models, whereas combustion characteristics (e.g., temperature and gas concentration) were predicted reasonably well by all models.

The modified version of the well-known eddy break-up (EBU) approach [13], known as finite-rate kinetic/eddy dissipation model (FRK/EDM) [14], has been widely adopted for simulating a variety of combustion systems due to its low computational cost and high stability [15, 9, 16, 17]. For FRK/EDM, both kinetic and mixing rates of reactions are calculated and the lowest of the two reaction rates determines whether the combustion process is mixing or kinetically limited. In the case of biomass combustion, FRK/EDM with reduced chemical reaction mechanisms (e.g., two-step mechanism) has been widely employed. Yin et al. [18] applied FRK/EDM along with a two-step reaction mechanism with CO as the intermediate species to simulate the combustion of a wheat straw grate-fired boiler. They achieved reasonable predictions of temperature and major species in

comparison with their counterpart's experimental data. The study discussed earlier by Collazo et al. [9] adopted FRK/EDM combustion sub-model together with the global two-step kinetic mechanism proposed by Westbrook and Dryer [19]. Yin et al [20] examined the influence of chemistry scheme and combustion sub-model on the simulation of a co-firing straw with coal in a dual-feed burner. They tested the four-step reaction mechanism proposed by Jones and Lindstedt [21] using EDC model [22] and compared the predictions against those of Westbrook and Dryer [19] reaction mechanism using FRK/EDM. Their results showed improved performance of the former approach (i.e., EDC) with respect to the prediction of flame volume (i.e., the region with high CO and low O_2 concentrations) [20].

The drawback of FRK/EDM is its inability of considering detailed chemistry for mixing limited conditions and consequently its inaccurate predictions of the intermediate species and pollutant emissions such as CO and NO_x [23]. In order to overcome this handicap, eddy dissipation concept (EDC), as an extended version of EBU models, has been proposed by Magnussen [22] to incorporate detailed chemistry in turbulent reacting flows. EDC has been widely used in biomass combustion applications. For instance, Klason and Bai [4] adopted EDC with fast gas-phase combustion assumption to model a small lab-scale grate firing biomass furnace. They reported that air inlets' turbulence intensity has a significant impact on the predictions. Sukumaran and Kong [2] used EDC with a modified version of GRI 3.0 [24] mechanism to model fuel NO_x formation from biomass-derived gas in a large-scale burner. They reported that their model can reasonably capture the level and trend of NO_x emissions. Bugge et al. [25] simulated a biomass grate fired combustor with more emphasis on the prediction of NO_x emissions using EDC along with three different chemistry schemes proposed for gas-phase biomass combustion [26]. Their predictions revealed significant effect of the chosen reaction mechanism on the prediction of NO_x emissions,

especially in the primary zone of the burner. It is well-known that despite the ability of EDC to employ detailed chemistry in turbulent flames, its capability to model weakly turbulent reacting flows and slow chemistry poses a real challenge (e.g., [27, 28, 29, 23]). In fact, there exist only a few studies which examined and addressed its limitations in biomass combustion (e.g., [30, 23]). For instance, Shiehnejadhesar et al. [30] proposed a hybrid FRK/EDC model suitable for weakly and highly turbulent flow conditions. Later on, they examined the performance of the standard EDC against their hybrid model for simulating a small-scale biomass boiler, and reported that the standard EDC over predicted CO concentration [7]. Farokhi and Birouk [23] performed a sensitivity analysis on EDC coefficients for both weakly and highly turbulent reactive flow conditions and suggested a method for modifying EDC coefficients based on turbulent flow characteristics (i.e., turbulent Reynolds number and turbulent time scale). They then simulated the gas-phase combustion of a small lab-scale biomass furnace using the modified EDC and reported improved predictions of temperature and species when compared with its standard version [31].

Another disadvantage of EDC is associated with its relatively high computational cost, especially when detailed chemistry is employed for simulating industrial combustion plants. That is why these types of simulations are restricted to reduced chemical schemes (i.e., two-step to four-step mechanisms) [32]. Mixture fraction approaches (i.e., steady flamelet model (SFM) [33] and unsteady flamelet model (UFM) [34]), which are capable of incorporating detailed chemistry at low computational cost, as alternative combustion sub-models are considered in the present study. In most commercial CFD softwares, such as FLUENT [35], the application of SFM and UFM are limited to one type of combustible mixture which can be used with different mixture fraction through different inlet boundaries. In the case of grate-firing biomass furnaces, this can be applied by assuming a uniform mixture of volatile gases throughout the bed, which is an acceptable

assumption for most small-scale biomass furnaces. Mixture fraction approaches (e.g., SFM and UFM) have been rarely used in biomass combustion. Albrecht et al. [36] performed a comparison between a mixture fraction-PDF method and EDC for grate-firing biomass combustion using GRI-Mech 2.11 chemical mechanism [37]. They found comparable results by using either of two sub-models. Tabet et al. [8] also presented a CFD platform for modeling domestic biomass heating systems, which employs a mixture fraction method with pre-assumed PDF turbulence-chemistry interaction for gas-phase combustion modeling. Venturini et al. [38] performed CFD modeling of a biomass-fed furnace using gas-phase combustion sub-model combined with a stretched laminar flamelet mixture fraction approach. In another work by the same research group, Borello et al. [39] carried out a CFD simulation using SFM approach to investigate its applicability for modeling a biogas-fed small furnace which uses packed-bed wood as a fuel. In a recent work, Buchmayr et al. [5] compared SFM and EDC approaches by simulating a small-scale biomass burner equipped with enhanced air staging. While the same detailed chemical mechanism of heptane-air flame [40] is adopted for both combustion approaches, they reported a better species predictions with the SFM approach. SFM is a suitable combustion model for turbulent reacting flows when the fast chemistry assumption is applicable [35]. However, this approach/model has repeatedly shown poor predictions of the formation or destruction of slow chemistry species such as CO and NO_x [41, 42, 43]. To overcome this shortcoming, a transient history of the strain rate evolution has to be considered in a flamelet approach [41, 44]. This can be applied on a converged steady state flowfield achieved through SFM by using an unsteady flamelet model (UFM) approach [35]. While many studies have stated the importance of unsteadiness on flamelet based turbulent diffusion flame models (e.g., [45, 41, 34]), to the best knowledge of the present authors, there exist only a few published studies on the application of UFM for modeling grate firing biomass furnaces.

For instance, Knudsen et al. [46] used UFM approach in combination with large eddy simulation (LES) to model a biomass combustor. While they reported that the magnitude of CO concentration could not be accurately predicted, the model was able to predict the experimentally observed sensitivities to the combustor test conditions.

The present study aims to investigate the performance of turbulence and combustion models as well as chemistry scheme for simulating the gas-phase combustion of a grate firing biomass furnace. The influence of $k-\varepsilon$ turbulence models (i.e, STD, RNG and RKE) as well as different combustion sub-models (i.e., SFM, UFM and EDC) is examined in the present study. The effect of chemical mechanism on the simulation predictions is also examined using detailed and reduced chemistry schemes. Simulations are performed on a 8-11 kW small lab-scale biomass furnace and the predictions are validated against published experimental measurements from Refs. [47, 4].

4.3 Methodology

The combustion of the volatile gases within the freeboard is simulated where the combustible gas-phase is assumed to obey the incompressible ideal gas law. Reynolds Averaged Navier-Stokes (RANS) conservation equations of continuity, momentum, energy and species transport are solved. The radiation is accounted for using P_1- approximation model [48] along with the domain based weighted-sum-of-gray-gas (WSGG) method [49]. The enthalpy transport due to species diffusion in the energy equation is also considered in this study.

4.3.1 Mass and energy conservation for the bed

An empirical bed model, which is described in Ref. [4] is adopted in the present study. The volatile gases produced from the bed are assumed to consist of CH_4 as light hydrocarbon, C_6H_6 as heavy hydrocarbon [50, 9], and CO_2, O_2, H_2O, CO and N_2 [4]. It is assumed that the concentration of the gases coming out of the bed is uniform throughout the bed. While this simplification may impose

a limit on the fuel bed boundary information (e.g., local information of temperature and species concentrations within the bed), studies have shown that the overall temperature and species in the freeboard can still be reasonably predicted when compared to the experiments [4, 51]. The temperature of the gases is known from the measurements at $2\,cm$ above the bed [4, 47]. This temperature can be assumed as the bed temperature to calculate the enthalpy of the gases at the bed boundary [4]. As discussed in Ref [4], the concentrations of CO and O_2 were estimated based on the closest experimental measurement to the bed (i.e., at $13\,cm$ above the bed), while the concentration of CO_2 was selected by trial and error in order to have physically feasible mass fraction for all species using the bed model [4, 47]. Also, the sensitivity analysis on the bed model was also performed which revealed that the final predictions are only sensitive to the assumed values of species mass fractions in vicinity of the bed [4]. Fuel properties and the mass and energy balance between the inlet and outlet of the bed are given in Table 4-1 and Table 4-2, respectively. The mass balance calculation is based on the conservation of the mass between the inlet and outlet of the bed of C, H, O and N elements. The energy balance calculation is based on energy (sensible and chemical) conservation between the inlet and outlet of the bed. The inlet boundary conditions of the bed consist of the primary air and fuel mass flows, and the outlet boundary conditions of the bed consist of volatile gases at specified temperature. The chemical energies for inlet and outlet boundary of the bed are calculated using the lower heating values (LHV) of the raw biomass and volatile gases [47, 52]. The compositions and mass fractions of the volatile gases are presented in the primary boundary conditions section of Table 4-4.

4.3.2 Near-wall modelling approach

Enhanced wall treatment [53] is used as wall function for flow modelling in the vicinity of the furnace wall. This model employs a so-called enhanced wall function (e.g., blending function

suggested by Kader [54]) to combine a two-layer approach (i.e., linear for laminar region, and logarithmic for turbulent region) [35, 7]. This consequently allows the model to produce predictions with reasonable accuracy for both fine and coarse grids near the wall, where the first near-wall node may be located either in the viscous sub-layer, buffer layer or fully-turbulent region. More details about this model can be found in Ref. [35].

Table 4-1. Fuel properties used for the simulation [47]

Ultimate analysis dry ash-free basis (wt%)

C	O	H	N
51.1	42.5	6.3	<0.1

Proximate analysis (wt%)

Volatile	Fixed Carbon	Moisture	Ash
79.4	14.2	6.0	0.4

Table 4-2. Mass- and energy-balance between inlet and outlet of the bed section of the furnace

Energy balance:

	Mass flux	Temperature	Enthalpy flux	Chemical energy flux	Total energy flux
	[kg/s]	[K]	[kJ/s]	[kJ/s]	[kJ/s]
Fuel (bed inlet)	4.61e-4	300	0.2351	8.87	9.105
Primary air (bed inlet)	5.81e-4	300	0.1743	N/A.	0.1743
Total primary (bed outlet)	-1.04e-3	1373 [3]	-2.5	-7.14	-9.64
Relative error (%)					3.89

Mass balance:

Element mass fraction:	C(%)	O(%)	H(%)	N(%)
Ultimate analysis (fuel + air)	22.7	31.9	2.79	42.9
Calculation (assumed composition)	-22.1	-31.7	-2.96	-43.2
Relative error (%)	2.36	0.53	5.9	0.81

4.3.3 Turbulence model

The sensitivity of the predictions to the adopted turbulence model is examined using $k-\varepsilon$ turbulence model (i.e., the standard $k-\varepsilon$ model (STD) [35, 55], renormalization group (RNG) $k-\varepsilon$ model [56] and realizable (RKE) $k-\varepsilon$ model [57]). The main difference between these

models is in the way of calculating turbulence viscosity and turbulent Prandtl number, as well as using different transport equations for turbulent dissipation rate [35]. STD model has been widely used for simulating industrial flows including biomass combustion (e.g. [58, 59]). This model has been originally developed for high-Reynolds number turbulent flows [35, 15]. RNG and RKE models have been shown to produce accurate results at low-Reynolds number and highly strained flows compared to STD $k-\varepsilon$ [35, 60, 61, 28]. In particular, RNG model employs analytical methods for calculating turbulent Prandtl number and effective viscosity whereby the effect of low-Reynolds number is accounted for [35]. On the other hand, in comparison to STD model, RKE model employs an alternative turbulent viscosity formulation, as well as a modified transport equation of turbulent dissipation rate [35, 57].

4.3.4 Combustion model

Three different combustion models are used and their predictions are compared in this study. SFM is examined in the present study using detail chemical mechanisms (ME.1-3, see Table *4-5*). For SFM, instead of solving one transport equation for each gas-phase species, only the mean enthalpy, mean mixture fraction and its variance are calculated. The effect of detailed chemistry is accounted for using one-dimensional (1D) laminar flamelet structures, which are generated and tabulated into a flamelet library [5, 62]. The generated flamelet is embedded in the turbulent reacting flow via transferring data (i.e., species mass fraction and temperature) from a physical space (flamelet) to a mixture fraction space, which then allows describing the temperature and species mass fraction as a function of local mixture fraction and local scalar dissipation [5, 35, 62]. To account for the influence of diffusion flamelet into a turbulent reacting flow, the mass fraction and temperature in the diffusion flamelet are determined using the probability density function (PDF) of mixture fraction, scalar dissipation, and enthalpy. In order to improve the accuracy of the predictions in

local high gradient of flow and combustion characteristics (e.g., temperature, species concentration, etc.) zones, "Automatic Grid Refinement (AGR)" method is used with the SFM approach in commercial software, such as Fluent [35]. This method increases the density of the grid points in flow regions of high gradient to smoothen the profiles of the calculated quantities. This approach is best considered for reacting flow cases with detailed chemistry with many short lifetime radical species. Table 4-3 reports the settings used for generating the flamelet and PDF look-up tables.

Table 4-3. Settings for generating flamelet and PDF look-up table

Parameter	Value [unit]
Maximum number of flamelets	20 [-]
Number of flamelet grid points	40 [-]
Number of scalar dissipation step	5 [-]
Initial scalar dissipation	0.01 [S^{-1}]
Initial number of grid points in the flamelet (AGR method)	8 [-]
Maximum number of grid points in the flamelet (AGR method)	64 [-]
Number of mean mixture fraction points in PDF table	31 [-]
Number of fraction variance point in PDF table	31 [-]
Number of mean enthalpy points in PDF table	41 [-]
Maximum number of species	20 [-]
Minimum temperature	298.15 [K]

Table 4-4. Details of the inlet boundary conditions [4]

	Mass Fraction							$\dot{m}$	Temp	Turbulence	
	C_6H_6	CH_4	CO_2	O_2	H_2O	CO	N_2	[kg/s]	[K]	I(%)	L[m]
Primary	0.1305	0.0297	0.264	0.0194	0.109	0.015	0.432	1.04e-3	1373	5	7e-2
Secondary	-	-	-	0.233	-	-	0.767	1.18e-3	300	23	4e-2
Tertiary	-	-	-	0.233	-	-	0.767	1.89e-3	300	58	4e-2

UFM using a detailed chemical mechanism (i.e., ME-3, see Table *4-5*) is also examined in the present study. As mentioned previously, in a flamelet approach, turbulence and chemistry are coupled via the flowfield strain rate, which is known as the scalar dissipation [41]. SFM assumes steady state solution for all species even under conditions where there is a steep change in the strain rate. This consequently causes inaccurate predictions of slow chemistry species [44]. However, UFM is a promising approach as it accounts for the effect of unsteadiness of strain rate,

which makes it possible to improve the predictions of slow forming species. The transient history of the scalar dissipation evolution is used to perform post-processing of the converged flowfield obtained using SFM model [35, 41]. Published studies (e.g., [34]) have shown that the transient effect on the predictions of the heat release and the concentrations of major species can be negligible. Therefore, in comparison with SFM, it is expected that the influence of UFM prevails only for slow chemistry species.

EDC approach is employed using global two-step and four-step reaction mechanisms of the combustion of hydrocarbon (ME.4 and 5, see Table 4-5). In this approach, reactions take place at the so-called fine structures in which the combustible fluid is mixed at the micro-scale level [28, 29]. EDC assumes that each computational fluid cell is divided into a volume fraction of a fine structure, $\gamma^* = \gamma^3$, and volume fraction of its surroundings, $(1 - \gamma^3)$. The length fraction of fine scales, γ, and the mean residence time of the mass exchange between fine structures and the surroundings fluid, τ_{EDC}, can be described based on the flow turbulence characteristics as follows [63]:

$$\gamma = C_\gamma (Re_t)^{-0.25} \tag{4-1}$$

$$\tau_{EDC} = C_\tau \tau_\eta = C_\tau (Re_t)^{-0.5} \frac{k}{\varepsilon} \tag{4-2}$$

where $\tau_\eta = (\vartheta/\varepsilon)^{0.5}$ is the Kolmogorov time scale, $Re_t = (k^2/\vartheta\varepsilon)$ is the turbulent Reynolds number, k is the turbulent kinetic energy, ε is the turbulent dissipation rate, ϑ is the kinematic viscosity, and $C_\gamma = 2.1377$ and $C_\tau = 0.4082$ are the default (standard) values of the fine structure volume and its residence time constants, respectively [64, 65]. Based on the EDC formulation, the mean reaction rate of each species (i.e., $R_{i,EDC}$) can be defined as follows:

$$R_{i,EDC} = \bar{\rho}\frac{\gamma^2}{(1-\gamma^3)\tau_{EDC}}(Y_i^* - \overline{Y}_i) = \frac{\bar{\rho}}{\tau_{mix}}(Y_i^* - \overline{Y}_i) \quad (4\text{-}3)$$

where $\overline{Y}_i$ and Y_i^* denote, respectively, the mean and fine scale mass fractions of species i, $\bar{\rho}$ is the mixture average density, and τ_{mix} is the characteristic mixing time scale which can be defined as follows [23, 28, 30]:

$$\frac{1}{\tau_{mix}} = \frac{\gamma^2}{(1-\gamma^3)\tau_{EDC}} = \frac{1}{(1-\gamma^3)}\frac{C_\gamma^2}{C_\tau T_t} \quad (4\text{-}4)$$

where $T_t = (k/\varepsilon)$ is a turbulent time scale. According Eq.(4-4), one can define the ratios of EDC or turbulent time scale over mixing time scale (i.e., (τ_{EDC}/τ_{mix}) and (T_t/τ_{mix})), as a function of EDC model characteristics (i.e., γ, C_γ and C_τ). More details about the EDC model can be found elsewhere [28, 65, 23].

As mentioned earlier, the mixture fraction based models (i.e., SFM and UFM) employed using detailed chemistry schemes (i.e., ME.1-ME-3), whereas reduced chemical mechanisms (i.e., ME.4 and ME.5) are used with EDC approach. However, in order to assess the ability of combustion model on the CFD predictions using the same chemical mechanism, additional simulations are performed with all the aforementioned combustion models using the chemical mechanism (i.e., ME.4).

4.3.5 Chemical reactions mechanism

The effect of chemical reactions mechanism is investigated by examining three different detailed mechanisms with the steady/unsteady flamelet-PDF and two reduced mechanisms with EDC. The first chemical mechanism (referred to as ME.1) is a detailed chemical mechanism proposed by Marinov et al. [66] which has been developed for investigating the formation and consumption of

aromatics and poly aromatic hydrocarbons in n-butane/oxygen flame. Although this mechanism has firstly been employed to model rich premixed flames, it has also been used to investigate diffusion flames (e.g., Refs. [67, 68]). The second detailed chemical mechanism (referred to as ME.2) has been developed for the combustion of volatile gases released during the biomass conversion process [69, 70]. The third detailed chemical mechanism (referred to as ME.3) has been originally developed for the combustion of single-ring aromatic hydrocarbons in low-pressure premixed flames [71] and has been successfully used for modelling different flames (e.g., stoichiometric methane flame [72], rich acetylene, ethylene and benzene flames [71]). This mechanism has also successfully been employed at atmospheric pressure conditions (e.g., [73, 74]). Two reduced chemical mechanisms have also been examined in this study; a four-step (referred to as ME.4) and a two-step (referred to as ME.5) global reaction mechanisms of methane, respectively [21, 19]. Both reduced mechanisms have been used along with a two-step reaction mechanism of benzene with CO as the intermediate species [9]. The kinetic data of the two last mechanisms can be found in Ref. [75]. A summary of the kinetic mechanisms used for each combustion model are presented in Table 4-5.

Table 4-5. Summary of kinetic mechanisms and combustion models

Mechanism	Combustion model	Number of species	Number of reactions
ME.1 [66]	SFM-PDF	156	680
ME.2 [69]	SFM-PDF	137	4533
ME.3 [71]	SFM/UFM-PDF	158	872
ME.4 [21]	EDC	8	5
ME.5 [19]	EDC	7	3

4.4 Physical and numerical setups

The main purpose of the simulation is to assess the application (performance) of three different combustion approaches for modeling biomass combustion. A 8-11 kW small lab-scale biomass furnace [4, 47] is adopted for the present study. The furnace consists of a cylindrical combustor

having a diameter of 0.2 m. The primary air is injected through a grate with a mass flow rate of $0.581\text{e}-3\ kg/s$. The secondary and tertiary air inlet jets supply excess air above the bed with mass flow rates of 1.18 and $1.89e-3\ kg/s$, respectively. All air flow inlets are supplied at 100 KPa and 298 K. The furnace is fed with wood pellets, injected into the bed with a mass flow rate of $0.461e-3\ kg/s$. According to Ref [47], the feed rate is controlled within ± 2% of the mean mass flow rate, however, due to difficulties in maintaining a constant feed rate, occasional fluctuations in the mass flow rate value were observed during the experiment. The volatile gases coming out of the bed and the wall temperatures are measured to be 1373.15 K and 873.15 K, respectively [4, 47]. Figure 4-1 shows a schematic diagram of the physical setup. Additional details of the experiment can be found in Refs. [4, 47].

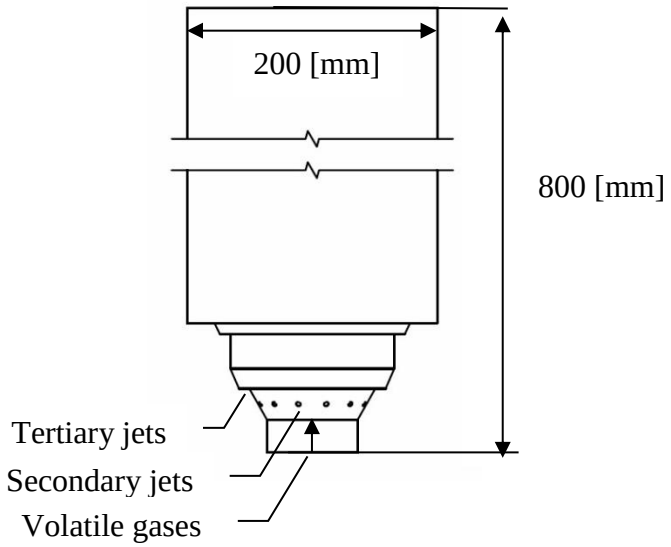

Figure 4-1. Schematic diagram of a 8-11 kW grate firing biomass furnace tested [4]

The CFD simulations are performed using the commercial code ANSYS-FLUENT 15.0. Second order upwind spatial discretization scheme is adopted for all conservation equations. SIMPLEC method is used for velocity-pressure coupling algorithm. The furnace geometry is modeled using a 3D non-uniform grid which consists of about 690,000 cells covering 820 mm above the bed.

Local increase in grid resolution is applied in the vicinity of the bed and at the exit of the secondary and tertiary jets, wherein high gradients of temperature, species concentrations and velocity are expected to occur (see Figure 4-5). Further grid refinement did not show significant change in the simulation predictions. In the case of EDC, the In-Situ Adaptive Tabulation (ISAT) [76] algorithm is used to increase the CPU-intensive treatment of the detailed kinetics of the chemistry with ISAT an error tolerance of 10^{-5}.

Zero normal gradients of species mass fractions along with non-slip conditions and constant temperature of $873.15\ K$ are adopted for wall conditions. The emissivity of the bed and wall is set up as 0.9 [51, 4]. Pressure outlet condition is used for the outflow boundary. Table 4-4 reports the adapted boundary conditions for the simulation. The impact of most unmeasured parameters (i.e., level of the turbulence, gas concentration, etc.) at the inlet boundaries were investigated in Ref [4]. For instance, the influence of turbulence level at the inlet boundaries (i.e., turbulence intensity) on the combustion process was investigated. It was reported that the prediction of temperature and concentration fields is sensitive to the level of turbulence at the air inlet boundaries, while the level of turbulence from fuel bed boundary has a negligible effect on the results [4]. Therefore, all parameters associated with boundary conditions are provided based on the suggested values and experimental measurements reported in Ref [4].

4.5 Results and discussion

The simulations are carried out for fourteen different cases (C1 to C14) to examine the capability (performance) of different turbulence models, chemical reactions mechanisms and combustion models. The assessed turbulence models are STD, RNG and RKE $k-\varepsilon$. They are used with SFM (C1-C3) and EDC (C10-C12) combustion models. The predictions of the temperature and species are compared with their counterparts' experimental measurements. The effect of kinetic of

chemical reactions on temperature and species predictions is studied by testing different detailed kinetic mechanisms used with SFM (C1-C6) and reduced kinetic mechanisms used with EDC model (C7-C12). The performance of combustion model is examined using SFM (C1-C5), UFM (C6) and EDC (C7-C12) where their predictions of species and temperature are compared. In addition, the difference in the performance between all these combustion models is examined using the same chemistry scheme (cases SFM (C13), UFM (C14) and EDC (C9)). Details of all studied cases are summarized in Table 4-6.

Table 4-6. Details of the examined cases

Case	Chemical mechanism	Combustion model	Turbulence model	C_γ	C_τ
C1	ME.1	SFM	STD	N/A	N/A
C2	ME.1	SFM	RNG	N/A	N/A
C3	ME.1	SFM	RKE	N/A	N/A
C4	ME.2	SFM	RNG	N/A	N/A
C5	ME.3	SFM	RNG	N/A	N/A
C6/C6_AGR	ME.3	UFM/UFM-AGR	RNG	N/A	N/A
C7	ME.4	EDC	RNG	2.1377	0.4082
C8	ME.4	EDC	RNG	1.75	5.62
C9	ME.4	EDC	RNG	2.37	5.62
C10	ME.5	EDC	STD	2.1377	0.4082
C11	ME.5	EDC	RNG	2.1377	0.4082
C12	ME.5	EDC	RKE	2.1377	0.4082
C13	ME.4	SFM	RNG	N/A	N/A
C14	ME.4	UFM	RNG	N/A	N/A

4.5.1 Effect of turbulence model

The results of the effect of turbulence modeling on the predictions of temperature, species and velocity fields is presented in this section. STD, RNG and RKE $k-\varepsilon$ turbulence models are tested using two different combustion models; that is SFM (cases C1-C3) and standard EDC (cases C10-C12), as reported in Table 4-6. As stated earlier, since the UFM model is based on the post processing of the converged flowfield obtained in a SFM simulation, the effect of unsteady flamelets on the converged flowfield is neglected [35]. Hence, the flowfield characteristics (e.g.,

velocity and turbulence field) are not resolved using UFM, and therefore the effect of turbulence modeling is not investigated using UFM. It should be mentioned that experimental measurements are available only for local temperature and species at specified locations along the centerline of the adopted furnace. Hence, the predictions of the velocity field are not compared with experiments.

Figure 4-2 presents a comparison of the axial temperature profiles between the experimental measurements and numerical results along the centerline of the furnace. Figure 4-2a shows that the predictions of temperature is in a reasonable agreement with the experimental results. Figure 4-2b, which presents the predictions of the temperature using SFM combustion model while varying turbulence models (STD, RNG and RKE, represented by cases C1, C2 and C3, respectively), reveals that case C2, which adopts RNG turbulence model, produces the closest predictions to the measurements. This figure shows also that STD and RKE turbulence models (i.e., cases C1 and C3, respectively) produce almost similar predictions within most flow regions along the centerline of the furnace. Figure 4-2c shows the predictions of the temperature using EDC combustion model while varying the turbulence model (i.e., STD, RNG and RKE in cases C10, C11 and C12, respectively). While this figure indicates that all tested cases show nearly the same predictions, RNG turbulence model (i.e., case C11) produces slightly closer predictions of temperature in the local high temperature region when compared to the measurements. As it can be seen in Figs. 4-2b and 4-2c that, regardless of the turbulence model, SFM shows a slight over-prediction of the temperature in the middle of the furnace compared to EDC and experimental measurements. Figure 4-2a shows clearly that the best agreement between the predictions and experimental measurements is achieved using RNG turbulence model (i.e., cases C2 and C11).

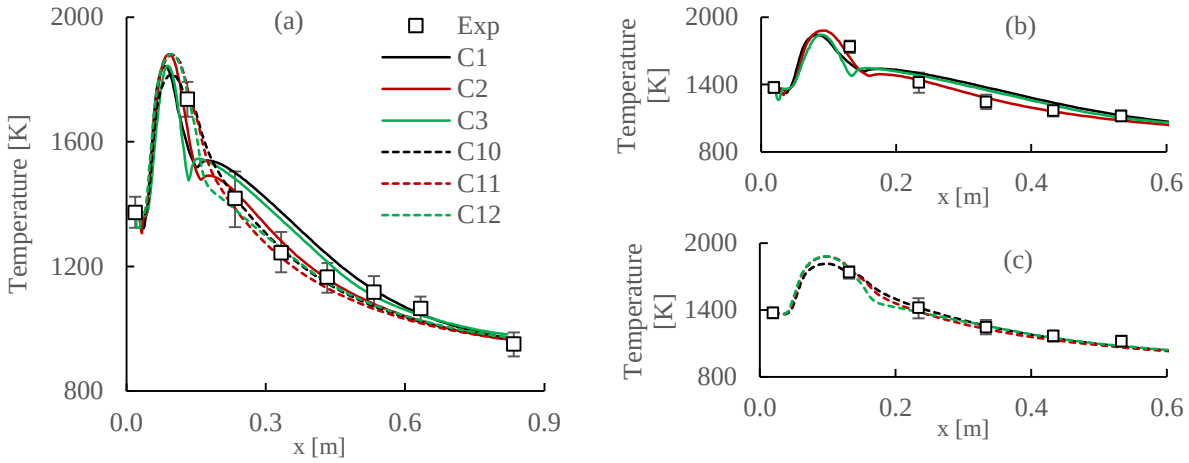

Figure 4-2. Temperature profiles along the furnace centreline for (a) SFM (cases C1-C3) and EDC (cases C10-C12), (b) SFM (cases C1-C3), and (c) EDC (cases C10-C12)

Figure 4-3 presents a comparison between the numerical predictions and experimental measurements of the concentration of CO along the centerline of the furnace. This figure clearly reveals that, regardless of the turbulence model, the standard EDC combustion model (i.e., cases C10-C12) shows over prediction, whereas the SFM (i.e., cases C1-C3) substantially underestimates the concentration of CO species. Also, this figure shows that, when using SFM combustion model, all examined turbulence models produce similar trend but slightly different predictions, whereas with EDC model, all cases exhibit the similar predictions. According to Figure 4-3, while cases C10-12 show better predictions, none of the simulated cases (i.e., cases C1-C3 and C10-C12) reproduce satisfactorily the experimental measurements. This is attributed to the limitations of combustion models (i.e., EDC and SFM) in predicting slow chemistry species (e.g., [35, 62, 77, 23]). More importantly, this figure shows that the effect of turbulence modeling on the prediction of CO is negligible.

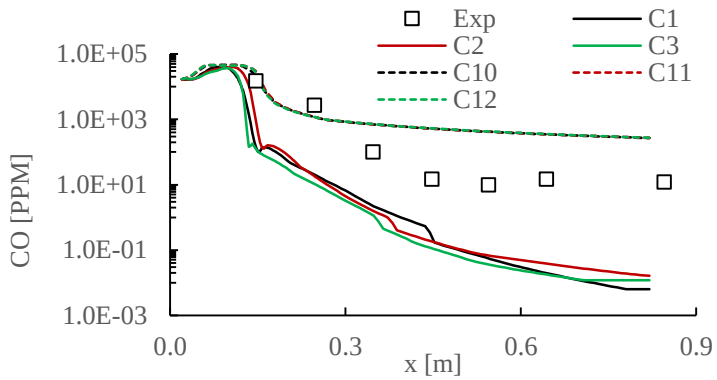

Figure 4-3. CO concentration profiles along the centerline of the furnace obtained using SFM (cases C1-C3), and EDC (cases C10-C12).

The effect of turbulence modelling on the predictions of other species (e.g., O_2 and CO_2) is presented in Figure 4-4. Figure 4-4a, which shows the predictions of CO_2 mole fraction for cases C1-C3 (with SFM) and C10-C12 (with EDC), reveals that the predictions of CO_2 is mostly independent of the turbulence model being used, whereas it is greatly influenced by the adopted combustion model. As can be seen in Figure *4-4*a, regardless of the turbulence model, the predictions of the two different combustion models show similar trend. Similar to the observations from Figure 4-4a, Figure 4-4b also shows great dependency of O_2 mole fraction predictions on the adopted combustion model. This figure reveals also that the predictions of O_2 mole fraction are independent of the turbulence model in the flow region downstream of the furnace away from combustion zone. The predictions displayed in Figure *4-4*b clearly suggest that the consumption of O_2 happens mostly earlier in all SFM cases compared to EDC. Moreover, the profiles in Figure *4-4*b indicate that the predictions of the STD turbulence model show slightly closer agreement with the experimental measurements regardless of the adopted combustion model (i.e., SFM or EDC). It can be concluded that, for all tested turbulence models, while the absolute magnitude differs between the predictions and measured values, the trends of both CO_2 and O_2 are overall adequately predicted when compared with their experimental counterparts.

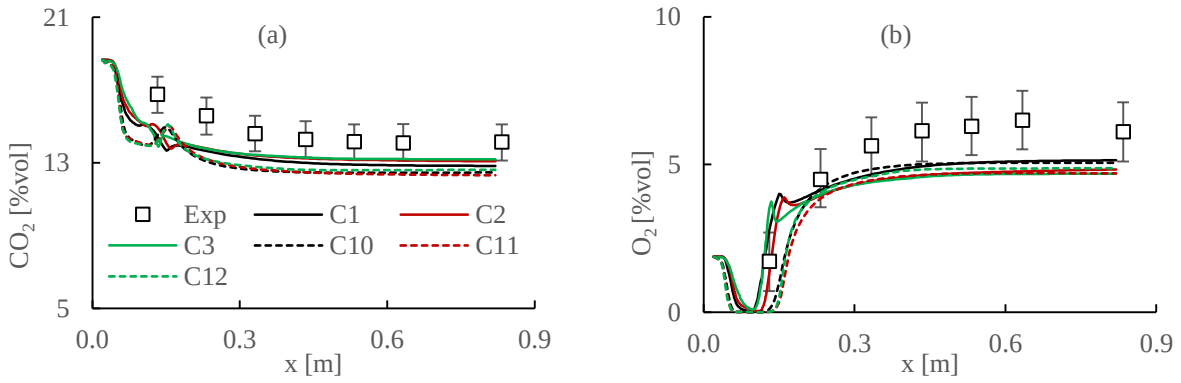

Figure 4-4. Profiles of CO_2 and O_2 mole fractions along the centerline of the furnace. (a) CO_2 profiles obtained with SFM (cases C1-C3), and EDC (cases C10-C12); (b) O_2 profiles obtained with SFM (cases C1-C3) and EDC (cases C10-C12).

Before examining the effect of turbulence modeling on the velocity field, it is worth introducing the flow zones in the high temperature regions within the furnace. Figure 4-5 presents the velocity vectors along with the temperature contours obtained using case C2. This figure displays the interaction of the airflow injected from the secondary jets and the creation of a first recirculation zone downstream of the bed (referred to as Z_1). Downstream of zone Z_1, a second "S" shaped recirculation zone (referred to as zone Z_2) is produced as a result of the interaction of airflow between the secondary and tertiary jets as well as with the furnace wall. Further downstream of zone Z_2, another recirculation zone (referred to as Z_3) is produced from the interaction of the flow coming out of zone Z_2 with shear flow created by the tertiary air jets. The length of each recirculation zone can be estimated as the distance between each two local zero mean-velocity points, shown as P_1 to P_4 in Figure 4-5, along the centerline of the furnace.

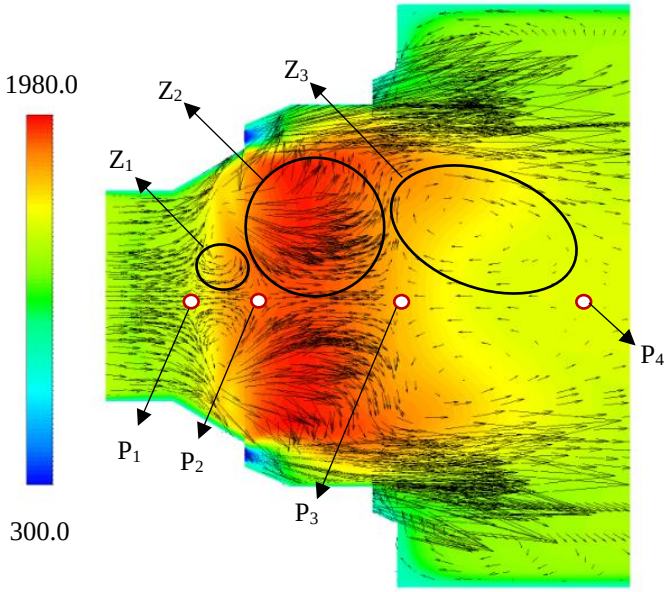

Figure 4-5. Velocity vectors and temperature contours for case C2 (Contours are in Kelvin [K]).

The interaction of the secondary jets produces a resistance to the flow coming out of the bed through zone Z_1. This causes the volatile gases to split and flow toward zones Z_1 and Z_2. When combustion occurs, oxygen from the fresh air injected via secondary air jets reacts with the combustible gases in zone Z_2 leading to an expansion and acceleration of the products/gases toward zone Z_3 as a consequence of the heat release from the reactions [78]. According to Figure 4-5, it is evident that the airflow injected through the secondary air is likely to flow farther toward zone Z_2 rather than zone Z_1. This is why a smaller recirculation zone (Z_1) is created in front of the primary gas flow. The remainder of the combustible gases reacts with fresh oxygen/air injected through the tertiary jets in zone Z_3. This figure also reveals that a high temperature gradient develops in the vicinity of the bed starting almost at the root of the first recirculation zone (indicated as P_1). As expected, the local low velocity flow in the first recirculation zone acts as an aerodynamic reaction zone holder where heat and chemically active species recirculate, which consequently increases flame stabilization and thus enhance chemical reactions [79, 80]. The temperature contour in Figure 4-5 also exhibits local high temperature regions in zone Z_2, which

is an indication of the locations of chemical reactions. This is caused by the enhanced mixing between the combustible volatile gases and oxygen in zone Z_2. Figure 4-5 shows that local high temperature in zone Z_3 appears near the shear layer produced as a result of the injection of tertiary jets where rapid mixing between oxygen and combustible gases occurs. This leads to the establishment of a turbulent diffusion flame from the reaction between fresh oxygen and the reminder of the volatile gases carried into zone Z_3 [4].

Figure 4-6 presents the velocity vectors and the normalized axial velocity profiles along the centerline of the furnace. Since no experimental measurement of the velocity field is available for the current furnace, the effect of turbulence modeling on the velocity field is focused only on the shape, size and position of the recirculation zones. The velocity vectors using STD, RNG and RKE turbulence models (cases C1-C3, respectively), and their corresponding normalized axial velocity are presented in Figs. 4-6a-c and 4-6d, respectively. The velocity vectors and normalized axial velocity for the same turbulence model but with the standard EDC combustion model (i.e., cases C10-C12) are presented in Figs. 4-6e-h. These figures (i.e., Figs. 4-6a-h) clearly show that the length of the first recirculation zone (i.e., the location of P_1 and P_2) is predicted to be nearly the same regardless of the turbulence and combustion models, though a slight shift in P_2 can be observed when varying turbulence model using SFM (see Figs. 4-6a-d). The velocity vectors and profiles in Figs. 4-6a-d show that both STD and RNG turbulence models predicted the same size, same position and almost the same strength the first recirculation zone (Z_1), while RKE turbulence model predicts a slightly smaller recirculation zone Z_1. In contrast, for EDC model, the position and size of zone Z_1 is predicted similarly by all turbulence models, as can be seen in Figs. 4-6e-h. However, for the second recirculation zone (i.e., zone Z_2), it can clearly be seen from Figure 4-6 that SFM cases predicted a smaller and weaker zone Z_2 compared with that of EDC model.

Figure 4-6d and 4-6h, which present the normalized axial velocity profiles, show the same position of P_3 predicted by STD and RKE models. Figure 4-6 also shows an overall stronger recirculation flow in zone Z_3 as predicted by SFM compared with that of EDC where higher axial velocity is predicted in cases C1-C3 for all examined turbulence models (see Figs. 4-6d and 4-6h). Moreover, for both EDC and SFM combustion models, STD and RKE turbulence models also predicted almost the same position of point P_4, as shown in Figs. 4-6d and 4-6h.

The predictions of combustion quantities (i.e., species mass fraction and temperature) depend strongly on the mixing field and consequently the adopted turbulence model [81]. Several published studies reported better predictions using simple turbulence models (e.g., STD $k-\varepsilon$) than when using more complex turbulence models (e.g., RSM, RNG and RKE $k-\varepsilon$, [82, 83, 84]). The present study revealed that the accuracy of the predictions depends on the combination of the sub-models (e.g., turbulence model and combustion model) which corroborates the conclusion reported in Ref [82].

Based on the results in Figs. 2-6, it can be concluded that, for the current geometry and test conditions, RNG turbulence model produces better predictions of the temperature field regardless of the adopted combustion model. In general, the predictions are more sensitive to the turbulence model when using SFM. Using RNG turbulence model with SFM produces the closest velocity and temperature fields to those of EDC model (see Figs. 4-2 and 4-6). Furthermore, for both combustion models, STD showed better prediction of O_2 mole fraction, while the difference in the predictions of O_2 between RNG and STD is reasonably negligible. Therefore, the RNG model is selected as the main turbulence model for the next steps of this study.

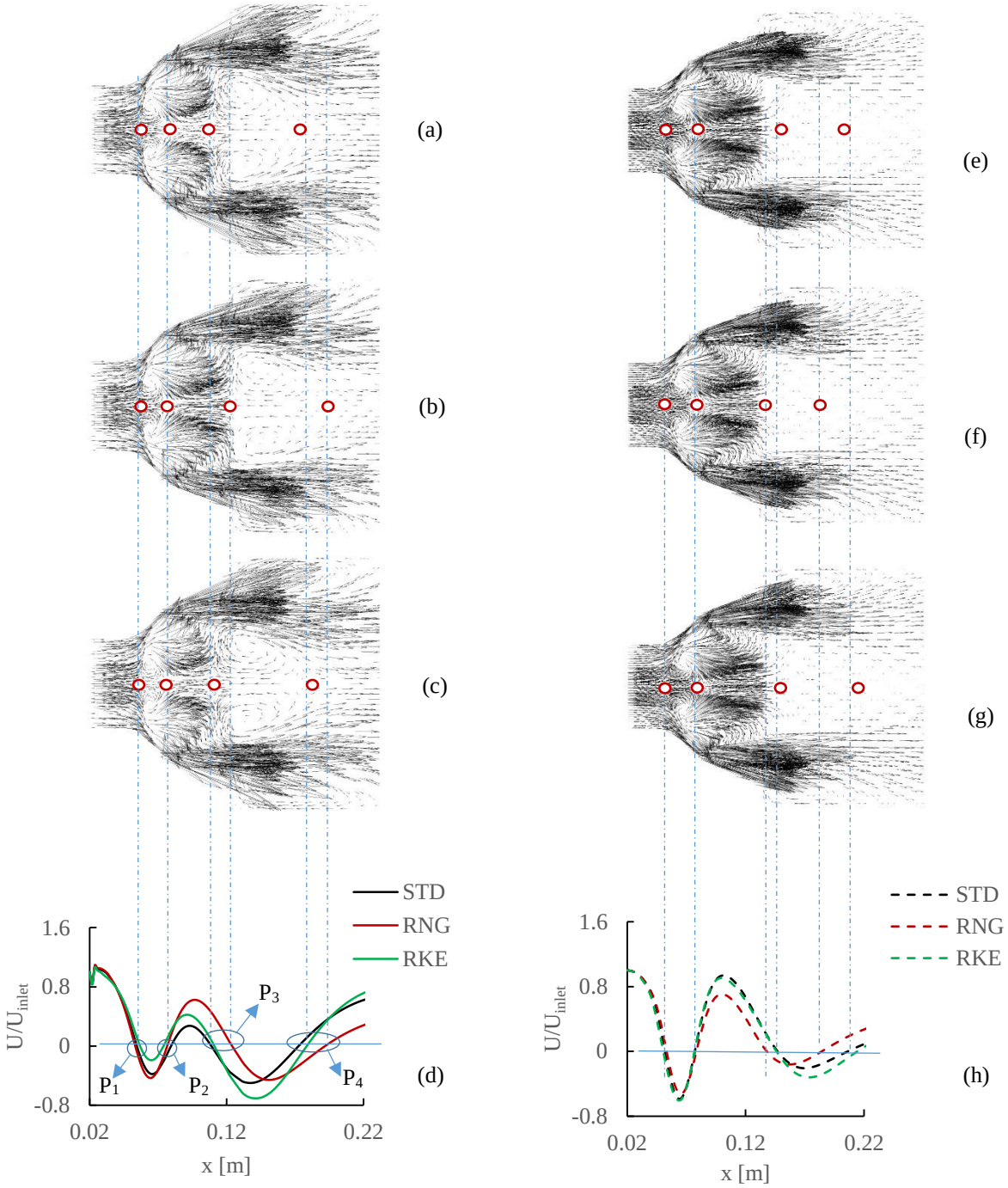

Figure 4-6. Velocity vectors and normalized axial velocity profiles along the centerline of the furnace; (a-c) velocity vectors for cases C1-C3, (d) normalized axial velocity profiles for cases C1-C3, (e-f) velocity vectors for cases C10-C12, and (h) normalized axial velocity profiles for cases C10-C12.

4.5.2 Effect of chemical mechanism

The effect of reaction mechanism on the predictions of temperature and species is investigated using different detailed mechanisms ME.1, ME.2 and ME.3 (see Table 4-5) with different combustion models: SFM (cases C2, C4 and C5) and EDC (cases C7 and C11) (see Table 4-6). Figure 4-7 presents the temperature profiles of the selected simulated cases along the centerline of the furnace. According to this figure, the prediction of the temperature field in the region where local high temperature occurs depends on the reaction mechanism. This is more evident with the EDC combustion model (see Figure 4-7c) and to less extent with SFM combustion model (see Figure 4-7b). For example, a significant difference in the local high temperature is observed between mechanisms ME.4 and ME.5 for cases C7 and C11, respectively (i.e., peak temperature $\approx 1878\ K$ for ME.4 and $1978\ K$ for ME.5, see Figure 4-7c). On the other hand, Figure 4-7b shows less difference in the same region when using SFM (i.e., peak temperature $\approx 1880\ K$ for case C2, and $\approx 1841\ K$ for both cases C4 and C5). Figure 4-7 also indicates that, downstream of the furnace, the prediction of the temperature is almost independent on the reaction mechanism as all cases produced almost the same results. This is attributed to the chemical equilibrium which is likely to occur in that region of the furnace. This will be explained later on when using species profiles in Figure 4-9. According to Figure 4-7b, with the SFM combustion model, the best prediction of the temperature downstream of the furnace is achieved with case C2 (i.e., mechanism ME.1), while case C4 (i.e., mechanism ME.2) produces slightly better prediction of the local high temperature region. It can also be seen from Figure 4-7c that case C11 (i.e., mechanism ME.5 with EDC) produces the best prediction of the local high temperature region.

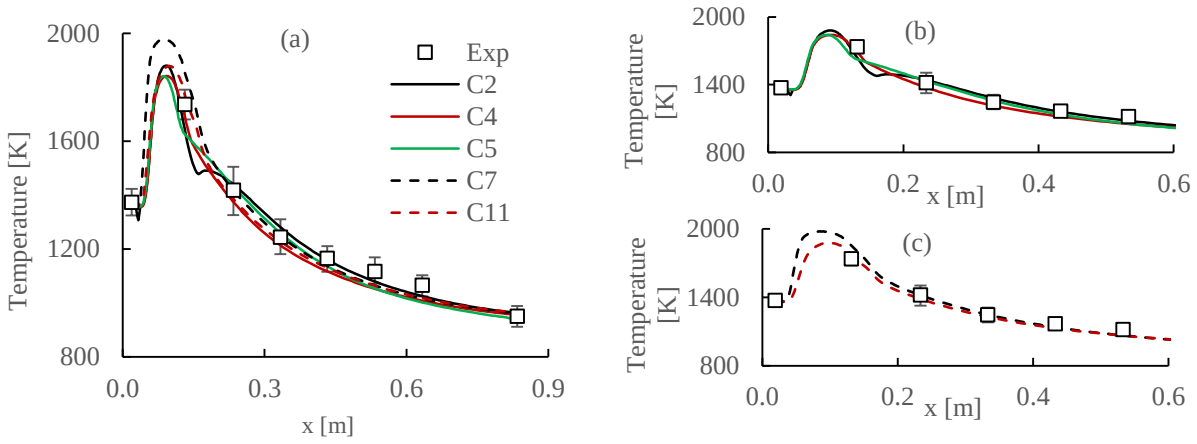

Figure 4-7. Temperature profiles along the furnace centreline for (a) SFM (cases C2, C4 and C5) and EDC (cases C7 and C11), (b) SFM (cases C2, C4 and C5), and (c) EDC (cases C7 and C11)

Figure 4-8 shows that the reaction mechanisms have minor influence on the prediction of CO, especially downstream of the furnace. However, the reaction mechanisms seem to influence the prediction of CO species in the high temperature region of the furnace, specifically with SFM (cases C2, C4 and C5). According to Figure 4-8, the detailed chemical mechanism ME.2 (case C4) produces a visibly higher concentration of CO in the high temperature regions (i.e., zones Z_2 and Z_3) where thermal dissociation of CO_2 is enhanced [85]. It can be seen in Figure 4-8 that none of the simulated cases produce reasonable agreement with measurements, especially downstream of the furnace. As stated earlier, this is attributed to the limitations of the examined combustion models in predicting slow chemistry species.

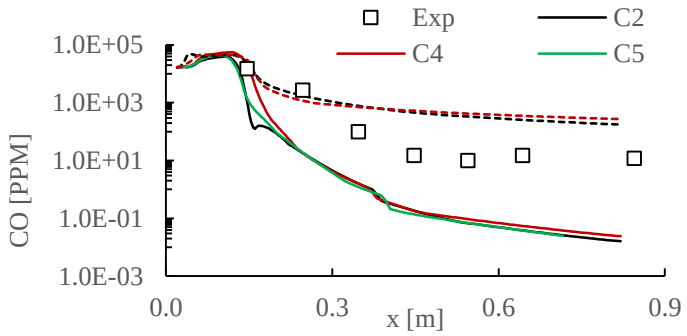

Figure 4-8. CO concentration profiles along the centerline of the furnace (SFM (cases C2, C4 and C5), and EDC (cases C7 and C11)).

The effect of chemical mechanism on the predictions of O_2 and CO_2 species is presented in Figure 4-9. As can be seen, with all tested reaction mechanisms, while differences between predicted profiles and measured values exist, the predictions fairly follow the same trends observed in the measurements. A notable observation from Figure 4-9 is that the influence of the reaction mechanism on the prediction of O_2 and CO_2 is more visible in the high local temperature region. In addition, all cases show almost the same trends of the profiles which also indicate that no more formation of CO_2 and no more consumption of O_2 after passing zone Z_3 (see Figure 4-5). This suggests that most of the combustion occurs in zones Z_1 to Z_3 as the concentration of species remains constant farther downstream of the furnace. Furthermore, downstream of the furnace, the level of turbulence decays and combustion is likely to be kinetically limited with equilibrium chemistry condition where almost no change in species concentrations is observed downstream of the furnace in Figs. 4-9a and 4-9b. Figure 4-9a, which presents the profiles of CO_2 mole fraction for cases C2, C4 and C5 with SFM, and C7 and C11 with EDC shows that all cases produce almost the same predictions, except case C11 which displays a slight under prediction of CO_2 profile compared to the other cases downstream of the furnace. This can also be observed by looking at the profile of O_2 mole fraction in Figure 4-9b where similar prediction can be seen downstream of the furnace for all cases.

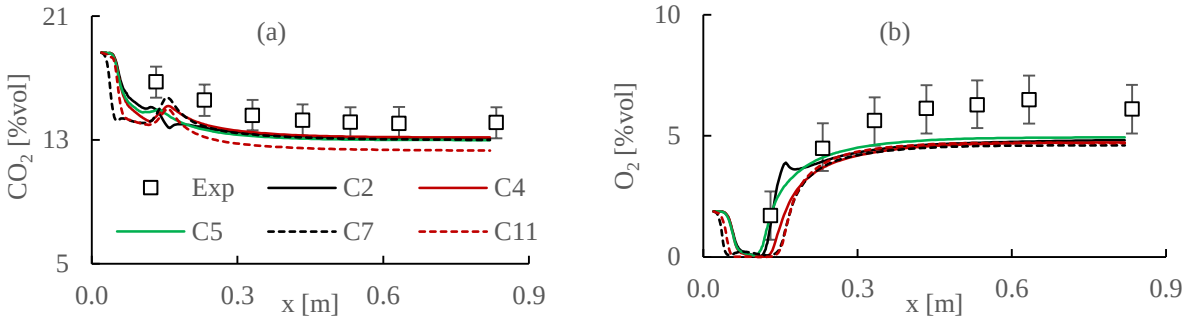

Figure 4-9. Profiles of (a) CO_2 and (b) O_2 mole fractions along the centerline of the furnace (SFM (cases C2, C4 and C5) and EDC (cases C7 and C11)).

The effect of chemical mechanism on the consumption of the main combustible volatile gases (i.e., CH_4 and C_6H_6) is presented in Figure 4-10 in the high temperature region (i.e., up to $x \approx 0.3\ m$) along the centerline of the furnace. Figure *4-10*a shows the mole fraction of CH_4 using SFM (cases C2, C4 and C5) and EDC (cases C7 and C11). This figure clearly shows that the EDC model, as a species transport approach, predicts significantly faster consumption of CH_4 compared to SFM. In non-premixed SFM approach, flamelets are parameterized by strain rates [35]. Hence, close to the bed where the flowfield contains low level of turbulence and strain rates, the combustion/reaction process is not adequately predicted and the concentration of combustible species remains almost unchanged. Figure *4-10*a also shows very similar consumption of CH_4 for all SFM models (where detailed chemistry schemes are used). Also, both reduced chemical mechanisms used with EDC approach show the same consumption of the aforementioned species.

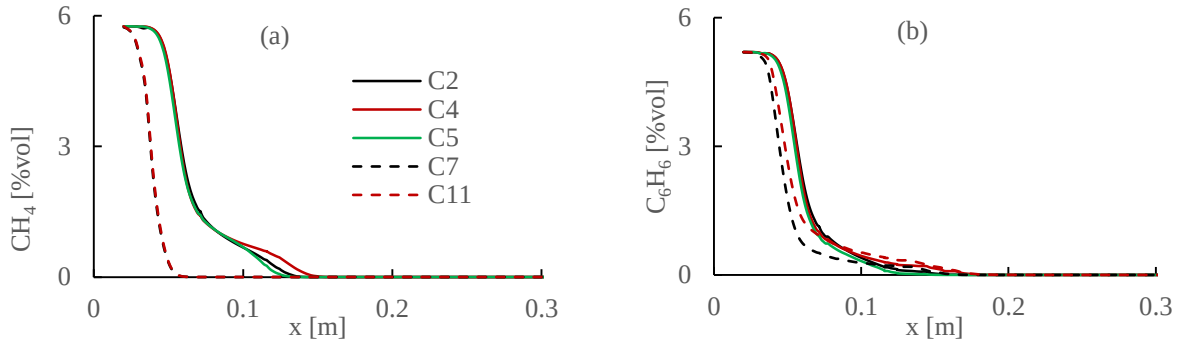

Figure 4-10. Profiles of (a) CH_4 and (b) C_6H_6 mole fractions along the centerline of the furnace (SFM (cases C2, C4 and C5) and EDC (cases C7 and C11)).

Figure 4-10b shows the mole fraction of C_6H_6 using SFM (cases C2, C4 and C5), and EDC (cases C7 and C11). Similar to CH_4 species, the profiles of C_6H_6 mole fractions, presented in Figure 4-10b, show very similar consumption of this species when detailed chemistry is used. On the other hand, the predictions of EDC model (i.e., cases C7 and C11) show a slight difference in the consumption of C_6H_6. It can be clearly seen from this figure that, compared to the predictions of SFM approach (i.e., cases C2, C4 and C5), reduced mechanisms used with EDC approach

slightly predict faster consumption of C_6H_6. It is also important to mention that, while the profiles presented in Figure *4-10* indicate faster consumption of both CH_4 and C_6H_6 when reduced chemistry schemes are used (i.e., cases C7 and C11), higher concentration of CO_2 is predicted when detailed chemical mechanisms are used (i.e., cases C2, C4 and C6) as shown in Figure 4-9. This could be the results of poor performance of SFM model in the prediction of slow forming species (e.g., CO), rather than the effect of chemistry scheme. Accordingly, EDC cases (i.e., cases C7 and C11) predict higher CO compared to SFM cases, which suggests that the rate of CO formation is higher than its rate of consumption to produce CO_2.

4.5.3 Effect of combustion model

The effect of combustion model on the predictions of temperature and species are investigated by examining three different models; that is SFM (case C5), UFM (case C6), and standard and modified EDC (cases C7-C9) (see Table 4-6). Additionally, in order to examine the effect of high density grid on the models' predictions, additional simulations are performed with UFM case using "Automatic Grid Refinement (AGR)" method (case C6_AGR). SFM approach with the chemical mechanism ME.3 is also investigated using AGR method (i.e., case C5 with AGR); however, since no significant difference in the predictions is observed between this case and those of case C5 without AGR, the results with AGR are not reported here. As explained previously, the application of EDC for modelling weakly turbulent flow conditions and slow chemistry poses a challenge. However, sensitivity analysis performed on the coefficients of this model showed that the predictions of both temperature and species can be improved for both weakly and highly turbulent flow conditions by adjusting/modifying these coefficients. Hence, in order to improve the capability of the EDC model, its coefficients (i.e., C_γ and C_τ) are modified based on turbulent flow characteristics (i.e., turbulent Reynolds number and turbulent time scale) via using (τ_{EDC}/τ_{mix})

and (T_t/τ_{mix}), as reported in Ref [23]. For the present geometry with the current conditions, the modification of each EDC coefficient has been done based on the flow conditions in the vicinity of the bed and also in high temperature regions on the basis of both weakly and highly turbulent flow conditions (i.e., cases C8 and C9, respectively) following the study reported in Ref [31]. The values of the modified constants are presented in Table 4-6. In addition to the modified EDC, the results of the standard EDC are also presented below (case C7).

Figure 4-11 presents the prediction of temperature (Figure 4-11a) and CO concentration (Figure 4-11b) along the centerline of the furnace. According to Figure 4-11a, the effect of combustion model on the temperature profiles is seen to be significant only in the vicinity of the bed and also in the high temperature regions (zones Z_1-Z_3). This figure also shows improvement in the prediction of temperature using the modified EDC model, as both cases C8 and C9 show closer predictions to the measurements, whereas the standard EDC over predicts the local temperature peak. Figure 4-11a also shows that the UFM approach (i.e., case C6) predicts a different temperature profile in zones Z_1-Z_3 (with higher peak temperature) compared to SFM (i.e., case C5). However, downstream of the bed, only a slight difference can be observed in the predictions between SFM and UFM. Figure 4-11a shows that, with the exception of a slightly higher peak temperature predicted in case C6_AGR, no significant difference can be observed when comparing the predictions of the temperature profiles between cases C6 and C6_AGR. This reveals that, in terms temperature field prediction, the adopted computational grid is likely to be fine enough in the region where the flame is established.

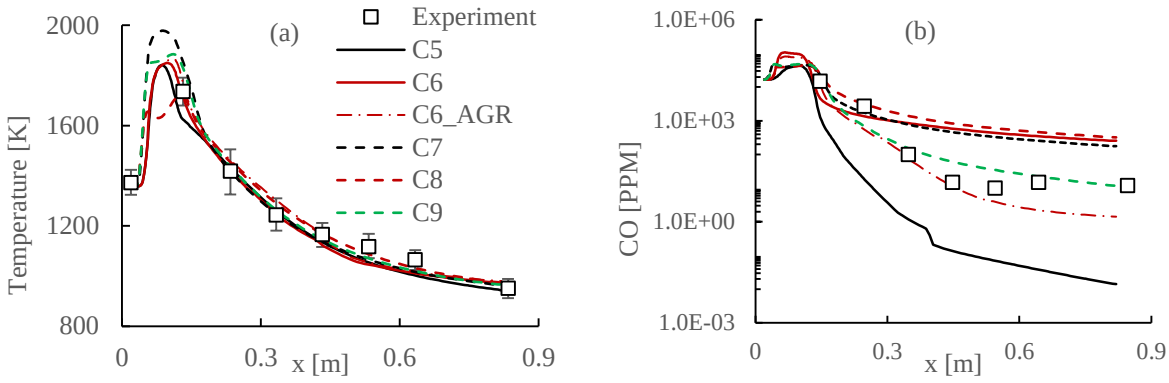

Figure 4-11. Profiles of (a) temperature and (b) CO concentration along the centerline of the furnace (SFM (case C5), UFM (case C6) and EDC (cases C7- C9)).

The main difference between SFM and UFM combustion models (i.e., cases C5 and C6, respectively) can be seen in the prediction of the slow chemistry species, CO, in Figure 4-11b. As mentioned earlier, the main drawback of SFM resides in its poor prediction of slow chemistry species, which can be improved using the UFM approach. As expected, Figure 4-11b shows significant under-prediction of CO concentration in case C5 (SFM). On the other hand, case C6, in Figure 4-11b, shows over prediction of CO concentration, which is closer to the prediction obtained by the standard EDC model. Also, this figure clearly exhibits the effect of AGR method on the predictions of slow-forming species when using UFM. That is, compared with case C6, a noticeable improvement in the prediction of CO concentration is obtained using UFM combined with AGR method (case C6_AGR). As can be seen in Figure 4-11, among all of the simulated cases, the modified EDC model (case C9) and UFM approach when using AGR method (case C6_AGR) produce comparable predictions of CO concentration. Nevertheless, case C9 predicts the best CO concentration downstream the bed. The constants/coefficients of the EDC model have been modified based on turbulence characteristics of the highly turbulent flow conditions (case C9). In comparison with the other EDC cases (i.e., cases C7 and C8), the EDC approach with modified fine-scale constant (i.e., C_{γ}=2.37 of case C9) and modified residence time constant (i.e.,

$C_\tau = 5.62$) is able to model a larger reaction zone along with sufficient time for the occurrence of the chemical reactions, and hence a better prediction of the slow chemistry species (see Ref [23]).

Figure 4-12 presents the predictions of the other species (i.e., CO_2 in Figure 4-12a and O_2 in Figure 4-12b) for selected cases. Similar to the temperature profiles, the main difference between the combustion models is clearly seen in the vicinity of the bed and in the high temperature regions. In general, cases C6 and C6_AGR (UFM) produce the closest prediction to the measurements (compared to case C6, case C6_AGR slightly predicts higher concentration of CO_2 and lower O_2 concentration), while the other cases also show acceptable agreement with experiments. According to Figs. 4-12a and b, in the region closer to the bed, less formation of CO_2 and less consumption of O_2 are predicted in case C8. This is related to EDC fine-scale constant (i.e., C_γ=1.78 of case C8) as this case uses the smallest value for this coefficient among all EDC cases, which results in the smallest reaction zone as compared to cases C7 and C9. This is more evident when looking at the O_2 mole fraction profiles closer to the bed and in the high temperature regions (Figure 4-12b), where the flow is likely to be weakly turbulent due to low velocity and high-temperature molecular viscosity [78, 30]. Moreover, Figure 4-12a shows that, by comparing the predictions of CO_2 between SFM (i.e., case C5) and UFM (i.e., case C6 and C6_AGR), UFM predictions of the concentration of CO_2 drops in the flame zone while the concentration of CO increases in the same region (see Figure 11). This also indicates the improvement of UFM predictions of slow forming species, as the predicted rate of formation of CO is higher than its rate of consumption for producing CO_2, when UFM is applied. Given the fact that the same chemical mechanism is used for both SFM and UFM approach (i.e., mechanism ME.3), this suggests that this observation is independent on the chemistry scheme and more related to combustion model.

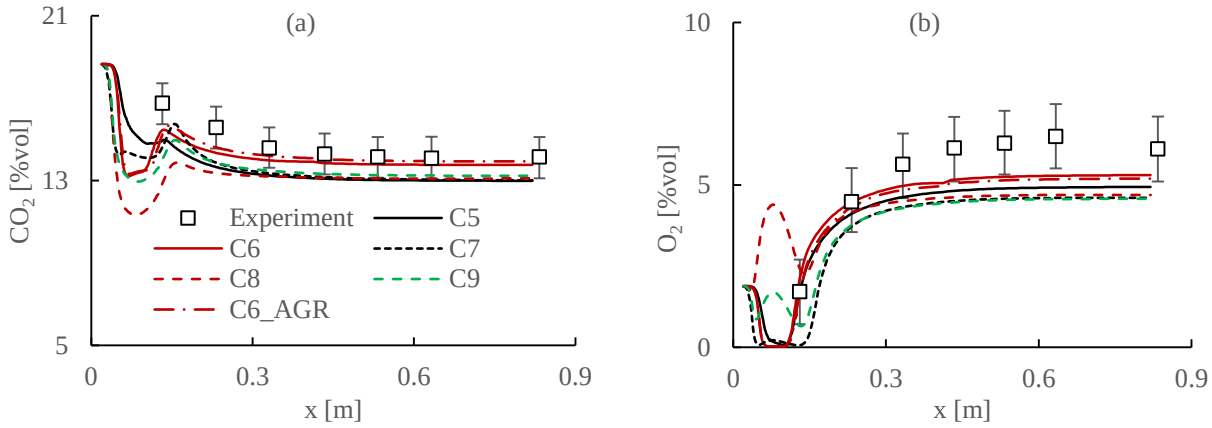

Figure 4-12. Profiles of (a) CO_2 and (b) O_2 mole fractions along the centerline of the furnace (SFM (case C5), UFM (case C6) and EDC (cases C7- C9)).

The performance of combustion model can also be evaluated through the imbalance of the carbon element in the computational domain. In order to provide a quantifiable comparison between the experiment and simulations, the predicted and measured values of the temperature and species mole fractions at specific locations along the centerline (i.e., $x = 0.13m$ and $x = 0.53m$) are reported in Table 4-8. Table 4-7 presents a comparison of the mass of carbon between the inlet (i.e., bed fuel boundary) and the outlet of the furnace. It should be mentioned that, in order to compare the effect of both chemistry and combustion scheme, results of cases C2, C4 and C11 are also included in this table. The results presented in this table show that the lowest and the highest carbon imbalance are, respectively, calculated in case C6 (i.e., UFM with detailed chemistry) and case C11 (i.e., standard EDC model with reduced chemistry scheme). Compared to all other cases (see Figure 4-9a), it is evident that case C6 predicts the highest concentration of CO_2 while case C11 shows the lowest prediction of CO_2 species in the production gases. Table 4-7 also indicates the effect of both mixture fraction based and species transport based combustion models on the results of carbon imbalance within the computational domain. Table 4-7 shows that, when using the same chemistry (cases C5 and C6), UFM approach produces less imbalance compared to SFM approach. However, the imbalance of carbon is significantly dependent on the adopted chemistry

scheme when species transport based model is used. Accordingly, cases C7, C8 and C9 (i.e., standard and modified EDC with chemical mechanism ME.4, respectively) results in a relatively similar imbalance, while case C11 (i.e., standard EDC with chemical mechanism ME.5) leads to the highest imbalance of carbon element. It should also be mentioned that the concentrations of both CH_4 and C_6H_6 are negligible at the exit boundary for all cases.

Table 4-7. Comparison of the inlet (bed fuel) and outlet (exit of the furnace) mass of carbon for all examined cases

Inlet carbon mass flow [kg/s]	**C2**	**Outlet carbon mass flow [kg/s]**							
		C4	**C5**	**C6**	**C6_AGR**	**C7**	**C8**	**C9**	**C11**
2.299e-4	2.206e-4	2.216e-4	2.189e-4	2.296e-4	2.288e-4	2.209e-4	2.22e-4	2.223e-4	2.160e-4
	Relative error (%)								
	4.05	3.61	4.78	0.13	0.49	3.49	3.39	3.32	6.03

Table 4-8. Temperature and species mole fractions at specific locations along the centerline

	Temperature [K]		CO **[ppm]**		CO_2 **[%vol]**		O_2 **[%vol]**	
X[m]	**0.13**	**0.53**	**0.13**	**0.53**	**0.13**	**0.53**	**0.13**	**0.53**
Exp	1680-1790	1070-1170	15000	10	15.8-18	13.2-15.2	0.71-2.7	5.3-7.3
C5	1625.57	1054.32	1274.62	0.072	14.918	13.028	1.74	4.895
C6	1719.715	1045.31	4640.202	443.362	15.472	13.79	2.126	5.25
C6_AGR	1772.9	1054.92	11863.62	3.8412	15.08	13.9	1.68	5.14
C7	1871.89	1066.76	24581.35	325.5389	14.643	13.084	0.076	4.576
C8	1717.37	1088.72	26385.8	591.89	12.89	13.106	2.352	4.674
C9	1843.97	1072.27	25586.4	33.86	14.055	13.27	0.65	4.536

As mentioned earlier, the main handicap of EDC model is its high computational time when using a multi-step chemistry scheme. Even though using ISAT algorithm which can reduce the computational time, still employing detailed chemistry with EDC, such as mechanisms ME.1 to ME.3, is impractical. However, it is worth investigating the performance of all the aforementioned combustion models (i.e., SFM, UFM and EDC) using the same chemical mechanism. Therefore,

chemistry scheme ME.4 along with AGR method are adopted for SFM (case C13) and UFM (case C14) in order to examine and compare the predictions with EDC model (case C9) when using reduced chemical mechanism.

Figure 4-13 presents the prediction of temperature (Figure 4-13a) and CO concentration (Figure 4-13b), along the centerline of the furnace, for cases C9 (EDC), C13 (SFM) and C14 (UFM). According to Figure 4-13a, there can be seen only slight difference in the predicted temperature using SFM and UFM, which is similar to what is observed from cases C6 and C6_AGR. However, Figure 4-13a clearly shows that, when comparing with EDC and experimental data, SFM and UFM significantly over predicted the temperature profiles along the centerline. This suggests that using reduced chemical mechanism with SFM/UFM approach results in over-prediction of the temperature field. Using the same chemistry scheme, the effect of combustion models on the prediction of slow-forming species (i.e., CO) can be seen in Figure 4-13b. Similar to cases C1-C6, the concentration of CO is under-predicted with SFM (i.e., case C13), and over-predicted with UFM (i.e., case C14). However, when compared with other SFM cases, it can be observed that the magnitude of the predicted CO concentration for case C13 is higher and, therefore, closer to the experimental measurements downstream of the furnace.

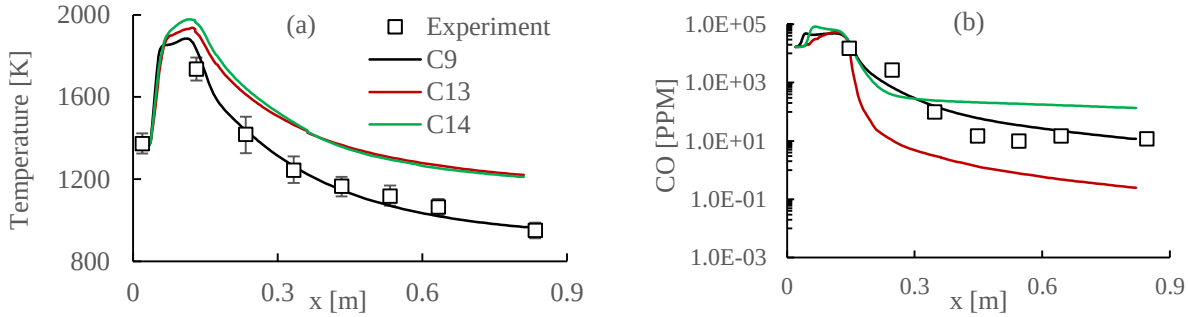

Figure 4-13. Profiles of (a) temperature and (b) CO concentration along the centerline of the furnace (EDC (case C9), SFM (case C13) and UFM (case C14)).

Figure 4-14 presents the predictions of the other species (i.e., CO_2 in Figure 4-14a, and O_2 in Figure 4-14b) for cases C9, C13 and C14. While all these cases produce reasonable prediction of CO_2 concentration, UFM (i.e., case C14) shows the highest prediction amongst all models. This also can be observed in Figure 4-12 for case C6 when detailed chemistry is used. On the other hand, a comparison of the prediction of O_2 concentration, in Figure 4-14b for cases C13 and C14, shows that the prediction is slightly improved with UFM. However, this improvement is not as significant as what is observed in case C6.

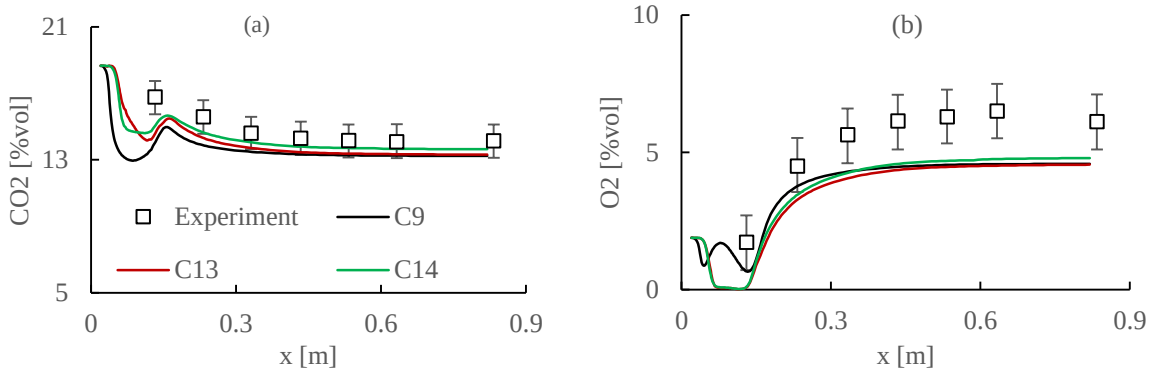

Figure 4-14. Profiles of (a) CO_2 and (b) O_2 mole fractions along the centerline of the furnace (EDC (case C9), SFM (case C13) and UFM (case C14)).

4.6 Conclusions

The influence of turbulence model (i.e., STD, RNG and RKE $k-\varepsilon$ models), chemistry scheme, and combustion model (i.e., SFM, UFM and EDC) on the predictions of species, temperature and velocity fields of the gas phase biomass combustion of a small-scale grate-firing biomass furnace is examined. Twelve different cases are simulated. Numerical predictions are validated against published experimental measurements [4, 47].

The results of turbulence modelling showed that, on the basis of temperature field, RNG turbulence model shows better predictions with either SFM or the standard EDC combustion models, especially in high temperature regions. The results showed that the predictions of species are more

influenced by the combustion rather than turbulence modelling. Results of the size and position of recirculation zones closer to the bed and high temperature regions showed that the velocity field is less sensitive to turbulence modelling using EDC combustion model. Overall, RNG turbulence model is found to produce better predictions compared to the other models regardless of the combustion model being used (i.e., EDC and SFM).

The results of the tested chemical reaction mechanisms indicated that predictions of the main species (e.g., CO_2 and O_2) and temperature field, particularly in high temperature regions, depend strongly on the chosen reaction mechanism. This is especially evident with the EDC combustion model even when using reduced chemistry mechanism. In addition, the results demonstrated that in the regions of equilibrium chemistry condition (i.e., downstream of the current furnace), where the level of turbulence and consequently mixing between gases decays, the predictions become less sensitive to reaction mechanism. It can be concluded that the SFM model when using the detailed chemical mechanism ME.2 produces better predictions than the other combination of SFM and chemical mechanisms especially closer to the bed; while the EDC model using the reduced chemical mechanism ME.5 yields better predictions compared to all other EDC cases. More importantly, the analysis showed insignificant difference between the predictions of these best cases (i.e., SFM combined with ME.2 and EDC with ME.5) especially close to the bed and in high temperature regions.

The effect of combustion (turbulence-chemistry interaction) model on the predictions is investigated using SFM, UFM, and standard and modified EDC models. The results revealed that the influence of combustion modelling on the temperature field is more evident in the vicinity of the bed and high temperature regions. The results demonstrated that the modified EDC and UFM when using AGR model produce slightly better predictions of the temperature field closer to the

bed in comparison with the SFM, UFM and standard EDC. Also, the present results showed that the predictions of the slow chemistry species (i.e., CO) is strongly influenced by the chosen combustion model. Accordingly, while SFM under predicts CO concentration, UFM and standard EDC produce almost similar predictions, particularly downstream of the furnace. However, UFM with AGR and the modified EDC produced comparable predictions of CO concentration. Moreover, when reduced chemistry is used with SFM and UFM, the temperature field is significantly over predicted, whereas the major species (e.g., CO_2 and O_2) are adequately predicted. In conclusion, the modified EDC model produced the best predictions of CO concentration, while UFM predicted slightly better predictions of CO_2 and O_2 species. As for the performance of these models in terms of carbon mass imbalance in the computational domain, the results showed that using UFM instead of SFM improves the calculation of the mass imbalance. However, for species transport based model (i.e., EDC), no significant influence was observed in terms of carbon mass imbalance even with the modified model's constants/coefficients.

The present study showed that the predictions are more sensitive to turbulence modelling when using mixture fraction based combustion modelling. The effect of chemical reaction mechanism is more pronounced closer to the bed and in high temperature regions. The analysis revealed that the most important parameter that influences the predictions is found to be the combustion model. It is found that while inexpensive mixture fraction based combustion models (e.g., SFM and UFM) produced reasonable predictions of the main species, temperature, and flowfield, their predictions of slow forming pollutant emissions (e.g., CO and NO_x) is found not reliable. However, UFM approach when using AGR method and adequate chemical mechanism can produce significant improvement in the predictions of slow forming pollutants. The best predictions of slow forming species is achieved using the modified EDC regardless of the adopted chemical mechanism.

Therefore, it can be concluded that despite its relatively high computational time, the modified EDC along with reduced chemical mechanism is a reliable approach for simulating gas-phase biomass combustion, especially for predicting slow forming gas pollutants. Finally, the results obtained with UFM approach suggest that it could be a promising combustion model for numerically investigating grate biomass furnaces.

4.7 References

[1] C. Yin, L. Rosendahl and S. Kaer, "Grate-firing of biomass for heat and power production," Progress in Energy and Combustion Science, vol. 34, pp. 725-754, 2008.

[2] S. Sukumaran and S. Kong, "Modeling fuel NOx formation from combustion of biomass-derived producer gas in a large-scale burner," Combustion and Flame, vol. 160, pp. 2159-2168, 2013.

[3] S. Van Loo and J. Koppenjan, Handbook of biomass combustion and co-firing, Twente University Press, 2002.

[4] T. Klason and X. Bai, "Computational study of the combustion process and NO formation in a small-scale wood pelletfurnace," Fuel, vol. 86, pp. 1465-1474, 2007.

[5] M. Buchmayr, J. Gruber, M. Hargassner and C. Hochenauer, "A computationally inexpensive CFD approach for small-scale biomass burners equipped with enhanced air staging," Energy Conversion and Management, vol. 115, pp. 32-42, 2016.

[6] J. Chaney, H. Liu and J. Li, "An overview of CFD modelling of small-scale fixed-bed biomass pellet boilers with preliminary results from a simplified approach," Energy Conversion and Management, vol. 63, pp. 149-156, 2012.

[7] A. Shiehnejadhesar, R. Scharler, R. Mehrabian and I. Obernberger, "Development and validation of CFD models for gas phase reactions in biomass grate furnaces considering gas streak formation above the packed bed," Fuel Processing Technology, vol. 139, pp. 124-148, 2015.

[8] F. Tabet, V. Fichet and P. Plion, "A comprehensive CFD based model for domestic biomass heating systems," Journal of the Energy Institute, vol. 2, pp. 166-+214, 2016.

[9] J. Collazo, J. Porteiro, J. Míguez, E. Granada and M. Gómez, "Numerical simulation of a small-scale biomass boiler," Energy Conversion and Management, vol. 64, pp. 87-96, 2012.

[10] D. Fletcher, B. Haynes, J. Chen and S. Joseph, "Computational fluid dynamics modelling of an entrained flow biomass gasifier," Applied mathematical modelling, vol. 22, pp. 747-757, 1998.

[11] D. Fletcher, B. Haynes, F. Christo and S. Joseph, "A CFD based combustion model of an entrained flow biomass gasifier," Applied mathematical modelling, vol. 24, pp. 165-182, 2000.

[12] H. Knaus, S. Richter, S. Unterberger, U. Schnell, H. Maier and K. Hein, "On the application of different turbulence models for the computation of fluid flow and combustion processes in small scale wood heaters," Experimental Thermal and Fluid Science, vol. 21, pp. 99-108, 2000.

[13] D. Spalding, "Mixing and chemical reaction in steady confined turbulent flame," Proceedings in combustion institute, vol. 13, pp. 649-657, 1971.

[14] B. Magnussen and B. Hjertager, "On the mathematical modeling of turbulent combustion with special emphasis on soot formation and combustion,"Proceedings in combustion institute, vol. 16, pp. 719-729, 1977.

[15] C. Yin, L. Rosendahl, S. K. Kær, S. Clausen, S. L. Hvid and T. Hille, "Mathematical Modeling and Experimental Study of Biomass Combustion in a Thermal 108 MW Grate-Fired Boiler," Energy & Fuels, vol. 22, pp. 1380-1390, 2008.

[16] A. Bhuiyan and J. Naser, "CFD modeling of co-firing of biomass with coal under oxy-fuel combustion in a large scale power plant," Fuel, vol. 105, pp. 504-511, 2015.

[17] D. Djurovic, S. Nemoda, B. Repic and D. A. M. Dakic, "Influence of biomass furnace volume change on flue gases burn out process," Renewable energy, vol. 76, pp. 1-6, 2015.

[18] C. Yin, L. Rosendahl, S. Clausen and S. Hvid, "Characterizing and modeling of an 88 MW grate-fired boiler burning wheat straw: Experience and lessons," Energy, vol. 41, pp. 473-482, 2012.

[19] C. K. WESTBROOK and F. L. DRYER, "Simplified Reaction Mechanisms for the Oxidation of Hydrocarbon Fuels in Flames," Combustion Science and Technology, vol. 27, pp. 31-43, 1981.

[20] C. Yin, S. Kær, L. Rosendahl and S. Hvid, "Co-firing straw with coal in a swirl-stabilized dual-feed burner: Modelling and experimental validation," Bioresource Technology, vol. 101, pp. 4169-4178, 2010.

[21] W. Jones and R. Lindstedt, "Global reaction schemes for hydrocarbon combustion," Combustion and Flame, vol. 73, pp. 233-249, 1988.

[22] B. Magnussen, "On the structure of turbulence and a generalized eddy dissipation concept for chemical reaction in turbulent flow," in 19th AIAA aerospace science meeting, St. Louis, Missouri, 1981.

[23] M. Farokhi and M. Birouk, "Application of Eddy Dissipation Concept for modeling biomass combustion, Part 1: Assessment of model coefficients," Energy and Fuels, 2016.

[24] G. Smith, D. Golden, M. Frenklach, N. Moriarty, B. Eiteneer, M. Goldenberg, C. Bowman, R. Hanson, S. Song, W. Gardiner, V. Lissianski and Z. Qin, "GRI 3.0 Mechanism," [Online]. Available: www.me.berkeley.edu/gri_mech.

[25] M. Bugge, Ø. Skreiberg, N. Haugen, P. Carlsson, E. Houshfar and T. Løvås, "Numerical simulation of staged biomass grate fired combustion with an emphasis on NOx emissions," Energy Procedia, vol. 75, pp. 156-161, 2015.

[26] T. Løvås, E. Houshfar, M. Bugge and Ø. Skreiberg, "Automatic Generation of Kinetic Skeletal Mechanisms for Biomass Combustion," Energy and Fuels, vol. 27, pp. 6979-6991, 2013.

[27] M. Rehm, P. Seifert and B. Meyer, "Theoretical and numerical investigation on the EDC-model for turbulent-chemistry interaction at gasification conditions," Computer and Chemistry Engineering, vol. 33, pp. 402-407, 2009.

[28] A. De, E. Oldenhof, P. Sathiah and D. Roekaerts, "Numerical Simulation of Delf-Jet-in-Hot-Coflow (DJHC) Flame Using Eddy dissipation Concept Model for Turbulent-Chemistry Interaction," Flow Turbulence Combustion, vol. 87, pp. 537-567, 2011.

[29] A. Parente, M. Malik, F. Contino, A. Cuoci and B. Dally, "Extension of the Eddy Dissipation Concept for turbulent/chemistry interaction to MILD combustion," Fuel, vol. 163, pp. 98-111, 2016.

[30] A. Shiehnejadhesar, R. Mehrabian, R. Scharler, G. M. Goldin and I. Obernberger, "Development of a gas phase combustion model suitable for low and high turbulence conditions," Fuel, vol. 126, pp. 177-187, 2014.

[31] M. Farokhi and M. Birouk, "Application of Eddy Dissipation Concept for modeling biomass combustion - Part 2: Gas-phase combustion modeling of a small-scale fixed bed furnace," Energy and Fuels, 2016.

[32] R. Prieler, M. Demuth, D. Spoljaric and C. Hochenauer, "Numerical investigation of the steady flamelet approach under different combustion environments," Fuel, vol. 140, pp. 731-743, 2015.

[33] N. Peters, "Laminar diffusion flamelet models in non-premixed turbulent combustion," Progress in Energy and Combustion Science, vol. 10, pp. 319-339, 1984.

[34] H. Pitsch, M. Chen and N. Peters, "Unsteady flamelet modeling of turbulent hydrogen-air diffusion flames,"Proceedings in combustion institute, vol. 27, pp. 1057-1064, 1998.

[35] ANSYS, "Ansys Fluent theory guide, Release 15.0," ANSYS.

[36] B. Albrecht, S. Zahirovic, R. Bastiaans, J. Van Oijen and L. de Goey, "A premixed flamelet - PDF model for biomass combustion in a grate furnace," Energy and Fuels, vol. 22, pp. 1570-1580, 2008.

[37] C. Bowman, R. Hanson, D. Davidson, W. Gardiner, J. V. Lissianski, G. Smith, D. Golden, M. Frenklach and M. Goldenberg, "GRI-Mech 2.11," [Online]. Available: http://www.me.berkeley.edu/gri_mech/.

[38] P. Venturini, D. Borello, C. Iossa, D. Lentini and F. Rispoli, "Modeling of multiphase combustion and deposit formation in a biomass-fed furnace," Energy, vol. 35, pp. 3008-3021, 2010.

[39] D. Borello, P. Venturini, F. Rispoli and S. Rafael, "Prediction of multiphase combustion and ash deposition within a biomass furnace," Applied Energy, vol. 101, pp. 413-422, 2013.

[40] M. BUI-PHAM and K. SESHADRI, "Comparison between Experimental Measurements and Numerical Calculations of the Structure of Heptane-Air Diffusion Flames," Combustion Science and Technology, vol. 79, pp. 293-310, 1991.

[41] R. Yadav, P. Nakod and P. Rajeshirke, "NO Prediction in Turbulent Diffusion Flame Using Multiple Unsteady Laminar Flamelet Modeling," ASME Journal of Engineering for Gas Turbines and Power, vol. 136, 2014.

[42] A. Benim and K. Syed, "Laminar ¯amelet modelling of turbulent premixed combustion," Applied Mathematical Modelling, vol. 22, pp. 113-136, 1998.

[43] A. Heyl and H. Bockhorn, "Flamelet modeling of NO formation in laminar and turbulent diffusion flames," Chemosphere, vol. 42, pp. 449-462, 2001.

[44] D. Haworth, M. Drake, S. Pope and R. Blint, "The importance of time-dependent flame structures in stretched laminar flamelet models for turbulent jet diffusion flames" Proceedings in combustion institute, vol. 22, pp. 589-597, 1989.

[45] B. Cuenot, F. Egolfopoulos and T. Poinsot, "An unsteady laminar flamelet model for non-premixed combustion," Combustion Theory and Modelling, vol. 4, pp. 77-79, 2000.

[46] E. Knudsen, H. Pitsch, D. J. Cook, K. Kedia and X. Li, "Unsteady flamelet modeling of CO emissions from a biomass combustor," Center for Turbulence Research, 2012.

[47] H. Wiinikka, writer, P.hd. thesis [Performance], High temperature aerosol formation and emission minimisation during combustion of wood pellet, Lulea University of Technology, Lulea, Sweden, 2005.

[48] M. Modest, Radiative Heat Transfer, Academic Press, 2003.

[49] N. Kayakol and N. Selcuk, "Evaluation of descrete ordinates method for radiative transfer in rectangular furnaces," International Journal of Heat and Mass Transfer, vol. 40, pp. 213-222, 1997.

[50] H. Khodaei, Y. M. Al-Abdeli, F. Guzzomi, Yeoh and G. H, "An overview of processes and considerations in the modelling of fixed-bed biomass combustion," Energy, vol. 88, pp. 946-972, 2015.

[51] T. Klason, X. Bai, M. Bahador, T. Nilsson and B. Sunden, "Investigation of radiative heat transfer in fixed bed biomass furnaces," Fuel, vol. 87, pp. 2141-2153, 2008.

[52] C. Borgnakke and R. E. Sonntag, Fundumental of Thermodynamics, John Wiley & sons, Inc..

[53] H. Grotjans and F. Menter, "Wall functions for industrial applications," in Proceedings of Computational Fluid Dynamics'98, ECCOMAS, Chichester, UK., 1998.

[54] B. Kader, "Temperature and concentration profiles in fully turbulent boundary layers," International Journal of Heat and Mass Transfer, vol. 9, pp. 1541-1544, 1981.

[55] B. Launder and D. Spalding, Lectures in Mathematical Models of Turbulence, London, England: Academic Press, 1972.

[56] S. Orszag, V. Yakhot, W. Flannery, F. Boysan, D. Choudhury, J. Maruzewski and B. Patel, "Renormalization group modeling and turbulence simulation," in International Conference on Near-Wall Turbulent Flows, Tempe, Arizona, 1993.

[57] T. Shih, W. Liou, A. Shabbir, Z. Yang and J. Zhu, "A New k-ε Eddy-Viscosity Model for High Reynolds Number Turbulent Flows - Model Development and Validation," Computers and Fluids, vol. 24, pp. 227-238, 1995.

[58] J. Porteiro, J. Collazo, D. Patiño, E. Granada, J. C. Moran Gonzalez and J. L. Míguez, "Numerical Modeling of a Biomass Pellet Domestic Boiler," Energy & Fuels, vol. 23, pp. 1067-1075, 2009.

[59] X. Zhang, Q. Chen, R. Bradford, V. Sharifi and J. Swithenbank, "Experimental investigation and mathematical modelling of wood combustion in a moving grate boiler," Fuel Process Technology, vol. 91, pp. 1494-1499, 2010.

[60] B. Launder and D. Spalding, "The numerical computation of turbulent flows," Computer Methods in Applied Mechanics and Engineering, vol. 3, pp. 269-289, 1974.

[61] N. Hashimoto, R. Kurose, S.-M. Hwang, H. Tsuji and H. Shirai, "A numerical simulation of pulverized coal combustion employing a tabulated-devolatilization-process model (TDP model)," Combustion and Flame, vol. 159, pp. 353-366, 2012.

[62] M. Emami and A. Eshghinejad Fard, "Laminar flamelet modeling of a turbulent CH4/H2/N2 jet diffusion flame using artificial neural networks," Applied Mathematical Modelling, vol. 36, pp. 2082-2093, 2012.

[63] A. Shiehnejadhesar, K. Schulze, R. Scharler and I. Obernberger, "A new innovative CFD-based optimisation method for biomass combustion plants," Biomass Bioenergy, vol. 53, pp. 48-53, 2013.

[64] B. Magnussen and I. Gran, "numerical study of a bluff-body stabilized diffusion flame. Part 2. Influence of combustion modeling and finite-rate chemistry," Combustion Science and Technology, vol. 119, pp. 191-217, 1996.

[65] B. Magnussen and I. Ertesvag, "The eddy dissipation turbulence energy cascade model," Combustion Science and Technology, pp. 213-235, 2000.

[66] N. M. Marinov, W. J. Pitz, C. K. Westbrook, A. M. Vincitore, M. J. Castaldi, S. M. Senkan and C. F. Melius, "Aromatic and Polycyclic Aromatic Hydrocarbon Formation in a Laminar Premixed n-Butane Flame," Combustion and Flame, vol. 114, pp. 192-213, 1998.

[67] S. Dworkin, Q. Zhang, M. Thomson, N. Slavinskaya and U. Riedel, "Application of an enhanced PAH growth model to soot formation in a laminar coflow ethylene/air diffusion flame," Combustion and Flame, vol. 158, pp. 1682-1695, 2011.

[68] N. Slavinskaya, U. Riedel, S. Dworkin and M. Thomson, "Detailed numerical modeling of PAH formation and growth in non-premixed ethylene and ethane flames," Combustion and Flame, vol. 159, pp. 979-995, 2012.

[69] E. Ranzi, A. Cuoci, T. Faravelli, A. Frassoldati, G. Migliavacca, S. Pierucci and S. Sommariva, "Chemical Kinetics of Biomass Pyrolysis," Energy & Fuels, vol. 22, pp. 4292-4300, 2008.

[70] M. Corbetta, A. Frassoldati, H. Bennadji, K. Smith, M. J. Serapiglia, G. Gauthier, T. Melkior, E. Ranzi and E. M. Fisher, "Pyrolysis of Centimeter-Scale Woody Biomass Particles: Kinetic Modeling and Experimental Validation," Energy & Fuels, vol. 28, pp. 3884-3898, 2014.

[71] H. Richter and J. B. Howard, "Formation and consumption of single-ring aromatic hydrocarbons and their precursors in premixed acetylene, ethylene and benzene flames," Physical Chemistry Chemical Physics, vol. 4, pp. 2038-2055, 2002.

[72] L. Dupont, A. El Bakali, J.-F. Pauwels, I. Da Costa, P. Meunier and H. Richter, "Investigation of stoichiometric methane/air/benzene (1.5%) and methane/air low pressure flames," Combustion and Flame, vol. 135, pp. 171-183, 2003.

[73] C. Li, S. Appari, R. Tanaka, K. Hanao, Y. Lee, S. Kudo, J. Hayashi, V. Janardhanan, H. Watanabe and K. Norinaga, "A CFD study on the reacting flow of partially combusting hot coke oven gas in a bench-scale reformer," Fuel, vol. 159, pp. 590-598, 2015.

[74] S. Appari, R. Tanaka, C. Li, S. Kudo, J. Hayashi, V. Janardhanan, H. Watanabe and K. Norinaga, "Predicting the temperature and reactant concentration profiles of reacting flow in the partial oxidation of hot coke oven gas using detailed chemistry and a one-dimensional flow model," Chemical engineering journal, vol. 266, pp. 82-90, 2015.

[75] J. Andersen, C. L. Rasmussen, T. Giselsson and P. Glarborg, "Global Combustion Mechanisms for Use in CFD Modeling under Oxy-Fuel Conditions," Energy & Fuels, vol. 23, pp. 1379-1389, 2009.

[76] S. Pope, "Computationally efficient implementation of combustion chemistry using in situ adaptive tabuilation," Combustion Theory and Modeling, vol. 1, pp. 41-63, 1997.

[77] L. Kjaldman, A. Brink and M. Hupa, "Micro mixing time in eddy dissipation concept," Combustion Science and Technology, vol. 154, pp. 207-227, 2000.

[78] G. Hartung, J. Hult, C. F. Kaminski, J. W. Rogerson and N. Swaminathan, "Effect of heat release on turbulence and scalar-turbulence interaction in premixed combustion," Physics of Fluids, vol. 20, 2008.

[79] M. Saediamiri, M. Birouk and J. A. Kozinski, "On the stability of a turbulent non-premixed biogas flame: Effect of low swirl strength," Combustion and Flame, vol. 161, pp. 1326-1336, 2014.

[80] M. Birouk, M. Saediamiri and J. A. Kozinski, "Non-premixed turbulent biogas flame: effect of the co-airflow swirl strength on the stability limits," Combustion Science and Technology, vol. 186, pp. 1460-1477, 2014.

[81] R. N. Roy and S. Sreedhara, "Modelling of methanol and H2/CO bluff-body flames using RANS based turbulence models with conditional moment closure model," Applied Thermal Engineering, vol. 93, pp. 561-570, 2015.

[82] A. Rebola, P. J. Coelho and M. Costa, "Assessment of the performance of several turbulence and combustion models in the numerical simulation of a flameless combustor," Combustion Science and Technology, vol. 185, pp. 600-626, 2013.

[83] B. Danon, W. de Jong and D. Roekaerts, "Experimental and numerical investigation of a flox combustor firing low calorific value gases," Combustion science and technology, vol. 182, pp. 1261-1278, 2010.

[84] F. Christo and B. Dally, "Modeling turbulent reacting jets issuing into a hot and diluted coflow," Combustion and Flame, vol. 142, pp. 117-129, 2005.

[85] A. H. Al-Abbas and J. Naser, "Effect of chemical reaction mechanisms and NOx modeling on Air-Fired and Oxy-Fuel combustion of lignite in a 100-KW furnace," Energy and Fuels, vol. 26, pp. 3329-3348, 2012.

Chapter 5: A new EDC approach for modeling turbulence/chemistry interaction in the gas-phase of biomass combustion

5.1 Abstract

Small-scale grate-firing biomass combustors generate high level of pollutants as a result of poor air/fuel mixing and short residence time of combustion. Reliable gas-phase combustion modeling can play a key role in the improvement and optimization of the design of a biomass furnace. This paper proposes a new combustion model based on the framework of the well-known eddy dissipation concept (EDC) approach. The ability of EDC to incorporate detailed chemical reactions in turbulent reacting flows has made it attractive for modeling combustion. However, its application poses a challenge especially for modeling weakly turbulent reacting flow conditions, as well as reacting flows with comparable flow and chemical time scales. The newly proposed combustion scheme can reasonably describe the interaction of chemistry and turbulent flow over a wider range of turbulence conditions. To validate the model, simulations are carried out using diffusion and partially premixed jet flames covering weakly to highly turbulent flow conditions. Moreover, the capability of the new model in predicting NO_x emissions, based on fuel bound nitrogen source as well as thermal NO_x, is investigated. All numerical results are compared with their counterparts' experimental measurements of temperature and species concentrations. Compared to the standard EDC, the results of the new EDC approach reveal noticeable improvement in the predictions, especially for slow-forming and kinetically dominated species such as CO and NO_x.

5.2 Introduction

The growing demand for more energy, along with global warming concerns and limited fossil fuel resources, have prompted interest in developing more efficient and environmentally-friendly technologies (e.g., moderate and intense low oxygen dilution (MILD) combustion for biomass furnaces) [1, 2]. In recent decades, energy conversion using grate firing biomass furnaces technology showed significant grow. This is mainly driven by the low investment cost of this technology and also the flexibility of feedstock (i.e., wide range of fuel particles size, ash and moisture contents) [2, 3, 4]. Despite being a CO_2-neutral-energy-source technology, small-scale grate firing combustors still generate high level of emissions (e.g., CO and NO_x), due mainly to their smaller furnace volume, poor air/fuel mixing and shorter residence time [3, 5]. Therefore, in order to comply with severe emissions regulations, more research is required to improve this technology [6].

Nowadays, numerical simulation (e.g., CFD modeling) is becoming on par with theory and experiment as an important research tool owing to its lower cost compared to physical tests, and also because of its capability of producing multi-scale information which cannot be achieved otherwise [7]. Biomass gas-phase combustion in furnaces occurs over multi scales; that is, flow and chemical time scales within a grate firing furnace vary over a wide rage [8]. CFD modeling can help in the understanding of this multi-scale phenomenon. However, the reliability of CFD predictions relies strongly on the accuracy of the adopted sub-models (e.g., turbulence modeling, flow/chemistry interaction modeling). For modeling the gas-phase of biomass combustion, flow/chemistry interaction is usually accounted for using eddy break up (EBU) [9] based models (e.g., finite-rate kinetic/eddy dissipation model (FKR/EDM) [10], eddy dissipation concept (EDC) [11]). Simple approaches, such as FKR/EDM, usually capture reasonably well the features of

mixing-dominated combustion processes. However, these models can only use few-step chemical reaction mechanisms which consequently makes unreliable the predictions of slow-forming and kinetically dominated gaseous pollutants (e.g., CO and NO_x) [12, 13, 14, 6]. It is also important to mention that, mixture fraction based models, which are capable of incorporating detailed chemistry (e.g., steady/unsteady flamelet model (SFM/UFM) [15, 16]), have also been examined in a few works related to biomass combustion (e.g., [5, 17, 18]). Nevertheless, since the flue gas released from solid fuels cannot be introduced in terms of only one single variable (i.e., mixture fraction) [6], the application of SFM/UFM is still limited to very small/lab-scale biomass combustors (see Ref. [5] for more details).

An extended version of EBU approach, known as eddy dissipation concept (EDC) [11], has been developed to incorporate detailed chemical kinetics in turbulent flows. This model has shown adequate predictions for premixed, partially premixed and non-premixed combustion regimes [19]. The applicability of EDC has been tested for different biomass combustion applications (e.g., [20, 21]). However, despite its widespread use, only a few studies have examined its limitation for simulating gas-phase biomass combustion (e.g., [18, 22, 14]).

Many studies have recently been performed on EDC with the aim of examining and also improving the model's capability under different flow/turbulence conditions. For instance, De et al. [23] employed EDC for simulating Delft-Jet-in-Hot-Coflow (DJHC) burner with MILD combustion regime, and reported that, in comparison with experiment, the standard EDC predicted a too early ignition. Rehm et al. [24] adopted EDC for simulating the gasification process and reported a partial agreement between the numerical predictions and their counterparts' experimental measurements. An extended version of EDC approach was proposed by Parante et al. [1]. With the argument that a large degree of partial premixing occurs in MILD combustion condition, the

model was developed for MILD combustion regime on the basis of premixed combustion theory (i.e., laminar flame speeds). They examined the proposed model by simulating an Adelaide Jet-in-Hot-Coflow (JHC) burner and reported remarkably better results of species and temperature profiles than those of standard EDC when compared with their experimental counterparts. Mardani [25] performed a parametric study under MILD combustion condition with the aim to propose some guidelines to modify the model's constants. The study reported that, compared to the standard EDC, using smaller values of the model's constants led to non-equilibrium condition within the reacting structures in the combustion regime, and consequently resulted in an extended and distributed reaction zone. Aminian et al. [26] developed a theoretical version of the EDC extinction model for MILD combustion regime. Their model assumed that the flame is locally extinguished when the fine structure residence time is lower than a new proposed critical time scale, which is determined by considering the effect of finite-rate chemistry. Their model was found to capture the local extinction behaviour of MILD flames. In the case of biomass combustion, Shiehnejadhesar et al. [2] developed a hybrid reaction rate model, which considers FKR and EDC mean reaction rates, to account for, respectively, weakly and highly turbulent flow regions. The model showed improved predictions in weakly turbulent flow condition when compared with the standard EDC. Farokhi and Birouk [27] performed a sensitivity analysis on EDC coefficients for weakly and highly turbulent flow conditions. Their study reported that modifying the coefficients of the model based on turbulent flow characteristics (e.g., turbulent Reynolds number and turbulent time scale), the model predictions can significantly be improved under both weakly and highly turbulent flow conditions. The same authors simulated the gas-phase combustion of a small-scale grate firing biomass combustor using the modified EDC coefficients and reported better predictions of temperature and species than the standard EDC [14].

Furthermore, they examined the capability of EDC by modifying its coefficients and using reduced chemistry, against SFM/UFM approaches using detailed chemistry, and reported that the modified EDC shows better predictions of, especially, slow-forming species concentration (i.e., CO).

As briefly reviewed above, EDC has weaknesses in modeling slow chemistry where the chemical and characteristic flow time scales are comparable (i.e., reacting flow with relatively low Damköhler number) [1, 2]. In addition, EDC approach is not suitable for modeling weakly turbulent flow condition. In grate-firing biomass combustion chambers, such condition may occur in the vicinity of the bed, where high temperature volatile gases leave the solid fuel with relatively low velocity and turbulence intensity [2]. Nonetheless, while the model has been originally developed for modeling highly turbulent flow regime (with a clear separation between large and small flow scales), its predictions in highly turbulent flow condition can still be improved by changing the model coefficients [27]. However, the modifications of the model coefficients are based on a particular turbulent reacting flow condition. That is, the investigation can only be performed on a weakly or a highly turbulent flow condition. This, in fact, limits the application of the modified model especially for complex industrial geometries where the reacting flow may occur under a variety of turbulence conditions. Only the study by Parante et al. [1] proposed locally modified EDC coefficients (i.e., based on local parameters of flow and chemistry, turbulent Reynolds number and Damköhler number). However, their proposed model was developed for predominantly premixed condition in MILD combustion regime.

The present study aims to propose a new modified EDC model suitable for a wide range of turbulent flow regimes, from weak to high turbulent flow condition including near flame extinction. The proposed model is examined by simulating different diffusion and partially premixed jet flames; where the H_2/N_2/air diffusion jet flame of Meier et al. [28] is chosen to cover

weakly turbulent flow condition, while the well-known methane/air jet flames of Barlow and Frank [29] are selected to cover moderate to highly turbulent flow conditions. Moreover, the capability of the model in predicting thermal NO_x and also NO_x emissions resulting from fuel bound nitrogen source (as one of the dominant source of NO_x in biomass combustion) is investigated by simulating a diffusion $CO/H_2/N_2$ jet flame doped with NH_3 [30]. These flames are chosen for the purpose of examination and validation of the numerical model as follows. The composition of the fuel released from solid biomass particles is independent on biomass origin (woody or herbaceous), and is similar to those of the selected flames [6, 27, 2]. Also, the selected jet flames reflect real situations that may occur in an industrial biomass furnace [6]. In order to highlight the performance of the current approach, all simulations are carried out using both the standard and modified EDC, and the results of both models are compared with published experimental measurements.

5.3 Methodology

Reynolds averaged Navier-Stokes (RANS) of continuity, energy, species and momentum transport equations are solved numerically. The effect of radiation is accounted for using P_1-approximation model [31], along with the domain-based weighted-sum-of-gray-gas (WSGG) method [32]. The effect of enthalpy transport due to species diffusion is considered in the energy equation. Turbulence is modeled using realizable (RKE) $k-\varepsilon$ model [33] which is shown to be better than the standard $k-\varepsilon$ model at low-Reynolds and highly strained flows (e.g., [34, 35, 36]). As stated and examined in [2], for weakly to moderate turbulent flow condition, considering molecular diffusion along with turbulent diffusion in the mixing process can significantly improve the predictions. Hence, the effect of molecular diffusion is considered in this study.

The EDC model is adopted to account for the interaction between chemistry and turbulent flow, and is developed on the basis of turbulent energy cascade method [11]. More details can be found

in the literature (e.g., [1]). In developing EDC model, Magnussen [11] assumed that combustion takes place in a region of reacting flow denoted as fine structures, where the dissipation of turbulent kinetic energy occurs [1]. These fine structures may behave as vortex tubes, sheets or slabs, whose characteristic length scales are of the order of Kolmogorov scale [11, 37]. In the modeling context of the EDC, it is assumed that each fluid cell in a computational domain is divided into volume fraction of a fine structure, γ^*, and volume fraction of a surrounding fluid, $\gamma^\circ = 1 - \gamma^*$ [11, 2]. According to the original EDC energy cascade method, the mass fraction occupied by fine structures (i.e., γ^*) is related to turbulence intermittency as follows [11, 38]:

$$\gamma^* = \left(\frac{u^*}{u'}\right)^{\alpha} = \left(\frac{l^*}{l'}\right)^{\beta} \tag{5-1}$$

where u^* and u' are, respectively, the velocity scales corresponding to the fine structure and energy containing range of the spectrum (i.e., turbulent integral length scale) [23]; l^* and l' represent fine structure and integral length scales, respectively. Assuming strong dissipation intermittency at high turbulent Reynolds number, the values of α and β are set as 3 and 1 [38]. Using the energy cascade approach, the values of γ^* and the time scale of mass transfer between a fine structure and its surrounding fluids, τ^*, can be expressed as a function of turbulent flow characteristics, as follows [39]:

$$\gamma^* = \left(\frac{3C_{D2}}{4C_{D1}^2}\right)^{3/4} \left(\frac{\vartheta\varepsilon}{k^2}\right)^{3/4} = \left(\frac{3C_{D2}}{4C_{D1}^2}\right)^{3/4} Re_t^{-3/4} \tag{5-2}$$

$$\tau^* = \left(\frac{C_{D2}}{3}\right)^{1/2} \left(\frac{\vartheta}{\varepsilon}\right)^{1/2} = C_\tau \tau_\eta = C_\tau Re_t^{-1/2} \left(\frac{k}{\varepsilon}\right) = C_\tau Re_t^{-1/2} T_t \tag{5-3}$$

where $Re_t = k^2/\vartheta\varepsilon$ and $T_t = k/\varepsilon$ are, respectively, Reynolds number and turbulent time scale based on the integral length scale (Re_t and T_t are, respectively, called hereafter as turbulent Reynolds number and turbulent time scale), $\tau_\eta = (\vartheta/\varepsilon)^{0.5}$ is the Kolmogorov time scale, C_τ is the EDC residence time coefficient, $C_{D1} = 0.135$ and $C_{D2} = 0.5$ are the model constants [1]. The standard EDC model's averaged reaction rate of species i is expressed as follows [40, 2]:

$$\overline{R_i} = \frac{\overline{\rho}{\gamma^*}^{2/3}}{(1-\gamma^*)\tau^*}\left(Y_i^* - \overline{Y_i}\right) = \frac{\overline{\rho}}{\tau_{mix}}\left(Y_i^* - \overline{Y_i}\right) \tag{5-4}$$

where $\overline{\rho}$ is the average density of the mixture, Y_i^* and $\overline{Y_i}$ are, respectively, the fine structure and the mean mass fraction of species i, and τ_{mix} denotes a new characteristic mixing time scale [23, 2, 27], which is obtained by applying linear relaxation process between mass fractions of species i in the fine structure and its surrounding fluids. The value of Y_i^* is achieved based on Arrhenius expression of chemical reactions over EDC time scale (i.e., τ^*) assuming perfectly stirred reactor (PSR) condition. However, in order to reduce the computational time, the assumption of plug flow reactor (PFR) condition is adopted here, as it is also the default method used by the commercial software ANSYS FLUENT [23]. The change from PSR to PFR condition may affect the calculated value of Y_i^*. However, a recent numerical simulation study of the JHC burner using EDC approach showed no significant difference using either of the two reactor models [41]. That is, the predictions of temperature and major species are found almost identical, and only a negligible difference in the predictions of minor species (e.g., CO and OH) was observed [41].

According to Eq.(5-2), since the value of γ^* is calculated based on turbulent characteristics of the flow, it is not explicitly related to the computational cell geometry. Hence, there must be an upper limit for γ^* to avoid unphysical size of the reaction zone, which may occur in the region where the

level of turbulence is weak [27, 42]. The upper limit of γ^* can be achieved by assuming that the ratio of EDC time scale over mixing time scale must be less than unity [23, 2]. Consequently, the upper limit of γ^* based on Re_t and using Eq.(5-2) can be expressed as follows:

$$\frac{\tau^*}{\tau_{mix}} = \frac{{\gamma^*}^{2/3}}{(1-\gamma^*)} < 1 \rightarrow {\gamma^*}^{1/3} < 0.75 \tag{5-5}$$

$${\gamma^*}^{1/3} = \gamma = \left(\frac{3C_{D2}}{4C_{D1}^2}\right)^{1/4} Re_t^{-1/4} = C_\gamma Re_t^{-1/4} \tag{5-6}$$

$$C_\gamma < 0.75 Re_t^{1/4} \tag{5-7}$$

where γ is known as the length fraction of fine scales and C_γ is defined as fine structure volume coefficient (with a default value of 2.1377 when using the standard coefficients $C_{D1} = 0.135$ and $C_{D2} = 0.5$) [2].

As mentioned previously, EDC was developed for flow fields with a clear separation between turbulent scales. In other words, the values of EDC model constants (i.e., C_{D1} and C_{D2}) were chosen in a way that the best predictions can be achieved when the level of turbulence is high enough. Therefore, the model's weakness is related to its application for weakly turbulent flow fields. To investigate the effect of turbulence on the EDC parameters, the sensitivity of γ and the ratio of time scales on the level of turbulence can be performed via their mathematical relationship with Re_t. Based on Eqs.(5-5) to (5-7), Figure 5-1 shows the effect of Re_t and C_γ on γ (Figure 5-1a), and on the ratio of time scales (Figure 5-1b). This figure shows tha the profiles of γ indicate that, using the default value of C_γ (= 2.1377), no acceptable value of γ can be achieved when $Re_t < 64$ ($\gamma > 0.75$). Hence, the EDC minimum turbulent Reynolds number ($Re_{tm} = 64$) is calculated

when the default value of C_γ is adopted. This figure also shows that, from a mathematical point of view, when 15% smaller or higher value than the default value of C_γ is used ($C_\gamma = 1.817$ and $C_\gamma = 2.458$, respectively), the value of Re_{tm} is accordingly shifted ($Re_{tm} = 34.45$ when $C_\gamma = 1.817$, and $Re_{tm} = 115.37$ when $C_\gamma = 2.458$). Consequently, C_γ is a key parameter which dictates the value of Re_{tm}. The limitation of the minimum turbulent Reynolds number can also be seen through the value of time scale ratio diagrams (Figure 5-1b) when different values of C_γ are used. The profiles in Figure 5-1b also indicate that the maximum acceptable value of τ^*/τ_{mix} is set to unity when $Re_t < Re_{tm}$.

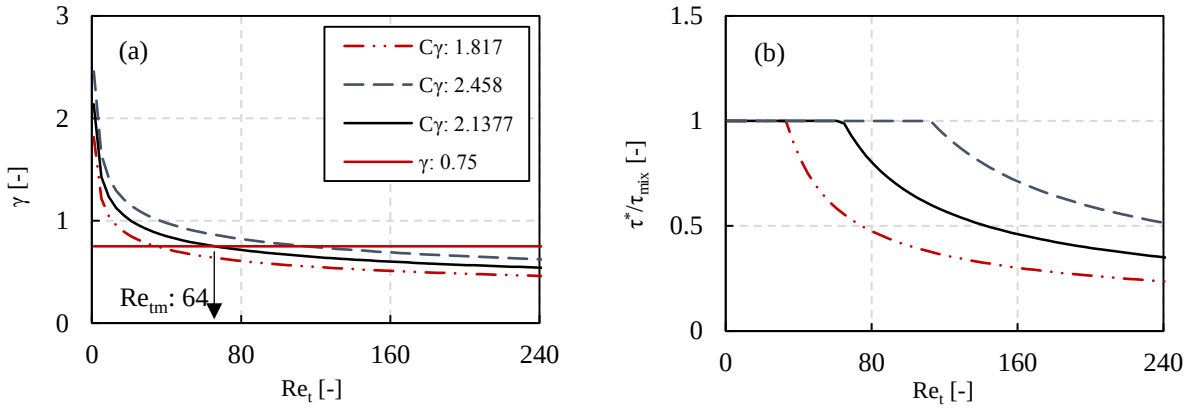

Figure 5-1. Effect of turbulent Reynolds number (Re_t) on (a) the value of (γ), and (b) the ratio of EDC time scale over the characteristic mixing time scale using the standard EDC.

The influence of Re_t on the EDC time scale coefficient (C_τ) is also studied. Based on Eq.(5-4), the mean reaction rate is also related to EDC time scale and consequently to the value of C_τ. The relation of C_τ to the characteristic mixing time scale, turbulent Reynolds number and fine structure volume coefficient, using Eq.(5-3), Eq.(5-6) and τ^*/τ_{mix}, can be expressed as follows:

$$\frac{\tau^*}{\tau_{mix}} = \frac{\gamma^2}{1-\gamma^3} \rightarrow C_\tau = \frac{C_\gamma^2(\tau_{mix}/T_t)}{1 - C_\gamma^3 Re_t^{-3/4}} \qquad (5\text{-}8)$$

Eq.(5-8) indicates a complex relationship between C_τ and the other parameters involved in EDC formulation (e.g., Re_t, τ_{mix}, etc.). Moreover, as explained previously, in the EDC reactor, chemical reactions proceed over EDC time scale, which is proportional to C_τ (see Eq.(5-3)). Thus, the effect of C_τ on the mean reaction rate is also evident on the value of Y_i^*. In other words, this parameter mathematically reflects the influence of chemical time scale on the reaction rate based on turbulent flow characteristics (e.g., τ_η).

A recent study of the present authors demonstrated that the predictions of EDC model can be improved by changing the model's coefficients for both weakly and highly turbulent flow conditions [27]. Particularly, in comparison with the standard EDC (i.e., EDC with the default values of C_γ and C_τ), the reported results indicated that the predictions significantly improved under weakly turbulent flow conditions when a lower value of C_γ was used. Moreover, while the standard EDC has been originally developed for highly turbulent flow conditions, better predictions were achieved when using a higher value of C_γ. Furthermore, at both weakly and highly turbulent condition, it was shown that using higher value of C_τ improved the predictions. In addition, the influence of C_γ on the predictions was found to be more pronounced than that of C_τ [27]. The main challenge is to develop a comprehensive physical expression of EDC coefficients that can be used regardless of the flow field turbulence conditions/level.

In the present study, in order to calculate the values of α and β in Eq.(5-1), we adopted turbulence intermittency in the inertial range of energy transfer using fractal modeling (FM) approach [43, 44]. It is considered that FM approach generates a vortex cascade which starts from a characteristic cell length scale (Δ) and ends at dissipative Kolmogorov length scale (η). Considering the inertial range of energy transfer from Δ to η, a relationship can be written as follows [45]:

$$\frac{E_\Delta}{T_\Delta} \approx N_\eta \frac{E_\eta}{\tau_\eta} \rightarrow \frac{(u_\Delta)^3}{\Delta} \approx N_\eta \vartheta \frac{u_\eta^2}{\eta^2} \tag{5-9}$$

where E_Δ and E_η represent the energy per unit mass at characteristic and Kolmogorov scales, respectively, ϑ is the molecular kinematic viscosity, u_η and η are Kolmogorov velocity and length scales, and N_η represents the number of locally generated dissipative scales. Introducing local Reynolds number on the basis of Δ as $(Re_\Delta = u_\Delta \Delta / \vartheta_\Delta)$, Eq.(5-9) can be re-written as

$$\frac{\eta}{\Delta} = N_\eta^{0.25} Re_\Delta^{-3/4} \left(\frac{\vartheta}{\vartheta_\Delta}\right)^{3/4} \left(\frac{u_\eta \eta}{\vartheta}\right)^{0.5} \tag{5-10}$$

where ϑ_Δ is the kinematic viscosity of surrounding fluid [44]. In Eq.(5-10), the term $\left(u_\eta \eta / \vartheta\right)$ is the Kolmogorov Reynolds number, which is equal to unity $\left(Re_\eta = 1\right)$. Giacomazzi et al. [45, 46] argued that N_η depends only on local Reynolds number and it is not dependent on the geometrical parameters of the fractal cascade. They also assumed a circular cross section to describe eddies in the fractal cascade and proposed a mathematical formulation for N_η as follows:

$$N_\eta = \pi^{-2/3} Re_\Delta \left(\frac{\vartheta}{\vartheta_\Delta}\right)^{-1} \tag{5-11}$$

Eq.(5-10) can be simplified using N_η from Eq.(5-11) and hence, another derivation of N_η can be written based on length scales as follows [46]:

$$\frac{\Delta}{\eta} = \pi^{1/6} Re_\Delta^{1/2} \left(\frac{\vartheta}{\vartheta_\Delta}\right)^{-1/2} \tag{5-12}$$

$$\frac{N_\eta}{\left(\Delta/\eta\right)^2} = \frac{\pi^{-2/3}}{\pi^{1/3}} \rightarrow N_\eta = \pi^{-1}\left(\frac{\Delta}{\eta}\right)^2 \quad (5\text{-}13)$$

As discussed previously, the original EDC cascade was developed based on turbulence intermittency (Eq.(5-1). The intermittency factor approximates the fraction of the volume filled with active eddies having a characteristic scale [43]. If it is assumed that fine structures represent those active eddies, the mass fraction occupied by fine structures as well as the ratio of fine structures velocity scale to the integral velocity scale can be written as follows [43]:

$$\gamma^* = \left(\frac{l^*}{l'}\right)^{3-D_c} \quad (5\text{-}14)$$

$$\frac{u^*}{u'} \sim \left(\frac{l^*}{l'}\right)^{\frac{D_c-2}{3}} \quad (5\text{-}15)$$

where D_c is an intermittency parameter which is commonly introduced as a fractal dimension [44]. While a value of D_c = 2.8 has been suggested in previous studies (e.g., [43, 47]), the mathematical methodology proposed by Giacomazzi et al. [44] is adopted in the present study to calculate it as $D_c = 1 + log(N_\eta)/log(\Delta/\eta)$.

The term $\left(\gamma^{*2/3}/\tau^*\right)$ in Eq.(5-5) represents the mass exchange rate of species i between a fine structure and its surrounding fluid [40, 48]. Assuming that the fine structure is located in constant energy regions, the coefficients $\gamma^{*2/3}$ and C_τ can be expressed, based on velocity scales using Eqs.(5-14) and (5-15), as follows [48, 11]:

$$\frac{\gamma^{*\frac{2}{3}}}{\tau^*} = 2\frac{u^*}{l^*}\gamma_\lambda^2 = \left(2\frac{u^*}{l^*}\right)\left(\frac{u^*}{u'}\right)^2 \quad (5\text{-}16)$$

$$\tau^* = 0.5\left(\frac{l^*}{u^*}\right) = 0.5\left(\frac{l^*}{l'}\frac{l'}{u'}\frac{u'}{u^*}\right) = 0.5T_t\gamma^{*\frac{1+\frac{2}{3}-\frac{D_c}{3}}{3-D_c}} \rightarrow C_\tau = \frac{\tau^*}{\tau_\eta} \tag{5-17}$$

$$\gamma_\lambda^2 \sim \left(\frac{u^*}{u'}\right)^2 \sim \left(\frac{l^*}{l'}\right)^{2\left(\frac{D_c-2}{3}\right)} \sim \gamma^{*\frac{2}{3}\left(\frac{D_c-2}{3-D_c}\right)} \tag{5-18}$$

where γ_λ is the fine structure volume fraction [48], and (l'/u') is estimated as turbulent time scale (T_t) [49]. As can be seen from Eqs.(5-13) to (5-18), all the introduced parameters (i.e., N_η, D_c, γ_λ^2, γ^* and τ^*) are a function of two main length scale ratios. That is, the ratio of the characteristic cell to Kolmogorov length scale (i.e., Δ/η) and the ratio of Kolmogorov to integral length scale (i.e., η/l'). Using RANS approach, it is plausible to assume that the characteristic length scale can be approximated by the integral length scale (i.e., $\Delta \sim l'$). Also, as discussed earlier, the fine structure length scale is of the order of the Kolmogorov scale (i.e., $l^* = \xi\eta$). Hence, considering the relationship between the integral and Kolmogorov scales via turbulent Reynolds number [23], it is possible to express all the aforementioned parameters as a function of Re_t as follows:

$$Re_t = \left(\frac{T_t}{\tau_\eta}\right)^2 = \left(\frac{l'}{\eta}\right)^{4/3} = \left(\frac{u'}{u_\eta}\right)^4 \tag{5-19}$$

$$N_\eta = \pi^{-1}Re_t^{3/2} \tag{5-20}$$

$$D_c = 1 + \frac{log\left(N_\eta\right)}{log\left({Re_t}^{3/4}\right)} \tag{5-21}$$

$$\gamma^* = \xi^{3-D_c}\left({Re_t}^{-3/4}\right)^{3-D_c} \tag{5-22}$$

The final description of the extended EDC model and the ratio of time scales can be written as follows:

$$\overline{R_i} = \frac{\overline{\rho}\gamma_\lambda^2}{(1-\gamma^*)\tau^*}\left(Y_i^* - \overline{Y_i}\right) = \frac{\overline{\rho}}{\tau_{mix}}\left(Y_i^* - \overline{Y_i}\right) \tag{5-23}$$

$$\frac{\tau^*}{\tau_{mix}} = \frac{\gamma_\lambda^2}{(1-\gamma^*)} = \frac{\gamma^{*\frac{2}{3}\left(\frac{D_c-2}{3-D_c}\right)}}{(1-\gamma^*)} \tag{5-24}$$

Similar to the standard EDC, we can introduce the term $\gamma_\lambda^2/\left((1-\gamma^*)\tau^*\right)$ as an average mass exchange rate between a fine structure and the computational cell. Hence, the term (τ^*/τ_{mix}) denotes the mass exchange rate coefficient. It is essential to re-investigate the upper limit of γ^* using the ratio of time scales (τ^*/τ_{mix}). Following the same strategy as that of the standard EDC, the limiting criteria is assumed as $(\tau^*/\tau_{mix}) < 1$. Figure 5-2 illustrates the influence of Re_t on D_c (Figure 5-2a), as well as the maximum limit value of γ^* (i.e., γ^*_{max}) using a different value of D_c (Figure 5-2b). According to Figure 5-2a, for flow regions of low turbulent Reynolds number, it can be seen that $D_c < 2.8$; whereas for flow regions with high turbulent Reynolds number, the profile of D_c tends toward the suggested value in literature (i.e., $D_c \approx 2.8$., see, e.g., [43, 47]). Figure 5-2b shows the diagrams of the ratio of time scales (i.e., τ^*/τ_{mix}) versus γ^* using different values of D_c. This figure clearly indicates that no acceptable value of τ^*/τ_{mix} can be achieved when $D_c < 2$. This figure also indicates that, for any value of D_c, γ^* reaches a particular maximum acceptable value. That is, based on the selected value of D_c $(2 < D_c < 2.8)$, the ratio of time scales can reach unity with a particular γ^* (e.g., $\gamma^*_{max} = 0$ for $D_c = 2$, while, $\gamma^*_{max} = 0.66$ for $D_c = 2.8$).

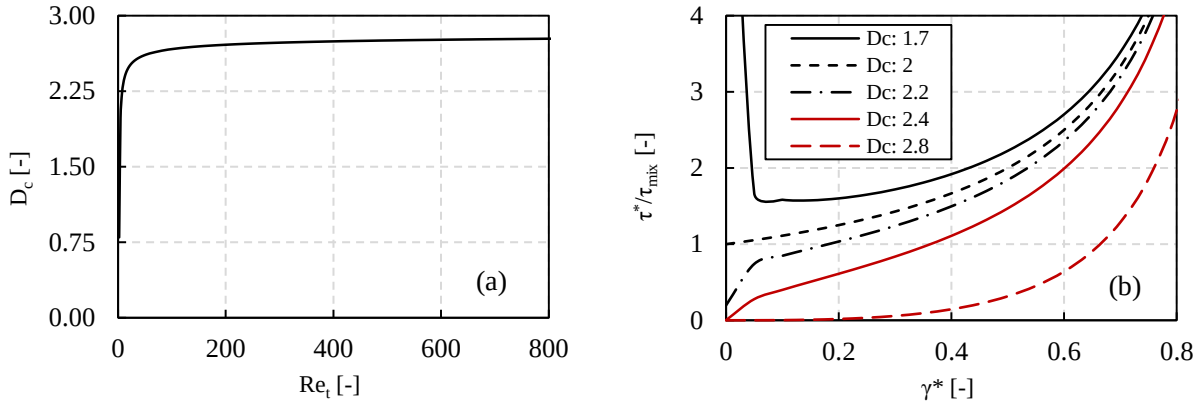

Figure 5-2. (a) Effect of turbulent Reynolds number (Re_t) on fractal dimension (D_c), and (b) effect of fractal dimension (D_c) on the ratio of EDC time scale over the characteristic mixing time scale.

5.4 Experimental and numerical setups

The main purpose of the present simulation is to compare the performance of the newly modified against standard EDC over a wide range of turbulent flow conditions (i.e., from weakly to highly turbulent flow conditions). To do so, different well-documented jet flames are chosen for the numerical simulation. The turbulent H_2/N_2/air diffusion jet flame investigated by Meier et al. [28] is selected to study weakly turbulent flow condition (referred here to as case A). For this flame, a fuel with a composition of 75% H_2 and 25% N_2 by volume is supplied with a velocity of 14.1 m/s through a nozzle with a diameter of d_j = 8 mm (Re_j = 3100). The fuel nozzle is surrounded by a co-axial pipe of D_{co} = 140 mm which supplies dry-air coflow with an exit velocity of 0.3 m/s. More details about the burner and the jet flame can be found in [28]. The piloted methane/air jet flames of Barlow and Frank, known as flames B, D and F [29], are selected to study flow conditions of moderate turbulence (i.e., flame B, referred here to as case B), high turbulence (i.e., flame D, referred here to as case C), and very high turbulence level nearing global extinction condition above the pilot region (i.e., flame F, referred here to as case D). The burner for these flames consists of a nozzle of d_j = 7.2 mm, which supplies fuel with a composition of 25% CH_4 and 75% air by

volume at an exit velocity of 18.2 m/s (case B, Re_j = 8200), 49.6 m/s (case C, Re_j = 22400) and 99.2 m/s (case D, Re_j = 44800). The fuel nozzle is surrounded by a co-axial cylinder of D_{pilot} = 18.2 mm, which supplies a pilot mixture of C_2H_2, H_2, CO_2, N_2 and air, having the same enthalpy and equilibrium composition as methane/air at an equivalence ratio 0.77 [29]. The piloted mixture is supplied with an exit velocity of 6.8 m/s (case B), 11.4 m/s (case C), and 22.8 (case D), at 1880 K. Also, the air coflow exits at a mean velocity of 0.9 m/s and 291 K. More details about the burner and these jet flames can be found in [2, 29, 50, 51]. Additional simulations are also carried out (referred here to as case E) in order to predict fuel bound nitrogen emissions (as the main source of NO_x emissions in grate-firing biomass combustor/furnace). To do so, a diffusion $CO/H_2/N_2$ jet flame doped with NH_3 is selected [30]; where the burner consists of a nozzle of d_j = 3.2 mm, which supplies fuel of a composition of 39.7% CO, 29.9% H_2, 0.7% CH_4 and 29.7% N_2 by volume at an exit velocity of 54.6 m/s (Re_j = 8500). The air coflow is supplied at an exit velocity of 2.4 m/s. While the experiment was performed with different NH_3 additions, only the case doped with 0.8% NH_3 is selected in the present study. More details about the burner and the jet flame can be found in [30, 6].

The numerical cases are simulated using the commercial code ANSYS FLUENT 15.0. The pressure-based coupled algorithm is used as the velocity-pressure coupling method. Second order upwind scheme is used for all conservation equations. All simulations are carried out using two-dimensional (2D) axisymmetric domain along with structured grids. The computational domain is extended from the fuel nozzle exit plane up to 90 d_j downstream in the axial direction (120 d_j for case E), and 25 d_j in the radial direction. For all flames except case E, the grid consists of 20,000 elements, with local increase in grid resolution close to the nozzle exit (case E is simulated using 10,000 elements with the same strategy of grid resolution as the other flames). While the

simulations are also performed with one step of grid refinement for high temperature regions (from ~800 K to ~2500 K), it is observed that grid refinement shows insignificant change in the simulations predictions for all cases. To increase the CPU-intensive treatment of the detailed chemistry, the In-Situ Adaptive Tabulation (ISAT) algorithm [52] is employed with an ISAT error tolerance of 10^{-4}. It should be mentioned that, the concentration of species is found to remain unchanged using ISAT error tolerance $<10^{-4}$. Velocity inlet conditions are specified for fuel jet, pilot jet and air coflow inlet. The pressure outlet condition is used for outflow boundary. Table 5-1 reports the boundary conditions used in all cases.

Table 5-1. Details of the boundary conditions for cases A-E

Case	Coflow		Pilot		Fuel (composition in %volume)			
	V [m/s]	T [K]	V [m/s]	T [K]	V [m/s]	T [K]	Re_j [-]	$CH_4/CO/N_2/O_2/H_2$
A	0.3	300	N/A	N/A	14.1	300	3100	-/-/25/-/75
B	0.9	291	6.8	1880	18.2	294	8200	25/-/59.25/15.75/-
C	0.9	291	11.04	1880	49.6	294	22400	25/-/59.25/15.75/-
D	0.9	291	22.8	1880	99.2	294	44800	25/-/59.25/15.75/-
E	2.4	294	N/A	N/A	54.6	294	8500	0.7/39.7/29.7/-/29.9

Two chemical kinetic mechanisms are used. For cases A and E, a detailed kinetic scheme of combustion CO/H_2 mixture was used. This chemical mechanism is particularly designed to study the role of NH_3 chemistry on the formation of NO_x in CO/H_2 flames [53, 54, 55]. For cases B-D, DRM-22 [56] is employed as a detailed kinetic scheme. The choice of this mechanism is motivated by its substantially less computational cost compared to more detailed kinetic schemes such as GRI-Mech 3.0 [57]. However, a comparison between the predictions achieved using reduced chemical scheme (i.e., DRM-22) and detailed chemistry scheme (i.e., GRI-Mech 3.0) is performed on the simulation of case B flame using the standard EDC. Figure 5-3 shows the profiles of temperature (Figure 5-3a), CO_2 mass fraction (Figure 5-3b), OH mass fraction (Figure 5-3c) and CO mass fraction (Figure 5-3d). As can be clearly seen in this figures, the difference between the two mechanisms is negligible in terms of temperature and CO_2 profiles, and it is reasonably

acceptable for OH and CO mass fractions. Thus, as the DRM-22 is capable of reproducing experimental measurements with an adequate accuracy and less computational cost, the use of this mechanism is justified for further simulations of cases B-D.

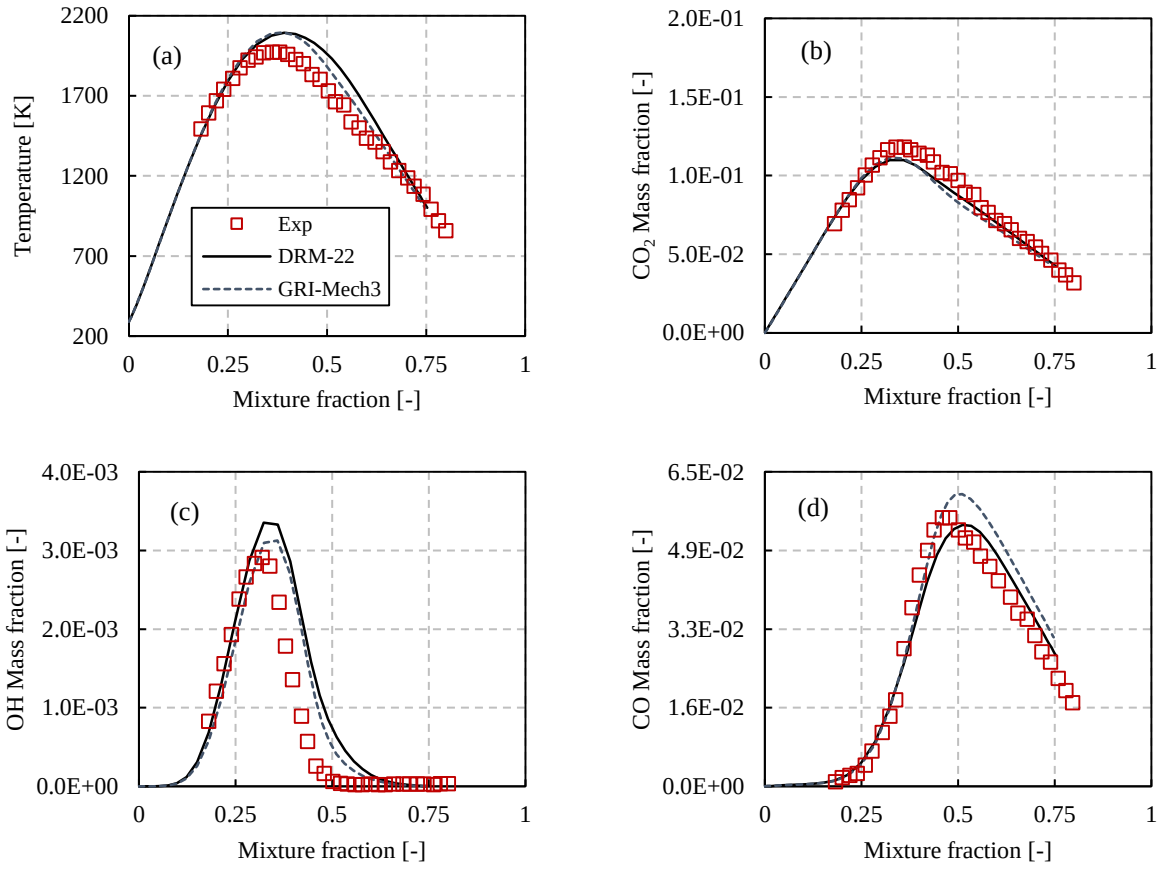

Figure 5-3. Effect of chemical mechanism on the accuracy of the predictions of (a) temperature, (b) CO_2 mass fraction, (c) OH mass fraction and (d) CO mass fraction. These are the results of the simulation of moderate turbulent jet flame (i.e., case B) in the radial direction at x/d_j= 15 using the standard EDC.

In order to implement the newly modified EDC into the ANSYS FLUENT, the required parameters (e.g., D_c, γ_λ^2, γ^*, τ^*, etc.) are calculated based on local values of Re_t, T_t and τ_η, using User-Defined Functions (UDF). Another UDF is also used to calculate the value of Y_i^*, and later on, the rate of reaction for each species, which is calculated from Eq.(5-23), is applied as a source term for each species transport equation.

5.5 Results and discussion

The simulation results of cases A through E are presented below. As mentioned above, cases A through D are for examining the performance of the modified EDC in simulating reacting flow conditions ranging from weakly turbulent (i.e., case A) to highly turbulent flow condition including those nearing global extinction (i.e., case D). Also, the performance of the modified EDC on the prediction of both slow-forming thermal NO_x, as well as NO_x concentration as the result of dominantly fuel bound nitrogen sources, which is one of the main source of gas emissions in grate firing biomass furnaces [3, 6], is examined in case E.

As discussed above, the fine structure length scale is assumed to be on the order of Kolmogorov length scale as ($\xi\eta$). To investigate the effect of the estimated value of ξ on the predictions, several simulations are carried out in cases A and D, respectively, as they represent weakly and highly turbulent flow conditions. The value $\xi = 1.75$ for weakly turbulent flow condition, and $\xi = 3.15$ for highly turbulent flow condition, ae found to provide overall satisfactory predictions. In the simulation of case B, a weighting function is used to account for both weakly and highly turbulent flow conditions. That is, in the regions of low turbulent Reynolds number, ξ is set approximately to 1.75, and in the region of high turbulent Reynolds number, ξ is set approximately to 3.15. To do so, a function similar to the proposed weighting function by Shiehnejadhesar et al. [2] is employed as follows:

$$\xi(Re_t) = \frac{w}{w + Re_t} 1.75 + \frac{(1/w) Re_t}{1 + (1/w) Re_t} 3.15 \qquad (5\text{-}25)$$

where w is the weighting coefficient. The first term on the right-hand side of Eq.(5-25) is approximately 1.75 at low Re_t, and zero at high Re_t. Similarly, the second term on the right-hand

side of Eq.(5-25) approaches approximately zero at low Re_t, and 3.15 at high Re_t. Figure 5-4a shows the profiles of $(w/(w+Re_t))$ as the low weighting factor, and $((1/w)Re_t/(1+(1/w)Re_t))$ as the high weighting factor, for different values of w. As this figure shows, the value of w dictates the power of the low and high weighting factors at moderate turbulent Reynolds number. The value of $w = 50$ is found to provide overall satisfactory predictions for case B. It is important to mention that the presented results for all studied cases (i.e., cases A through E) are achieved using Eq.(5-25) with $w = 50$.

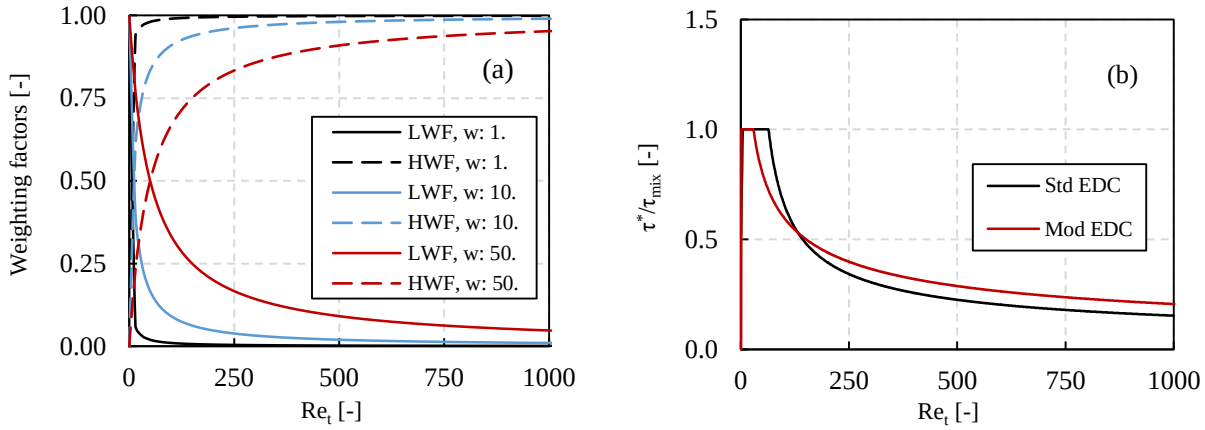

Figure 5-4. Effect of turbulence Reynolds number on (a) the low weighting factors (LWF) and high weighting factors (HWF) by using different weighting coefficient (w), and on (b) the ratio of EDC time scale over the characteristic mixing time scale using both the standard and modified EDC.

Figure 5-4b compares the profiles of τ^*/τ_{mix} for the standard and modified EDC approach. The profile of time scales ratio of the modified EDC was computed using Eq.(5-25) as discussed above. It can be seen from the profiles in Figure 5-4b that, compared to the standard EDC, at low and relatively moderate turbulent Reynolds number ($Re_t < 135$), the modified EDC exhibits smaller time scales ratio, whereas it produces larger time scales ratio for $Re_t > 135$. In the formulation of the standard EDC (i.e., Eq.(5-5)), larger and lower values of τ^*/τ_{mix} are attributed to, respectively, larger and smaller values of γ^*. Therefore, achieving lower value of τ^*/τ_{mix} with the modified

EDC is similar to using a smaller value of γ^* with the standard EDC; while larger value of τ^*/τ_{mix} with the modified EDC is similar to using larger value of γ^* with the standard EDC. It was reported that the same trend of γ^* was found to improve the predictions of temperature and species concentration [27]. That is, by lowering the size of γ^* via changing the value of its coefficient C_γ, better predictions can be achieved for the flow case of weakly turbulent Reynolds number; whereas better predictions can be produced by increasing the value of γ^* via changing C_γ for flow case with highly turbulent Reynolds number [27].

5.5.1 Weakly turbulent flow condition (case A)

A comparison between the experimental and numerical radial profiles of mixture fraction (Figure 5-5a), major species mass fractions (O_2 in Figure 5-5b and H_2O in Figure 5-5c), and temperature and NO mass fraction (Figure 5-5d) are presented here for case A. All profiles are taken at an axial position of $x/d_j = 5$, where the value of the mixture fraction is calculated based on Bilger's formula [58]. When compared with the experimental measurements, the predictions adequately capture the trend of mixture fraction, temperature and species. Mixture fraction close to the centerline of the domain is predicted better by the modified EDC, while the standard EDC shows better prediction of the mixture fraction away from the centerline. The profiles of mass fractions and temperature (Figure 5-5b-d) show that the trends of measured quantities are well-predicted using both EDC approaches. However, the peak values of temperature and H_2O mass fractions are unsatisfactorily predicted by both standard and modified EDC. Nonetheless, despite the discrepancies between the predictions and experimental measurements, the modified EDC shows improvement in the predictions compared to the standard EDC. The modified EDC exhibits better quantitative predictions of temperature, O_2 and H_2O mass fraction profiles (see Figure 5-5b-d). In addition, as can be seen in Figure 5-5d, while the standard EDC clearly under-predicts NO

mass fraction, the peak value of NO concentration is significantly improved using the modified EDC.

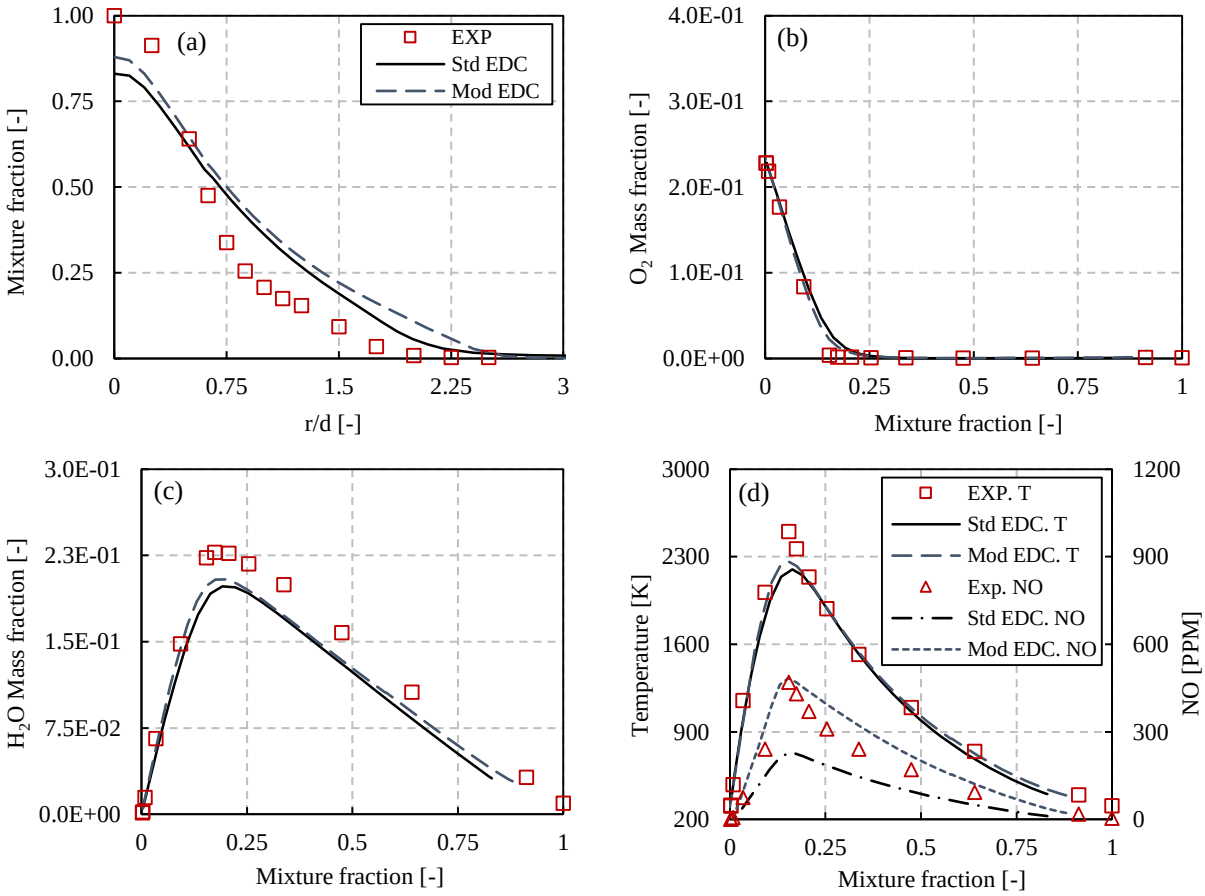

Figure 5-5. Radial profiles of (a) mixture fraction, (b) O_2 mass fraction, (c) H_2O mass fraction, (d) temperature and NO mass fraction. These are the results of the simulation of weakly turbulent jet flame (i.e., case A) at $x/d_j = 5$ using both the standard and modified EDC.

5.5.2 Moderate turbulent flow condition (case B)

The predictions of the radial profiles of temperature and mass fractions, and their comparison with published experimental data are presented in Figure 5-6. All profiles are taken only at an axial position of $x/d_j = 15$ based on the available published experimental measurements [29]. Note that no information about the measurements of the radial distribution of mixture fraction was reported in [29], and consequently no comparison with the predictions was performed in physical coordinate. Figure 5-6 shows that, for both EDC approaches (standard and modified), the

predictions are in reasonable agreement with their experimental counterparts, where all predictions adequately follow the trends of their experimental measurements. However, both the standard and modified EDC under-predict the maximum mixture fraction. This is believed to be due mainly to the adopted turbulence model (e.g., [59]). According to Figure 5-6a and e, the peak values of temperature and OH mass fraction are slightly over-predicted by the standard EDC. While these over-predictions were attributed to the influence of DRM-22 kinetic mechanism (e.g., [59]), a comparative study between DRM-22 and GRI-Mech 3.0 showed that the standard EDC predicts identical peak values of temperature and nearly similar OH radicals when using both kinetic mechanisms (see Figure 5-3). By comparing the predictions between the modified and standard EDC, the improvement in the predictions of the modified EDC is evident especially for peak values of temperature and H_2 profiles (Figure 5-6a and b, respectively). However, Figure 5-6e and f show that the modified EDC under-predicts CO and OH mass fractions when compared to those of the standard EDC. Also, the difference between the predictions of standard and modified EDC of major species (i.e., O_2 in Figure 5-6c and CO_2 in Figure 5-6d) is insignificant.

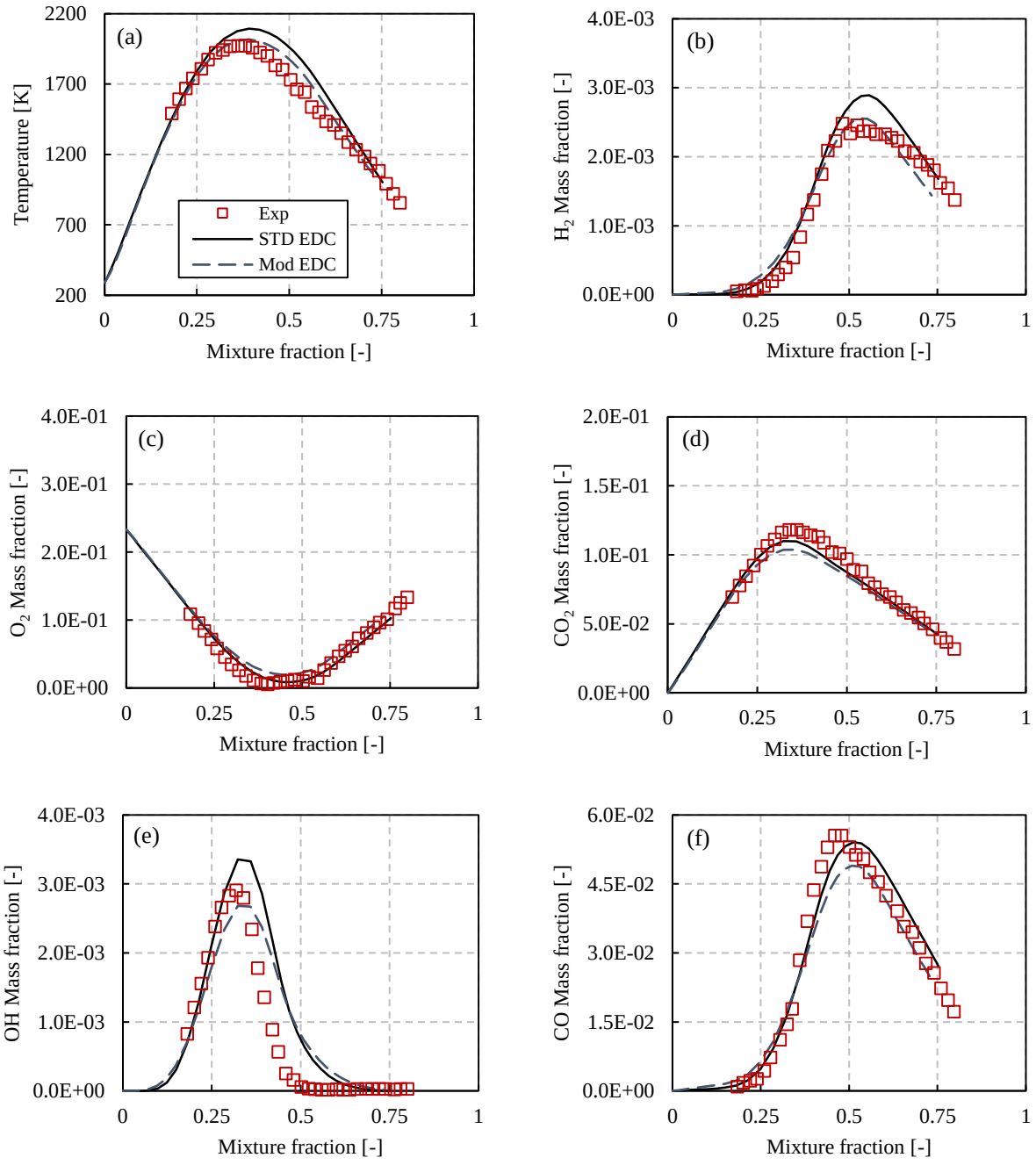

Figure 5-6. Radial profiles of (a) temperature, (b) H_2 mass fraction, (c) O_2 mass fraction, (d) CO_2 mass fraction, (e) OH mass fraction and (f) CO mass fraction. These are the results of the simulation of moderate turbulent jet flame (i.e., case B) at x/d_j= 15 using both the standard and modified EDC.

5.5.3 Highly turbulent flow condition (case C)

Figure 5-7 shows a comparison between the predictions and experiments of the mean mixture fraction at radial positions of x/d_j=15 (Figure 5-7a) and x/d_j=30 (Figure 5-7b). Figure 5-7a shows that both EDC models predict reasonably well the trend of the experimental radial distribution of mixture fraction. However, Figure 5-7 shows that, compared to the experimental measurement, the mixture fraction is under-predicted close to the centerline (for $r/d_j < 1$ in Figure 5-7a and $r/d_j <$ 1.5 in Figure 5-7b), and over-predicted away from the centerline by both models. Nonetheless, Figure 5-7a shows that the modified EDC slightly improves the prediction of the mixture fraction, especially its peak value close to the centerline (i.e., $x/d_j \approx 0$).

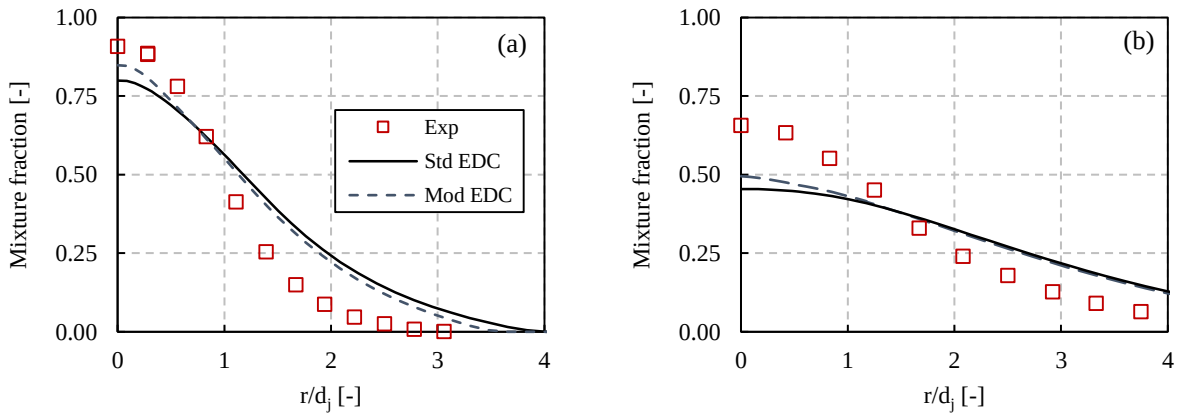

Figure 5-7. Radial profiles of mixture fraction at (a) x/d_j=15, and (b) x/d_j=30 of the highly turbulent jet flame case (i.e., case C).

Figure 5-8 shows a comparison of the predictions of the radial profiles of temperature (Figure 5-8a), and mass fraction of H_2 (Figure 5-8b), O_2 (Figure 5-8c), CO_2 (Figure 5-8d), OH (Figure 5-8e) and CO (Figure 5-8f) between the standard and modified EDC and their counterparts published experimental data at x/d_j=15. These figures show that while the trends of the predictions adequately follow those of their experimental counterparts, the modified EDC produces a significant improvement in the predictions. Compared to the standard EDC, its modified version showed slight improvement in the predictions of the peak value of temperature (Figure 5-8a) and

major species (O_2 in Figure 5-8c and CO_2 in Figure 5-8d). Moreover, the performance of the modified EDC is more pronounced in the predictions of intermediate species (H_2 in Figure 5-8b, OH in Figure 5-8e, and CO in Figure 5-8f) where their peak values are significantly improved. Nevertheless, while the radial profile of OH mass fraction is clearly better predicted by the modified EDC, its peak value is still over-predicted.

Figure 5-9 shows a comparison of the predictions of the radial profiles of temperature (Figure 5-9a), and mass fraction of H_2 (Figure 5-9b), O_2 (Figure 5-9c), CO_2 (Figure 5-9d), OH (Figure 5-9e) and CO (Figure 5-9f) between the standard and modified EDC and their counterparts published experimental data at x/d_j=30. These figures reveal that none of the two EDC models can quantitatively reproduce the distribution of the experimental measurements in high mixture fraction region, which is mainly due to the under-prediction of the mixture fraction field close to the centerline at x/d_j =30 (see Figure 5-7b). According to the profiles of temperature (Figure 5-9a), O_2 mass fraction (Figure 5-9c) and CO_2 mass fraction (Figure 5-9d), both the standard and modified EDC approaches produce almost similar predictions with a slight improvement by the modified EDC. The profiles of H_2 (Figure 5-9b) and CO (Figure 5-9f) mass fractions show that, when compared to the experimental measurements, the modified EDC shows better predictions and also significantly improves the trends and peak values of the profiles. Moreover, the profiles in Figure 5-9e show that the distribution of OH mass fraction is captured better by the modified EDC. Furthermore, while both the standard and modified EDC approaches over-predict OH concentration (Figure 5-9e), the modified EDC shows a significant improvement in the prediction of the peak value of OH mass fraction.

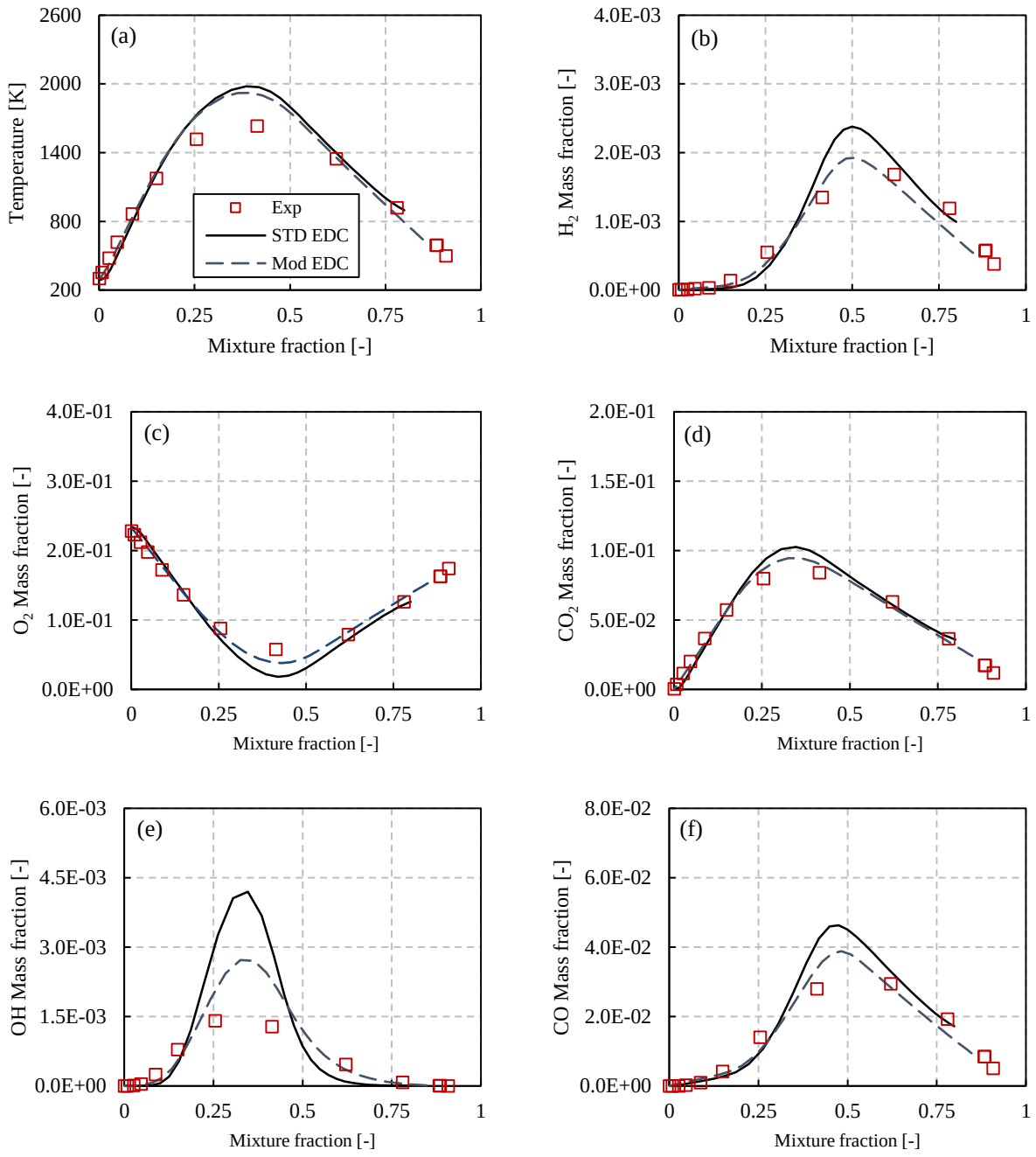

Figure 5-8. Radial profiles of (a) temperature, (b) H_2 mass fraction, (c) O_2 mass fraction, (d) CO_2 mass fraction, (e) OH mass fraction and (f) CO mass fraction. These are the results of the simulation of highly turbulent jet flame (i.e., case C) at x/d_j =15 using both the standard and modified EDC.

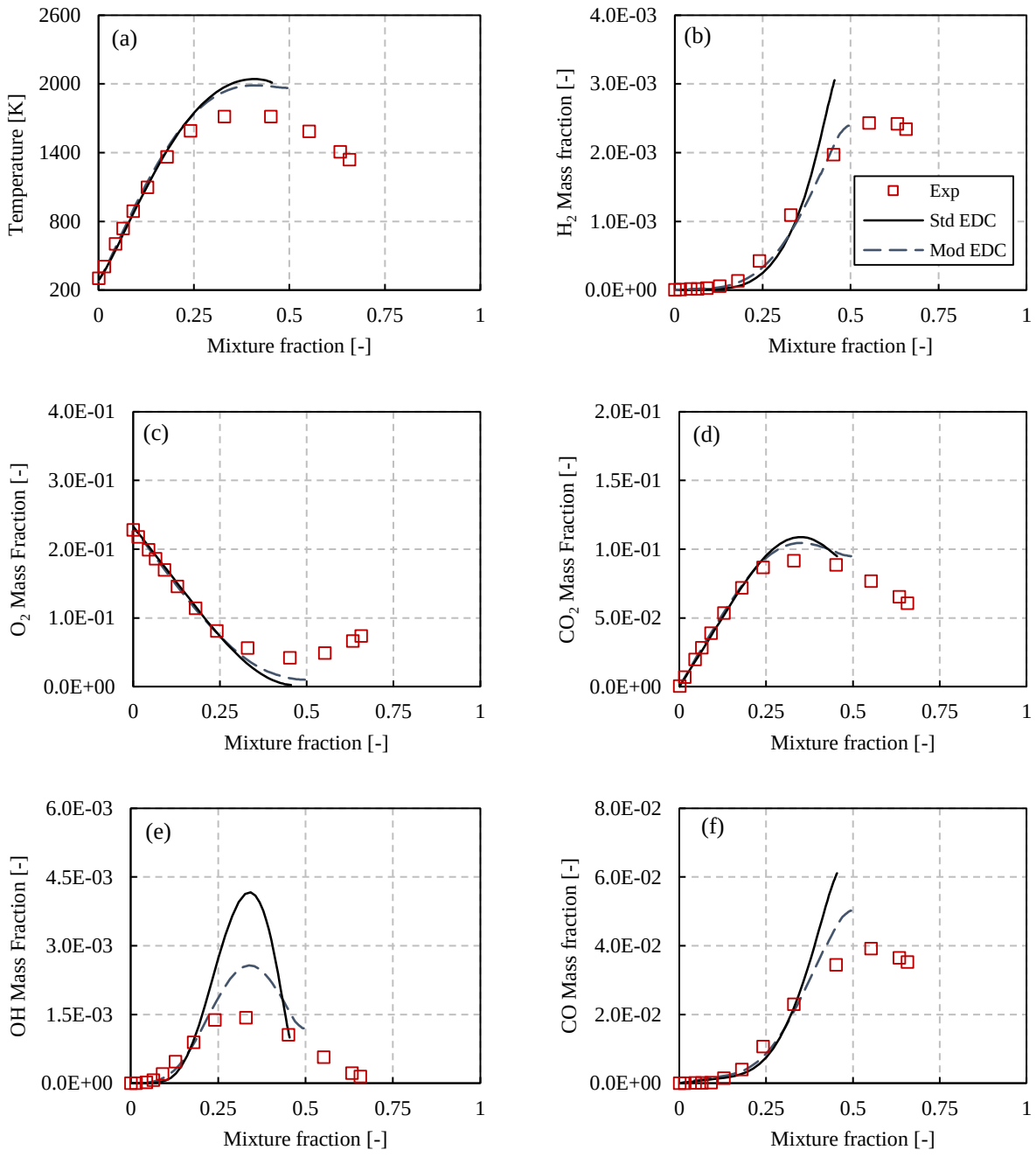

Figure 5-9. Radial profiles of (a) temperature, (b) H_2 mass fraction, (c) O_2 mass fraction, (d) CO_2 mass fraction, (e) OH mass fraction and (f) CO mass fraction. These are the results of the simulation of highly turbulent jet flame (i.e., case C) at x/d_j= 30 using both the standard and modified EDC.

5.5.4 Highly turbulent flow condition near global extinction (case D)

Figure 5-10 shows a comparison of the predictions of the mean mixture fraction, at radial positions of x/d_j=15 (Figure 5-10a) and x/d_j=30 (Figure 5-10b), between the standard and modified EDC and the experimental measurements. It is clear that both EDC models can reasonably reproduce qualitatively the measured mixture fraction. However, while both the standard and modified EDC exhibit almost similar predictions of the mixture fraction at x/d_j=15 (Figure 5-10a), the modified EDC predicts far better, quantitatively and qualitatively, of the mixture fraction at x/d_j = 30.

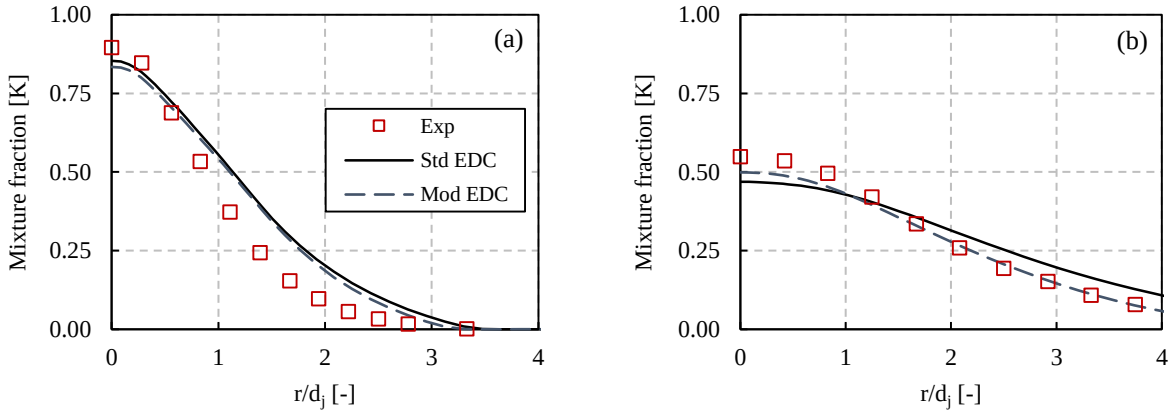

Figure 5-10. Radial profiles of mixture fraction at (a) x/d_j=15, and (b) x/d_j=30 for the highly turbulent jet flame case (i.e., case D).

Figure 5-11 shows a comparison between the predictions of the radial profiles of temperature (Figure 5-11a), and mass fraction of H_2 (Figure 5-11b), O_2 (Figure 5-11c), CO_2 (Figure 5-11d), OH (Figure 5-11e) and CO (Figure 5-11f) at x/d_j=15 between the modified and standard EDC and their experimental counterparts. Similarly to Figs. 5-8a-f, the profiles in Figs. 5-11a-f show that, compared with the experiments, the radial profiles are adequately captured by both models. This figure reveals significant improvements in the trends of these profiles, as well as their peak values predicted by the modified EDC. These improvements are more pronounced for the profiles of H_2 (Figure 5-11b) and CO (Figure 5-11f) mass fractions.

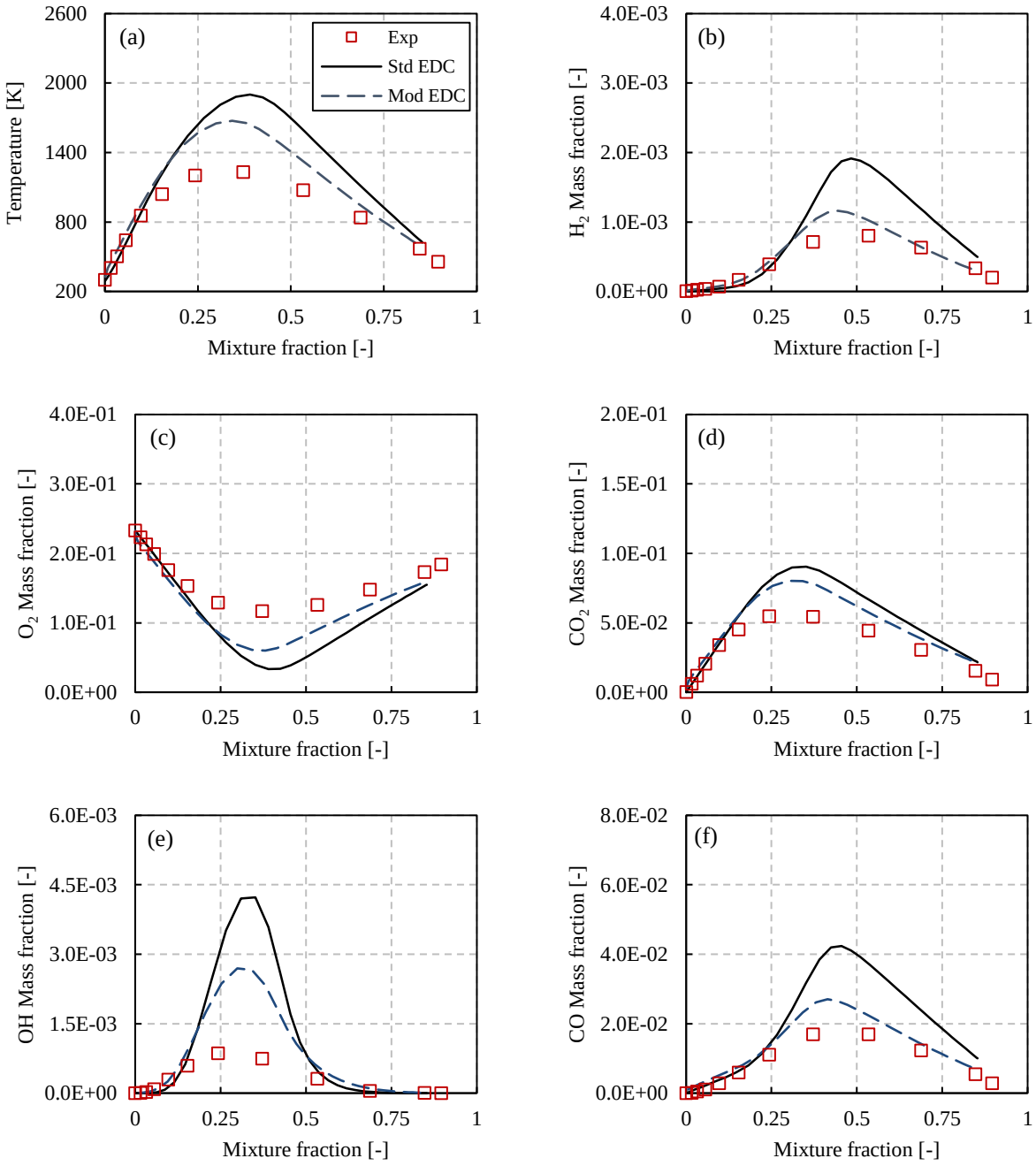

Figure 5-11. Radial profiles of (a) temperature, (b) H2 mass fraction, (c) O2 mass fraction, (d) CO2 mass fraction, (e) OH mass fraction and (f) CO mass fraction. These are the results of the simulation of highly turbulent jet flame (i.e., case D) at x/dj= 15 using both the standard and modified EDC.

Figure 5-12 presents a comparison of the predictions of the standard and modified EDC with their experimental counterparts, at x/d_j=30, of the radial profiles of temperature (Figure 5-12a), and

mass fraction of H_2 (Figure 5-12b), O_2 (Figure 5-12c), CO_2 (Figure 5-12d), OH (Figure 5-12e) and CO (Figure 5-12f). Similar to the results of case C (Figs. 5-9a, c and d), both the standard and modified EDC produce similar trends of predictions of temperature (Figure 5-12a), O_2 mass fraction (Figure 5-12c) and CO_2 mass fraction (Figure 5-12d). Moreover, similar to what is observed in case C, the modified EDC produces better predictions, both qualitatively and quantitatively (i.e., the trend of the predictions and their peak values), of H_2 mass fraction (Figure 5-12b) and CO mass fraction (Figure 5-12f). Furthermore, the modified EDC improves the predictions of the profile and peak value of OH mass fraction (Figure 5-12e), similar to what is seen in case C (Figure 5-9e). Comparing the predictions between the two EDC approaches, shown in Figs 5-5 to 5-12, it can be concluded that the modified EDC exhibits quantitative and qualitative improvements in the predictions (i.e., both peak values and trends of the temperature and species concentrations) at low to moderate turbulent flow conditions. However, when the level of turbulence increases up to near flame extinction (case D), the model produces qualitatively better improvement in the trends of profiles than the peak values.

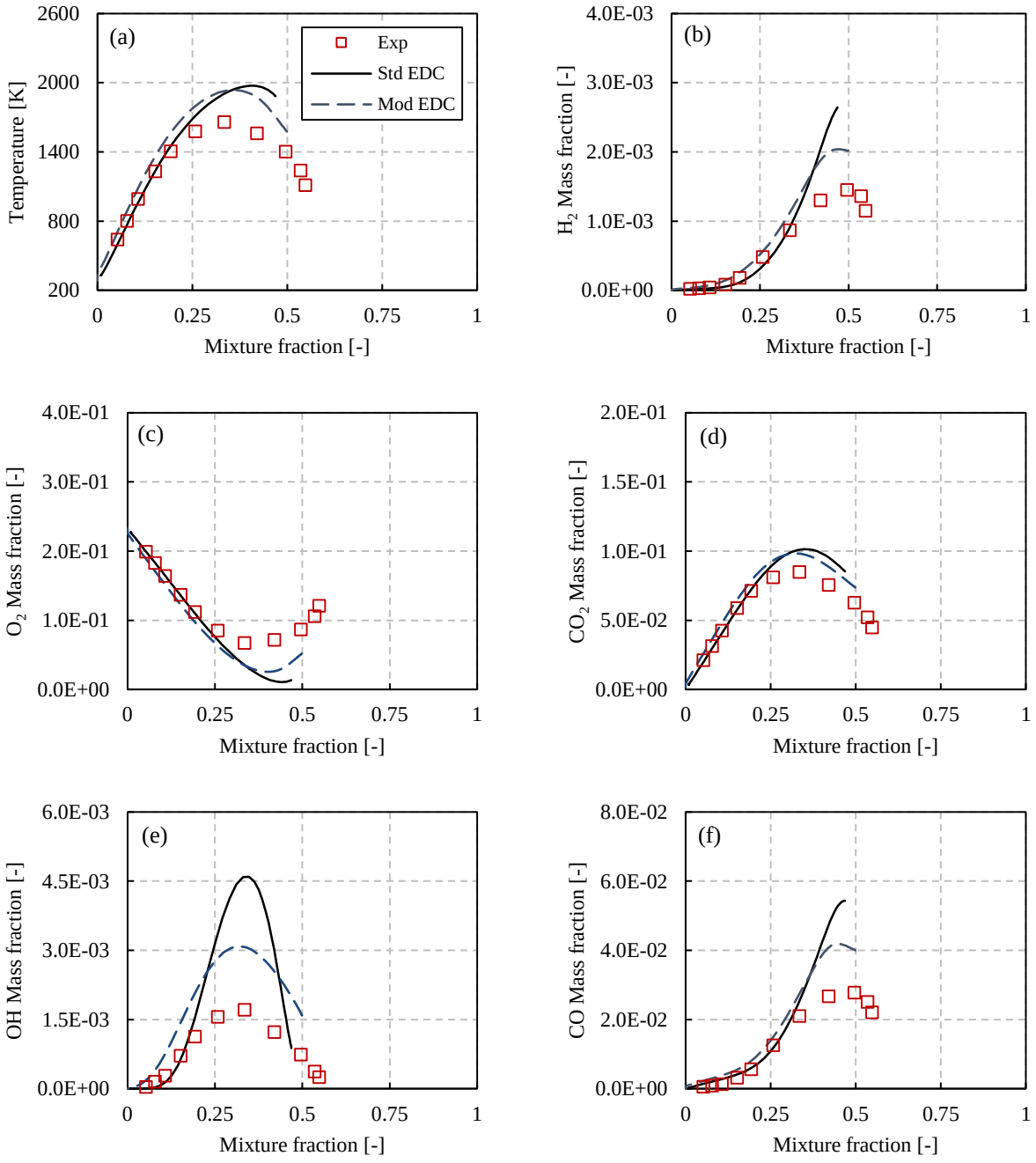

Figure 5-12. Radial profiles of (a) temperature, (b) H_2 mass fraction, (c) O_2 mass fraction, (d) CO_2 mass fraction, (e) OH mass fraction and (f) CO mass fraction. These are the results of the simulation of highly turbulent jet flame (i.e., case D) at x/d_j=30 using both the standard and modified EDC.

5.5.5 Discussion

According to Figs. 5-5 to 5-12, the predictions of both the standard and modified EDC show some level of discrepancies with their counterparts' experimental measurements. A possible reason for the discrepancy might be related to the poor prediction of the mixing field due to the inability of the adopted turbulence model [59]. This aspect has only been assessed here in terms of the mean mixture fraction field; however, the influence of the adopted turbulence model on the mixing field (i.e., velocity and turbulence fields) has not been examined as it is beyond the scope of the present study. Another possible reason might be related to the predictions inaccuracy of the reactant concentrations (e.g., O_2) and consequently the mixture fraction [60]. For instance, in the case of a weakly turbulent flow condition, according to Figure 5-5a, the mean mixture fraction is over-predicted in most flow regions between ($0.75 < r/d_j < 2.5$) by both EDC approaches. Depending on the reactions conditions, this can shift the kinetic reactions from stoichiometric to fuel rich, or from fuel lean to stoichiometric conditions. For instance, in case C, the predictions show lower concentration of O_2 (i.e., higher amount of O_2 consumption in Figure 5-8c), and accordingly higher temperature peak value (Figure 5-8a), which could be the results of shifting the kinetic reaction from lean to stoichiometric condition. The adopted chemical kinetic mechanism can also be another source of discrepancy between the predictions and their counterparts' measurements. As discussed in [61], DRM-22 has been developed for high temperature applications, and therefore, it might not be suitable/accurate for low temperature applications. This could be the conditions for case D (Figs.5-10 to 5-12), which has lower peak temperatures compared to other cases. Moreover, as explained comprehensively in [59], the endothermic thermal dissociation of CO_2 to CO yields the production of O atoms, which, in turn, produces HCCO at temperatures greater than 1400 K. However, with DRM-22, the HCCO radical is not considered and, therefore, the produced O atoms

from the aforementioned dissociation mechanism may participate in one the following chemical reactions [59]:

$$\begin{cases} CH_4 + O \rightarrow CH_3 + OH \\ CH_3 + O \rightarrow CH_2O + H \\ CH_2O + O \rightarrow HCO + OH \end{cases} \quad (5\text{-}26)$$

This may also be one of the reasons why the OH peak value is over-predicted, especially for cases C and D (Figs 5-8e, 5-9e, 5-11e and 5-12e). However, it is clear from the profiles of CO_2 and CO concentrations (Figs. 5-8d,f, 5-9d,f, 5-11d,f and 5-12d,f) that, while both the standard and modified EDC produced similar predictions of CO_2, the prediction of CO significantly improved, and consequently the under prediction of OH concentration by the modified EDC might be caused by the lower presence of O atoms due to the improvement in CO prediction (e.g., less dissociation of CO_2 to CO as shown in Figs. 5-8d,f, 5-9d,f, 5-11d,f and 5-12d,f). Another source of discrepancy between the predictions and their experimental counterparts might be related to the inability of the RANS/EDC approach to account for local temperature fluctuations, which is believed to result in inaccurate predictions of temperature and intermediate species concentrations [62, 59].

Figure 5-13 shows the predictions of the standard and modified EDC of the radial profiles of Re_t (Figs 5-13a-c, for cases A, B and C, respectively), τ^*/τ_{mix} (Figs 5-13d-f, for cases A, B and C, respectively), and the value of EDC time scale coefficient, C_τ, (Figs 5-13g-i, for cases A, B and C, respectively). These predictions are taken at an axial location of $x/d_j = 5$ for case A, and at $x/d_j = 15$ for cases B and C. It has been reported that turbulence characteristics, such as Re_t, might be quite weakly influenced by changes in EDC approach (standard or modified) [23]. However, the profile of Re_t in Figs. 5-13a-c show that, when the level of turbulence is low, the modified EDC produces different value of Re_t compared to the standard EDC (Figure 5-13a). However, the

profiles in Figs 5-13b and c clearly show that, for moderate to highly turbulent flow conditions, the predicted radial distribution of Re_t is nearly similar for both EDC models (case B in Figure 5-13b), and almost identical for case C (Figure 5-13c). This suggest that the characteristics of the turbulent field are more affected by the combustion model at low turbulent flow than at high turbulent flow conditions.

The radial distributions of τ^*/τ_{mix} are shown in Figs. 5-13d-f. As already mentioned above, within any region for which $Re_t < Re_{tm}$, the ratio of time scales reaches its maxima ($\tau^*/\tau_{mix} = 1$). According to Figs. 5-13d-f, the limitation of $\tau^*/\tau_{mix} = 1$ arises for all studied cases when the standard EDC is used; whereas this limitation happens only for weakly turbulent flow condition (case A) with the modified EDC. Figure 5-13d shows that, for flow regions with low turbulent Reynolds number, the overall τ^*/τ_{mix} of the modified EDC is lower than that of the standard EDC. This is expected according to Figure 5-4b that, for any $Re_t < 135$, the modified EDC has a lower value of τ^*/τ_{mix} compared to the standard EDC. The lower value of τ^*/τ_{mix} achieved with the modified EDC in weakly turbulent flow region is similar to that of the standard EDC when adopting smaller γ^* via using smaller C_γ (Eq.(5-6)) as reported in previous studies (e.g., [27, 23]). The profiles in Figure 5-13e show that, for moderate turbulent flow condition (case B) away from the centerline and low turbulence region (i.e., $2 < r/d_j < 4$), both models show almost similar values of τ^*/τ_{mix}. At highly turbulent flow condition (case C), the profiles in Figure 5-13f show that, compared to the standard EDC, the modified EDC yields slightly larger value of τ^*/τ_{mix}, which is expected according to the diagram in Figure 5-4b. The larger value of τ^*/τ_{mix}, achieved by the modified EDC in highly turbulent flow region, is similar to employing larger γ^* when using larger C_γ with the standard EDC formulation (Eq.(5-6)), as indicated in the literature for this flow condition (e.g., [27, 5]).

The radial distribution of C_τ is shown in Figs. 5-13g-i. The standard EDC has a constant value of $C_\tau = 0.4083$. However, the radial profiles of C_τ in Figs. 5-13g-i show that, when the modified EDC is used, C_τ becomes no longer a constant. Moreover, C_τ reaches its minima in the flow regions where Re_t achieves its minima (Figs. 5-13g-i). Furthermore, it can be clearly seen in Figs. 5-13g-i that, for flow regions where $Re_t > Re_{tm}$, the modified EDC results in $1 < C_\tau < 1.5$. That is, for flow regions where Re_t is higher but close to Re_{tm}, C_τ tends to be larger but close to unity, whereas C_τ tends to be lower but closer to 1.5 (Figure 5-13i) with increasing Re_t. It is important to mention that, at moderate turbulent flow condition, $C_\tau \approx 1.25$ (Figure 5-13h). The radial profiles of C_τ in Figure 5-13g-i suggest a longer residence time than that of the standard EDC at moderate to highly turbulent flow conditions. The same trend of C_τ was also found to improve the predictions of temperature and species concentrations at highly turbulent flow conditions [27]. It can also be seen in Figure 5-13g that, in the flow regions with very low turbulent Reynolds number (weakly turbulent flow condition), the modified EDC exhibits a lower C_τ value compared to that of the standard EDC.

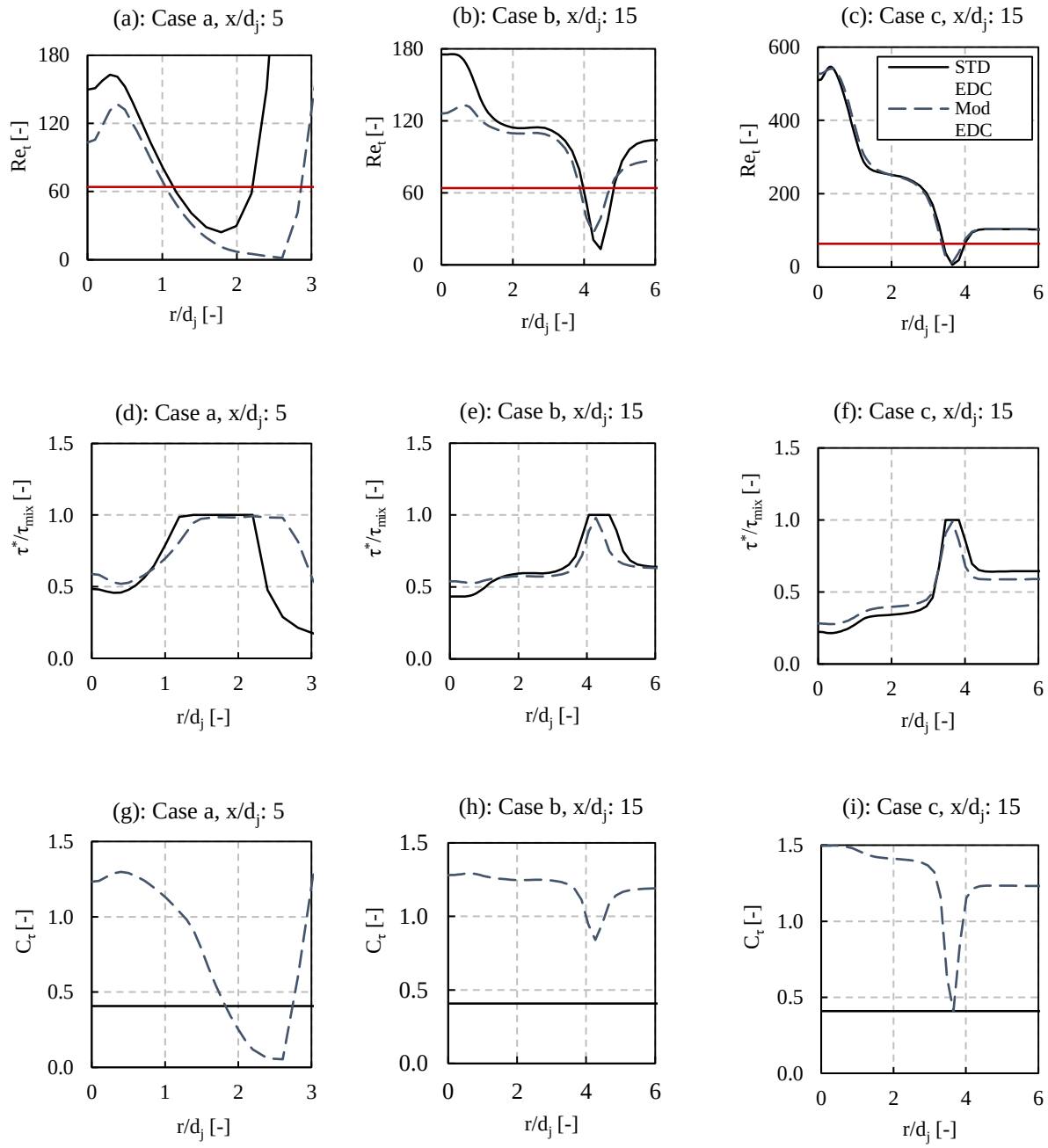

Figure 5-13. Radial profiles of (a-c) turbulent Reynolds number, (d-f) EDC time scale over characteristic mixing time scale, and (g-i) EDC time scale coefficient. These are the results of the simulations of cases A-C using both the standard and modified EDC.

In the case of weakly turbulent flow condition (case A), the thermal NO mechanism is likely to be the dominant NO_x, as it is well-known that the overall thermal NO formation rate is slow [63]. According to Figure 5-5d, the peaks of temperature and NO concentration are located in the region

of the flow where the mean mixture fraction ranges approximately between 0.12 and 0.25 (i.e., 1.4 < r/d_j < 1.8 as seen in Figure 5-5a). In the same region of the flow in case A, the profiles in Figure 5-13g indicate a higher value of C_τ calculated by the modified EDC in comparison to that of the standard EDC. This might be one of the reasons for the improvement of the peak value of NO concentration predicted by the modified EDC, since the chemical kinetic rates of NO formation improves with longer residence time (i.e., larger C_τ). Moreover, the overall over-prediction of NO concentration by the modified EDC within the higher mixture fraction regions (Figure 5-5d) can also partly related to the higher value of C_τ and consequently higher chemical kinetic rate of NO formation. Note that while the modified EDC slightly under-predicts the peak value of the temperature profile (Figure 5-5d), it produces far better predictions of the corresponding NO profile (Figure 5-5d). One may expect that higher temperature would result in a higher peak value of NO concentration, which is not the case in Figure 5-5d. Nevertheless, according to Figure 5-13a, d and g, the level of turbulence and consequently the value of C_τ would decrease in the high temperature region. This, consequently, may imply that the value of C_τ in the very high temperature region decreases, which, in turn, reduces the overall NO formation reaction rate. Note that while the standard EDC predicts almost the same trend of NO concentration as that predicted by the modified EDC (Figure 5-5d), the former model still under-predicts NO concentration which is likely caused by lower value of C_τ, and hence lower chemical kinetics rate of NO. The improvement in the prediction of CO concentration by the modified EDC in cases B-D can also be partly attributed to the larger value of C_τ (compared to that of the standard EDC), which consequently improves the formation/consumption of CO [27].

5.5.6 Diffusion $CO/H_2/N_2$ jet flame doped with NH_3 (Case E)

The aim of the simulations presented in this section is to investigate the capability of the modified EDC for the predictions of thermal NO_x and also the formation of NO_x from fuel bound nitrogen source. The study of thermal NO_x formation is performed by simulating $CO/H_2/N_2$ jet flame without considering CH_4 and NH_3. In addition, other simulations are carried out by considering CH_4 with 0.8% (by volume) addition of NH_3. For the latter case, Zahirovic et al. [64] modified the chemistry scheme by considering the oxidation of CH_4 by global reactions adopted from the well-known four-step reaction mechanism of methane, which is proposed by Jones and Lindstedt [65]. This simplified treatment of CH_4 breakdown is believed to be justified for the intended application, since the concentration of CH_4 in the present flame is low (i.e., ~ 0.7% by volume) [64]. As already discussed in previous studies (e.g., [6]), due to very low concentrations of CH_4 and NH_3, the addition of these species has a significant impact only on the concentration of minor species (e.g., NO), whereas the predictions of temperature and major species remain almost unchanged compared to the simulation without CH_4 and NH_3. As this is also confirmed in the present simulations (not shown here), only the simulation results without the addition of CH_4 and NH_3 for the prediction of temperature is presented.

Figure 5-14 shows the predictions of the radial profiles of temperature (Figure 5-14a), thermal NO concentration (Figure 5-14b), and NO concentration for the simulation with addition of CH_4 and NH_3 (Figure 5-14c). The experimental measurements and numerical predictions are compared at an axial position of $x/d_j = 100$, and the concentration of NO is presented on dry basis mole fraction. Figure 5-14a shows that the prediction of the peak value of temperature is slightly improved with the modified EDC; however, both the standard and modified EDC over-predict the temperature especially in the vicinity of the centerline ($r/d_j \approx 0$). The profiles in Figure 5-14b show that the

standard EDC over-predicts NO concentration. On the other hand, the prediction of thermal NO concertation is significantly improved using the modified EDC (Figure 5-14b). In the case of the flame doped with NH_3 (Figure 5-14c), both the standard and modified EDC predict a narrower radial distribution of NO concentration compared to its experimental counterpart. Nevertheless, the radial profile of NO concentration in Figure 5-14c show that the standard EDC slightly produces closer prediction to the experiments than that of the modified EDC. However, the predicted level of NO concentration, by both standard and modified EDC, is relatively in good agreement with experimental measurements.

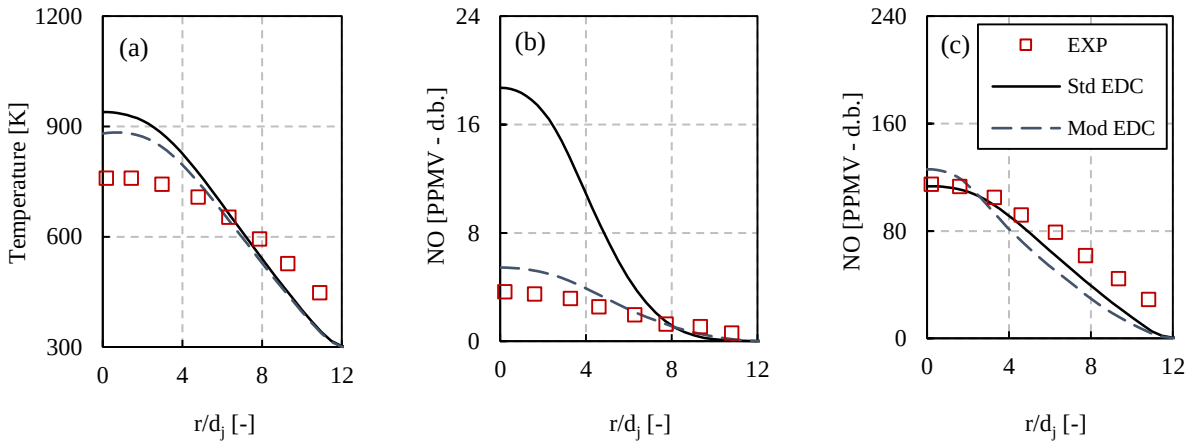

Figure 5-14. Radial profiles of (a) temperature, (b) NO mole fraction (without NH_3), and (c) NO mole fraction (with addition of 0.8 vol% NH_3). These are the results of the simulation of $CO/H_2/N_2$ diffusion jet flame (i.e., case E) at x/d_j= 100 using both the standard and modified EDC.

There exist numerous studies in the literature which comprehensively examined the pathways of the formation of both thermal and fuel NO_x (e.g., [6, 64, 20]). However, in the present study, only the effect of combustion model on the prediction of NO_x is discussed. Figure 5-15 presents the radial profiles of Re_t and C_τ for Case E predicted by the modified EDC at a radial position of x/d_j = 100. The radial profile of Re_t in this figure indicates that the level of turbulence is relatively high at this section of the flow field (according to the diagram of τ^*/τ_{mix} in Figure 5-4b).

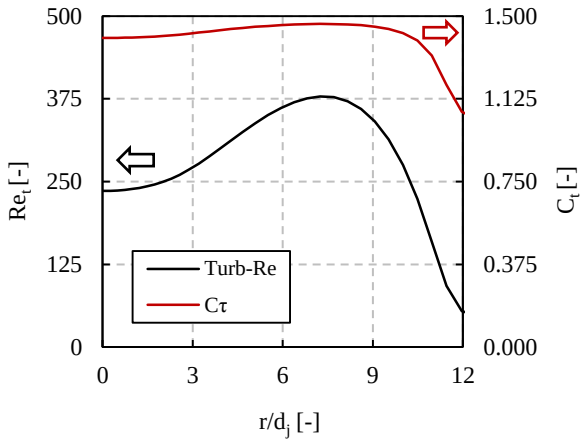

Figure 5-15. Radial profiles of turbulent Reynolds number and EDC time scale coefficient for case E. The predictions are produced using the modified EDC at x/d$_j$= 100.

By considering the term τ^*/τ_{mix} (i.e., the mass exchange rate coefficient according to Eqs.(5-23) and (5-24)) for highly turbulent flow condition, the modified EDC produces a larger mass exchange rate coefficient (Figure 5-4b), which is similar to a larger γ^* for the standard EDC. This is expected to improve the prediction of slow-forming species such as CO and thermal NO_x, as discussed in [27, 5]. It is suggested by Kjaldman et al. [66] that the prediction of slow-forming species using the EDC approach could be improved if the modeled reaction zone partially extends into the surrounding fluid. Hence, the observed improvement in the predictions of slow-forming species for case E might be due to the fact that a part of surroundings fluid is accounted for in the reaction zone (i.e., extension of the volume of fine structure into the surrounding fluid) [27].

The radial profile of C_τ in Figure 5-15 indicates a larger value of EDC residence time compared to that of the standard EDC. That is, while a constant value of $C_\tau = 0.4083$ is employed by the standard EDC, the diagram in Figure 5-15 shows that $1.125 < C_\tau < 1.5$ for the modified EDC, which is an indication of a longer residence time for the chemical reaction mechanism. A longer residence time of the chemical reactions leads to improvement in the prediction of NO concentration as the kinetic rates of the thermal NO is believed to be slower than that of the mixing

process [3]. Previous studies also revealed that the level of NO concentration is not only highly sensitive to NH_3 content in the fuel stream, but also the rate of NO produced by the contribution of NH_3 is much higher than that of the thermal NO_x [20, 67]. This change in NO concentration is an indication of the predominant effect of NH_3 in the current flame, as the concentration of NO is significantly increased with the addition of NH_3 in the fuel stream (Figure 5-14c).

5.6 Conclusions

A modified version of Eddy Dissipation Concept (EDC) model is developed and examined in the present study. The model is modified on the basis of turbulence intermittency in the inertial range energy transfer using fractal modeling approach. Numerical simulations are carried out on four predominantly non-premixed jet flames in order to examine the capability of the model under different turbulent flow conditions. An additional set of simulations is also performed on a $CO/N_2/H_2$ non-premixed jet flame with and without the addition of NH_3. The aim of simulating the latter flame is to investigate the ability of the modified EDC for predicting the thermal NO_x and fuel bound nitrogen NO_x. The main findings are summarized as follows:

- Compared to the standard EDC, the modified EDC approach uses a smaller mass exchange rate coefficient at weakly turbulent flow condition. The predictions of the modified EDC are qualitatively improved in terms of mixture fraction in the vicinity of the flow centerline. However, while both models predict almost similar trends of temperature and species concentrations, the modified EDC significantly improved the predictions of the peak values, especially for NO concentration.
- In the case of moderate turbulent flow condition, both the standard and modified EDC showed relatively similar predictions. This is mainly attributed to the almost similar value of mass exchange rate coefficients for both models under this flow condition.

Nevertheless, the peak values of temperature and H_2 mass fraction are better captured by the modified EDC. However, CO and OH concentrations are under-predicted.

- For highly turbulent flow condition, the modified EDC produces a slightly larger mass exchange rate coefficient than that of the standard EDC. The modified EDC showed significant improvement in the predictions of CO, H_2 and OH mass fractions; whereas the temperature and major species mass fractions (e.g., CO_2, O_2) are captured adequately with slight improvement in the predictions of the modified EDC over its standard version.
- Compared to the standard EDC, the modified EDC uses a larger value of EDC time scale coefficient in most regions of the flow field. However, the value of this time scale coefficient decays close to the region of low turbulent Reynolds number. In the case of moderate to highly turbulent flow conditions, it can be concluded that the modified EDC employs a longer residence time of the chemical reactions compared to the standard EDC, which could be the reason for improved predictions of slow-forming species (e.g., NO and CO). Also, under very low turbulent flow condition, the modified EDC might yield lower EDC time scale coefficient compared to that of the standard EDC.
- The modified EDC produced a significant improvement in the predictions of thermal NO concentration of $CO/N_2/H_2$ non-premixed jet flame. However, the standard EDC showed slightly better agreement with experimental measurements when the level of NO concentration is influenced by the addition of NH_3 in the fuel stream.

The results of this study clearly showed that the temperature field and species concentrations can reasonably be predicted under different turbulent flow conditions using the proposed modified EDC approach. Thus, it is expected that this modified version of EDC approach will be able to capture the flow field of a grate firing biomass furnace, which encompasses a range of flow

regimes, varying from weakly turbulent (e.g., in the vicinity of the bed) to highly turbulent close to extinction (e.g., close to over-fire air jets in the freeboard) conditions. Furthermore, the promising predictions of CO and NO_x concentrations using the modified EDC is an indication of the reliability of this approach in simulating the gas-phase biomass combustion especially for predicting slow-forming and kinetically dominated pollutants.

5.7 Reference

[1] A. Parante, M. Malik, F. Contino, A. Cuoci and B. Dally, "Extension of the eddy dissipation concept for turbulent/chemistry interaction to MILD combusiton," Fuel, vol. 163, pp. 98-111, 2016.

[2] A. Shiehnejadhesar, R. Mehrabian, R. Scharler, G. M. Goldin and I. Obernberger, "Development of a gas phase combustion model suitable for low and high turbulence conditions," Fuel, vol. 126, pp. 177-187, 2014.

[3] T. Klason and X. Bai, "Computational study of the combustion process and NO formation in a small-scale wood pelletfurnace," Fuel, vol. 86, pp. 1465-1474, 2007.

[4] S. Van Loo and J. Koppejan, The Handbook of Biomass Combustion and Co-firing, Earthscan, 2008.

[5] M. Farokhi, M. Birouk and F. Tabet, "A computational study of a small-scale biomass burner: The influence of chemistry, turbulence and combustion sub-models," Energy Conversion and Management, vol. 143, pp. 203-214, 2017.

[6] S. Zahirovic, R. Scharler, P. Kilpinen and I. Obernberger, "Validation of flow simulation and gas combustion sub-models for the CFD-based prediction of NOx formation in biomass grate furnaces," Combustion Theory and Modelling, vol. 15, pp. 61-87, 2010.

[7] D. Veynante and L. Vervisch, "Turbulent combusition modeling," Progress in energy and combustion science, vol. 28, pp. 193-266, 2002.

[8] W. Li, Z. Dai and F. Wang, "Characteristic chemical time scale analysis of a partial oxidation flame in hot syngas coflow," Energy and fuels, vol. 31, pp. 4382-4390, 2017.

[9] D. Splading, "Mixing and chemical reaction in steady confined turbulent flames," in Proceedings of the 13th Symposium on combustion, The combustion institu, 1970.

[10] B. Magnussen and B. Hjertager, "On the mathematical modeling of turbulent combustion with special emphasis on soot formation and combustion," Proceedings in combustion institute, vol. 16, pp. 719-729, 1977.

[11] B. Magnussen, "On the structure of turbulence and a generalized eddy dissipation concept for chemical reaction in turbulent flow," in 19th AIAA aerospace science meeting, St. Louis, Missouri., 1981.

[12] J. Collazo, J. Porteiro, J. Míguez, E. Granada and M. Gómez, "Numerical simulation of a small-scale biomass boiler," Energy Conversion and Management, vol. 64, pp. 87-96, 2012.

[13] D. Djurovic, S. Nemoda, B. Repic and D. A. M. Dakic, "Influence of biomass furnace volume change on flue gases burn out process," Renewable energy, vol. 76, pp. 1-6, 2015.

[14] M. Farokhi and M. Birouk, "Application of eddy dissipation concept for modeling biomass combustion, part 2: gas-phase combustion modeling of a small-scale fixed bed furnace," Energy and fuels, vol. 30, pp. 10800-10808, 2016.

[15] N. Peters, "Laminar diffusion flamelet models in non-premixed turbulent combustion," Progress in Energy and Combustion Science, vol. 10, pp. 319-339, 1984.

[16] H. Pitsch, M. Chen and N. Peters, "Unsteady flamelet modeling of turbulent hydrogen-air diffusion flames," Proceedings in combustion institute, vol. 27, pp. 1057-1064, 1998.

[17] B. Albrecht, S. Zahirovic, R. Bastiaans, J. Van Oijen and L. de Goey, "A premixed flamelet - PDF model for biomass combustion in a grate furnace," Energy and fuels, vol. 22, pp. 1570-1580, 2008.

[18] M. Buchmayr, J. Gruber, M. Hargassner and C. Hochenauer, "A computationally inexpensive CFD approach for small-scale biomass burners equipped with enhanced air staging," Energy Conversion and Management, vol. 115, pp. 32-42, 2016.

[19] I. Gran, M. Melaaen and B. Magnussen, "Numerical simulation of local extinction effects in turbulent combustor flows of methane and air," in Twenty-Fifth Symposium (International) on CombustionfFhe Combustion Institute, 1994.

[20] S. Sukumaran and S. Kong, "Modeling fuel NOx formation from combustion of biomass-derived producer gas in a large burner," Combustion and flame, vol. 160, pp. 2159-2168, 2013.

[21] A. Shiehnejadhesar, K. Schulze, R. Scharler and I. Obernberger, "A new innovative CFD-based optimization method for biomass combustion plants," Biomass bioenergy, vol. 53, pp. 48-53, 2013.

[22] A. Shiehnejadhesar, R. Scharler, R. Mehrabian and I. Obernberger, "Development and validation of CFD models for gas phase reactions in biomass grate furnaces considering gas streak formation above the packed bed," Fuel Processing Technology, vol. 139, pp. 124-148, 2015.

[23] A. De, E. Oldenhof, P. Sathiah and D. Roekaerts, "Numerical simulation of Delft-Jet-in-Hot-Coflow (DJHC) flame using eddy dissipation concept model for turbulent-chemistry interaction," Flow, turbulent and combustion, vol. 87, pp. 537-567, 2011.

[24] M. Rehm, P. Seifert and B. Meyer, "Theoretical and numerical investigation on the EDC-model for turbulent-chemistry interaction at gasification conditions," Computer and Chemistry Engineering, vol. 33, pp. 402-407, 2009.

[25] A. Mardani, "Optimization of the Eddy Dissipation Concept (EDC) model for turbulence-chemistry interactions under hot diluted combustion of CH4/H2," Fuel, vol. 191, pp. 114-129, 2017.

[26] J. Aminian, C. Galletti and L. Tognotti, "Extended EDC local extinction model accounting finite-rate chemistry for MILD combustion," Fuel, vol. 165, pp. 123-133, 2016.

[27] M. Farokhi and M. Birouk, "Application of Eddy Dissipation Concept for modeling biomass combustion, Part 1: Assessment of model coefficients," Energy and Fuels, vol. 12, pp. 10789-10799, 2016.

[28] W. Meier, A. Vyrodov, V. Bergmann and W. Stricker, "Simultaneous Raman/LIF measurements of major species and NO in turbulent H2/air diffusion flames," Applied physics B, vol. 63, pp. 79-90, 1996.

[29] R. Barlow and J. Frank, "Effect of turbulence on species mass fractions in methane/air jet flames," in 27th Symposium (International) on Combustion, The combustion institude, 1998.

[30] M. Drake, R. Pitz, S. Correa and M. Lapp, "Nitric oxide formation from thermal and fuel-bound nitrogen sources in a turbulent non-premixed syngas flame," Proceedings in combustion institute., vol. 20, pp. 1983-1990, 1984.

[31] M. F. Modest, Radiative heat transfer, New yourk: Academic press, 2003.

[32] N. Selçuk and N. Kayakol, "Evaluation of descrete ordinates method for radiative transfer in rectangular furnaces," International Journal of Heat and Mass Transfer, vol. 40, pp. 213-222, 1997.

[33] T. Shih, W. Liou, A. Shabbir, Z. Yang and J. Zhu, "A New k-ε Eddy-Viscosity Model for High Reynolds Number Turbulent Flows - Model Development and Validation," Computers and Fluids, vol. 24, pp. 227-238, 1995.

[34] ANSYS, "Ansys Fluent theory guide, Release 15.0," ANSYS.

[35] N. Hashimoto, R. Kurose, S.-M. Hwang, H. Tsuji and H. Shirai, "A numerical simulation of pulverized coal combustion employing a tabulated-devolatilization-process model (TDP model)," Combustion and Flame, vol. 159, pp. 353-366, 2012.

[36] B. Launder and D. Spalding, "The numerical computation of turbulent flows," Computer Methods in Applied Mechanics and Engineering, vol. 3, pp. 269-289, 1974.

[37] H. Tennekes, "Simple model for the small-scale structure of turbulence," The physics of fluids, vol. 11, pp. 669-671, 1968.

[38] R. Rydén, L. Eriksson and S. Olovsson, "Large Eddy Simulation of Bluff Body Stabilised Turbulent Premixed Flames," in ASME 1993 International Gas Turbine and Aeroengine Congress and Exposition, Cincinnati, Ohio, USA, 1993.

[39] B. Lilleberg, D. Christ and I. Ertesvag, "Numerical Simulation with an Extinction Database for Use with the Eddy Dissipation Concept for Turbulent Combustion," Flow turbulence combustion, vol. 91, pp. 319-346, 2013.

[40] I. Gran and B. Magnussen, "A Numerical Study of a Bluff-Body Stabilized Diffusion Flame. Part 2. Influence of combustion modeling and finite-rate chemistry," Combustion science and technology, vol. 119, 1996.

[41] Z. Li, A. Cuoci, A. Sadiki and A. Parente, "Comprehensive numerical study of the Adelaide Jet in Hot-Coflow burner by means of RANS and detailed chemistry," Energy, vol. 139, pp. 555-570, 2017.

[42] M. Karalus, "An investigation of lean blowout of gaseous fuel alternatives to natural gas, PhD thesis," University of Washington, 2013.

[43] O. Gulder, "Contribution of small scale turbulence to burning velocity of flamelets in the thin reaction zone regime," Proceedings of the Combustion Institute, vol. 31, pp. 1369-1375, 2007.

[44] E. Giacomazzi, C. Bruno and B. Favini, "Fractal modelling of turbulent combustion," Combustion Theory and Modelling, vol. 4, pp. 391-412, 2000.

[45] E. Giacomazzi, V. Battaglia and C. Bruno, "The coupling of turbulence and chemistry in a premixed bluff-body flame as studied by LES," Combustion and Flame, vol. 138, pp. 320-335, 2004.

[46] E. Giacomazzi, C. Bruno and B. Favini, "Fractal modelling of turbulent mixing," Combustion Theory and Modelling, vol. 3, pp. 637-655, 1999.

[47] F. Anselmet, Y. Gagne and E. Hopfinger, "High-order velocity structure function in turbulent shear flows," Journal of fluid mechanics, vol. 140, pp. 63-89, 1984.

[48] H. Bao, Writer, Development and Validation of a New Eddy Dissipation Concept (EDC) Model for MILD Combustion. [Performance]. MS.c. thesis, the Delft University of Technology, 2017.

[49] D. Veynante and L. Vervisch, "Turbulent combustion modeling," Progress in energy and combustion science, vol. 28, pp. 193-266, 2002.

[50] S. N. Labratories, "Sandia/TUD Piloted CH4/AIR jet flames," Sandia National Labratories, 2003.

[51] R. Barlow and J. Frank, "SandiaPilotDoc21.pdf," [Online]. Available: http://www.sandia.gov/TNF/DataArch/FlameD.html.

[52] S. Pope, "Computationally efficient implementation of combustion chemistry using in situ adaptive tabuilation," Combustion Theory and Modeling, vol. 1, pp. 41-63, 1997.

[53] A. Frassoldati, T. Faravelli and E. Ranzi, "The ignition, combustion and flame structure of carbon monoxide/hydrogen mixtures. Note 1: Detailed kinetic modeling of syngas combustion also in presence of nitrogen compounds," International Journal of Hydrogen Energy, vol. 32, pp. 3471-3485, 2007.

[54] A. Cuoci, A. Frassoldati, G. Buzzi Ferraris, T. Faravelli and T. Ranzi, "The ignition, combustion and flame structure of carbon monoxide/hydrogen mixtures. Note 2: Fluid dynamics and kinetic aspects of syngas combustion," International Journal of Hydrogen Energy , vol. 32, pp. 3486-3500, 2007.

[55] A. Ranzi, A. Frassoldati, R. Grana, A. Cuoci, T. Faravelli, A. Kelley and C. Law, "Hierarchical and comparative kinetic modeling of laminar flame speeds of hydrocarbon and oxygenated fuels," Progress in Energy and Combustion Science, vol. 38, pp. 468-501, 2012.

[56] A. Kazakov and M. Frenklach, "DRM-22 chemical mechanism," [Online]. Available: http://www.me.berkeley.edu/drm/.

[57] G. Smith, D. Golden, M. Frenklach, N. Moriarty, B. Eiteneer, M. Goldenberg, C. Bowman, R. Hanson, S. Song, J. Gardiner, V. Lissianski and Z. Qin, "GRI-Mech 3.0," [Online]. Available: http://www.me.berkeley.edu/gri_mech/.

[58] R. Bilger, S. Starner and R. Kee, "On reduced mechanisms for methane/air combustion in nonpremixed flames," Combustion and flame, vol. 80, pp. 135-149, 1990.

[59] J. Aminian, C. Galletti, S. Shahhosseini and L. Tognotti, "Numerical Investigation of a MILD Combustion Burner: Analysis of Mixing Field, Chemical Kinetics and Turbulence-Chemistry Interaction," Flow Turbulence Combustion, vol. 88, pp. 597-623, 2012.

[60] A. Frassoldati, P. Sharma, A. Cuoci, T. Faravelli and E. Ranzi, "Kinetic and fluid dynamics modeling of methane/hydrogen jet flames in diluted coflow," Appled. Thermal. Engineering., vol. 30, pp. 376-383, 2010.

[61] A. Parente, C. Galletti and L. Tognotti, "A simplified approach for predicting NO formation in MILD combustion of CH4-H2 mixtures," Proceedings in combustion institute., vol. 33, pp. 3343-3350, 2011.

[62] J. Aminian, C. Galletti, S. Shahhosseini and L. Tognotti, "Key modeling issues in prediction of minor species in diluted-preheated combustion conditions," Appled Thermal Engineering, vol. 31, pp. 3287-3300, 2011.

[63] A. Al-Abbas and J. Naser, "Effect of Chemical Reaction Mechanisms and NOx Modeling on Air-Fired and Oxy-Fuel Combustion of Lignite in a 100-kW Furnace," Energy and fuels, vol. 26, pp. 3329-3348, 2012.

[64] S. Zahirovic, R. Scharlera, P. Kilpinenc and I. Obernbergera, "A kinetic study on the potential of a hybrid reaction mechanism for prediction of NOx formation in biomass grate furnaces," Combustion Theory and Modelling, vol. 15, pp. 645-670, 2011.

[65] W. Jones and R. Lindstedt, "Global reaction schemes for hydrocarbon combustion," Combustion and flame, vol. 73, pp. 233-249, 1988.

[66] L. Kjaldman, A. Brink and M. Hupa, "Micro mixing time in eddy dissipation concept," Combustion Science and Technology, vol. 154, pp. 207-227, 2000.

[67] T. Weydahl, M. Bugge, I. Gran and I. Ertesvåg, "Computational modeling of nitric oxide formation in biomass combustion," International Journal of Applied Mechanics and Engineering, vol. 7, pp. 125-141, 2001.

Chapter 6: Modeling of the gas-phase combustion of a grate-firing biomass furnace using an extended approach of Eddy Dissipation Concept

6.1 Abstract

The ability of the standard Eddy Dissipation Concept (EDC) approach to account for the chemical kinetic rates during the interaction between chemistry and turbulent flow field made it a suitable scheme for simulating gas-phase combustion. However, its application poses a challenge for modeling weakly turbulent reacting flow conditions, and also reacting flows with comparable flow and chemical time scales. An extended version of EDC approach (referred to here as extended EDC) has recently been developed for predominantly non-premixed turbulent flames. This led to significant improvement in the predictions of species and temperature fields of biomass-derived gas jet flames over a wide range of turbulence conditions (from weakly to highly turbulent flow conditions). The present study examines the application of the extended EDC for the simulation of a small-scale updraft biomass combustor. The predictions of the model are compared with those of the standard EDC and their counterparts' experimental temperature and species concentrations. Moreover, the pathway of formation/destruction of gas-fuel species and pollutants (e.g., NO_x) is investigated. The present findings reveal a significant improvement in the predictions of temperature field and species of the gas-phase of a grate-firing biomass combustion.

6.2 Introduction

Considering the limited fossil fuel resources and its consequences on global warming, green renewable energy generation using carbon-neutral fuel (e.g., biomass) has become very attractive [1, 2, 3]. For instance, grate-firing biomass combustion furnace is one of the most widespread used technology available in the market owing to its flexibility of feedstock (i.e., ability to use wide range of fuel particles size, moisture and ash contents), as well as its low investment cost [4, 5]. Nevertheless, biomass combustion is still not emissions-free, as it may generate even higher emissions of pollutants such as NOx emissions compared to fossil fuels combustion [6]. This is particularly the case for small-scale grate-firing combustors, as they usually suffer from generating relatively high level of pollutants such as CO and NOx because of their poor air/fuel mixing and combustion short residence time [5]. Thus, research is required to better understand and hence further develop this technology [7, 8].

Computational fluid dynamics (CFD) is becoming increasingly on par with experimental tests and theoretical methods as an important research tool owing to its noticeably lower cost and its ability to produce multi-scale information which cannot be achieved by either experiments or theory [9, 10]. CFD simulation of grate-firing biomass combustion usually consists of two main separate sub-stages; decomposition of solid fuels in the bed section of the furnace (i.e., conversion process), and gas-phase combustion process above the bed (known as freeboard combustion) [3, 5]. The decomposition process of solid fuel in the grate is accounted for via using a bed model. The bed model converts solid fuel into equivalent gas-species, which carry the same elemental mass and energy as those of biomass. Simple bed models provide the average species mass fractions and temperature profiles of the gases coming out of the bed. These profiles can be obtained experimentally, or calculated on the basis of mass and energy balance between the inlet (biomass

particles and primary air) and outlet (interface between the bed and freeboard) of the bed section [11]. Complex bed models usually use separate sub-models (e.g., drying, devolatilization, etc.) for each conversion process, where the data is shared and coupled between the bed and freeboard through an interface surface [11, 12, 13]. Gas-phase combustion within the freeboard is usually accounted for using species transport models (e.g., finite-rate kinetic/eddy dissipation model (FRK/EDM) or Eddy Dissipation Concept (EDC)). It is important to mention that mixture fraction based models, which are capable of incorporating detailed chemistry (e.g., steady/unsteady flamelet model (SFM/UFM)), have been also examined in a few published works related to grate-firing biomass combustion (e.g., [8, 14, 3]). However, since the flue gas released from solid biomass particles cannot be introduced using a single mixture fraction parameter, additional variables are required to account for a tabulated flamelet database [7]. Hence, the application of SFM/UFM for simulating grate-firing biomass combustion is mostly limited to small-scale combustors [3].

FRK/EDM approach is usually able to reasonably capture the features of a turbulent mixing-dominated process. Nevertheless, this approach can only be coupled with simple few-step chemical mechanisms and consequently the prediction of intermediate, slow-forming and kinetically dominated species (e.g., NO and CO) cannot be adequately predicted [11]. To overcome this handicap, EDC approach [15] has been introduced to incorporate chemical kinetics in turbulent reacting flows. EDC has widely been used in modeling combustion process including biomass combustion (e.g., [1, 16, 11]). However, despite its widespread use, only a few studies have addressed its limitations for simulating gas-phase biomass combustion (e.g., [10, 17, 18, 11]). Several studies were recently performed on EDC approach with the aim to improve its performance in the simulation of different combustion/turbulent conditions (especially in the case of moderate

and intense low oxygen dilution (MILD) combustion regime). For instance, Mardani [19] performed a parametric study on EDC's coefficients in order to provide some guidelines for choosing adequate values of the model's constants for MILD combustion. De et al. [20] performed an investigation on MILD combustion regime using EDC and reported that standard EDC predicts a too early ignition process. Parante et al. [21] made a modification to EDC on the basis of premixed combustion theory (i.e., laminar flame speed) for MILD combustion. The performance of their model was examined by simulating Adelaide Jet-in-Hot-Coflow (JHC) burner and reported better predictions of species and temperature fields compared with the standard EDC. In the case of biomass combustion, a hybrid combustion model was developed by Shiehnejadhesar et al. [17] to describe the reaction rate at both weakly and highly turbulent flow conditions using both FKR and EDC reaction rates. Their proposed model was further improved using a correlation between the local gas residence time and a characteristic mixing time, which was successfully applied to simulate a grate-firing biomass furnace. These authors reported remarkable improvements in the predictions of temperture and species compared to those of the standard EDC [10]. Recently, Farokhi and Birouk [18] performed a sensitivity analysis on the EDC coefficients for simulating biomass-derived jet flames at different flow condtions (i.e., weakly and highly turbulent reacting flows). They reported that the predictions of the gas-phase combustion (i.e., temperature, species concentration) can be improved by adjusting the model's coefficients based on the turbulent flow characteristics (i.e., turbulent Reynolds number and turbulent time scale) over a wide range of turbulence conditions. The same authors simulated the gas-phase combustion of a small-scale grate-firing biomass combustor using the modified EDC coefficients and they reported remarkebly better predictions of species and temperature fields, especially CO emissions [11]. Thereafter, they examined the performance of EDC with the modified coefficients (using redcued chemical

mechanisms) againts SFM/UFM approaches using detailed chemistry, and reported that the modified EDC produced better predictions of species concentration, especially CO [3].

The formation of pollutants such as CO and NOx is greatly dependent on the adopted chemical mechanism as well as combustion model. A detailed reaction mechanism leads to a better description of the formation/destruction pathway of minor and intermediate species. However, the combustion model plays a key role in the prediction of minor species, especially slow-forming and kinetically dominated species such as CO and NOx [3]. In the case of biomass combustion, it was shown that the effect of the type of reaction mechanisms on the prediction of CO concentration is pronounced only in the high temperature regions of a furnace [3]. Also, this influence was found to be more evident when using detailed chemistry as the thermal dissociation of CO2 is likely to best described in high temperature regions using detailed chemistry [3]. Overall, as reported in [3], the prediction of CO concentration was found unsatisfactory when using either reduced chemistry with standard EDC, or detailed chemistry with steady flamelet model (SFM). Nevertheless, EDC with modified coefficients (and using reduced chemistry) and also the unsteady flamelet approach (with detailed chemistry) were able to predict CO emissions comparable to experimental measurements [3].

NOx emissions are mainly generated through three main pathways; thermal NOx, prompt NOx and fuel NOx [22]. In biomass combustion, the oxidation of fuel-bound nitrogen (FBN) is recognized as the dominant source of NOx pollutant (i.e., fuel NOx), and only very small amount to none of NOx is generated due to other nitrogen oxide formation pathways (e.g., thermal NOx) [23, 24]. The FBN is released partly during devolatilization, and part of it remains in the char component [6]. Hupa et al. [24] reported that, in the case of combustion of wood pellets at ~1170 K, around 15% of FBN forms NO during devolatilization while 10% of FBN results in the

generation of NO during char oxidation. It is well-known that HCN and NH3 are the main FBN intermediate species released during thermal conversion of solid biomass particles, which contribute to the formation of NOx [25, 6]. The mass ratio of the released NH3/HCN depends strongly on the type of biomass fuel as well as the devolatilization temperature [26]. For instance, Liu and Gibbs [27] suggested a ratio of 9:1 for NH3/HCN in the case of woody-biomass fuel. In another study, it was shown that, in a large scale fluidised biofuel boiler, the main released form of FBN as an intermediate species was NH3 [28]. Also, NH3 and NO, as the main products of FBN from the bed, were found in the case of wood-chips feedstock boilers [25, 29]. Particularly, it was found that under fuel-rich conditions, NH3 is the main product of FBN, while the amount of HCN is negligible; whereas under air-rich conditions, NO can also be released from the bed [25]. In updraft feedstock gasification of wood pellets, under fuel-rich condition in the bed, FBN is mostly released during devolatilization (during the formation and then cracking of tar component) [29]. Experimental investigations of packed-bed furnaces showed that the released intermediate FBN species (e.g., NH3 and HCN) were mostly generated during fuel-rich conditions within the bed, while the formation of NO took place under air-rich conditions in the oxidation zones where NH3 and HCN partly react with oxygen to from NOx (mainly NO) [29]. Modeling of NO emissions is also strongly dependent on the adopted chemical mechanism. That is, better predictions may be achieved quantitatively using a derailed chemistry scheme which obviously requires a high computational cost [14]. On the other hand, a common method of predicting NOx is via using post-processing [7]. In post-processing NOx formation method, it is assumed that NOx species are present in a significantly low concentration compared to major species, and consequently, they do not affect the overall combustion process [7, 30]. Therefore, NOx formation can be modeled using post-processing upon convergence of the simulation of the reacting turbulent

flow field. This approach leads to a significant less computational effort compared to resolving real-time flow field/detailed chemistry interaction (e.g., [14, 7]). Nevertheless, the prediction of NOx emissions is also strongly dependent on the prediction of the combustion field (temperature and major species), and consequently on the adopted combustion model [30, 31].

The briefly reviewed literature above revealed that the development of reliable and computationally affordable combustion schemes for biomass combustion, especially for the predictions of, e.g., CO and NOx, still require further research. Combustion models (such as EDC) are incapable of simulating weakly turbulent flow conditions, as well as modeling reacting flow conditions in which chemical and mixing time scales are comparable [18, 3, 21]. In grate-firing biomass furnaces, such conditions occur especially in the vicinity of the bed, where high temperature volatile gases leave the bed at low velocity and turbulence [17]. The present authors recently developed an extended version of EDC approach [31] for modeling the gas-phase of biomass combustion based on the observations reported in [18, 11]. The extended model was developed for modeling predominantly non-premixed turbulent flames, and its performance was examined by simulating a variety of jet flames covering a wide range of weakly to highly turbulent flow conditions. The present study is a continuation of the development of the extended model reported in [31]. More specifically, the objective of the present study is to evaluate its performance for modeling the gas-phase of grate-firing biomass combustion. The simulations are performed on a small-scale updraft biomass boiler adopted from the available studies in the literature (e.g., [5, 32]). To account for the conversion of solid fuel, a particle-based bed model is adopted in the present study. To highlight the performance of the extended EDC, simulations are also carried out using the standard EDC approach, and consequently the predictions obtained from the standard and extended EDC models are compared with published experimental measurements of

temperature and species. Moreover, the pathway of the consumption of the gas-fuel components as well as the formation and reduction of NO pollutant are discussed.

6.3 Methodology

The decomposition process of solid wood particles into volatile gases in the furnace grate is accounted for using a bed model, while the combustion of volatile gases within the freeboard is simulated using EDC. It is assumed that the released volatile gases obey the incompressible ideal gas law. Reynolds Average Navier-Stokes (RANS) conservation of energy, continuity, momentum and species are solved. P_1-approximation model [33] along with the domain based weighted-sum-of-gray-gas (WSGG) method [34] are employed to account for the effect of radiation. The transport of enthalpy due to species diffusion is also considered in the energy equation. The sensitivity analysis of turbulence model on the predictions was performed in previous study for the current furnace with the same operating condition [3]. It is reported that renormalization group (RNG) $k-\varepsilon$ model led to reproducing the closest predictions to the experiment's counterparts and hence, RNG $k-\varepsilon$ approach is used here to model turbulence. Moreover, enhanced wall treatment approach is used as wall function for modeling the flow in the vicinity of the furnace wall [3].

6.3.1 Bed modeling

A simple particle-based bed model is employed in this study. The conversion processes of the solid fuel particles are performed using discrete phase model (DPM) in ANSYS Fluent [30]. This methodology ignores the particle-particle collisions and thus, it is not suitable for particle tracking in fixed bed conditions [35]. However, the standard DPM model in Fluent offers different sub-models to account for thermal conversion (e.g., drying, devolatilization, etc.) as well as char combustion, leading to adequately model the fuel bed section [35]. The spherical-equivalent particles are assumed with uniform temperature throughout the particle body (i.e., thermally thin

assumption) [36]. Convection heat transfer mechanism is considered between solid particle and gas phases, whereas radiation heat transfer is assumed for both particle-particle as well as particle-gas interaction. The drying process is divided into two main sub-processes known as vaporisation and boiling [30]. In the vaporization law provided in DPM, the thermodynamically equilibrium condition is assumed between local vaporized water and liquid water within the particle [30, 37]. In this approach, the vaporization rate is assumed to be diffusion controlled, meaning it is proportional to the difference between the concentrations of vaporized water at the particle surface and in the bulk gas [35, 37]. However, in the present study, the rate of vaporization is considered to be convection/diffusion controlled as [30, 38]:

$$\frac{dm_p}{dt} = \rho K_c A_p \ln(1 + \frac{Y_{w,s} - Y_w}{1 - Y_{w,s}}) \quad (6\text{-}1)$$

where m_p and A_p are, respectively, the particle's mass and surface area, ρ is the bulk gas density, $Y_{w,s}$ and Y_w are, respectively, mass fractions of vapor at the surface and in the bulk gas. The particle temperature is also determined using convection and radiation heat transfer mechanisms as [30]:

$$m_p C_p \frac{dT_p}{dt} = hA_p\left(T - T_p\right) - \frac{dm_p}{dt} h_{fg} + A_p \varepsilon \sigma (\theta^4 - T_p^4) \quad (6\text{-}2)$$

where T is the bulk gas temperature, C_p is the particle's heat capacity, h_{fg} is the latent heat of water, ε is the particle's emissivity, σ is Stefan-Boltzmann constant and $\theta = (0.25G/\sigma)^{0.25}$ is radiation temperature (G is the incident radiation [30]). The diffusion mass transfer coefficient (K_c) and convective heat transfer coefficient (h) are calculated using, respectively, Sherwood and Nusselt number correlations, as follows [30, 39, 40]:

$$K_c = \frac{D_{w,m}\left(2 + 0.6Re_d^{1/2}\,Sc^{1/3}\right)}{d_p} \tag{6-3}$$

$$\frac{hd_p}{k} = \frac{Y_{w,s} - Y_w}{1 - Y_{w,s}}\left(2 + 0.6Re_d^{1/2}Pr^{1/3}\right) \tag{6-4}$$

where $D_{w,m}$ is the diffusion coefficient of vapor in bulk gas, d_p is the particle's diameter, k is the thermal conductivity of the bulk gas, Re_d is the particle's Reynolds number [30], Sc and Pr are, respectively, Schmidt and Prandtl number of the bulk gas.

The vaporization process takes place as long as particle's temperature is between the vaporization temperature (i.e., T_{vap}= 284 K) and boiling temperature (i.e., T_{boil}= 373 K). Once the particle's temperature reaches T_{boil}, the drying process occurs assuming constant particle temperature (i.e., $T_p = T_{boil}$). The rate of drying in the boiling process is determined using heat transfer rate, as follows [35]:

$$h_{fg}\frac{dm_p}{dt} = hA_p\left(T - T_p\right) + A_p\varepsilon\sigma(\theta^4 - T_p^4) \tag{6-5}$$

A simplified devolatilization model is adopted here. The model assumes that the rate of devolatilization can be approximated using a single-step kinetic rate. The mass exchange rate during devolatilization can be expressed as follows [35]:

$$\frac{dm_p}{dt} = -A\exp(-\frac{E}{RT})\left[m_p - (1 - Y_{v,0})(1 - Y_{w,0})m_{p,0}\right] \tag{6-6}$$

where $m_{p,0}$ is the initial mass of particle, $Y_{w,0}$ and $Y_{v,0}$ are, respectively, the initial mass fractions of moisture and volatile in the particle, R is the universal gas constant, A = 1.5e-2 s^{-1} and E=20 kJ/mol are conversion rate constants [41]. The emitted volatile gases released during the devolatilization process are assumed to be CO, CO_2, H_2O, H_2 and CH_4 as light gas/hydrocarbons

[37], and levoglucosan ($C_6H_{10}O_5$) as a representative of heavy hydrocarbon [41]. The mass fractions of the assumed species released during devolatilization are determined following the work of Thunman et al. [42]. It is important to mention that DPM approach allows only for one chemical composition as the volatile product along with char. Thus, in the first step, the light and heavy hydrocarbons are lumped together as an artificial species, which carries the same mass and energy of the volatile mixture. The composition of this artificial hydrocarbon can be determined using ultimate and proximate analysis of biomass fuel particles. A UDF code is employed to convert the mass fraction of each species in each iteration in the bed section.

It is well known that the oxidation of char is significantly faster than char gasification and, therefore, the gasification of char becomes important when oxygen is depleted [43]. As the current furnace features an updraft fuel feeding system, volatile gases (i.e., gasifying agent) are likely to be released prior to the position of the bed where char formation begins. This is also due to the limitation of DPM approach, as heterogeneous reactions are initiated when the volatile gases are completely evolved from the particle [30]. Hence, the oxidation of char with primary air is considered in this study. The primary products of char oxidation are CO_2 and CO. The ratio of CO/CO_2 is dependent on whether the char undergoes partial or full oxidation [37]. However, for simplicity, it is assumed that the only product of char oxidation is CO [44]. This assumption, which was previously used in the literature (e.g., [45, 46, 35]), is based on the fact that CO is the main product of char oxidation of a woody particle [35]. The rate of char combustion is calculated using a combination of chemical kinetic rate and oxygen diffusion rate, as follows [37]:

$$\frac{dm_p}{dt} = -A_p \left(\frac{\rho R T Y_{ox}}{MW_{ox}}\right) \frac{R_{dif} R_{kin}}{R_{dif} + R_{kin}} \tag{6-7}$$

where Y_{ox} is the mass fraction of oxidizer, MW_{ox} is the molecular weight of the oxidizer, R_{kin} and R_{dif} are, respectively, the kinetic and diffusion rates of char combustion. Details about kinetic and diffusion rates of char oxidation can be found in [47, 48, 44]. Note that the bed model requires the fuel properties as input the model. Fuel properties are adopted from Refs. [5, 32] and are given in Table 6-1.

Table 6-1. Fuel properties [32]

Ultimate analysis (dry-ash-free) (wt%)			
C	O	H	N
51.1	42.5	6.3	<0.1
Proximate analysis (wt%)			
Volatile	Fixed Carbon	Moisture	Ash
79.4	14.2	6.0	0.4
Particle diameter	Lower heating value		
6.0 (mm)	19.24 (MJ/kg)		

6.3.2 Gas-phase combustion

Gas-phase combustion of the volatile gases are accounted for using EDC approach, where it is assumed that combustion takes place within the so-called fine structure (also known as fine-scale) of the reacting flow where dissipation of turbulent kinetic energy occurs [21]. These fine structures are assumed to behave as vortex tubes, slabs or sheets, whose characteristic length scale are of the order of Kolmogorov length scale (η) [15]. The model divides each computational cell into two main regions, known as volume fraction of fine-scale (γ^*), and volume fraction of a surrounding fluid ($\gamma^\circ = 1 - \gamma^*$). The volume fraction of a fine-scale and the residence time of mass transferring between a fine-scale and its surrounding fluid (i.e., the EDC time scale: τ^*) can be expressed using the characteristics of turbulent flow as follows [21]:

$$\gamma^* = {C_\gamma}^3 \left(\frac{\vartheta\varepsilon}{k^2}\right)^{3/4} = {C_\gamma}^3 {Re_t}^{-3/4} \tag{6-8}$$

$$\tau^* = C_\tau \left(\frac{\vartheta}{\varepsilon}\right)^{1/2} = C_\tau \tau_\eta \tag{6-9}$$

where ϑ, k and ε are, respectively, kinematic viscosity, turbulent kinetic energy and turbulent dissipation rate, Re_t is the turbulent Reynolds number based on the integral scale (for simplicity, hereafter Re_t will be called turbulent Reynolds number), τ_η is Kolmogorov time scale, $C_\gamma = 2.1377$ and $C_\tau = 0.4082$ are the volume fraction and the EDC residence time coefficients, respectively [21]. For the standard version of EDC model, the average reaction rate of species i can be written as follows [49, 20]:

$$\overline{R_i} = \frac{\overline{\rho}{\gamma^*}^{2/3}}{(1-\gamma^*)\tau^*}\left(Y_i^* - \overline{Y_i}\right) = \frac{\overline{\rho}}{\tau_m}\left(Y_i^* - \overline{Y_i}\right) \tag{6-10}$$

where Y_i^* and $\overline{Y_i}$ are, respectively, the fine structure and mean mass fractions of species i, and τ_m is a so-called mixing time scale, which is on the order of the time scale of turbulent energy containing eddies which can be derived by applying a linear relationship between the mass fraction of species i in fine-scale and its surrounding fluids, as explained in [20]. The value of γ^* is achieved based on the characteristics of turbulence flow (i.e., Re_t) and it is not directly related to the cell geometry. Hence, there may be conditions particularly at low Re_t, where a reaction zone larger than the size of the computational cell is predicted [18]. Therefore, to avoid unphysical size of the reaction zone, it is well explained in the literature that there has to be an upper limit of γ^*, which can be achieved by assuming that the EDC time scale never becomes larger than mixing time scale. That is [20]:

$$\frac{\tau^*}{\tau_m} = \frac{{\gamma^*}^{2/3}}{(1-\gamma^*)} \leq 1 \rightarrow {\gamma^*}^{1/3} = C_\gamma {Re_t}^{-1/4} \leq 0.75 \quad (6\text{-}11)$$

Based on Eq.(6-11) and by using the default value of $C_\gamma = 2.1377$, it can be easily found that the lowest acceptable value of turbulent Reynolds number (i.e., introduced here as Re_{tm}), is $Re_{tm} \approx 64$. As previously mentioned, the application of EDC approach poses a challenge when modeling a weakly turbulent reacting flow and kinetically dominated species with comparable chemical and flow time scales. However, a sensitivity analysis on EDC coefficient revealed that, for modeling the combustion of biomass-derived-gas jet flames, the predictions of temperature and species concentrations can be improved by changing the model's coefficients, not only under weakly turbulent flow but also in highly turbulent flow conditions [18, 11]. Comparison with the standard value of C_γ, in particular, the predictions were improved when using lower value of C_γ at weakly turbulent flow condition, whereas higher value of C_γ resulted in better predictions at highly turbulent flow condition. Moreover, under both weakly and highly turbulent flow conditions, the higher value of C_τ led to better predictions in comparison to its standard value [18]. Therefore, based on the findings reported in [18, 11], an improvement of the EDC approach for biomass combustion was proposed [31]. The new modified EDC model (referred to hereafter as extended EDC approach) was examined for the simulation of different biomass-derived-gas diffusion jet flames (encompassing both weakly and highly turbulent flow conditions) and compared to standard EDC. The results revealed better predictions of temperature, intermediate and minor species (e.g., CO, H_2, OH, NO, etc.) [31]. Since the extended EDC approach was comprehensively described in [31], only a brief overview of the model is presented below.

The standard EDC has been developed based on turbulent energy cascade method, while the mass fraction of species and EDC residence time are related to turbulence intermittency [15, 50].

However, the assumption of strong dissipation intermittency at high turbulent Reynolds number makes the application of the model more suitable for highly turbulent flow conditions. By considering the transfer of turbulent kinetic energy to dissipative structures, the intermittency factor for fine structure regions can be expressed as follows [50]:

$$\gamma^* = \left(\frac{u^*}{u'}\right)^3 = \left(\frac{l^*}{l'}\right) \tag{6-12}$$

$$\tau^* = 0.5\left(\frac{l^*}{u^*}\right) \tag{6-13}$$

$$\frac{\gamma^{*2/3}}{\tau^*} = \left(2\frac{u^*}{l^*}\right)\left(\frac{u^*}{u'}\right)^2 = \left(2\frac{u^*}{l^*}\right)\gamma_\lambda^2 \tag{6-14}$$

where γ_λ is the fine structure volume fraction [51], u' and l' are, respectively, the velocity and length scales corresponding to the energy containing range of the energy spectrum [20], and u^* and l^* represent the velocity and length scale of fine structures, respectively. As already mentioned, the fine structure length scale is assumed to be on the order of Kolmogorov length scale ($l^* = \xi\eta$). For the extended EDC, fractal modelling (FM) approach is adopted for turbulent intermittency in the inertial range energy transfer [52, 53]. Just to mention that while FM approach has commonly been used in studies related to the wrinkling of the flame front of turbulent premixed combustion (e.g., [54]), it has also successfully been applied for the simulation of turbulent non-premixed flames (e.g., [31, 55]). It is well accepted that, in a turbulent reacting flowfield, the flame structure is independent on the global flame topology and has to be viewed locally. This is why FM approach could be applied to non-premixed, partially premixed or premixed flame regime [55]. Based on this method, the mass fraction occupied by the fine structures, as well as the ratio of velocity of a fine structure to the integral velocity scale can be expressed as [31, 52]:

$$\gamma^* = \left(\frac{l^*}{l'}\right)^{3-D_c} \tag{6-15}$$

$$\frac{u^*}{u'} \sim \left(\frac{l^*}{l'}\right)^{\frac{D_c-2}{3}} \tag{6-16}$$

where D_c is an intermittency parameter introduced as fractal dimension [53]. As explained in [31], the value of D_c can be related to the characteristics of turbulent flow (i.e., Re_t), and it can be calculated using the mathematical methodology reported in Giacomazzi et al. [53]. All introduced parameters in Eqs.(6-12) to (6-14) can be re-written using the intermittency and FM approach from Eqs.(6-15) and (6-16). It is worth mentioning that, for simplicity, all aforementioned parameters (i.e., D_c, γ^*, τ^*, γ_λ, u' and l') can be correlated to the characteristics of turbulent flow (e.g., Re_t, and turbulent time scale: $T_t \sim (l'/u') \sim (k/\varepsilon)$). The final expressions of the extended EDC's γ^*, τ^* and the average species reaction rate can be written as follows (the mathematical derivation is comprehensively described in [31]):

$$\gamma^* = \xi^{3-D_c}\left(Re_t{}^{-3/4}\right)^{3-D_c} \tag{6-17}$$

$$\tau^* = 0.5 T_t \gamma^{*\frac{1+\frac{2}{3}-\frac{D_c}{3}}{3-D_c}} \tag{6-18}$$

$$\overline{R_i} = \frac{\overline{\rho}\gamma^{*\frac{2}{3}\left(\frac{D_c-2}{3-D_c}\right)}}{(1-\gamma^*)\tau^*}\left(Y_i^* - \overline{Y_i}\right) = \frac{\overline{\rho}}{\tau_{mix}}\left(Y_i^* - \overline{Y_i}\right) \tag{6-19}$$

Where, for the extended EDC, τ_{mix} is a new characteristic mixing time scale (similar to τ_m of the standard EDC). The sensitivity analysis was performed on the value of ξ with respect to the level of turbulence, and was reported in Ref [31]. As a result, the values of 1.75 and 3.15 were selected, respectively, for weakly and highly turbulent flow conditions and consequently a weighting function is employed to approximate the value of ξ based on the level of turbulence (i.e., the value

of Re_t) between low turbulent flow value (i.e., $\xi = 1.75$) and high turbulent flow value (i.e., $\xi = 3.15$). Additional details can be found in [31].

The mathematical definition of γ^* for the standard and extended EDC is different and hence a direct comparison between these two models based on this parameter is not possible. However, a comparison between the two models can performed using the time scale ratios (i.e., τ^*/τ_m for the standard EDC, versus τ^*/τ_{mix} for the extended EDC). Figure 6-1 shows the profiles of τ^*/τ_m and τ^*/τ_{mix} as a function of Re_t. As can be seen in Figure 6-1, for low and moderate turbulent Reynolds number (i.e., $Re_t < 135$), the time scale ratio of the extended EDC is lower than that of the standard EDC. However, when the level of turbulence increases (i.e., $Re_t > 135$), the extended EDC shows higher time scale ratio compared than the standard EDC. Given the standard EDC formulation (i.e., Eq.(6-11)), lower and higher values of τ^*/τ_m are attributed to, respectively, lower and larger values of γ^*. Literature showed that, for biomass-derived-gas jet flames, the predictions of temperature and species concentrations in weakly turbulent flow conditions can be improved using a lower value of γ^*, while using larger value of γ^* leads to improvement in highly turbulent flow conditions [18]. It is expected that, based on the level of turbulence (i.e., the value of Re_t), these observations apply when using the extended EDC.

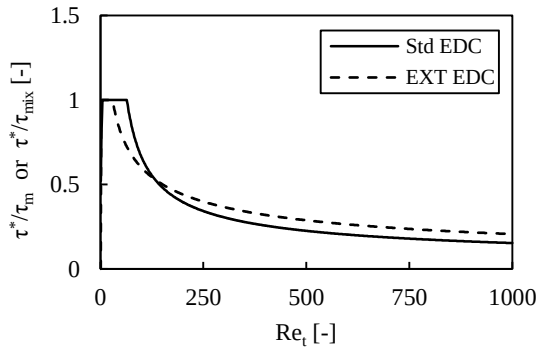

Figure 6-1. EDC over mixing time scales ratio of the standard and extended EDC approaches.

The chemical mechanism adopted in the present study is a reduced mechanism of methane-air combustion proposed by Jones and Lindstedt [54] along with combustion chemistry of levoglucosan [55]. The reduced chemical mechanism is mainly selected owing to its low computational cost. It is well known that employing reduced chemistry leads to the predictions of high peak temperature. Moreover, since the pathway of the formation/destruction of intermediate and minor species cannot be comprehensively described via reduced chemical mechanisms, their concentration is usually not accurately predicted. However, a previous study on the current furnace showed that, when adopting a proper reduced chemical mechanism, EDC approach is able to adequately reproduce the temperature field and both major and minor species concentrations [3].

6.3.3 Modeling of pollutants (CO, NO)

As previously stated, employing a detailed chemical mechanism can describe better the pathway of formation/destruction of intermediate species and pollutants. However, incorporating detailed chemistry with EDC model requires substantial computational cost. In the present study, the chemical mechanism proposed by Jones and Lindstedt [54] is adopted for CO concentration, which has already been used in a previous study of the current furnace with the same operating conditions [3]. This mechanism was found to reproduce the experimental measurements of CO [3].

Modeling NO_x formation is performed using the standard post-processing of NO_x formation/destruction method of ANSYS Fluent [30]. The global chemistry scheme used in this method is adopted based on the work of De Soete [56]. Three pathway of formation/destruction of NO_x is used for the simulation; that is, thermal NO_x, fuel NO_x and NO_x re-burning/reduction. It is assumed that all FBN in a biomass fuel is converted to the NH_3 and it is released during devolatilization process. However, for NO_x re-burning process, HCN is assumed as the intermediate species that is formed during the interaction of NO and hydrocarbon radicals (i.e.,

CH_i). The contribution of HCN to formation/destruction of NO depends on the favorable fuel-rich or oxygen-rich conditions within the furnace. Therefore, the formation of fuel-NO_x via HCN is also considered. The re-burning process of NO takes place in the temperature range of 1600 K<T<2100 K [30]. The concentration of CH_i species (e.g., CH, CH_2, CH_3), which is not part of the adopted chemical mechanism, is required to describe the pathway of NO reduction. Therefore, a partial equilibrium approach based on the work of Kandamby et al. [57] is used, which adds a reduction path of NO in the fuel-rich re-burning zone to the fuel NO_x formation mechanism of De Soete [30]. The concentrations of CH_i are assumed based on the assumption of partial equilibrium between CH-radicals and re-burning equivalent fuel, which is assumed to be CH_4 [30]. Consequently, it can be concluded that as the concentration of CH_i is modeled based on the concentration of equivalent fuel species (i.e., CH_4), the accuracy of this approach is strongly dependent on the prediction of the reacting turbulent flowfield, temperature and species concentrations (i.e., mass fraction of CH_4 and O_2). The interaction of turbulent/chemistry is considered using the probability density function (PDF) method of temperature along with Beta-PDF option to account for the mean reaction rate of NO. More details about the adopted NO_x formation/destruction approach can be found in [30].

6.4 Physical and numerical setups

A 8-11 kW small lab-scale updraft feeding grate firing biomass combustor [5, 32] is adopted. This furnace consists mainly of a cylindrical combustor having a diameter of 0.2 m, which can be supplied with under-fire air-flow (i.e., primary air supply), as well as two sets of over-fire air-flow injectors (i.e., secondary and tertiary air supplies). For the examined operating conditions (i.e., 8 kW), the primary air with a mass flow rate of 0.581e-3 kg/s is injected through the grate. The secondary and tertiary excess air jets are supplied above the bed with a mass flow rate of,

respectively, 1.18e-3 and 1.89e-3 kg/s. All air flow rates are injected at 100 kPa and 298 K. The furnace is also fed with wood pellets at a mass flow rate of 0.461e-3 kg/s. The fuel feed rate is controlled within ±2% of the mean fuel mass flow rate. Occasional fluctuations in the mass flow rate was observed during experiment due mainly to difficulties in maintaining a constant feeding rate [32]. The furnace wall temperature is measured to be 873.15 K [5, 32]. Figure 6-2 shows a schematic view of the physical setup. More details about the experiment can be found in [5, 32].

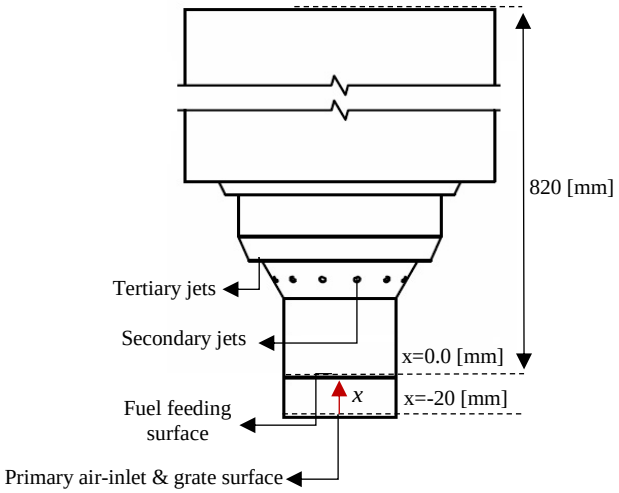

Figure 6-2. Schematic view of the 8-11 kW biomass combustor (adopted from Ref. [5]).

The CFD simulations are carried out using ANSYS Fluent R15.0. The spatial discretization of all conservation equations is performed using second order upwind scheme. The pressure-based coupled algorithm is employed as the pressure-velocity coupling method. A 3D non-uniform grid is used to model the furnace geometry. Due to azimuthal symmetry of the furnace, only a section of 60° of the furnace is modeled. The grid consists of about 201000 cells covering a domain which extendes from -20 mm below the top bed surface up to 820 mm above the bed. Local increase in grid resolution is used in the zone close to the bed as well as at the exit of secondary and tertiary jets, wherein high gradients of velocity, species concentration and temperature are expected to occur. It is worth mentioning that further grid refinement did not show significant change in the

predictions. Moreover, it is important to mention that due to the lack of information about the height of the bed [5, 32], the height of 20 mm for the bed (i.e., from x = -20.0 mm to x= 0.0 mm) was suggested based on trial and error in order to keep the top-bed surface at x = 0.0 mm. The In-Situ Adaptive Tabulation (ISAT) [58] algorithm with an ISAT error tolerance of $Err_{isat} = 10^{-4}$ is also used for increasing the CPU-intensive treatment when using chemical kinetics. It should be mentioned that the concentration of species remained unchanged when $Err_{isat} < 10^{-4}$.

The top bed surface (i.e., x = 0 mm in Figure 6-2) is used as a surface injector of the fuel particles. Non-slip condition at a constant temperature of 875.15 K along with zero normal gradients of species mass fractions are adopted for wall boundary conditions. Following previous simulations performed on the same furnace, the emissivity of the bed and walls is set as 0.9 [59]. Pressure-outlet condition is adopted for the outlet boundary. The influence of turbulence intensity on the predictions for the current furnace was reported in [5]. It was reported that while turbulent intensity in primary air has almost negligible effect on the results, the predictions of temperature field and species concentrations are sensitive to the level of turbulence intensity of the secondary and tertiary inlet boundaries. Hence, turbulence intensity for all inlet boundaries are selected here using the suggested values in Ref [5]. Table 6-2 summarizes the adopted boundary conditions for the simulation.

Table 6-2. Boundary conditions (Mass flows were calculated based on 1/6 of mean magnitudes [5])

	Mass flow	temperature	Turbulence	
	[kg/s]	[K]	I (%)	L [m]
Primary	0.968e-4	298	5	7e-2
Secondary	1.967e-4	298	23	4e-2
Tertiary	3.150e-4	298	58	4e-2
Fuel feeding	0.768e-4	298	N/A	6e-3

6.5 Results and discussion

The simulations are carried out to examine the performance of the extended EDC (EXT EDC) on the predictions of flow field, temperature and species concentrations of the gas-phase combustion of the aforementioned biomass furnace. The predictions of the standard EDC (STD EDC) are used for reference. The predictions of major species (i.e., O_2 and CO_2), minor species (i.e., CO and NO) and temperature field are compared with their experimental counterparts reported in [5, 32]. All measurements of temperature and species concentrations are taken along the centerline of the furnace.

Figure 6-3 presents the experimental and its counterpart's predictions, by both the standard and extended EDC models, of the axial temperature profiles along the centerline of the furnace (Figure 6-3a), as well as the temperature contours in the vicinity of the bed, secondary and tertiary airflow jets (Figure 6-3b). Figure 6-3a shows that the predictions of both EDC models can reasonably reproduce their experimental counterparts in most regions of the furnace. However, close to the fuel-bed surface (i.e., x = 0 [m]), although the extended EDC shows higher and closer predictions to the measurement, the overall prediction of both models is still not satisfactory. According to the profiles in Figure 6-3a, close to the bed and secondary air injection positions (i.e., $0 < x < 0.15$ [m]), the extended EDC approach predicts significant higher temperature along the centerline of the furnace in comparison with the standard EDC. On the other hand, compared to the extended EDC, the standard EDC shows slightly higher predictions of the temperature away from the centreline region of the furnace (i.e., $0.15 < x < 0.4$ [m]). This difference in the axial temperature profiles predicted by two models might be attributed to the different predicted heat released, which will be explained later.

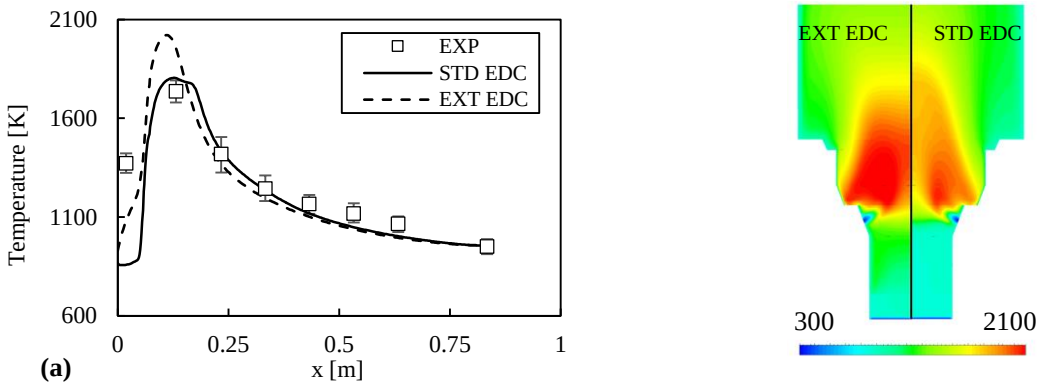

Figure 6-3. (a) Temperature profiles along the furnace centerline, and (b) temperature contours in Kelvin [K].

It is evident from Figure 6-3b that the core of the gas-phase combustion occurs close to the injection of secondary airflow jets. Fresh oxygen injected through secondary jets reacts with combustible volatile gases coming out of the bed, leading to an expansion of the products as a consequence of the heat release from the reactions [60]. However, the expansion of gases due to the heat released is predicted differently by the two EDC approaches. As can be seen in Figure 6-3b, shorter lengthwise (i.e., along the centerline) and wider (i.e., in the radial direction) high temperature region is predicted by extended EDC approach, whereas the standard EDC exhibits a longer lengthwise high temperature region distributed within a much narrower radial region position. This is an indication of a better prediction, by the extended EDC, of mixing between fresh oxygen and combustible volatile gases close to secondary jet injection, which leads to higher heat release and consequently a wider radial high temperature region [3]. The reminder of combustible volatile gases reacts with the fresh oxygen supplied from tertiary air jets. This appears near the shear layer produced by the injection of tertiary jets, where rapid mixing between oxygen and volatile gases takes place [3]. Figure 6-3b shows that a high temperature region occurs in this shear layer where a diffusion flame is established as the result of the interaction between tertiary air and volatile gases [5, 11]. As shown in Figure 6-3b, a wider temperature gradient is

predicted by the extended EDC which may be attributed to higher mixing rate and consequently higher reaction rate predicted in comparison with the standard EDC.

Figure 6-4 presents the profiles of CO_2 (Figure 6-4a) and O_2 (Figure 6-4b) along the centerline of the furnace. The major observation in Figure 6-4a and 6-4b is that, the extended EDC shows better predictions in the high temperature region and closer to the bed. The extended EDC predicts higher CO_2 concentration over $0 < x < 0.2$ [m] compared to its counterpart's standard EDC, which is an indication of higher consumption of fuel. This is also evident in Figure 6-3a where a higher temperature profile is predicted by the extended EDC within the same region as a result of greater fuel consumption and consequently higher heat release. On the other hand, the extended EDC shows slight under prediction of CO_2 (Figure 6-4a) and over prediction of O_2 (Figure 6-4b) over $0.2 < x < 0.3$ [m] but still within the experimental error. The observation that CO_2 is under-predicted by the extended EDC in the region of $0.2 < x < 0.3$ [m]) can be attributed to lower fuel consumption and consequently lower heat compared to the standard EDC (Figure 6-3a). Further downstream the furnace, the extended EDC approach shows better predictions of both CO_2 and O_2 concentration compared to the standard EDC. Nonetheless, the trends of the predicted profiles of both CO_2 and O_2 mole fractions are similar for both EDC models. The fact that the concentrations of species remain approximately unchanged downstream the furnace (Figure 6-4a and b) is an indication of the chemical equilibrium condition in this region of the furnace [3]. Under chemical equilibrium conditions, it is expected that both models have the same value of Y_i^* (i.e., mass fraction within the fine structure) for the duration of the EDC residence time of mass transfer between a fine-structure and its surrounding fluid (i.e., τ^*). The fact that almost similar trend is predicted by both models under equilibrium chemistry condition, the main quantitative difference

in prediction of species concentrations is only attributed to the difference in the characteristic mixing time scale (i.e., τ_m for STD EDC, and τ_{mix} for EXT EDC) computed by each model.

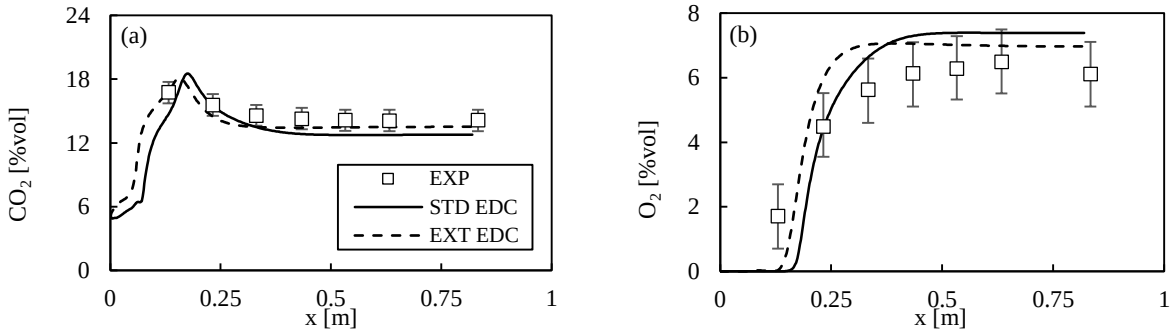

Figure 6-4. Profiles of (a) CO_2 and (b) O_2 mole fractions along the furnace centerline.

Figure 6-5 shows the profiles of CO concentration along the centerline of the furnace as predicted by the standard and extended EDC models and compared with their experimental counterparts. The first observation in this figure is that the standard EDC approach exhibits a significant over-prediction of CO concentration especially downstream of the furnace. This also can be observed from the conservation of carbon element in Figure 6-4a, where the standard EDC shows under-prediction of CO_2 concentration downstream of the furnace (i.e., x > 0.4 [m]). On the other hand, Figure 6-5 shows a significant improvement in the prediction of CO concentration using the extended EDC approach. The better prediction of CO concentration with the extended EDC is an indication of its suitability for weakly and highly turbulent flow conditions and hence, its ability for predicting slow-forming species [31]. However, both models predict similar trend of CO concentration profile along the centerline of the furnace. Figure 6-6 presents the profiles of CO net reaction rate (Figure 6-6a) and EDC residence time (Figure 6-6b) along the centerline of the furnace as predicted by the standard and extended EDC models. As can be seen in Figure 6-6a, the two models predict quantitatively different rate of CO production in the vicinity of the bed. However, farther away from the bed and close to the high temperature region (x<0.25 [m]), the profiles of Figure 6-6a show also that the standard EDC model predicts a relatively larger

magnitude of CO net-reaction rate compared to its counterpart extended approach. Moreover, downstream of the furnace and away from the high temperature region (x>0.25 [m]), both models show no significant difference in the prediction of the production rate of CO concentration (Figure 6-6a). Therefore, the overall quantitative improvement in the prediction of CO concentration by the extended EDC model might be related to its better predictions of CO concentration in the high temperature region. Figure 6-6b shows the predicted profiles of EDC residence time along the centerline. As already stated in [31], compared to the standard EDC, the extended EDC approach shows relatively longer combustion residence time at different levels of turbulence conditions. The sensitivity analysis revealed a significant improvement in the prediction of slow-forming CO species, at both weakly and highly turbulent flow conditions, when a larger EDC residence time scale is adopted instead of the standard EDC time scale [18]. This improvement might be attributed to better prediction of CO in the fine structure region using chemical kinetic rates; that is, a better prediction of Y_{CO}^{*} [18, 31]. As can be seen in Figure 6-6b, while both EDC models predict relatively similar trend of EDC residence time profiles, the extended approach predicts a larger EDC time scale along the centerline (almost three times larger than that of standard EDC). Thus, the quantitatively better prediction of CO concentration by extended EDC might be related to an improved Y_{CO}^{*} as a result of a larger EDC residence time scale.

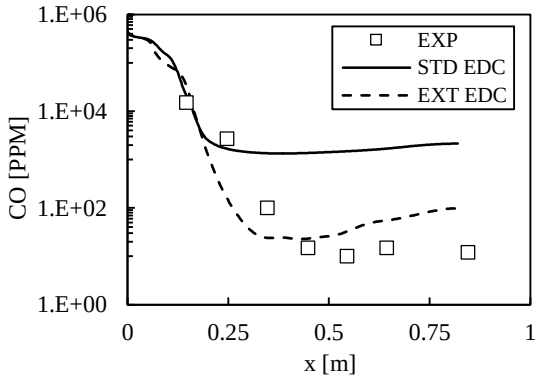

Figure 6-5. Profiles of CO concentrations along the furnace centerline.

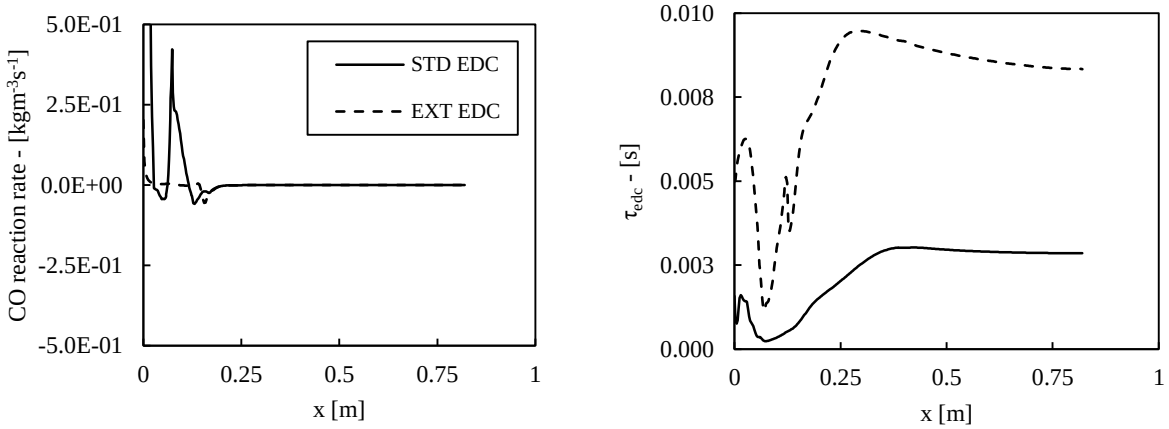

(a) (b)

Figure 6-6. Profiles of (a) CO reaction rate and (b) EDC residence time scale along the furnace centerline.

Figure 6-7 presents the contours of mass fractions of $C_6H_{10}O_5$ (Figure 6-7a) and CH_4 (Figure 6-7b) as predicted by the standard and extended EDC. It can be seen from the mass fraction contours in Figure 6-7 that both models show the formation of heavy and light hydrocarbons within the bed section, with approximately same maxima. However, the consumption of both $C_6H_{10}O_5$ and CH_4 is predicted differently by the two EDC models, especially in the vicinity of the bed region and before secondary air injection. These contours in Figure 6-7 clearly show that higher consumption of fuel components within the region close to the bed is predicted by the extended EDC, while the standard EDC predicts a slightly higher consumption of fuel species in the vicinity and after the

position of secondary air injection. These observations are in line with the predicted temperature field; where the extended EDC predicted higher temperature in the vicinity of the bed compared to standard EDC, which is due to higher consumption of fuel components in this region (i.e., lower mass fractions of $C_6H_{10}O_5$ and CH_4 close to the bed, as seen in Figure 6-7). On the other hand, the contours in Figure 6-7 show also that, in comparison with the standard EDC, the extended EDC model predicts slightly lower consumption of the fuel components close to the secondary and tertiary air injections, (i.e., higher mass fraction of $C_6H_{10}O_5$ and CH_4, see Figure 6-7). This lower consumption of the fuel components predicted by the extended EDC might be the reason of lower heat released and consequently lower temperature field in these regions of the furnace (Figure 6-3). It is important to mention that the yields of hydrocarbon gases (e.g., CO, CH_4) may increase in higher temperature regions due to the crack of tar composition (i.e., $C_6H_{10}O_5$) into other hydrocarbons in the vicinity of the bed [61]. As the flow field in vicinity of the bed is relatively weakly turbulent, the chemical and mixing time scale become more comparable, leading to having kinetically dominated condition. It is well known that using a detailed chemical mechanism leads to improve the predictions of species concentrations and temperature field in high temperature region and kinetically dominated condition [3]. This clearly demonstrates that using a detailed chemical reaction mechanism for tar oxidation will improve the description of the pathway of tar consumption and may consequently improve the predictions of species and temperature concentration. However, implementing such a detailed chemical mechanism, which contains a number of sub-reaction pathways and additional intermediate species, will consequently increase the computational cost. Moreover, previous studies on the current furnace showed that away from the bed, the predictions of temperature and species concentrations are not much influenced by either of adopted chemical mechanism, or adopted bed model (i.e., the change in mass fractions of

the assumed species coming out of the bed) [3, 5]. Therefore, due to the limited computational resources of the present study, only a partial oxidation of $C_6H_{10}O_5$ to produce carbon monoxide is assumed for the reaction pathway of tar combustion.

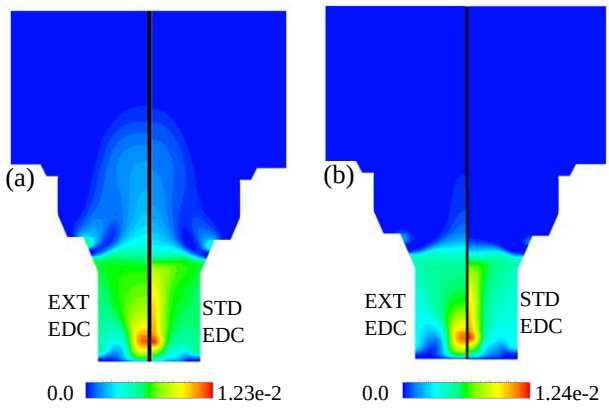

Figure 6-7. Contours of (a) $C_6H_{10}O_5$ and (b) CH_4 mass fractions.

Figure 6-8 presents the contours of CH_4 (Figure 6-8a), CO (Figure 6-8b) and CO_2 (Figure 6-8c) mass fractions, as well as temperature (Figure 6-8d) within the bed section (starting from the grate; i.e., x=-20 [mm]) up to 2 cm above the fuel-bed surface. Using the same bed model, the two simulated cases may generate different predictions of species concentration and temperature within the bed section due to the following reasons. The gas-phase combustion model is also considered within the bed area and hence, the two EDC approaches may lead to different predictions in the bed section. Moreover, using either of the EDC combustion models, the simulation of the freeboard combustion produce different predictions of the temperature fields and consequently different radiative heat fluxes above the bed (see Figure 6-3), which, in turn, can affect the species and temperature predictions within the bed. The effect of the adopted EDC model on the devolatilization process is evident. This can be observed by looking, for example, at the mass fraction of CH_4 in Figure 6-8a, which is one of the volatile gases released from the solid biomass fuel during devolatilization process. According to Figure 6-8a, most of the mass fraction of CH_4 spreads toward the centerline of the furnace within the bed section (slightly wider when using the extended EDC). However, close to the furnace wall and also above the fuel-bed surface, the extended EDC shows lower mass fraction of CH_4 compared to that of standard EDC. The results of CO mass fraction in Figure 6-8b also show that, while the maxima of CO mass fraction is

predicted close to the centerline and also in the vicinity of the grate by both models, higher concentration of CO is predicted by the standard EDC. In the case of CO_2 mass fraction (Figure 6-8c), its maxima is distributed away from the centerline regardless of the adopted combustion model. Moreover, the extended EDC model predicts slightly higher amount of CO_2 mass fraction (Figure 6-8c). The contours in Figure 6-8d also show that both EDC models produce slightly different predictions of temperature distributions within the bed. On the other hand, according to Figure 6-8d, a higher temperature field is predicted above the fuel-bed surface when using the extended EDC, which corroborates the results in Figure 6-7. The contours of CO mass fraction in Figure 6-8b indicate that the char burn-out reaction is initiated close to the grate and toward the centerline of the furnace. Nevertheless, the extended EDC predicts a greater distribution of CO in the radial direction inside the bed, while the standard EDC predicts a higher CO within a narrow region of the bed. On the other hand, one may expect that, within this region of the furnace, a portion of the lower mass fraction of CO predicted by the extended EDC close to the centerline might be related to the destruction of CO into CO_2. However, the mass fractions of CH_4 and CO_2 (Figure 6-8a and c, respectively), as predicted by both models within the same region of the bed, are relatively similar. This suggests that most of the primary air-oxygen in this region of the bed is consumed during char burn-out reactions, which consequently results in insufficient (very lean) oxygen concentration to react with either CO or CH_4. The formation of CO_2 within the bed section might be related to three different processes; a faction of CO_2 could be generated from the destruction of CO into CO_2, generated during devolatilization process or might be related to the consumption of combustible volatile gases within the bed section. It should be mentioned that, compared to the standard EDC, the higher concentration of CO_2 close to the wall, as predicted by the extended EDC in Figure 6-8c, might be related to higher consumption of volatile gases (e.g., CH_4). This is supported by the lower presence of CH4 in the same region of the bed (see Figure 6-8a). Moreover, the similar mass fraction of CO within this region of the furnace (close to the wall, see Figure 6-8b) indicates that the rate of destruction of the first product of reactions between volatile hydrocarbons and oxygen (i.e., CO) to form CO_2 is predicted very similarly using either of the EDC approaches.

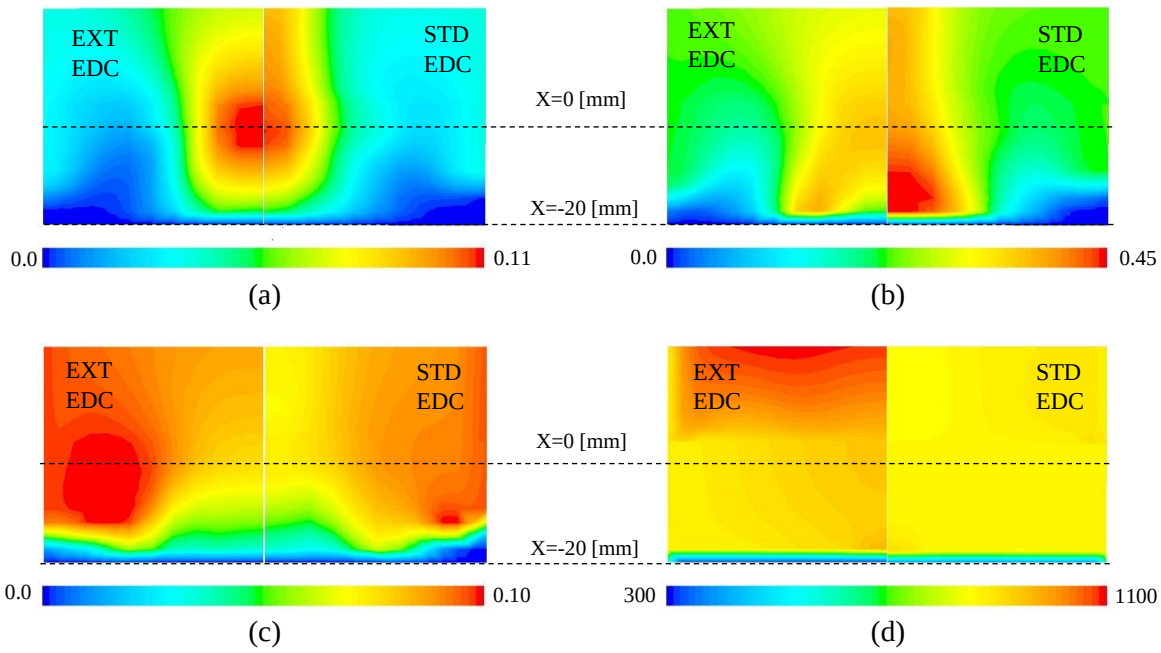

Figure 6-8. Contours of (a) CH_4, (b) CO, (c) CO_2 mass fraction and (d) temperature (in Kelvin [K]).

Figure 6-9 presents the predictions of mass fractions of NH_3 (Figure 6-9a), HCN (Figure 6-9b) and NO (Figure 6-9c) in the vicinity of the bed as well as close to the secondary and tertiary air injections. As discussed earlier, NH_3 is introduced as the only intermediate species of fuel NO_x. The contours of NH_3 mass fractions in Figure 6-9a shows that, similar to the observation of fuel consumption in Figure 6-7, both EDC approaches predict approximately similar formation of NH_3 from solid fuel particle with similar maxima. However, it is clear from Figure 6-9a that the predicted consumption of NH_3 is higher by the extended EDC compared to the standard EDC. The formation of HCN is considered only as the intermediate species in re-burning/reduction of NO_x, However HCN may also contribute to form NO species as one of the fuel-NO_x intermediate. The reduction of NO_x due to re-burning of NO takes place in the presence of CH_i radicals [1].

According to the contours of HCN mass fraction in Figure 6-9b, the highest concentration of CH_i radical occurs in the vicinity of the secondary jet spreading close to the center of the flame where the high temperature region start to establish (see Figure 6-3b and Figure 6-9b). However, compared to the standard EDC, the extended EDC model also predicts higher formation of HCN due to re-burning pathway in the vicinity of the bed. In a staged combustion (i.e., by introducing primary, secondary and tertiary airflow), if favorable fuel-rich condition exists, HCN species may produce N_2 rather than contributing in producing NO_x. Such condition may occur in the region between the bed and secondary air, where the concentration of fuel species is high (Figure 6-7) with low level of oxygen (Figure 6-4b). However, for the region close to the secondary air, where the level of both HCN and O_2 is high (see Figure 6-9b), HCN may contribute to the formation of NO. Nevertheless, the low level of HCN concentration shown in Figure 6-9b is an indication that the contribution of HCN to the formation or reduction of NO is negligible.

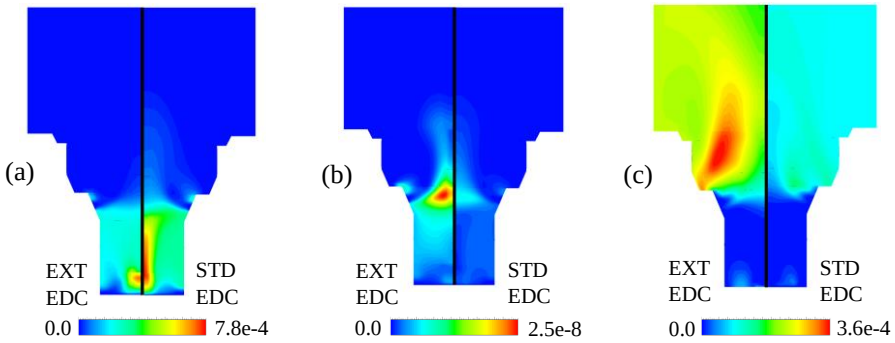

Figure 6-9. Contours of (a) NH_3, (b) HCN, and (c) NO mass fractions.

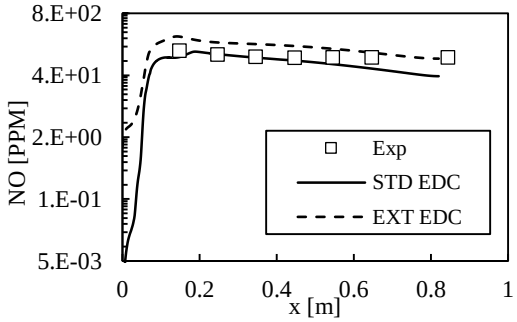

Figure 6-10. Profiles of NO concentrations along the furnace centerline.

Figure 6-9c presents the prediction of mass fraction of NO using the standard and extended EDC models. According to this figure, the extended EDC clearly predicts higher level of NO pollutant compared to standard EDC. The contours in Figure 6-9c show that both models predict the highest level of NO concentration in the region between the spread of secondary and tertiary air injections (in the shear layers produced in the wake of the air injection zone) where rapid mixing between oxygen and fuel gases occurs. However, the magnitude of NO mass fraction predicted by the extended EDC is significantly higher. This might be the result of higher temperature field in this region, and consequently the production of NO via the thermal NO_x pathway (Figure 6-3). Moreover, higher temperature also results in higher chemical kinetic rates of the formation of NO from NH_3. Figure 6-10 shows the EDC models' predictions of NO concentration profiles along the centerline of the furnace. The profiles of NO in this figure reveal that, compared to extended EDC, the standard EDC model predicts significantly lower level of NO concentration close to the bed. Also, compared to experimental measurements, the extended EDC shows an over-prediction of NO concentration especially close to high temperature region, while the standard EDC shows better agreement with measurements in the same region. However, the profiles in Figure 6-10 show that, farther downstream the furnace, the concentration of NO is quantitatively better predicted by the extended EDC. Nevertheless, Figure 6-10 shows that, overall, the predicted profiles of NO concentration are qualitatively and quantitatively in agreement with the measurements.

6.6 Summery and Conclusions

This study examined the performance of an extended version of the Eddy Dissipation Concept (EDC) model for simulating the gas-phase combustion of a grate firing biomass combustor. To account for the conversion of solid biomass fuel within the bed section, a particle-based bed model was adopted. The pathway of consumption of assumed gas-fuel component (i.e., CH_4 and

$C_6H_{10}O_5$), as well as the pathway of formation/reduction of NO were studied. The predictions of the extended EDC were compared with its standard version and published experiments. The main findings are summarized below.

- A simplified particle-based bed model was found to satisfactorily account for the conversion of solid biomass fuels.
- Both standard and extended EDC approaches were able to reasonably reproduce the experimental measurements of temperature, major species concentration, and NO emissions. However, the prediction of CO was only satisfactory predicted by the extended EDC.
- The heat release was predicted slightly differently using either of the extended or standard EDC models. The extended EDC approach shows a wider (azimuthal) high temperature field close to the secondary and tertiary air injectors. On the other hand, the standard EDC predicts longer lengthwise high temperature region along the centerline of the furnace. A wider and high temperature region predicted by the extended EDC might be attributed to greater mixing rate of this model compared to its standard EDC counterpart.
- The production of gas-fuel species as well as NH_3 within the bed were predicted similarly by both EDC approaches. However, its consumption was predicted relatively differently; where the extended EDC predicted higher consumption of CH_4, $C_6H_{10}O_5$ and NH_3 in the vicinity of the bed.
- The prediction of NO emissions was satisfactory predicted by both model. However, the extended EDC slightly over-predicted NO concentration in the high temperature region compared to standard EDC and experimental measurements. This over-prediction might be the result of partial contribution from thermal NO_x to the total NO emissions. It was also

found that the reduction of NO to HCN in fuel-rich zones was negligible under the current operating condition of air-staged technology furnace.

Finally, it can be concluded that, overall, the extended EDC approach exhibited better performance than its counterpart's standard version for simulating the gas phase combustion of a grate-firing biomass furnace. While the extended EDC produced better profiles of temperature and major species concentrations, its prediction of CO and NO concentrations (i.e., slow-forming and kinetically dominated pollutants) is significantly improved.

6.7 References

[1] S. Sukumaran and S. Kong, "Modeling fuel NOx formation from combustion of biomass-derived producer gas in a large-scale burner," Combustion and Flame, vol. 160, pp. 2159-2168, 2013.

[2] C. Yin, L. Rosendahl and S. Kaer, "Grate-firing of biomass for heat and power production," Progress in Energy and Combustion Science, vol. 34, pp. 725-754, 2008.

[3] M. Farokhi, M. Birouk and F. Tabet, "A computational study of a small-scale biomass burner: The influence of chemistry, turbulence and combustion sub-models," Energy Conversion and Management, vol. 143, pp. 203-217, 2017.

[4] S. Van Loo and J. Koppenjan, Handbook of biomass combustion and co-firing, Twente University Press, 2002.

[5] T. Klason and X. Bai, "Computational study of the combustion process and NO formation in a small-scale wood pelletfurnace," Fuel, vol. 86, pp. 1465-1474, 2007.

[6] S. Zahirovic, R. Scharlera, P. Kilpinenc and I. Obernbergera, "A kinetic study on the potential of a hybrid reaction mechanism for prediction of NOx formation in biomass grate furnaces," Combustion Theory and Modelling, vol. 15, pp. 645-670, 2011.

[7] S. Zahirovic, R. Scharler, P. Kilpinen and I. Obernberger, "Validation of flow simulation and gas combustion sub-models for the CFD-based prediction of NOx formation in biomass grate furnaces," Combustion Theory and Modelling, vol. 15, pp. 61-87, 2010.

[8] M. Buchmayr, J. Gruber, M. Hargassner and C. Hochenauer, "A computationally inexpensive CFD approach for small-scale biomass burners equipped with enhanced air staging," Energy Conversion and Management, vol. 115, pp. 32-42, 2016.

[9] D. Veynante and L. Vervisch, "Turbulent combusition modeling," Progress in energy and combustion science, vol. 28, pp. 193-266, 2002.

[10] A. Shiehnejadhesar, R. Scharler, R. Mehrabian and I. Obernberger, "Development and validation of CFD models for gas phase reactions in biomass grate furnaces considering gas streak formation above the packed bed," Fuel Processing Technology, vol. 139, pp. 124-148, 2015.

[11] M. Farokhi and M. Birouk, "Application of Eddy Dissipation Concept for modeling biomass combustion, Part 2" Gas-phase combustion modeling of a small-scale fixed bed furnace," Energy and fuel, vol. 30, pp. 10800-10808, 2016.

[12] X. Zhang, Q. Chen, R. Bradford, V. Sharifi and J. Swithenbank, "Experimental investigation and mathematical modelling of wood combustion in a moving grate boiler," Fuel Process Technology, vol. 91, pp. 1494-1499, 2010.

[13] J. Porteiro, J. Collazo, D. Patiño, E. Granada, J. C. Moran Gonzalez and J. L. Míguez, "Numerical Modeling of a Biomass Pellet Domestic Boiler," Energy & Fuels, vol. 23, pp. 1067-1075, 2009.

[14] M. Buchmayr, J. Gruber, M. Hargassner and C. Hochenauer, "Performance analysis of a steady flamelet model for the use in small-scale biomass combustion under extreme air-staged conditions," Journal of the Energy Institute, 2017.

[15] B. F. Magnussen, "On the structure of turbulence and a generalized eddy dissipation concept for chemical reaction in turbulent flow," in Proceedings of the 19th AIAA Aerospace Science Meeting, St. Louis, 1981.

[16] M. Bugge, Ø. Skreiberg, N. Haugen, P. Carlsson, E. Houshfar and T. Løvås, "Numerical simulation of staged biomass grate fired combustion with an emphasis on NOx emissions," Energy Procedia, vol. 75, pp. 156-161, 2015.

[17] A. Shiehnejadhesar, K. Schulze, R. Scharler and I. Obernberger, "A new innovative CFD-based optimization method for biomass combustion plants," Biomass bioenergy, vol. 53, pp. 48-53, 2013.

[18] M. Farokhi and M. Birouk, "Application of Eddy Dissipation Concept for modeling biomass combustion, Part 1: Assessment of model coefficients," Energy and Fuels, vol. 12, pp. 10789-10799, 2016.

[19] A. Mardani, "Optimization of the Eddy Dissipation Concept (EDC) model for turbulence-chemistry interactions under hot diluted combustion of CH4/H2," Fuel, vol. 191, pp. 114-129, 2017.

[20] A. De, E. Oldenhof, P. Sathiah and D. Roekaerts, "Numerical simulation of Delft-Jet-in-Hot-Coflow (DJHC) flame using eddy dissipation concept model for turbulent-chemistry interaction," Flow, turbulent and combustion, vol. 87, pp. 537-567, 2011.

[21] A. Parante, M. Malik, F. Contino, A. Cuoci and B. Dally, "Extension of the eddy dissipation concept for turbulent/chemistry interaction to MILD combusiton," Fuel, vol. 163, pp. 98-111, 2016.

[22] J. Warnatz, U. Mass and R. Dibble, Combustion Physical and Chemical Fundamentals, Modeling and Simulation, Experiments, Pollutant Formation, Berlin: Springer, 1995.

[23] P. Glarborg, A. Jensen and J. Johnsson, "Fuel nitrogen conversion in solid fuel fired systems," Progress in energy and combustion science, vol. 29, pp. 89-113, 2003.

[24] M. Hupa, O. Karlström and E. Vainio, "Biomass combustion technology development - It is all about chemical details," Proceedings of the Combustion Institute, vol. 36, pp. 113-134, 2016.

[25] G. Stubenberger, R. Scharler, S. Zahirovi´c and I. Obernberger, "Experimental investigation of nitrogen species release of different solid biomass fuels as a basis for release models," Fuel, vol. 87, pp. 793-806, 2008.

[26] H. Zhou, A. Jensen, P. Glarborg and A. Kavaliauskas, "Formation and reduction of nitric oxide in fixed-bed combustion of straw," Fuel, vol. 85, pp. 705-716, 2006.

[27] H. Liu and B. Gibbs, "Modelling of NO and N2O emissions from biomass-fired circulating fluidized bed combustors," Fuel, vol. 81, pp. 271-280, 2002.

[28] E. Vainio, A. Brink, M. Hupa, H. Vesala and T. Kajolinna, "Fate of Fuel Nitrogen in the Furnace of an Industrial Bubbling Fluidized Bed Boiler during Combustion of Biomass Fuel Mixtures," Energy and fuels, vol. 26, pp. 94-101, 2012.

[29] C. Mandl, I. Obernberger and R. Scharler, "Characterisation of fuel bound nitrogen in the gasification process and the staged combustion of producer gas from the updraft gasification of softwood pellets," Biomass and Bioenergy, vol. 35, pp. 4595-4604, 2011.

[30] ANSYS., "ANSYS Fluent Theory Guide, Release 15.0," Ansys.

[31] M. Farokhi and M. Birouk, "A new EDC based approach for modelig turbulence/chemistry interaction of the gas-phase of biomass combustion," Fuel, vol. 220, pp. 420-436, 2018.

[32] H. Wiinikka, Writer, Ph.d. thesis [Performance], High Temperature Aerosol Formation and Emission Minimisation during Combustion of Wood Pellets. Luleå University of Technology, 2005.

[33] M. F. Modest, Radiative heat transfer, New yourk: Academic press, 2003.

[34] N. Selçuk and N. Kayakol, "Evaluation of descrete ordinates method for radiative transfer in rectangular furnaces," Int. J. Heat Mass Transfer, vol. 40, pp. 213-222, 1997.

[35] R. Mehrabian, R. Scharler, A. Weissinger and I. Obernberger, "Optimisation of biomass grate furnaces with a new 3D packed bed combustion model - on examle of a small-scale underfeed stocker furnace," in 18th European Biomass Conference and Exhibition, 3-7 May 2010, Lyon, France, 2010.

[36] M. GÃ³mez, J. Porteiro, D. Patiño and J. Míguez, "CFD modelling of thermal conversion and packed bed compaction in biomass combustion," Fuel, vol. 117, pp. 716-732, 2014.

[37] H. Khodaei, Y. Al-Abdeli, F. Guzzomi and G. Yeoh, "An overview of processes and considerations in the modeling of fixed-bed biomass combustion," Energy, vol. 88, pp. 946-972, 2015.

[38] R. S. Miller, K. Harstad and J. Bellan, "Evaluation of Equilibrium and Non-Equilibrium Evaporation Models for Many Droplet Gas-Liquid Flow Simulations," International Journal of Multiphase Flow, vol. 24, pp. 1025-1055, 1998.

[39] W. Ranz and W. Marshall, "Vaporation from Drops, Part I," Chem. Eng. Prog., vol. 48, pp. 141-146, 1952.

[40] S. Sazhin, "Advanced Models of Fuel Droplet Heating and Evaporation," Progress in energy and combustion science, vol. 32, pp. 162-214, 2006.

[41] E. Girgis and W. L. H. Hallett, "Wood Combustion in an Overfeed Packed Bed, Including Detailed Measurements within the Bed," Energy and fuels, vol. 24, pp. 1584-1591, 2010.

[42] H. Thunman, F. Niklasson, F. Johnsson and B. Leckner, "Composition of Volatile Gases and Thermochemical Properties of Wood for Modeling of Fixed or Fluidized Beds," Energy and fuels, vol. 15, pp. 1488-1497, 2001.

[43] R. Mehrabian, S. Zahirovic, R. Scharler, I. Obernberger, S. Kleditzsch, S. Wirtz, V. Scherer, H. Lu and L. L. Baxter, "A CFD model for thermal conversion of thermally thick biomass particles," Fuel processing technology, vol. 95, pp. 96-108, 2012.

[44] K. M. Bryden and K. W. Ragland, "Numerical Modeling of a Deep, Fixed Bed Combustor," Energy and fuels, vol. 10, pp. 269-275, 1996.

[45] H. Fatehi and X. Bai, "A Comprehensive Mathematical Model for Biomass Combustion," Combustion Science and Technology, vol. 186, pp. 574-593, 2014.

[46] F. Tabet, V. Fichet and P. Plion, "A comprehensive CFD based model for domestic biomass heating systems," Journal of energy Institude, vol. 89, pp. 199-214, 2016.

[47] T. Jurena, Writer, Numerical modelling of grate combustion. [Performance]. Faculty of mechanical engineering, Institute of Process and Enviromental Engineering. Brno university of Technology, 2012.

[48] S. K. Kaer, Writer, Numerical Investigation of Ash Deposition in Straw-fired Boilers. [Performance]. PhD thesis, Aalborg University, Denmark, 2001.

[49] B. Lilleberg, D. Christ and I. Ertesvag, "Numerical Simulation with an Extinction Database for Use with the Eddy Dissipation Concept for Turbulent Combustion," Flow turbulence combustion, vol. 91, pp. 319-346, 2013.

[50] R. Rydén, L. Eriksson and S. Olovsson, "Large Eddy Simulation of Bluff Body Stabilised Turbulent Premixed Flames," in ASME 1993 International Gas Turbine and Aeroengine Congress and Exposition, Cincinnati, Ohio, USA, 1993.

[51] H. Bao, Writer, Development and Validation of a New Eddy Dissipation Concept (EDC) Model for MILD Combustion. [Performance]. MS.c. thesis, the Delft University of Technology, 2017.

[52] O. Gulder, "Contribution of small scale turbulence to burning velocity of flamelets in the thin reaction zone regime," Proceedings of the Combustion Institute, vol. 31, pp. 1369-1375, 2007.

[53] E. Giacomazzi, C. Bruno and B. Favini, "Fractal modelling of turbulent mixing," Combustion Theory and Modelling, vol. 3, pp. 637-655, 1999.

[54] O. Gulder, "Turbulent premixed combustion modelling using fractal geometry," in Twenty-Third Symposium (International) on combustion/The Combustion Institute, 1990.

[55] E. Giacomazzi, C. Bruno and B. Favini, "Fractal modelling of turbulent combustion," Combustion Theory and Modelling, vol. 4, pp. 391-412, 2000.

[56] W. Jones and R. Lindstedt, "Global reaction schemes for hydrocarbon combustion," Combustion and flame, vol. 73, pp. 233-249, 1988.

[57] A. L. Sullivan and R. Ball, "Thermal decomposition and combustion chemistry of cellulosic biomass," Atmospheric Environment, vol. 47, pp. 133-141, 2012.

[58] G. De Soete, "Overall reaction rates of NO and N2 formation from fuel nitrogen," in Symposium (international) on combustion, 1975.

[59] N. Kandamby, G. Lazopoulos, F. C. Lockwood, A. Perera and L. Vigevano, "Mathematical Modeling of NOx Emission Reduction by the Use of Reburn Technology in Utility Boilers," in ASME Int. Joint Power Generation Conference and Exhibition, Houston, Texas, 1996.

[60] S. Pope, "Computationally efficient implementation of combustion chemistry using in situ adaptive tabuilation," Combustion Theory and Modeling, vol. 1, pp. 41-63, 1997.

[61] T. Klason, X. Bai, M. Bahador, T. Nilsson and B. Sunde´n, "Investigation of radiative heat transfer in fixed bed biomass furnaces," Fuel, vol. 87, pp. 2141-2143, 2008.

[62] G. Hartung, J. Hult, C. F. Kaminski, J. W. Rogerson and N. Swaminathan, "Effect of heat release on turbulence and scalar-turbulence interaction in premixed combustion," Physics of Fluids, vol. 20, 2008.

[63] R. Mehrabian, Writer, CFD Simulation of the Thermal Conversion of Solid Biomass in Packed Bed Furnaces. [Performance]. (PhD thesis) the Institute for Process and Particle Engineering Graz University of Technology, 2013.

Chapter 7: Conclusions and recommendations for future studies

A summary of the findings of this research is presented below, followed by a highlight of the major contributions of the current study along with suggested future research directions.

7.1 Research summary and major findings

A numerical model for simulating the gas-phase combustion of grate firing biomass furnaces was developed. To account for the conversion of solid biomass fuel into the volatile gases within the bed section, two simplified bed models were adopted; namely a semi-empirical bed model, and a particle-based bed model which uses thermal conversions processes (i.e., drying and devolatilization) and heterogeneous char reaction sub-models. The validation of the simulation was carried out using published measurements of a 8kW lab-scale grate-firing biomass furnace. The effects of the adopted chemical mechanism and turbulence model on the gas-phase predictions of temperature and species concentrations were investigated. Moreover, a comprehensive study was conducted on the role of combustion model in gas-phase biomass combustion, and as the result, a novel combustion model on the framework of EDC approach was proposed and examined. Briefly, the findings and contributions of this research are summarized below:

- The application of the standard EDC poses a challenge in modeling weakly turbulent flow condition and turbulent reacting flow with comparable chemical and mixing time scales. Such conditions may occur in the vicinity of the bed section of a grate-firing biomass

furnace, where the chemistry and turbulent flow are strongly coupled. The study of this thesis showed that the performance of the EDC model can be improved by modifying the values of its coefficients depending of the turbulent flow conditions.

- The sensitivity analysis on the EDC's coefficients (i.e., C_γ and C_τ) revealed that, compared to the standard value of C_γ, using a smaller value for this coefficient can improve the predictions in weakly turbulent flow conditions and a higher value of C_γ results in better predictions in highly turbulent flow condition. However, the predictions were improved in both weakly and highly turbulent flow conditions when using a larger value of C_τ than its standard. In conclusion, the predictions showed more sensitivity to the value of C_γ than the value of C_τ.
- Based on the results of sensitivity analysis on the EDC's coefficients, a method of improving the values of C_γ and C_τ was proposed (chapter 3). That is, a mathematical methodology was used to calculate the values of C_γ and C_τ via using the turbulent flow characteristics (i.e., turbulent Reynolds number and turbulent time scale).
- The EDC with modified coefficients was examined and compared with the standard EDC model, in simulating a gas-phase combustion of a small-scale grate-firing biomass combustor, and the improvements in the predictions of temperature and CO concentrations were highlighted using EDC with modified coefficients (chapter 3). Briefly, it was found that if the modification is performed for weakly turbulent flow condition, the prediction of temperature field will be improved only in vicinity of the bed. On the other hand, the best prediction of CO concentration was achieved when modifying the EDC's coefficients based on highly turbulent flow condition.

- The modifications of the values of EDC's coefficients, which were performed based on the turbulent flow characteristics (i.e., turbulent Reynolds number and turbulent time scale), can affect the performance of the model within the entire computational domain (chapter 3). It is concluded that this general modification of the EDC's coefficients is not suitable for complex industrial geometries in which a flow-field with different levels of turbulence exists. Thus, such a modification was then performed based on local flow-field information, which is referred to here as extended EDC approach. The results of the sensitivity analysis performed in chapter 2 were used in developing the extended EDC approach.
- The effect of chemical mechanism on the predictions of temperature and species concentrations was found to be more pronounced only in high temperature regions, where the dissociation of major species to intermediate species takes place. In general, adequate predictions of temperature, major species and slow-forming CO pollutant of the gas-phase of biomass combustion was achieved by employing a reduced chemical mechanism. As discussed in details in chapters 4 and 6, the four-step chemical mechanism of combustion of methane in combination with the reduced chemical mechanism of levoglucosan ($C_6H_{10}O_5$) oxidation can lead to adequate predictions of the concentrations of major and minor slow-forming species in simulation of the gas-phase biomass combustion.
- The effect of turbulence model was found to be significant when using mixture fraction based combustion models, and the predictions showed insignificant improvements when the EDC approach was adopted with different $k-\varepsilon$ turbulence models.
- This study showed that, in the case of small scale grate-firing biomass combustors, mixture fraction based combustion models (SFM and UFM) can be applied to account for the

interaction of chemistry/flow-field. However, only UFM approach produced predictions of slow-forming CO emissions comparable to its experimental counterpart (chapter 4).

- The results in chapters 5 and 6 demonstrated the suitability of the extended EDC approach for the simulation of non-premixed turbulent flames with different fuel-mixture compositions at different turbulent flow conditions. This is an indication of the possibility to apply the extended EDC approach to model various combustion devices which feature non-premixed flame regimes, such as industrial-size scale grate-firing furnaces.

7.2 Recommendation for future studies

There are still many areas of research in biomass combustion which require further studies. Some research directions are highlighted below.

1. In grate-firing biomass furnaces, the inhomogeneity of biomass fuel (i.e., variation in quality and moisture content of biomass particles) and insufficient mixing between under-fire injected air and solid char particles within the bed results in a non-uniform char surface combustion and a non-uniform devolatilization process within the bed [1]. While there exist numerous studies in the literature on bed models (e.g., homogeneous bed models, heterogeneous thermally thin or thick bed models, etc. [2, 3, 4, 1]), more studies are still required to better describe the non-uniform characteristics of the thermal conversion and char-combustion processes in the bed section.
2. The influence of the assumed composition of heavy hydrocarbon (i.e., tar) released during devolatilization is another challenge in modeling the bed section. While there are still ongoing studies for determining the composition of tar (based on the biomass origin and particle temperature during the devolatilization process [5]), the composition and properties of this species were mostly approximated by those of levoglucosan ($C_6H_{10}O_5$)

in modeling the bed section [6]. However, the chemical interactions between levoglucosan with oxygen and other volatile gases have to be described by a set of complex reaction mechanisms, which contains numerous intermediate species [7, 8]. Therefore, to accurately describe the pathway of tar consumption in the gas-phase freeboard modeling, a detailed chemical mechanism seems necessary. On the other hand, it is well known that tar becomes very reactive when in contact with a hot layer of char, leading to breaking down the tar component into secondary lighter hydrocarbons (e.g., CO, CH_4, C_6H_6, C_2H_4, etc.) [5, 9, 10]. Assuming the secondary products from tar cracking may affect the temperature and species profiles released from the fuel bed boundary with the freeboard, which consequently can affect the overall gas-phase combustion within the freeboard [5]. Therefore, comprehensive studies on the influence of the composition of tar, and the effects of detailed and reduced reaction mechanisms of tar oxidation and tar gasification are required. Moreover, a sub-model may also need to be developed in order to better describe the cracking process of tar component into lighter hydrocarbons.

3. As stated in chapter 4, the mixture fracture based combustion models have been examined in a few published works related to grate-firing biomass combustion (e.g., [10, 11, 12]). Describing the thermal conversion of solid biomass particles and char surface reactions with only one mixture fraction parameter is challenging and requires further studies [13]. In the case of small-scale fixed bed furnaces, in which the overall length of the bed is small enough, the average temperature and mass fraction of the species can be used to define a tabulated flamelet library and mixture fraction [11, 10]. However, such an assumption for grate-firing furnaces with a larger bed's length poses a considerable challenge, as it may lead to inaccurate definition of the fuel bed boundary. The overall challenges related to

the description of the bed section using mixture fraction variable are related, first, to the correlation of the lengthwise temperature and mass factions of the species along the bed with only one single mixture fraction variable (e.g., [14]); and second, how to best define the inlet mass fractions of reactors for defining a flamelet library. Thus, the application of mixture fraction based combustion requires further investigation to account for chemistry/flow-field interaction in biomass combustion of grate-firing furnaces.

4. The extended EDC approach proposed in this thesis is a step further in the simulation of the gas-phase biomass combustion in the freeboard section of the furnace. This model showed superior performance for modeling biomass-gas-derived flames over a wide range of turbulent reacting flow conditions. However, the performance of this model needs to be evaluated for modeling other combustion devices such as swirling burners. Moreover, as the model performance was examined on predominantly non-premixed flames, the coefficients of the model may need to be adjusted for modeling other combustion regimes such as turbulent partially premixed regimes. Therefore, further studies are required to enlarge the application of the extended EDC approach for modeling other biomass-related combustion applications (e.g., biogas burners, biomass gasifiers, fluidised bed biomass furnaces, etc.).

7.3 References

[1] R. Mehrabian, A. Shiehnejadhesar, R. Scharler and I. Obernberger, "Multi-physics modelling of packed bed biomass combustion," Fuel, vol. 122, pp. 164-178, 2012.

[2] R. van der Lans, L. Pedersen, A. Jensen, P. Glarborg and K. Dam-Johansen, "Modelling and experiments of straw combustion in a grate furnace," Biomass and bioenergy, vol. 19, pp. 199-208, 2000.

[3] J. Saastamoinen, R. Taipale, M. Horttanainen and P. Sarkomaa, "Propagation of the ignition front in beds of wood particles," Combustion and flame, vol. 123, pp. 214-226, 2000.

[4] S. Hermansson and H. Thunman, "CFD modelling of bed shrinkage and channelling in fixed-bed combustion," Combustion and flame, vol. 158, pp. 988-999, 2011.

[5] R. Mehrabian, Writer, CFD Simulation of the Thermal Conversion of Solid Biomass in Packed Bed Furnaces. [Performance]. (PhD thesis) the Institute for Process and Particle Engineering Graz University of Technology, 2013.

[6] E. Girgis and W. L. H. Hallett, "Wood Combustion in an Overfeed Packed Bed, Including Detailed Measurements within the Bed," Energy and fuels, vol. 24, pp. 1584-1591, 2010.

[7] A. L. Sullivan and R. Ball, "Thermal decomposition and combustion chemistry of cellulosic biomass," Atmospheric Environment, vol. 47, pp. 133-141, 2012.

[8] E. Ranzi, A. Cuoci, T. Faravelli, A. Frassoldati, G. Migliavacca, S. Pierucci and S. Sommariva, "Chemical Kinetics of Biomass Pyrolysis," Energy and fuels, vol. 22, pp. 4292-4300, 2008.

[9] R. Yin, R. Liu, J. Wu, C. Sun and C. Wu, "Influence of particle size on performence of a pilot-scale fixed-bed gasification system," Bioresource technology, vol. 119, pp. 15-21, 2012.

[10] M. Farokhi, M. Birouk and F. Tabet, "A computational study of a small-scale biomass burner: The influence of chemistry, turbulence and combustion sub-models," Energy Conversion and Management, vol. 143, pp. 203-217, 2017.

[11] M. Buchmayr, J. Gruber, M. Hargassner and C. Hochenauer, "A computationally inexpensive CFD approach for small-scale biomass burners equipped with enhanced air staging," Energy Conversion and Management, vol. 115, pp. 32-42, 2016.

[12] M. Buchmayr, J. Gruber, M. Hargassner and C. Hochenauer, "Performance analysis of a steady flamelet model for the use in small-scale biomass combustion under extreme air-staged conditions," Journal of the Energy Institute, 2017.

[13] R. S. P. K. I. O. S. Zahirović, "Validation of flow simulation and gas combustion sub-models for the CFD-based prediction of NOx formation in biomass grate furnaces," Combustion Theory and Modelling, vol. 15, pp. 61-87, 2010.

[14] B. Albrecht, S. Zahirovic, R. Bastiaans, J. Van Oijen and L. de Goey, "A premixed flamelet - PDF model for biomass combustion in a grate furnace," Energy and fuels, vol. 22, pp. 1570-1580, 2008.

[15] S. Zahirovic, R. Scharlera, P. Kilpinenc and I. Obernbergera, "A kinetic study on the potential of a hybrid reaction mechanism for prediction of NOx formation in biomass grate furnaces," Combustion Theory and Modelling, vol. 15, pp. 645-670, 2011.

[16] S. Sukumaran and S. Kong, "Modeling fuel NOx formation from combustion of biomass-derived producer gas in a large-scale burner," Combustion and Flame, vol. 160, pp. 2159-2168, 2013.

[17] E. Houshfar, R. Khalil, T. Lovas and O. Skreiberg, "Enhanced NOx reduction by combined staged air and flue gas recirculation in biomass grate combustion," Energy and fuel, vol. 26, pp. 3003-3011, 2012.

[18] C. Mandl, I. Obernberger and R. Scharler, "Characterisation of fuel bound nitrogen in the gasification process and the staged combustion of producer gas from the updraft gasification of softwood pellets," Biomass and Bioenergy, vol. 35, pp. 4595-4604, 2011.

[19] E. Houshfar, O. Skreiberg, D. Todorovic, A. Skreiberg, T. Lovas, A. Jovovic and L. Sorum, "NOx emission reduction by staged combustion in grate combustion of biomass fuels and fuel mixtures," Fuel, vol. 98, pp. 29-40, 2012.

Appendix A: UDF codes

The in-house developed UDF codes presented below were part of the development of the extended EDC approach using Fluent software. These codes were used in chapters 5 and 6. At first, the required parameters for determining the average reaction rate of species by the extended EDC were calculated. Later on, the average reaction rate of each species was implemented in Fluent using a source term in the transport equation of the species. Moreover, another UDF code was developed to describe to mass fraction of the gas species released during devolatilization process (chapter 6).

A.1. Global UDF functions and variables

The following functions and variables are used by all UDF codes related to the extended EDC approach. These functions are used to calculate the values of turbulent Reynolds number (i.e., *ret*), Kolmogorov time scale (i.e., *kolt*) and turbulent time scale (i.e., *turbt*).

```
double mwii[60];
real hfii[60];
real hfii2[60];

double ret(cell_t c,Thread *t)
{return MAX(1e-10,pow(C_K(c,t),2)*C_R(c,t)/(C_D(c,t)*C_MU_L(c,t))); }

double turbt(cell_t c,Thread *t)
{return (C_K(c,t)/C_D(c,t)); }

double kolt(cell_t c,Thread *t)
{return pow(C_MU_L(c,t)/(C_R(c,t)*C_D(c,t)),0.5); }
```

A.2. Extended EDC's coefficients

This UDF code is used to determine the required coefficients for the extended EDC model. This function stores the values of the required parameters of the extended EDC in the local memories associated to each computational cell (i.e., *C_UDMI(c,t,i)*, where "*i*" represents the i[th] local memory associated to cell(c,t)). The values of N_η, D_c, τ^*, γ^*, γ_λ^2, l^* and C_τ are calculated here. Later on, based on the calculated values of the aforementioned parameters, the value of the average mass exchange rate between a fine structure and the computational cell (i.e., $\gamma_\lambda^2/\left((1-\gamma^*)\tau^*\right)$) is determined.

```
DEFINE_ADJUST(edc_cte, d)
{
        Thread *t;
        cell_t c;
        int i;
        double cs,cv,alfa,alfa1,alfa2,d3,gmaxlow,gmaxhigh,f1,n1,top1,bot1;

        cs=.35;
        alfa1=1.75;
        alfa2=3.15;
        thread_loop_c (t,d)
        {
                begin_c_loop (c,t)
                {
                        C_UDMI(c,t,200)=50./(ret(c,t)+50.);
                        C_UDMI(c,t,201)=0.02*ret(c,t)/(0.02*ret(c,t)+1.);
                        C_UDMI(c,t,202)=pow(ret(c,t),1.5)/(3.1415);
                        C_UDMI(c,t,212)=alfa1*C_UDMI(c,t,200)+alfa2*C_UDMI(c,t,201);

                        C_UDMI(c,t,203)=1.+log(C_UDMI(c,t,202))/log(pow(ret(c,t),0.75));
                        C_UDMI(c,t,203)=MAX(C_UDMI(c,t,203),2.001);
                        C_UDMI(c,t,203)=MIN(C_UDMI(c,t,203),3.0);

                        gmaxlow=0.01;
                        gmaxhigh=0.80;
                        f1=0.01;
                        C_UDMI(c,t,204)=f1;
                        for (f1=0.01; f1<0.80; f1=f1+0.0125)
                        {
                                top1=(2./3.)*(C_UDMI(c,t,203)-2.)/(3.-C_UDMI(c,t,203));
                                top1=pow(f1,top1);
                                bot1=1.-f1;
```

```
                    n1=top1/bot1;
                    if(n1<1) {
                    C_UDMI(c,t,204)=f1;
                    }
                    else {
                            break;
                    }
            }

            C_UDMI(c,t,205)=pow(ret(c,t),-0.75);
            C_UDMI(c,t,210)=ret(c,t);
            C_UDMI(c,t,206)=pow(C_UDMI(c,t,212),3.-
            C_UDMI(c,t,203))*pow(C_UDMI(c,t,205),3.-C_UDMI(c,t,203));
            C_UDMI(c,t,206)=MIN(C_UDMI(c,t,206),C_UDMI(c,t,204));
            C_UDMI(c,t,206)=MAX(C_UDMI(c,t,206),0.);
            C_UDMI(c,t,207)=(2./3.)*(C_UDMI(c,t,203)-2.)/(3.-
            C_UDMI(c,t,203));
            C_UDMI(c,t,207)=pow(C_UDMI(c,t,206),C_UDMI(c,t,207));
            C_UDMI(c,t,208)=(1.+(2./3.)-C_UDMI(c,t,203)/3.);
            C_UDMI(c,t,208)=C_UDMI(c,t,208)/(3.-C_UDMI(c,t,203));
            C_UDMI(c,t,208)=pow(C_UDMI(c,t,206),C_UDMI(c,t,208));
            C_UDMI(c,t,103)=0.5*turbt(c,t)*C_UDMI(c,t,208);
            C_UDMI(c,t,211)=C_UDMI(c,t,103)/kolt(c,t);
            C_UDMI(c,t,209)=1.-C_UDMI(c,t,206);
            C_UDMI(c,t,209)=C_UDMI(c,t,207)/C_UDMI(c,t,209);
            C_UDMI(c,t,209)=MIN(1.,C_UDMI(c,t,209));
            C_UDMI(c,t,209)=MAX(0.,C_UDMI(c,t,209));
            C_UDMI(c,t,104)=C_R(c,t)*C_UDMI(c,t,209)/C_UDMI(c,t,103);
        }
        end_c_loop (c,t)
    }
}
```

A.3. Setting the properties

The following UDF sets the required molecular weights and enthalpy of formations of the species. The code sets the values of molecular weight and enthalpy of formation of each species into the global variable *mwii* and *hfii2*, respectively:

```
DEFINE_ON_DEMAND(set_prop)
{
    Domain *d=Get_Domain(1);
    Thread *t;
    cell_t c;
    int i,j,k;
    Material *m=mixture_material(d), *sp;
    double mw[500],h_f[500],h_fi[500];
```

```
        mixture_species_loop(m,sp,k)
        {
                mw[k]=(double)MATERIAL_PROP(sp,PROP_mwi);
                h_f[k]=(double)MATERIAL_PROP(sp,PROP_hform);
                h_fi[k]=(double)MATERIAL_PROP(sp,PROP_href);
                mwii[k]=mw[k];
                hfii[k]=h_fi[k];
                hfii2[k]=h_f[k];
        }
}
```

A.4. Source terms

This UDF code calculates the energy source term due to the extended EDC reaction rates.

```
DEFINE_SOURCE(heat,c,t,ds,eqn)
{
        int i;
        double rr1,rr2;
        real source;
        double tst1=0.2;

        rr1=0.;
        rr2=0.;

        for (i=0; i<n_spe; ++i)
        {
                rr2=C_UDMI(c,t,104)*(C_YI(c,t,i)-C_UDMI(c,t,i+60));

                /* No need to use flag-check if CHEM_STEP used */
                if(C_UDMI(c,t,111)<1.)
                {
                        rr2=C_UDMI(c,t,104)*C_UDMI(c,t,103);
                        rr2=rr2/(C_UDMI(c,t,211)*tst1);
                        rr2=rr2*(C_YI(c,t,i)-C_UDMI(c,t,i+60));
                /* --> without flag: rr2=C_UDMI(c,t,104)*(C_YI(c,t,i)-C_UDMI(c,t,i+60)); */

                }
                if (C_UDMI(c,t,i+60) <= 0.)
                {
                        rr2=0.;
                }
                rr1 +=rr2*(hfii2[i]);
        }

        source=(real)rr1;
        ds[eqn]=0;
        return source;
}
```

The following UDF codes calculate the species source term due to the average reaction rates using the extended EDC. The value of Y_i^* can be either estimated using '*ts_check*' UDF macro, or be calculated using '*react_chg*' and '*stage_det*' UDF macros.

```
DEFINE_ADJUST(ts_check, d)
{
	Thread *t;
	cell_t c;
	real tst=0.2;
	int i;

	/* caution about ts ---> tst ---> tst0, species & energy relaxation factors
	/* suitable for chem-equilibrium condition. */

	thread_loop_c (t,d)
	{
		begin_c_loop (c,t)
		{
			C_UDMI(c,t,110)=C_UDMI(c,t,110)+C_UDMI(c,t,211)*tst;
			C_UDMI(c,t,110)=MIN(C_UDMI(c,t,110),C_UDMI(c,t,103));

			for(i=0; i<n_spe; ++i)
			{
				C_UDMI(c,t,i+60)=C_YI_EDC(c,t,i);
			}

			if(C_UDMI(c,t,110)<C_UDMI(c,t,103))
			{
				C_UDMI(c,t,110)=C_UDMI(c,t,110)+C_UDMI(c,t,211)*tst;
				C_UDMI(c,t,111)=0.;
			}
			else{
				C_UDMI(c,t,110)=0.;
				C_UDMI(c,t,111)=2.;
			}
		}
		end_c_loop (c,t)
	}
}

/* without flag; ts_check */
/* Note: ISAT connection has to be defined, see --->
/* R. Gordon, PhD thesis at: hdl.handle.net/2123/4944
/* <--- */

static void stage_det(cell_t c,Thread *t,struct particle_struct *pp,double dt,double p,double *s0,double
*s1,int tab_index)
```

```
{
        /* if used, 'isat_par', 'h0_mix' and 'h1_mix' has to be globally defined */

        s0[n_spe]=h0_mix;
        isat_par->isat_step(c,t,pp,dt,p,rho_star,s0,s1,tab_index);
        h0_mix= s1[n_spe];
}
```

The variable '*isat_par*' is a data structure variable related to ISAT library, and has to be connected to the available ISAT tables. The method of connecting a data structure ISAT variable to an ISAT table is presented in [1].

```
DEFINE_CHEM_STEP(react_chg,c,t,pp,nump,n_spe,dt,pres,temp,yk)
{
        int i;
        double c1,rmwt,r_mix;
        Domain *d=Get_Domain(1);
        Material *mix1=mixture_material(d);
        double h1[300],h2,stage0[300],stage1[300];
        real temp_stage0,p_stage0;

        /* if used, 'h0_mix' and 'h1_mix' have to be globally defined */

        c1=C_UDMI(c,t,103);
        c1=MAX(c1,1.e-7);
        temp_stage0=(real)(*temp);
        p_stage0=(real)(*pres);
        rmwt=0.;

        for (i=0; i<n_spe; ++i)
        {
                /* species enthalpy - fine scale - j/kg -> species.h */
                h1[i]=(real)species_enthalpy(c,t,mix1,i,temp_stage0);
                stage0[i]=yk[i]/mwii[i];
                rmwt +=yk[i]/mwii[i];
        }
        r_mix=UNIVERSAL_GAS_CONSTANT*rmwt;
        rho_star=(p_stage0/temp_stage0)/((real)r_mix);

        /* mixture enthalpy -> prop.h */
        h0_mix=(double)Enthalpy(mix1,temp_stage0,rho_star,p_stage0,yk,h1);
        stage_det(c,t,pp,c1,p_stage0,stage0,stage1,0);

        for (i=0; i<n_spe; i++)
        {
                C_UDMI(c,t,i+60)=stage1[i]*mwii[i];
                yk[i]=C_UDMI(c,t,i+60);
```

```
        }

        /* temperature - fine scale – may NOT be required */
        *temp=(double)Temperature(mix1,h2,rho_star,p_stage0,temp_stage0,yk,h1);
}

DEFINE_SOURCE(sp_0,c,t,ds,eqn)
{
        int i=0;
        real rr1,rr2;
        real source;

        /* This is a sample UDF for species "0" (e.g., O2).
        /* No need to use flag-check if CHEM_STEP used */

        if(C_UDMI(c,t,111)>1.)
        {
                source=(real)(C_UDMI(c,t,104)*C_UDMI(c,t,i+60))-
                (real)(C_UDMI(c,t,104)*C_YI(c,t,i));
                ds[eqn]=(real)(-C_UDMI(c,t,104));
        }
        else{
                source=0.;
                ds[eqn]=0.;
        }
        return source;
}
```

A.5. Volatile compositions

The following UDF code breaks down the composition of the artificial volatile species to appropriate volatile gases.

```
DEFINE_EXECUTE_AT_END(devol2)
{
        Domain *d=Get_Domain(1);
        Thread *t;
        cell_t c;
        int num_vol,i;
        double mass_tot,mass_vol,MW_vol;
        double n_spe_coef[20],mass_spe[20],mass_extra[20],y_spe[20],per[20];
        for(i=0; i<n_spe; ++i)
        {
                n_spe_coef[i]=0.;
        }
        n_spe_coef[1]=10.4;
        n_spe_coef[2]=2.2;
```

```
        n_spe_coef[3]=9.7;
        n_spe_coef[4]=5.4;
        n_spe_coef[5]=0.957;
        n_spe_coef[9]=0.101;
        thread_loop_c (t,d)
        {
                begin_c_loop (c,t)
                {
                        mass_tot=0.;
                        for(i=0; i<n_spe; ++i)
                        {
                                mass_spe[i]=C_R(c,t)*C_YI(c,t,i);
                                mass_tot=mass_tot+mass_spe[i];
                        }
                        mass_vol=mass_spe[0];
                        mass_spe[0]=0.;
                        MW_vol=mwii[0];
                        for(i=0; i<n_spe; ++i)
                        {
                                per[i]=n_spe_coef[i]*mwii[i]/MW_vol;
                                mass_extra[i]=mass_vol*per[i];
                                mass_spe[i]=mass_spe[i]+mass_extra[i];
                                y_spe[i]=mass_spe[i]/mass_tot;
                                if(i==0)
                                {
                                        y_spe[i]=0.;
                                }
                                C_YI(c,t,i)=y_spe[i];
                        }
                }
                end_c_loop (c,t)
        }
}
```

A.6. References

[1] R.L. Gordon, writer, P.hd. thesis [Performance], A numerical and experimental investigation of autoignition, PhD thesis; The University of Sydney, Australia. 2008.

Appendix B: Uncertainties of experimental measurements

In this research, as already mentioned in chapters 2-6, the experimental data chosen for verifications and validations of the numerical simulations are selected from the work of Barlow and Frank [1] (jet flames), Sandia $CO/N_2/H_2$ flame [2], as well as Wiinikka [3] and Klason and Bay [4] (biomass furnace). Therefore, the discussion about the uncertainty of experimental measurements are limited to the available information provided and reported in the aforementioned experimental studies.

B.1. Methodology on error analysis in experimental measurements

As explained in Ref [5], the uncertainty E_V of a measured quantity $V(x_i)$, is commonly defined as follows (x_i and V are, respectively, the independent and dependent variables):

$$E_V^2 = B_V^2 + P_V^2 \tag{B1}$$

where, B_V and P_V are biased (or systematic) and precision errors, respectively [6]. The biased error can be determined as follows [6]:

$$B_V^2 = \sum a_{xi}^2 \, B_{xi}^2 \tag{B2}$$

where B_{xi} is the systematic uncertainty of x_i in measuring variable V by an experimental probe, which can be obtained from manufacturer's specification catalogue, and a_{xi} is the sensitivity coefficient defined as $a_{xi} = \partial V / \partial x_i$ [5, 6]. To obtain the value of the precision error, the method outlined by Rabinowicz [7] and Holman and Gajda [8] might be used, as follows:

$$P_V = t\sigma/\sqrt{N} \quad \text{(B3)}$$

where N is the number of sample measurements, σ is the standard deviation of V (i.e., $\sigma = \sqrt{\sum_1^N (V_i - \bar{V})^2/N}$), $\bar{V} = \sum_1^N V_i/N$ is the average value of V, and $t = 2$ for a 95% confidence level of measurement [5].

B.2. Sample uncertainties reported in experimental measurements of piloted jet flames

According to the experimental work of Barlow and Frank [1], the estimates of the biased uncertainties are based on analysis of calibration methods, considerations of calibration drift, repeatability of calibrations and allowances for the interpolated calibration curves for CO and H_2 concentrations. Table B1 reports a sample of systematic uncertainty and the relative standard deviation of temperature and species concentrations measured for flames B, D and F of Barlow and Frank (used in chapter 5) [1].

Table B1. Relative standard deviations and biased uncertainties of the scalars [1]

Scalar	σ (rms)	Condition (Y_i, T)	Biased uncertainty
T	1%	N/A, 2140 [K][a]	3%
Y_{CO2}	6%	0.14, 2140 [K] [a]	4%
Y_{OH}	8%	0.0016, 2140 [K] [a]	10%
Y_{H2O}	5%	0.12, 2140 [K] [a]	4%

[a] Premixed CH_4/air with ∅=0.96, uncooled (Hencken) burner, see [1].

B.3. Sample uncertainties reported in experimental measurements of biomass furnace

In case of biomass furnace, while there is only limited available information related to uncertainties of the measurements, nevertheless, the values of standard deviation of the temperature and major species mole fractions (i.e., CO_2, O_2) are reported on the plots of experimental scalar measurements [4]. Table B2 reports the average and standard deviation of temperature measurements from the

eight experimental thermocouple probes located consecutively along the centerline of the furnace. These data are adopted from Refs [3, 4].

Table B2. Average and standard deviations of axial temperature along the centerline of the biomass furnace [3, 4]

	Port1	**Port2**	**Port3**	**Port4**	**Port5**	**Port6**	**Port7**	**Port8**
Ave Temp [K]	1371.85	1734.88	1415.13	1178.14	1211.70	1121.14	1065.58	913.10
Deviation [K]	±49.33	±56.50	±90.00	±66.85	±48.55	±47.75	±40.00	±38.20

B.4. References:

[1] R. Barlow and J. Frank, "Effect of turbulence on species mass fractions in methane/air jet flames," in 27th Symposium (International) on Combustion, The combustion institude, (1998).

[2] R. Barlow, G. Fiechtner, C. Carter and M. Flury, "Sandia/ETH-Zurich CO/H2/N2 flame data - Release 1.1," Sandia, 2002. [Online]. Available: http://www.ca.sandia.gov/TNF.

[3] H. Wiinikka, writer, P.hd. thesis [Performance] “High Temperature Aerosol Formation and Emission Minimisation during Combustion of Wood Pellets”. Luleå University of Technology, (2005).

[4] T. Klason and X. Bai, "Computational study of the combustion process and NO formation in a small-scale wood pelletfurnace," Fuel, vol. 86, pp. 1465-1474, (2007).

[5] M. Akbarzadeh, Writer, P.hd. thesis [Performance] “An Experimental Study on the Liftoff of a Co-Flowing non-Premixed Turbulent Methane Flame: Effect of the Fuel Nozzle Geometry”. University of Manitoba, (2014).

[6] H. Coleman and W. Steele, “Engineering application of experimental uncertainty analysis” AIAA J. 33 (1995)

[7] E. Rabinowicz, “An introduction to experimentaion”. Addison-Wesley Publishing Company (1970).

[8] J. Holman and W. Gajda, “Experimental methods for engineers”. McGraw Hill Inc., New York, (1994).

Appendix C: Mathematical description of sub-models

In this section, a brief mathematical description of the adopted sub-models are presented below. It is notable to mention that a side-by-side comparison of the sub-models may help better understand the differences among the models as well as their level of complexity.

C.1. Species transport approach

In species transport approach, the local mass fraction of species Y_i is achieved though resolving a convection-diffusion transport equation of the ith species, as follows [1]:

$$\frac{\partial(\rho Y_i)}{\partial t} + \nabla.(\rho \vec{v} Y_i) = -\nabla.\vec{J_\iota} + \omega_i + S_i \qquad \text{(C1)}$$

where ω_i is the net rate of production of species i, S_i is the rate of creation of species i from DPM approach, and $\vec{J_\iota}$ is the diffusion flux of species i which is explained comprehensively in [1]. In addition, when using species transport approach, two additional terms may be included in the source term of the energy transport equation as follows: the first term represents the transport of enthalpy due to species diffusion (i.e., $-\nabla.\left[\sum_{i=1}^{N} h_i \vec{J_i}\right]$, where h_i is the enthalpy of species i), which may have a significant effect on the enthalpy field [1]. The second term is energy source due to chemical reaction (i.e., $-\sum_{i=1}^{N} h_i^0 \omega_i / M_i$, where h_i^0 and M_i are the enthalpy of formation and molecular weight of species i, respectively). The combustion model (e.g., EDC) accounts for the net rate of production of species i, which is represented by ω_i in Eq C1.

C.2. Finite-kinetic rate (FKR) approach

The comprehensive description of the EDC approach provided in chapters 2-6, express how this model applies the effect of finite kinetic rate on the average reaction rate of species. In this section, it will be explained how the finite-kinetic rates are accounted for in the EDC model. As explained previously in chapter 2, the fine structure mass fraction of species i (i.e., Y_i^*) is calculated from resolving/integrating the Arrhenius expression of the finite-kinetic rates within the fine-scale over the EDC residence time scale. To do this, the fine structure has to be modeled as either a perfectly stirred or plug flow reactors (i.e., PSR or PFR). If we assume that the Arrhenius description of the finite-kinetic rate (FKR) of the species i coming from a chemical mechanism is represented by ω_i^*, by assuming the fine structure in PSR condition, it can be written that [2, 3]:

$$\frac{dY_i^*}{dt} = \frac{\omega_i^*}{\rho^*} + \frac{(Y_i^0 - Y_i^*)}{\tau^*} \tag{C2}$$

where τ^* and Y_i^0 are, respectively, the EDC residence time and mass fraction of species i in the surrounding fluid of the fine structure. The value of Y_i^* is then calculated by integrating Eq C2 over EDC residence time (i.e., τ^*). On the other hand, if the fine structure is assumed to be in PFR condition, Eq C2 is simplified by eliminating the second term on its right hand side [3]:

$$\frac{dY_i^*}{dt} = \frac{\omega_i^*}{\rho^*} \tag{C3}$$

As mentioned before, Eq C2 or C2 has to be integrated over τ^*. For instance in PFR condition (i.e., Eq C3), by assuming the initial and final mass fractions of species i as, respectively, Y_i^{*0} (before τ^*) and Y_i^{*1} (after τ^*), we can write $Y_i^{*1} = Y_i^{*0} + \int_0^{\tau^*} \frac{\omega_i^*}{\rho^*} dt$. In order to solve this equation, the In-Situ Adaptive Tabulation (ISAT) algorithm may be used [1].

C.3. Flamelet-PDF approach

In the flamelet model offered in ANSYS Fluent, the mass fraction of species i is achieved by solving the flamelet equations in mixture fraction coordinate as follows (by assuming the unity Lewis number) [1]:

$$\rho \frac{\partial Y_i}{\partial t} = 0.5\rho\chi \frac{\partial^2 Y_i}{\partial f^2} + \omega_i \tag{C4}$$

$$\rho \frac{\partial T}{\partial t} = 0.5\rho\chi \frac{\partial^2 T}{\partial f^2} - \frac{1}{c_p}\sum h_i\omega_i + \frac{1}{2c_p}\rho\chi\left(\frac{\partial c_p}{\partial f} + \sum c_{pi}\frac{\partial Y_i}{\partial f}\right)\frac{\partial T}{\partial f} \tag{C5}$$

where f is mixture fraction, χ is scalar dissipation, h_i is the specific enthalpy of species i, c_p and c_{pi} are, respectively, the mixture-averaged and ith species heats [1]. The scalar dissipation is defined as $\chi = 2D|\nabla f|^2$ where D represents diffusion coefficient. Nonetheless, the modeling of scalar dissipation is based on the laminar counter-flow diffusion flame, and it can be modeled as follows [1]:

$$\chi(f) = 0.25\chi_{st}\frac{3\left(\sqrt{\rho_\infty/\rho}+1\right)^2}{2\sqrt{\rho_\infty/\rho}+1}\frac{exp\left(-2\left(erfc^{-1}(2f)\right)^2\right)}{exp\left(-2\left(erfc^{-1}(2f_{st})\right)^2\right)} \tag{C6}$$

where ρ_∞ is the density of the oxidizer stream, χ_{st} and f_{st} represent, respectively, the scalar dissipation and mixture fraction at stoichiometric condition [1]. Based on the laminar diffusion flamelet methodology [4], a turbulent non-premixed flame brush can be modeled as an ensemble of diffusion flamelets [1]. By assuming an adiabatic condition, the species mass fraction and temperature in a diffusion flamelet is parameterized only by mixture fraction and stoichiometric scalar dissipation. The density-weighted mean mass fraction and temperature can be determined using a PDF of f and χ_{st} as follows [1]:

$$\overline{\emptyset} = \iint \emptyset(f, \chi_{st}) P(f, \chi_{st}) df d\chi_{st} \quad \text{(C7)}$$

where $\emptyset$ is temperature or mass fraction, and $P(f, \chi_{st})$ is a joint PDF function which can be simplified to $P_f(f)P_\chi(\chi_{st})$ [1]. Briefly, in order to specify P_f and P_χ, the transport equations of $\bar{f}$ and $\overline{f'^2}$ are solved separately [1]. Later on, a β PDF shape function is considered for P_f, whereas a delta PDF function is assumed for P_χ in which χ_{st} is correlated to $\overline{f'^2}$ following the methodology outlined in [1]. It is notable mentioning that in Eq C5, the effect of radiation is omitted in the flamelet energy equation. Instead, a separate transport equation for mean enthalpy, in which the effect of radiation is accounted for in its source term, is solved [1]. Later on, the non-adiabatic PDF table of temperature is generated where the effect of mean enthalpy is also added as a new dimension to the look-up table (e.g., $\overline{T}(\bar{f}, \overline{f'^2}, \chi_{st}, \overline{H})$).

C.4. P_1-approximation radiation model

In P_1 radiation model, a transport equation is solved to account for the local incident radiation in the computational domain, as follows [1, 5]:

$$\nabla.\left(\frac{1}{3(a+a_s)-Ca_s}\nabla G\right) - aG + 4an^2\sigma T^4 = 0 \quad \text{(C8)}$$

where C is a linear-anisotropic phase function coefficient, a and a_s are, respectively, the absorption and the scattering coefficients, n is the refractive index of the medium, and σ is the Stefan-Boltzman constant [1, 5]. By defining the radiation heat flux as $q_r = -\nabla G/(3(a+a_s)-Ca_s)$ [1, 5], the effect of the radiation heat flux can be introduced as a source term in energy transport equation (i.e., S_h), as follows [1]:

$$S_h = -\nabla.\, q_r = aG - 4an^2\sigma T^4 \quad \text{(C9)}$$

The Weighted-sum-of-Gray-Gases (WSGG) approach is used to account for the absorption coefficient (a) in Eq C8. In WSGG model, the total emissivity over a distance 's' can be approximated as follows:

$$\varepsilon = \sum_{i=0}^{I} a_{\varepsilon,i}(T)(1 - e^{-k_i Ps}) \quad \text{(C10)}$$

where $a_{\varepsilon,i}(T)$ is the emissivity weighting factor of the ith fictitious gray gas as a function of temperature, k_i represents the absorption coefficient of the ith gray gas, and P is the sum of the partial pressures of all absorbing gases (the values of $a_{\varepsilon,i}$ and k_i are provided in FLUENT's database from the works of Coppalle and Vervisch [6], and Smith et al. [7]). If the value of $k_i Ps$ is much smaller than unity for all absorbing gases, Eq (C10) is simplified as $\varepsilon = \sum_{i=0}^{I} a_{\varepsilon,i} k_i Ps$. Using the estimated value of the emissivity (ε), the absorption coefficient (a) can be approximated as the following [1]:

$$a = \sum_{i=0}^{I} a_{\varepsilon,i} k_i P \quad s < 10^{-4}[m] \quad \text{(C11)}$$

$$a = \frac{-\ln(1-\varepsilon)}{s} \quad s > 10^{-4}[m] \quad \text{(C12)}$$

C.5. References

[1] ANSYS, ANSYS Fluent Theory Guide, Release 15.0, Ansys, 2013.

[2] M. Rehm, P. Seifert and B. Meyer, "Theoretical and numerical investigation on the EDC-model for turbulent-chemistry interaction at gasification conditions," Computers and Chemical Engineering, vol. 33, pp. 402-407, 2009.

[3] Z. Li, A. Cuoci, A. Sadiki and A. Parente, "Comprehensive numerical study of the Adelaide Jet in Hot-Coflow burner by means of RANS and detailed chemistry," Energy, vol. 139, pp. 555-570, 2017.

[4] N. Peters, "Laminar diffusion flamelet models in non-premixed turbulent combustion," Progress in Energy and combust. Science., vol. 10, pp. 319-339, 1984.

[5] T. Klason and X. Bai, "Computational study of the combustion process and NO formation in a small-scale wood pelletfurnace," Fuel, vol. 86, pp. 1465-1474, 2007.

[6] A. Coppalle and P. Vervisch. "The Total Emissivities of High-Temperature Flames". Combustion and Flame. 49. 101–108. 1983.

[7] T. F. Smith, Z. F. Shen, and J. N. Friedman. "Evaluation of Coefficients for the Weighted Sum of Gray Gases Model". J. Heat Transfer. 104. 602–608. 1982.

Appendix D: Mesh independency and quantitative analysis

In this section, at first a brief explanation of how the mesh independency procedure has been performed is presented. Later, quantitative comparisons between the predictions and measurements are reported for some simulated cases to better clarify which model leads to closer predictions to the experimental measurements.

D.1. Mesh independency

Mesh independency was performed for all simulations of jet flames and grate firing biomass furnace. In case of jet flames, the initial mesh was generated based on what is reported and suggested in other numerical studies on those flames in the archival literature. After achieving the initial results, the simulations were also performed on the refined grids and the results of axial and radial temperature and mixture fractions achieved from all grids were compared. It is notable mentioning that in most cases, the further grid refinement from those resolution suggested in the literature led to insignificant changes in terms of numerical results of temperature and mixture fraction.

In case of grate firing biomass furnace, the grid was generated based on the previous numerical study performed on the same furnace. However, more simulations were performed using refined grids and it was found that the increase of grid resolution above the bed and close to the exit of the secondary and tertiary jet injectors where high gradients of temperature, species and velocity are expected to occur, has significant impact on the predictions of temperature and velocity fields. On

the other hand, the axial temperature results of the simulations showed insignificant impact of grid refinement performed in downstream of the furnace away from the aforementioned regions.

The procedure of grid independency studied in chapter 6 is presented here. Figures D1a and b show the results of, respectively, axial temperature and velocity along the centerline of the furnace using three different grids (e.g., the coarse grid which consists of 153501 cells, the medium resolution grid which consists of 201227 cells, and the fine resolution grid which consists of 247308 cells). As can be seen from this figure, there can be seen almost identical results of temperature and velocity profiles close to the bed section and downstream of the furnace. On the other hand, there are visibly changes in the results in high temperature region of the furnace, which is more evident for temperature profiles. However, as can be seen in Figure D1a and b, the relative change in both temperature and velocity profiles from medium to fine grids is not considerable and therefore, the medium resolution grid is selected for simulations.

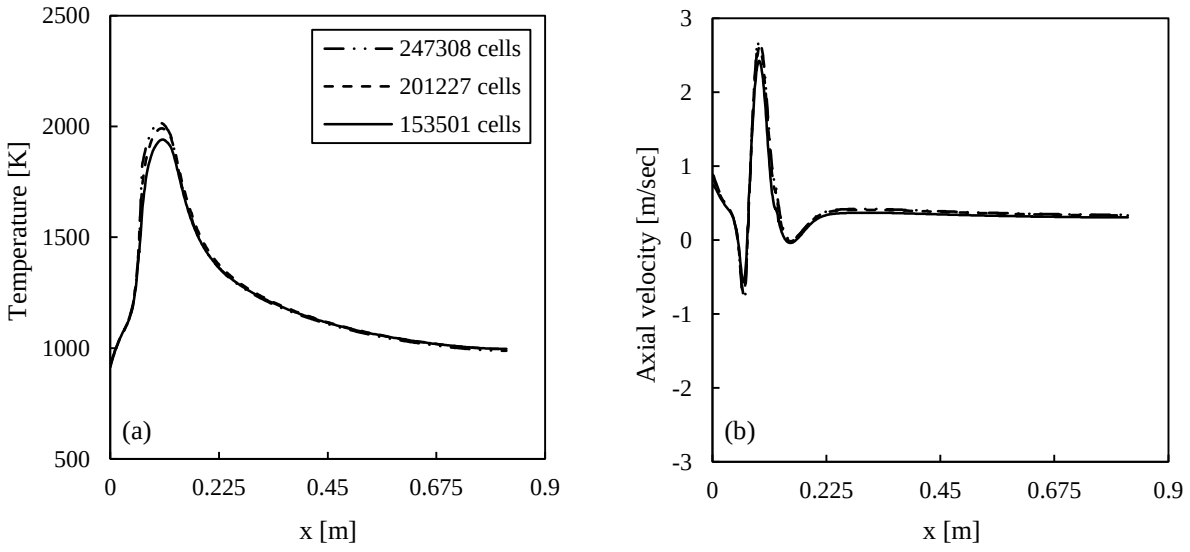

Figure D1. Numerical results of axial (a) temperature and (b) velocity along the centerline of the grate-firing biomass furnace using three different grids.

D.2. Quantitative analysis

In this section, some sample of quantitative analysis between the predictions and experimental measurements are presented using standard and extended versions of the EDC approach. Tables D1 and D2 present the quantitative comparisons between the numerical results of, respectively, mixture fraction and temperature, along with experimental measurements at selected locations of r/d<1 for the weakly turbulent jet flame studied in chapter 5 (i.e., case A in chapter 5). According to Table D1, close to the centerline up to r/d=0.5, the extended EDC results in better quantitative agreement between the measured and predicted mixture fraction, whereas standard EDC provides closer prediction when r/d>0.5. In terms of temperature, the extended EDC provides closer quantitative prediction to the experiment with lower relative errors compared to the standard EDC (see Table D2).

Table D1. Quantitative comparison between measured and simulated values of mixture fraction for case A of chapter 5

r/d	**0.0**	**0.25**	**0.5**	**0.625**	**0.75**	**0.875**
Exp	1.0	0.9128	0.6406	0.4748	0.3376	0.2541
Std EDC	0.8305	0.7642	0.6168	0.5315	0.4751	0.4091
Rel. error (% - Std EDC)	16.95	16.28	3.71	11.94	40.73	61.0
Ext EDC	0.8795	0.8029	0.6471	0.5677	0.5009	0.4312
Rel. error (% - Ext EDC)	12.05	12.04	1.01	19.56	48.37	69.7

Table D2. Quantitative comparison between measured and simulated values of temperature for case A of chapter 5

Mixture fraction	**1.0**	**0.9128**	**0.6406**	**0.4748**	**0.3376**	**0.2541**
Exp	307.5	395.5	743.7	1093.6	1518.7	1884.7
Std EDC	N/A.	N/A.	668.95	1051.46	1586.32	1888.71
Rel. error (% - Std EDC)	N/A.	N/A.	10.051	3.85333	4.4525	0.2127
Ext EDC	N/A.	N/A.	711.841	1065.41	1507.12	1889.07
Rel. error (% - Ext EDC)	N/A.	N/A.	4.28385	2.57774	0.7625	0.2318

Tables D3 and D4 present the quantitative comparisons between the numerical results of, respectively, mixture fraction and temperature, with experimental measurements at selected

locations of r/d<3 for highly turbulent jet flame studied in chapter 5 (i.e., case C in chapter 5). According to Table D3, the extended EDC leads to better quantitative agreement between the measured and predicted mixture fraction in overall. Similarly, in terms of temperature, the extended EDC provides closer quantitative predictions to the experimental measurements with lower relative errors compared to the standard EDC (see Table D4).

Table D3. Quantitative comparison between measured and simulated values of mixture fraction for case C of chapter 5 at x/D=15

r/d	**0.0**	**0.28**	**0.83**	**1.39**	**1.94**	**2.5**
Exp	0.9082	0.8829	0.621	0.2547	0.0873	0.026
Std EDC	0.7995	0.7730	0.6182	0.4193	0.2623	0.1255
Rel. error (% - Std EDC)	11.967	12.439	0.4460	64.639	200.46	382.98
Ext EDC	0.8480	0.8097	0.6120	0.3982	0.2418	0.1041
Rel. error (% - Ext EDC)	6.6289	8.2852	1.4415	56.341	177.04	300.49

Table D4. Quantitative comparison between measured and simulated values of temperature for case C of chapter 5 at x/D=15.

Mixture fraction	**0.9082**	**0.8829**	**0.621**	**0.2547**	**0.0873**	**0.026**
Exp	498	592	1346	1516	864	478
Std EDC	N/A.	N/A.	1334.36	1754.8	813.5	377.17
Rel. error (% - Std EDC)	N/A.	N/A.	0.86478	15.752	5.845	21.094
Ext EDC	N/A.	N/A.	1346.37	1677.1	862.5	447
Rel. error (% - Ext EDC)	N/A.	N/A.	0.02749	10.627	0.177	6.4853

Table D5 shows the quantitative comparisons between the numerical results of temperature, O_2 and CO_2 concentration, with experimental measurements along the centerline of the furnace studied in chapter 6. The relative errors reported in Table D5 are calculated using average value of the measurements. The results in this table show that the extended version of EDC model leads to better quantitative prediction of temperature in vicinity of the bed, whereas both models show comparable quantitative predictions of temperature elsewhere within the furnace. However, in case of predictions of CO_2 and O_2 concentrations, the extended EDC model lead to closer predictions

to the measurements compared to its standard version, evidently downstream of the furnace. Note that the experimental data related to biomass furnace are adopted from Refs [3, 4] of Appendix B.

Table D5. Quantitative comparison between measured and simulated values of temperature, O_2 and CO_2 concentration for study of biomass furnace in chapter 6.

		port1	**port2**	**port3**	**port4**	**port5**	**port6**
Exp T [K]	Max	1422.75	1791.38	1505.13	1313.42	1259.69	1169.89
	Ave	1372.75	1734.88	1415.13	1246.57	1211.14	1122.14
	Min	1322.75	1678.38	1325.13	1179.72	1162.59	1074.39
Std EDC	Value	858.383	1803.26	1434.93	1234.29	1118.97	1048.64
	Rel. error (%)	37.4702	3.94148	1.39916	0.98510	7.61018	6.54998
Ext EDC	Value	1098.01	1924.96	1374.17	1221.72	1112.8	1047.87
	Rel. error (%)	20.0142	10.9564	2.89443	1.99347	8.11962	6.61860
Exp O_2 (%vol)	Max	N/A.	2.70	5.52	6.58	7.09	7.29
	Ave	N/A.	1.72	4.49	5.63	6.14	6.29
	Min	N/A.	0.72	3.55	4.60	5.11	5.32
Std EDC	Value		0.0007	4.4334	6.6425	7.2962	7.38983
	Rel. error (%)		99.959	1.2608	17.984	18.831	17.4853
Ext EDC	Value		0.0935	5.8943	6.9236	6.9524	6.91461
	Rel. error (%)		94.563	31.276	22.976	13.231	9.93021
Exp CO_2 (%vol)	Max	N/A.	17.80	16.61	15.56	15.25	15.16
	Ave	N/A.	16.77	15.58	14.59	14.29	14.15
	Min	N/A.	15.80	14.57	13.61	13.28	13.19
Std EDC	Value		14.814	15.498	13.454	12.846	12.7479
	Rel. error (%)		11.662	0.5531	7.8266	10.086	9.93249
Ext EDC	Value		16.928	14.491	13.516	13.449	13.4802
	Rel. error (%)		0.9446	7.0131	7.3998	5.8661	4.75884

Appendix E: Evaluation of weighting factor coefficient in the extended EDC approach

The performance of the extended EDC model presented in chapter 5 depends strongly on the chosen value of w (i.e., the weighting function coefficient in Eq. (5-25)). The impact of w on the ratio of EDC time scale over the characteristic mixing time is expressed mathematically. The purpose of using weighing function is to pronounce the influence of the specific dependent parameter (i.e., ξ) over a desired range of independent variable (i.e., Re_t). As explained in chapter 5, the mathematical relationship between ξ and w can be expressed as follows:

$$\xi(Re_t) = \frac{w}{w+Re_t}\xi_{low\_Re_t} + \frac{(1/w)Re_t}{1+(1/w)Re_t}\xi_{high\_Re_t} \quad \text{(E1)}$$

where $\xi_{low\_Re_t}$ and $\xi_{high\_Re_t}$ are, respectively, the values of ξ at weakly and highly turbulent flow conditions. Also, the first and second right-hand side of Eq. E1 denote the low and high weighting factors of the weighting function, respectively. Consequently, at low Re_t, the value of ξ tends to approach $\xi_{low\_Re_t}$, whereas at high Re_t, ξ becomes close to $\xi_{high\_Re_t}$. In addition, the value of w dictates how the transition of ξ between $\xi_{low\_Re_t}$ and $\xi_{high\_Re_t}$ takes place (see Figure 5-4).

Figure E1 presents the effect of ξ on the ratio of EDC time scale over the characteristic mixing time scale, τ^*/τ_{mix}. This ratio is also plotted for the standard EDC model as a reference diagram. It is important to mention that in order to better evaluate the influence of ξ on τ^*/τ_{mix} in both low and high turbulent Reynolds number regions, no weighting function is used in the diagrams plotted in Figure E1. As can be seen in this figure, compared to the standard EDC model, when $\xi > 1.75$, the extended EDC diagrams show a tendency of the model to reach lower and higher values of

τ^*/τ_{mix}, at, respectively, low and high turbulent Reynolds numbers. In addition, the profiles in Figure E1 clearly indicate that by using the larger values of ξ, the value of τ^*/τ_{mix} tends to increase under both weakly and highly turbulent flow conditions.

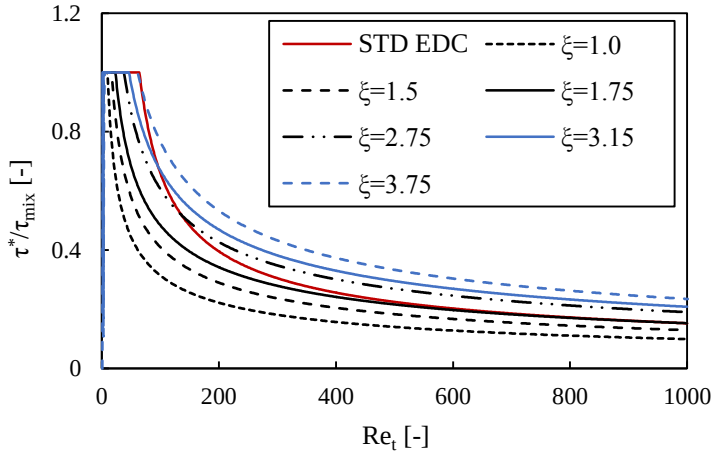

Figure E1. Profiles of τ^*/τ_{mix} by using different values of ξ

The values of $\xi_{low\_Re_t} = 1.75$ and $\xi_{high\_Re_t} = 3.15$ in Eq. (E1) were chosen. As explained in chapter 5, these values led to the best predictions for the simulations of cases A and C (i.e., weakly and highly turbulent diffusion jet flames, see chapter 5). Figure E2 shows the effects of the chosen value of w on τ^*/τ_{mix}. As can be seen in this figure, by increasing the value of w, the impact of low weighting factor (see Eq. (E1)) becomes more pronounced. Similarly, increasing w leads to a decrease in the value of τ^*/τ_{mix} at moderate turbulent Reynolds numbers, whereas its impact at high turbulent Reynolds number is negligible. Hence, according to Figure E2, the effect of w is more pronounced under weakly and moderate turbulent flow conditions.

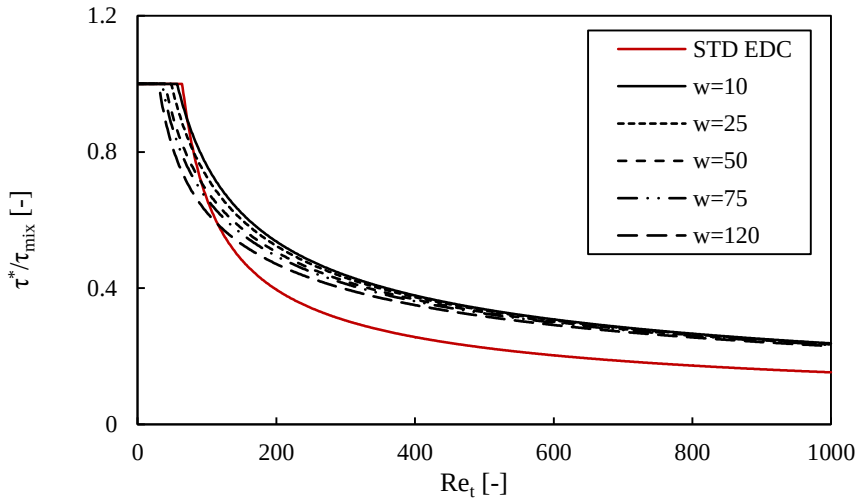

Figure E2. Profiles of τ^*/τ_{mix} by using different values of w

In order to determine the best value of w, a set of sensitivity analysis on this parameter was performed for cases A and B of chapter 5 (i.e., weakly and moderate turbulent jet flames). Figure E3 presents the predictions of mixture fraction (Figure E3a), temperature (Figure E3c) and NO mass fraction (Figure E3e) of a weakly turbulent jet flame at x/D=5, as well as temperature (Figure E3b), H_2 mass fraction (Figure E3d) and CO mass fraction (Figure E3f) of a moderate turbulent jet flame at x/D=15. According to Figure E3a, when increasing the value of w, the prediction of mixture fraction is improved close to the centerline of the burner, whereas smaller values of w lead to better predictions of mixture fraction away from the centerline. In terms of the predictions of temperature and NO mass fractions, the profiles in Figure E3c and e show that for weakly turbulent flow conditions, the best peak values were achieved when $w = 50$. On the other hand, $w = 25$ leads to the best predictions of NO mass fraction in moderate to high mixture fraction regions. In the case of moderate turbulent jet flame, the profiles in Figure E3b, d and f indicate that the effect of w is only noticeable for the predictions of the peak values of H_2 and CO mass fractions. Consequently, the value of $w = 50$ was chosen in order to achieve the best peak values

of mass fractions of slow forming species (CO and NO) and intermediate species (H_2) under both weakly and moderate turbulent flow conditions.

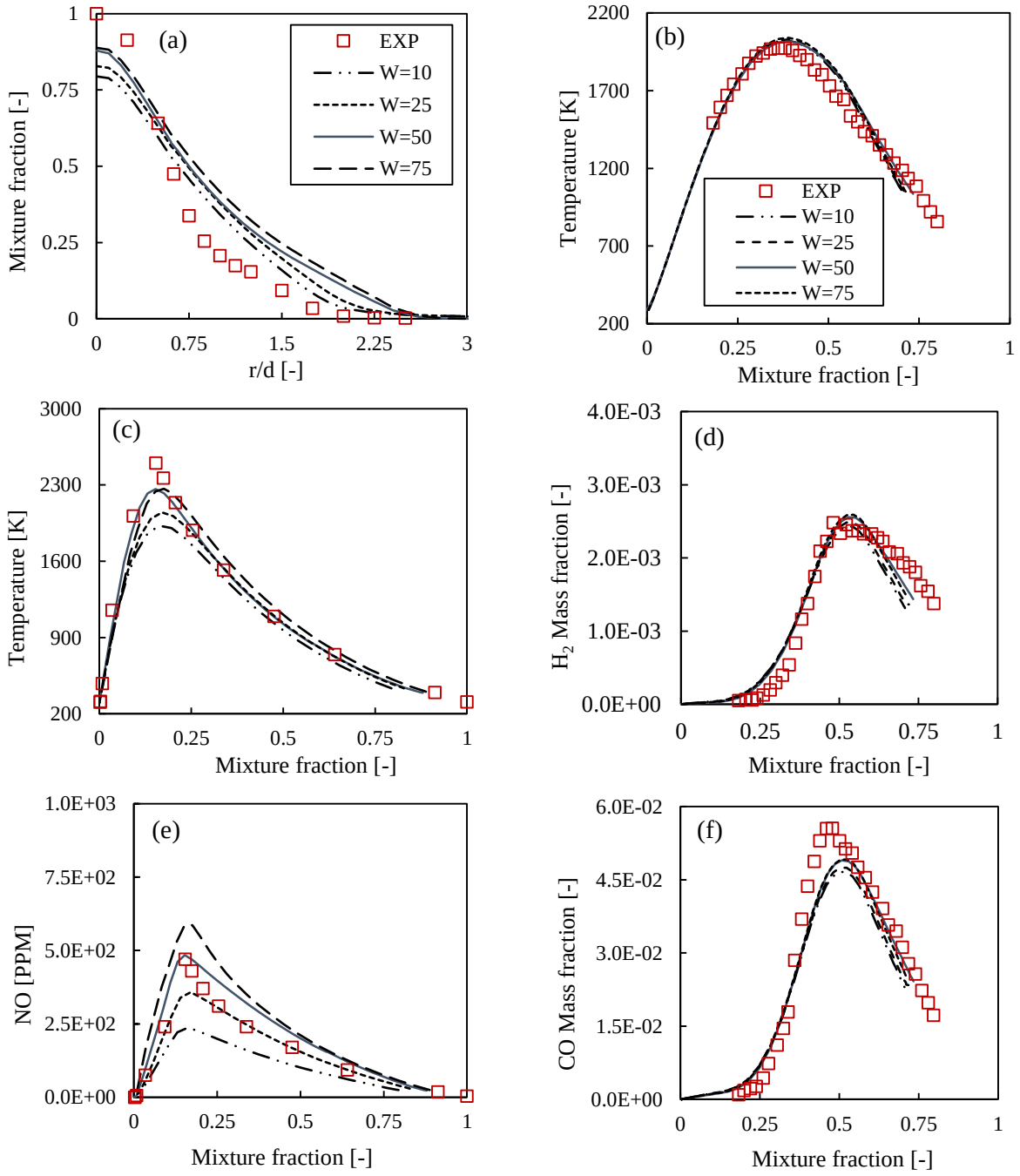

Figure E4. Profiles of (a) mixture fraction, (b and c) temperature, (d) H2 mass fraction, (e) NO mass fraction and (f) CO mass fraction using different values of *w*. Panels a, c and e belong to weakly turbulent jet flames, and panels b, d and f belongs to moderate turbulent jet flame.